Neutrino Induced Showers From Gamma-Ray Bursts

Cover: From the sky to the water, Sandra Perticarari, Trieste © 2011

Neutrino Induced Showers From Gamma-Ray Bursts

academisch proefschrift

ter verkrijging van de graad van doctor
aan de Universiteit van Amsterdam
op gezag van de Rector Magnificus
prof.dr. D.C. van den Boom
ten overstaan van een door het college voor promoties
ingestelde commissie, in het openbaar te verdedigen
in de Agnietenkapel
op vrijdag 27 mei 2011, te 12:00 uur

door

Eleonora Presani

geboren te Trieste, Italie

Promotor: Prof. Dr. P. Kooijman
Co-promotor: Dr. C. J. Reed
Co-promotor: Dr. E. de Wolf

Faculteit der Natuurwetenschappen, Wiskunde en Informatica

All this has already happened, all this will happen again
BSG

Contents

1

Neutrino Astrophysics

> *Two protons expelled at each coupling site creates the mode of force, the embryo becomes a fish though we don't enter until a plate, we're here to experience, evolve the little toe, atrophy, don't ask me how, I'll be dead in a thousand light years, thank you, thank you, genesis turns to its source, reduction occurs step wise though the essence is all one, end of line.*
>
> Hybrid

Introduction

Astronomy is one of the oldest sciences. Since the very beginning of his history, humans started wondering about Nature, and the first objects that caught their attention were astrophysical objects, such as the Sun, the Moon, and the stars. Prehistoric cultures left behind astronomical artefacts such as the Egyptian monuments and Stonehenge, and early civilizations such as the Babylonians, Greeks, Chinese, Indians, and Maya performed methodical observations of the night sky. The technical difficulties in studying such far away objects have always represented the main obstacle to overcome. It is sufficient to think that from prehistoric time the observation of celestial objects could not really improve until the discovery of the telescope, made thousands of year afterwards by Galileo Galilei. Even then, observations were limited to the visible light, a very tiny band of the electromagnetic spectrum.

Centuries after Galileo, at the beginning of the XIX century, Fraunhofer managed to see things invisible up to that moment, and discovered about 600 bands in the spectrum of the Sun using the technique known as spectrography. From that moment it has been possible to observe the sky at different wavelengths, and to disclose new aspects of the sky in different bands of the electromagnetic spectrum. New branches of astronomy arose, such as radio astronomy, infrared, x-ray and gamma astronomy. Each slice of the spectrum can provide different information, and many aspects especially related to the higher end of the spectrum are yet to be completely understood.

Our time is the time in which astrophysics is not looking only at the electromagnetic spectrum any more. With developments in detector technology, new opportunities appeared, giving the possibility to look at different components of our Universe. A new branch of astronomy started, with the name of astroparticle physics. This science aims to look at any signal coming from the Universe, that is not of electromagnetic nature. The sizes and the energies involved in astrophysical phenomena raised the interest in the detection of gravitational waves. Although extremely interesting for the comprehension of the nature of many astrophysical objects and of the fundamental laws of our Universe, gravitational waves are extremely difficult to detect.
Another approach to observe cosmological objects is to measure not only their electromagnetic radiation, but also elementary particles that are generated inside the stars and at the center of the galaxies and that can travel to the Earth. Charged particles coming from the sky have been measured since 1912, when the first "cosmic rays" have been discovered. The question of their origin and their composition, especially for the extremely high energy ones, is still a very open question. This question can be approached in different ways. On the one hand, measuring charged particles at different energy ranges and from different directions in the sky can lead to the comprehension of their origin and composition. Studying the possible sources, for example looking at the highest energies of the electromagnetic spectrum, such as gamma, can also help understanding the physical processes that take place in these objects.
One small and almost invisible particle, though, could carry many of the answers we need to disclose the secrets of the Universe. Neutrinos are very light and neutral particles, extremely difficult to detect because of their small probability of interacting with matter. These particles are produced in several astrophysical sources, such as stars and supernovae, and carry information of processes happening in the very core of these objects.

Neutrino telescopes such as Antares search for neutrinos with very high energies, that can travel extremely long distances in the Universe. Detecting such neutrinos can provide information on processes absolutely invisible by other means. As neutrinos are neutral particles, they do not suffer electromagnetic field deflections while travelling to Earth. This provides a wonderful mean to pinpoint to source of these particles, doing astronomy at energies never reached before.

1.1 History of neutrinos

Like my old particle physics professor said (1), physicists are so attached to the empirical law of energy conservation that they are ready to invent a new particle to defend it. This happened in 1930, when Wolfgang Pauli postulated the existence of a neutral particle to preserve the conservation of energy, momentum, and angular momentum in the beta decay:

$$n \rightarrow p + \mathrm{e}^{-} + \bar{\nu}_e \tag{1.1}$$

In his formulation, Pauli had difficulties in explaining the difference between his neutral particle and the neutral proton theorized by Majorana (2), eventually discovered by Chadwick and identified with the now well known neutron. It was only with the contribution of Enrico Fermi, and his postulation of the weak interactions in 1933-34 that the two particles have been clearly identified as different particles. Fermi is also responsible for the naming of this particle, neutrino, from the Italian "a small neutron".

Immediately, Bethe and Peierls estimated the cross section for such a particle to induce so called "inverse beta decay":

$$\bar{\nu}_e + p \rightarrow e^+ + n. \tag{1.2}$$

Their conclusion was that this cross section was so small that, around 1 MeV, its mean free path in solid matter would be of the order of tens of light-years. This left little hope for a direct detection, and explains why still in the present neutrino detection is so technically challenging.

Things became even more complicated when, in 1937, the particle called muon was discovered in cosmic rays, opening the possibility of a neutrino of a second flavour. The consternation of the physics community is well described by the exclamation of Rabi: "Who ordered that?!"(2). When the decay of the muon was observed in 1941, the habit of explaining the lack of energy with a neutrino was already acquired. Pontecorvo tried another Italian naming calling this second neutrino "neutretto", but this name never caught-on.

In 1955 the pessimistic predictions of Bethe and Peierls were proved wrong by Reines and Cowan, in the experiment that led to the first direct detection of a reactor antineutrino and that earned a Nobel prize for the two scientists (3). In this experiment, antineutrinos created in a nuclear reactor by beta decay were shot into protons producing neutrons and positrons. The positron quickly finds an electron, and they annihilate each other. The two resulting gamma rays are detectable. The neutron can be detected by its capture on a Cadmium nucleus, releasing a gamma ray. The coincidence of both events – positron annihilation and neutron capture – gives a unique signature for an antineutrino interaction.

Another neutrino Nobel prize was awarded to Leon M. Lederman, Melvin Schwartz and Jack Steinberger for their proof, in 1962, that electron neutrinos and muon neutrinos are completely different particles.

The discoveries related to neutrinos did not finish here, but at this point people started to look to the sky to disclose more secrets of this particle.

1.2 Astrophysical Neutrinos

There are several motivations for neutrino astronomy, and cover a variety of fields of physics, from the fundamental physics of these particles, to new discoveries in astroparticle physics. The difficulties of neutrino detection also provide the key to their importance for astrophysics. While charged particles can be deflected by magnetic fields and photons can be absorbed by dense matter, neutrinos can travel through matter and electromagnetic fields without suffering any consequence. They will eventually reach Earth carrying information from the very core of astrophysical objects, at possibly very long distance from our own Galaxy. The different origins and energy ranges of measured neutrinos can help in understanding many of the mysteries in the Universe and in Nature.

1.2.1 Solar neutrinos

One of the first observations of neutrinos coming from outside our planet is the measurement, in the late 1960's, of the first neutrino flux from the Sun. Ray Davis and John N. Bahcall set up the Homestake experiment, a chlorine-based detector. The expected number of solar neutrinos had been computed based on Bahcall's Solar Model which gave a detailed account of the Sun's internal operation. The measured flux, however, was around three times less than expected. Only in the year 2001 the SNO (Sudbury Neutrino Observatory) collaboration presented the scientific results (4) fully explaining the reason for this lack of neutrinos. They showed how neutrinos can oscillate and change their flavour while travelling through the Sun. With the capability to detect both charged current (CC) and neutral current (NC) interactions, they finally resolved the question of the missing neutrinos.

1.2.2 Supernova neutrinos

While searching for proton decay, the Japanese experiment Kamiokande II (5) observed neutrinos in coincidence with the supernova 1987A, that happened in the Magellanic Cloud. Supernovae are today the only confirmed sources of neutrinos outside the Solar System. They are very promising sources to study, but the energy range of supernovae neutrinos is around few MeV, and therefore too low to be detected by high energy neutrino telescopes such Antares. Studies are performed to attempt the detection of an overall increase in the singles rate in the detector caused by a large number of MeV neutrinos interacting inside the volume of the Antares detector (6).

1.2.3 Cosmic neutrinos

One of the main reasons to look for high energy neutrinos is to contribute towards answering the question of the origin and nature of high energy cosmic rays. Cosmic rays are highly energetic charged particles, originating from outer space, that interact in Earth's atmosphere, generating secondary showering particles. Although the exact composition of cosmic rays at very high energies is still under discussion (7, 8), it is known for a vast energy range: about 89% of incoming cosmic ray particles are simple protons, nearly 10% are helium nuclei, and slightly under 1% of cosmic rays are composed of heavier elements. Solitary electrons constitute about 1% of the particles that make up galactic cosmic rays (9).

Cosmic rays have been observed over more than 13 orders of magnitude in energy, up to 10^{20} eV. At energies below ~ 100 GeV the cosmic ray flux, with approximately one particle per square meter and second, is still large enough for direct observations with balloon or satellite experiments. The steep fall of the flux with energy requires larger detectors for observations of the cosmic ray flux above few TeV. At these energies only indirect measurements of the primary particles are possible. This is done using detector arrays, which record secondary particles that are produced in extensive air showers initiated by high energy particles penetrating the atmosphere. The observed spectrum is shown in Figure 1.1. It follows a power spectrum (E^{-a}) and shows an increase in slope at an energy of about 10^{15} eV. This first break is referred to as the "knee". At around 3×10^{18} eV the spectrum flattens again, and this second break is called the "ankle". After the ankle, the origin of the cosmic rays is uncertain. It is unlikely for charged particles of such high energy to travel trough the Cosmos without interacting with background photons and thereby being depleted in energy. Little is known about the sources of these high

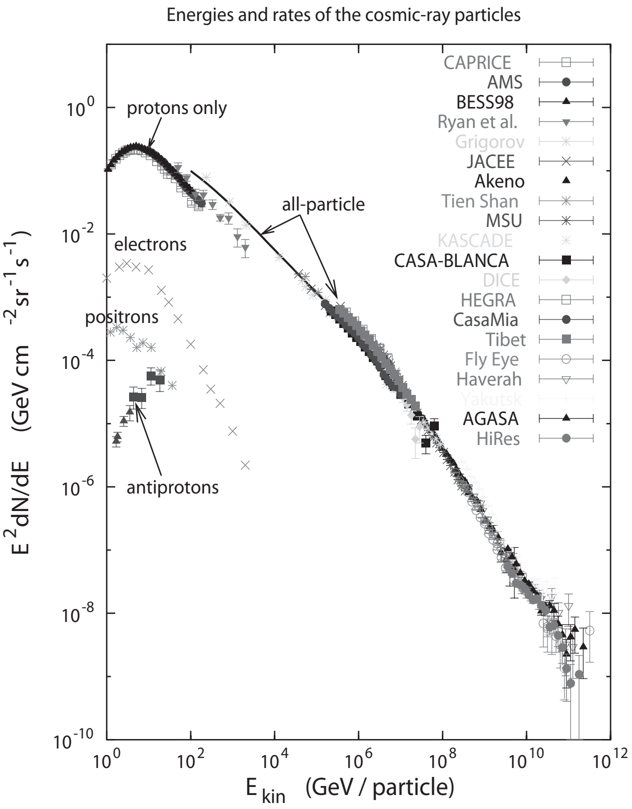

Figure 1.1: Cosmic Ray spectrum from 10^9 to 10^{21} eV as measured on Earth. The flux in the vertical axis has been multiplied by E^2. Figure taken from (10)

energy particles. Detecting high energy neutrinos from point-like sources could provide evidence that the neutrino source is the origin of the high energy cosmic rays. Several possible sources are considered. Active Galactic Nuclei (AGN) are candidates to be such neutrino and high energy cosmic ray sources. An AGN is a compact region at the centre of a galaxy that has a luminosity much higher than normal over possibly all the electromagnetic spectrum. The radiation from AGN is thought to be the result of accretion of mass by the supermassive black hole at the centre of the host galaxy. During the accretion process two highly collimated and fast outflows emerge in opposite directions perpendicular to the disc. These outflows contain highly relativistic matter and can be (one of) the sources of high energy cosmic rays. Another possibility for cosmic ray sources are Gamma Ray-Bursts (GRBs). If charged particles such as protons are present in the jets of AGN or GRBs, neutrinos would also be produced as interaction products of these accelerated charged particles with matter and photon fields. The detection of such neutrinos, or the lack of them, will contribute to understanding the processes involved in the production of high energy particles. The work developed for this thesis is primarily aimed to search for neutrinos in coincidence with GRBs.

2

Gamma-Ray Bursts

> *I don't want to be human! I want to see gamma rays! I want to hear X-rays! And I - I want to - I want to smell dark matter!*
>
> Number One

Gamma-Ray Bursts (GRBs) are extremely intense and relatively short bursts of gamma radiation that occur a few times per day in the detectable Universe. They are the brightest source of gamma radiation in the Universe and their emission exceeds the gamma emission of any other source (in that short period of time, their photon emission is about a 10^5 times brighter than the Sun). For instance, the GRB 080319B[1] was detected by the Swift satellite (11) at 06:12 UTC on March 19, 2008 and was the brightest event in the known sky, second only to the Big Bang itself. The burst set a new record for the most distant object that could be seen with the naked eye, it had a peak apparent magnitude of 5.8 and remained visible to the human eye for approximately 30 seconds (12). The apparent magnitude of an object is a logarithmic measure of its brightness as seen from the Earth. For comparison, the value 0 used to be assigned to the star Vega.

Although much theoretical effort has been expended in calculations regarding the production of gamma rays and other particles from the GRBs, it is now time for the experiments to provide an answer to what really happens during a GRB. Present knowledge suggests that GRBs occur in random directions in the sky and at cosmological distances. The time integrated fluxes, or the fluences, range from $\sim 10^{-4}$ to 10^{-7} ergs cm^{-2} (or from $\sim 10^{-7}$ to 10^{-10} J m^{-2}). This corresponds to a isotropic luminosity of $\sim 10^{51} - 10^{52}$ erg, equivalent to $\sim 10^{44} - 10^{45}$ J. As the high energy emission of these objects is collimated, the actual total energy release is around 10^{51} erg, comparable to that of a Supernova explosion.

In astronomy many transient sources have generally rather simple time structures, which allows for the physics of the object to be understood. Gamma-ray bursts are very peculiar from this point of view, as their light curves vary significantly (Figure 2.1). There are no two identical GRBs: the duration, the number of peaks, the maximum brightness, in fact every parameter can be different.

---

[1] Gamma-ray bursts are named according to the date they have been detected.

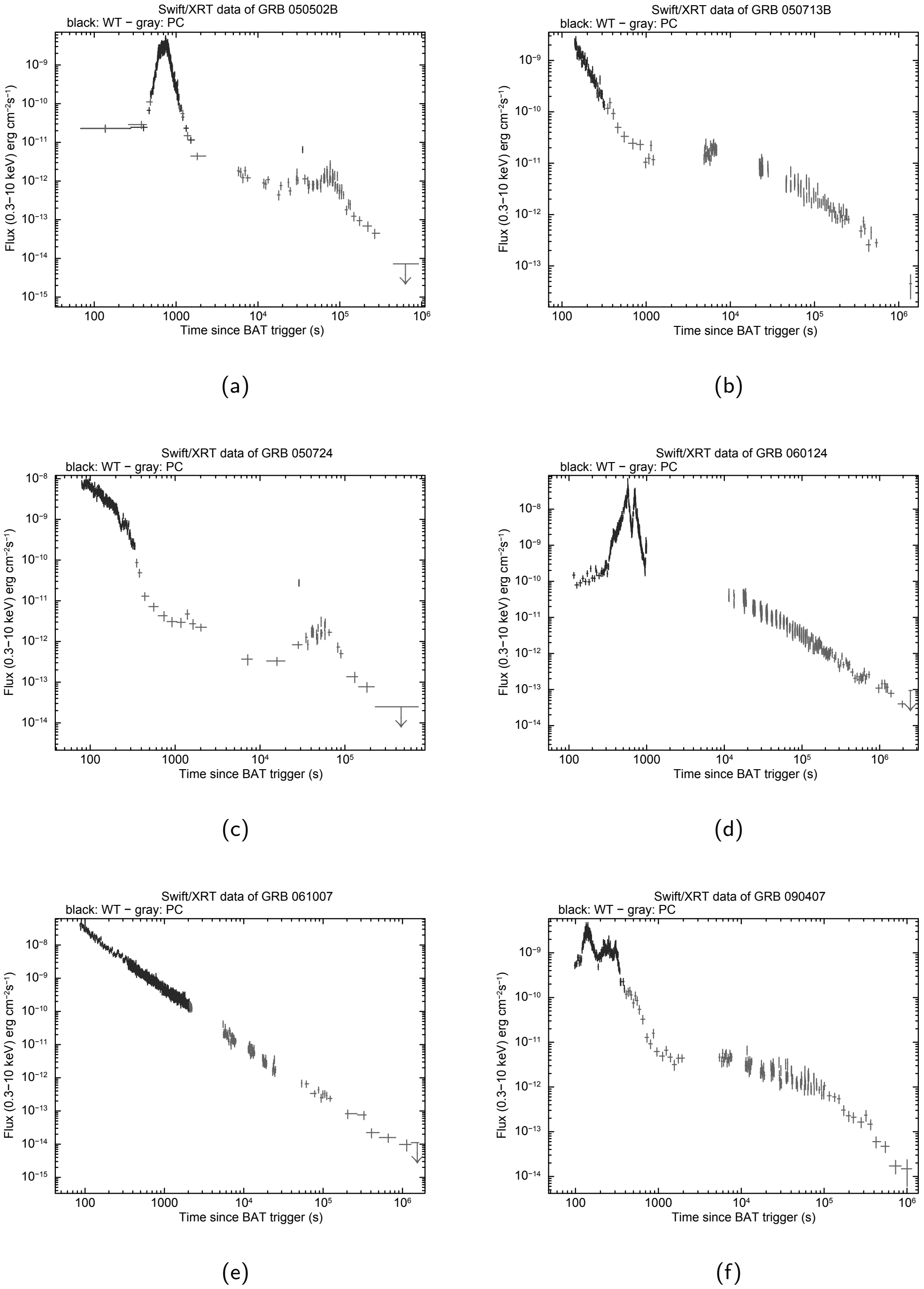

(a) (b)

(c) (d)

(e) (f)

Figure 2.1: Different light curves for six GRBs measured by Swift. The black points are measured using the Photon Counting (PC) method, for low rates, while for higher rates the Windowed Timing (WT) method is used (grey line). A detailed description of Swift light curves can be found in (13)

2.1 History of the GRBs

As many discoveries in science, also gamma-ray bursts were discovered accidentally. In the 1960s, both the United States and the former Soviet Union deployed military satellites to monitor adherence to the nuclear test-ban treaty. These satellites were gamma-ray detectors, as the signature of a nuclear detonation is a brief, but intense, pulse of gamma rays. While most satellites orbited at about 800 kilometers above Earth's surface, the Vela satellites orbited at an altitude of more than 100,000 kilometers. At this height, the satellites orbited above the Van Allen radiation belt, reducing the noise in the sensors. The extra height also meant that the satellites could detect explosions behind the Moon, a location where the United States government suspected the Soviet Union would try to conceal nuclear weapon tests (for a more detailed description see (14) or (15)). On July 2, 1967 the U.S. Vela satellites indeed detected a gamma-ray signal, but it had neither the intense initial flash nor the gradual fading that characterise the nuclear weapon explosion. Instead there were two distinct peaks in the light curve. The signal appeared curious, but not of particular interest for the Los Alamos team that was analysing the results of these satellites. It was only in 1973 that Ray Klebesadel, Roy Olson, and Ian Strong of the University of California Los Alamos Scientific Laboratory published Observations of Gamma-Ray Bursts of Cosmic Origin (16), identifying a cosmic source for the previously unexplained observations of gamma-rays. Following the chronological order in the discovery of gamma-ray bursts is very convenient to understand the different properties and aspects of these phenomena. This is due to the fact that the advancement in technology allows for increase in sensitivity for the different properties of GRBs. We can identify a few milestones in the history of GRBs, and the first one is surely the launch of the Compton Gamma Ray Observatory (CGRO) satellite in April 1991. It was equipped with several instruments, two of which were of particular interest for gamma-ray studies: the Burst and Transient Experiment (BATSE), made by 8 γ-ray detectors sensitive in the 20-600 keV range, and the Energetic Gamma-Ray Experiment Telescope (EGRET), sensitive above 100 MeV. The main result achieved by the BATSE detector is the conclusive proof that GRBs occur isotropically distributed in the sky (Figure 2.2). The BATSE instrument was the first to reveal that the GRBs can be split in two families: short and long duration GRBs, which have corresponding different spectra (see Section 2.2). Thanks to the BATSE data it has also been possible to measure the fluence of the typical GRB: this quantity ranges between $10^{-4} - 10^{-7}$ erg cm^{-2}.

The emission spectra of the GRBs show a peculiar non-thermal behaviour, peaking at around few hundreds keV and extending up to several GeV. The best description has been given by Band using the BATSE data. Figure 2.3 shows the so called Band Spectrum (17): two smoothly connected power laws, defined as $N(E) \propto E^{\alpha}$ at low energies and $N(E) \propto E^{\beta}$ at high energies (see Section 3.1).

Due to their short duration, GRBs were very difficult to localise precisely. In this respect the real breakthrough was made by the Italian-Dutch satellite BeppoSAX, launched in April 1996. Its Wide Field Camera, sensitive to the medium-hard X-ray energy range [2–25 keV], allowed for the first time to measure the position of the GRB with uncertainties of only few arcminutes. The satellite could then observe the pinpointed region with the Narrow Field Instrument (NFI, covering the 0.1-10 keV range). It was then possible to detect a newly discovered feature:

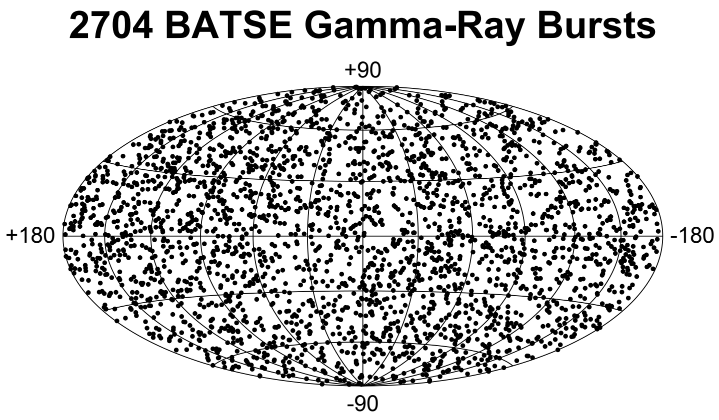

Figure 2.2: This map shows the locations of a total of 2704 Gamma-Ray Bursts recorded with the Burst and Transient Source Experiment on board NASA's Compton Gamma-Ray Observatory during the nine-year mission. The isotropy of the GRB distribution is evident from this figure. The projection is in galactic coordinates; the plane of the Milky Way Galaxy is along the horizontal line at the middle of the figure.

the X-ray afterglow of the GRB. In the meantime Scott Barthelmy set up a Gamma-ray Burst Coordinates Network (the GCN system) that transmits a GRB alert to a network of selected instruments (among which also the Antares telescope, see Section 4.8). The combination of BeppoSAX with the field camera trigger and the GCN system allowed for all ground based telescopes to point in the direction of the detected GRB and detect optical, IR and radio afterglows.

The observation of these afterglows, in different wavelengths, allowed for the first time for the characterisation of gamma-ray bursts using additional information to the gamma ray data. For example, it was possible to measure the redshift of several gamma-ray bursts (20 up to the year 2001). The redshift is the Doppler shift toward the red wavelength of the observed radiation due to the motion of the object away from Earth. In the case of extragalactic objects this quantity is also related to the distance of the object. The expansion of the Universe causes the object to move away from the Earth. Knowing the redshift of a GRB, therefore, provides an extremely useful additional information to classify and study each GRB. Determining the host galaxy of a gamma-ray burst has been historically very challenging, as in most cases there were several relatively bright galaxies contained within the position uncertainty of the GRB. Optical observations after the gamma-ray burst were a breakthrough in this respect (18): it has been possible to show that the long GRBs come from not very bright galaxies, and that the location of the source is never very far from the center of its host galaxy. This information is useful to infer that long gamma-ray bursts are generally associated with massive and short lived progenitors (see Section 2.3).

During the BeppoSAX era another feature revealed the nature of the emitting material in

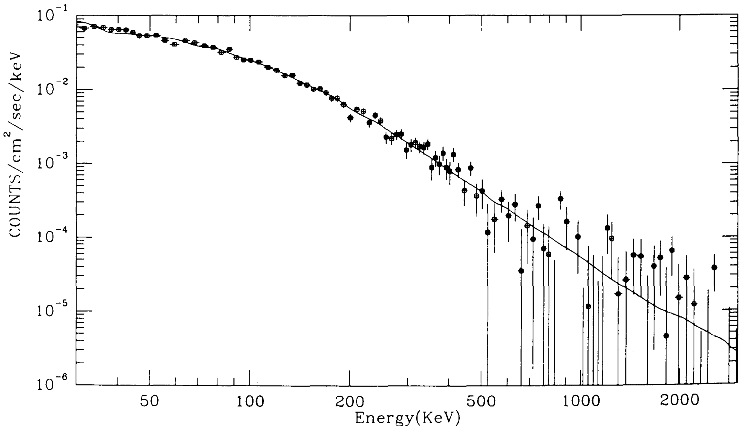

Figure 2.3: Example of the fit of the Band function, fitted to the average spectrum of 1B 911127. Figure taken from (17)

gamma-ray bursts. Five GRBs showed evidence of material emitting X-ray lines around the location of the GRB itself. By observing these "iron lines" and assuming a duration and a peak for the line emission in standard range (19), it is possible to determine the quantity of iron present in the initial stage of the GRB. To avoid requiring an unreasonable mass of iron, strong constraints on the recombination of the iron can be set: it is necessary to have large densities of iron at not so large temperatures. What is more, it is possible to claim that the iron material cannot be between the observer and the explosion, as otherwise absorption lines should show up and the amount of material would have stopped the gamma-ray explosion and the related afterglow. These constraints have very deep impact on the model of the GRB acceleration process, both from a chemical component and geometrical point of view (see Section 2.4).

The Swift satellite succeeded BeppoSAX. The sensitivity of its burst alert detector (BAT, in the range 20-150 keV) was higher than the previous instruments. The speed with which the higher angular resolution x-ray and UV-optical detectors can turn toward the burst is less than 100 seconds from the occurrence of the trigger. These two advantages significantly improved the measurements capabilities for GRBs, especially the ones shorter than two seconds (short GRBs). Nine short burst were detected before December 2005, in five of them an X-ray afterglow was measured. In three also an optical afterglow showed up and one afterglow appeared also in the radio frequency. These were the first measurements of an afterglow after a short GRBs. This led to the measurement of red shifts and eventually to the determination of host galaxies. Finally, GRB 060218 could be unequivocally associated with the supernova SN1998bw (see 2.3).

The latest milestone for gamma-ray burst research was reached in April 2008. On that date the Fermi satellite (formerly the Gamma-ray Large Area Space Telescope, or GLAST) was launched and since then the very high energy regime is under investigation. Roughly one GRB per week is detected with the Gamma-ray Burst Monitor (GBM, 8 keV-30 MeV), and roughly one a month is detected with the Large Area Telescope (LAT, 20 MeV-300 GeV, can be considered the successor of the EGRET instrument). Several bursts have been detected by the LAT at energies above 1 GeV (11 GRBs from August 2008 to January 2010 (20)), improving considerably our knowledge of high energy gamma ray emission. These observations can be useful also for fields of physics not strictly related with GRBs. For example in May 2009 GRB090510 has been observed. This particular GRB is characterised by its very high redshift (8.2, the farthest object ever observed) and with a extremely high peak in energy. The most energetic photon detected reached an energy of 31 GeV. Such distances and energies can be used to put a limit on Lorentz Invariance Violation, by determining whether the speed of light varies with energy (for more detailed explanation see (21)). Another achievement of the Fermi satellite is the calculation of the minimum required value for the boost Lorentz factor Γ. Theoretical considerations (see paragraph 2.4) put a limit on the lowest value of the Lorentz factor of the jets, but this value has never been measured. Considerations that link this value to the maximum energy of the observed photons and the distance of the GRB can constrain this value (20).

2.2 Classification

Observations from the BATSE instrument led to the separation of gamma-ray bursts into two families. The main classification is "long GRBs" and "short GRBs", where the "long" population has an average duration of about 30 seconds, while the "short" last on average 0.3 seconds. An often used measure of the duration of the GRB is T_{90}, that is the time during which 90% of the counts are made by the detector. As shown in Figure 2.4 there is a clear separation between two families of GRBs (22). Gamma-ray bursts are defined as "long" when they last more than two seconds and "short" if they last less than that. The short bursts spectrum is significantly harder than the long bursts, therefore they can also be found in literature as "short hard bursts" (SHBs). The GRB hardness ratio is defined as the $\sim$ 100 to 300 keV fluence divided by that in the $\sim$ 50 to 100 keV energy band.

Long GRBs are the most observed and, therefore, also the most understood. Each family of GRB is associated with a different progenitor (see Section 2.3). Observations show that long GRB host galaxies are active star forming galaxies (23). In several cases it has been proved that long GRBs happen in correlation with supernovae. This has linked unambiguously long gamma ray bursts with the death of a massive star. Investigations into the origin of the short GRBs had to wait for the detection by Swift of signals happening after the burst itself (afterglows). With the information provided by the afterglow studies, it has been ruled out that short GRBs have the same origin of long ones. As a matter of fact, almost all of the short GRBs come from areas of the Universe with little or no star formation. The origin of the short GRBs is yet to be understood, although the hypothesis gives an origin in the merging of a double compact object.

2.3 Progenitors of the GRBs

Progenitors for long and short gamma-ray burst are different and therefore treated separately.

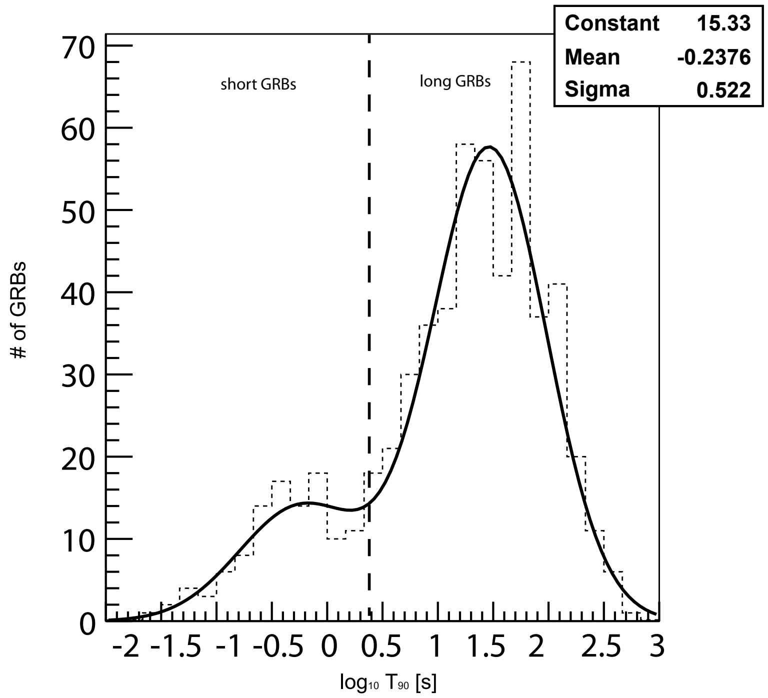

Figure 2.4: Distribution of GRBs that occurred in 2008-2009 as a function of the log of the T_{90} in seconds. It is possible to see how the gamma ray bursts are split in two groups depending on their duration and how the choice of 2 seconds to separate the two families is appropriate.

Long Gamma Ray Burst

Observations of optical and X-ray afterglow are useful in constraining the environment in which the gamma-ray burst has formed and exploded. The association of long GRBs with supernovae and host blue galaxies, suggests an origin of these GRBs in some type of stellar death. The experimental association of GRBs with supernova events provide further evidence for this.

Core-collapse supernovae (SNe) are the explosive deaths of massive stars that occur when their iron cores collapse to neutron stars or black holes (24). It is interesting to note that they are generally not accompanied by a highly relativistic mass ejection, and they are visible from all angles and can last up to a few months. Supernovae are classified of Type I if they have lost their hydrogen shell, whereas they are called Type II otherwise (25). The connection between supernovae and gamma-ray bursts is to first order given by the total kinetic energy emitted: it is around 10^{50} ergs both for supernovae and GRBs. The observation of a GRB on April 25, 1998 (GRB980425) in conjunction with SN 1998bw (26) showed this connection unambiguously. These two events were coincident both in time and space, and the energetic coincidence left few doubts about the connection. This supernova is located in a spiral arm of the nearby galaxy ESO 184G82, at a distance of 40 Mpc. In his paper, Galama calculated that the probability that any supernova with peak optical flux a factor of 10 below that of SN 1998bw would be found accidentally to coincide with the GRB is 10^{-4}.

For Type I supernovae, where the star is not surrounded by a thick hydrogen envelope, the jet material can make its way up to the stellar surface and, as it will find less and less material in its way, the material in the jet will accelerate, reaching a Lorentz factor of 100 or more. Once the jet is freed from the stellar medium, it releases most of its energy in form of gamma-rays.

In the *hypernova* or *collapsar model* of gamma-ray bursts this connection has been further developed. In this model a very massive star in the latest stages of its life has fused all its central material to iron, and is therefore not longer able to generate energy by nuclear fusion. It subsequently collapses in a supernova, under the pressure of the gravitational force, forming a black hole. If the star is rotating rapidly (i.e. with a high angular momentum) the collapsed matter swirls into a high-density accretion disk. This accretion of material into the center of the black hole causes two relativistic jets to be ejected along the rotational axis, where the matter density is lower than in the accretion disc. In these jets relativistic shock waves are created (27).

Only few ($\sim 10^{-6}$) stars manage to develop a gamma-ray burst event. This is because, according to this model, there are some preliminary conditions that must be satisfied. First of all the star must be massive enough to generate a central black hole. Secondly, it must be rapidly rotating, in order to be able to form the accretion disc capable of emitting the relativistic jets. Finally the star has to have low metallicity, in order to get rid of the hydrogen shell around it. It is reasonable that, also for stars where the conditions do not allow the jets to traverse the pre-burst material, the initial phase would stay the same. The system would then release its energy in form of neutrinos or gravitational waves. This scenario is described as a “choked” gamma ray burst, and is described in Section 2.6

Short Gamma Ray Burst

The total kinetic energy emitted by short GRBs exceeds that of long GRBs by many order of magnitudes. Such a high energy in such compact objects indicates a relatively small number of solar masses accreting onto a massive black hole. Possible candidates for such a process are mergers of neutron star binaries or neutron star - black hole binaries, which lose angular momentum and undergo a *merger* (28). Neutron star - neutron star binaries are observed in our galaxy, and the existence of neutron star - black hole binaries is plausible. Such structures lose energy due to gravitational radiation, as predicted by the General Relativity, and the two objects will spiral closer and closer until tidal forces will disintegrate the neutron star and will free an enormous quantity of energy before merging to form a single black hole. This process is thought to be extremely fast and to last no more than few seconds, in agreement with the observation of short GRBs.

Observation of afterglows connected with short gamma-ray bursts events allowed for the identification of host galaxies also for these short GRBs. Short GRBs are distributed uniformly among galaxies that contain a considerable quantity of old stars. In these galaxies there is no evidence of significant star formation, and such an old population is compatible with the presence of neutron star binary systems. Furthermore, the lack of connection with a supernova observation supports the model of a merger, where no explosion is required.

It is important to notice that although the two families of gamma ray bursts are known

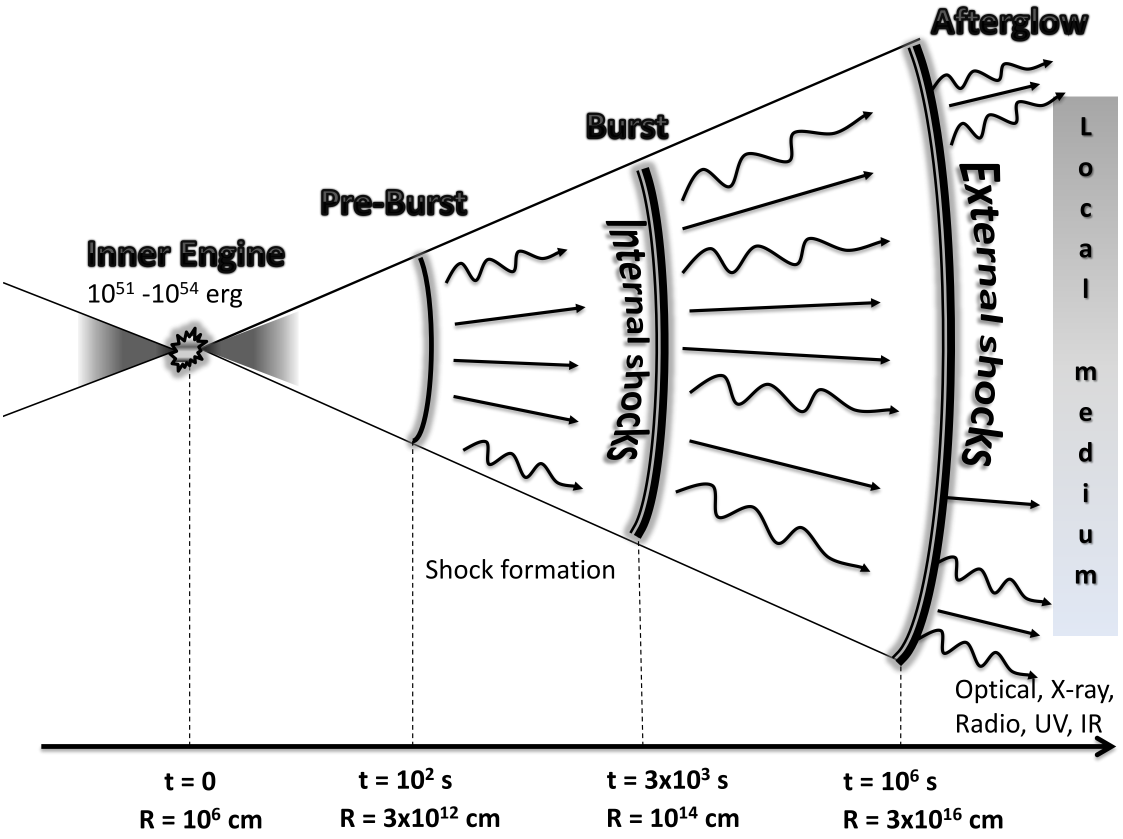

Figure 2.5: The internal-external fireball shocks model. A compact source produces a relativistic outflow. Internal shocks within the outflow produce the prompt gamma ray emission while external shocks with the surrounding matter produce the lower energy and longer lasting afterglow.

to have different progenitors, the acceleration mechanism that gives rise to the gamma rays themselves and to the production of neutrinos, is most likely independent of the progenitor of the event. The model explained in the following paragraph 2.4 could be applied in both cases.

2.4 The Fireball Model

The Fireball model is the most widely used theoretical framework to describe the physics of the Gamma Ray Bursts. It originates from considerations on the total energy release of a GRB and its extremely short variability time (see Section 2.4.1). It describes a compact object (inner engine) forming from the collapsing core of a massive star or the merger of two compact obects. This causes an explosion that sends blast waves moving through the star at speeds close to the speed of light. This “fireball” expands keeping its total energy constant by transforming entropy into kinetic energy. Two opposite jets form at the two poles of the accretion disc and during the acceleration of matter in the jets, newly formed material accelerates faster and forms consecutive shells with different speeds. Interaction of shells with the external medium or collision between shells reconvert the kinetic energy into internal energy, ready to be radiated in form of gamma-rays or transferred to baryons via baryon-photon coupling. Shocks between shells are collisionless due to the low density of material in the jets. This means that there is no Coulomb interaction between two particles in the jet, but rather the acceleration of matter in the shock waves is driven by plasma instabilities (29). These shocks (see 2.4.3) are responsible for the emission of gamma-rays. Gamma rays burst out from the star's surface just ahead of the shock.

Behind the shock, the blast wave pushes the stellar material through the star surface and sweeps through space at nearly the speed of light, colliding with external gas and dust, producing additional emission of photons. These emissions are the afterglow.

This model is also called Fireball Shock Model. In Figure 2.5 a schematic of this model is shown.

Although this scenario is widely accepted, the discussion is still open regarding the form in which the energy is carried out. In some models, the energy outflow is carried out in the form of kinetic energy of baryons, while in other models the flow is of electromagnetic nature. The models we shall consider in this thesis are those which have baryons in the outgoing flow. Measurements of neutrinos from a Gamma Ray Burst would then provide evidence for the presence of these baryons.
The next paragraph provides a brief description of the physics of the Gamma Ray Bursts following the above considerations. More detailed reviews on the subject appear elsewhere (30, 31).

Two apparent paradoxes arise from the observation of GRB behaviour. One is related to the size of the inner engine in relation with the time scale of the GRB emission variability, and one is on the duration (T_{90}) of the GRB.

2.4.1 Compactness problem and relativistic beaming

The large variability of GRB light curves in very short times, δt, puts an upper limit on the size of the emitting object of $c\delta t$, implying a very compact object (32). The energy of a typical GRB generated in such a small size would imply a very dense source. Because of the process of photon-photon pair production, this density would reduce significantly the gamma ray brightness of the object and provide a thermal spectrum, in contrast to the observations.

Introducing a relativistic motion of the source toward the observer direction solves this apparent paradox. If the emitting object is moving with a Lorentz boost factor Γ toward the Earth, the observed photons will be blue-shifted, therefore their energy at the source frame is lower by a factor Γ, implying a factor Γ less energy in the source.

The scale of GRB time variability poses also another question. Observed variability times are of the order of a millisecond. This would imply a maximum size of the object of around $\delta d \sim 300$ km. On the other hand observations show that the typical size of a GRB remnant is of the order of 0.1 light year so, even if the emission is coming only from the internal shocks happening inside the star, this δd seems yet too small.

If the flow moves with a relativistic boost Γ the time difference between two photons emitted

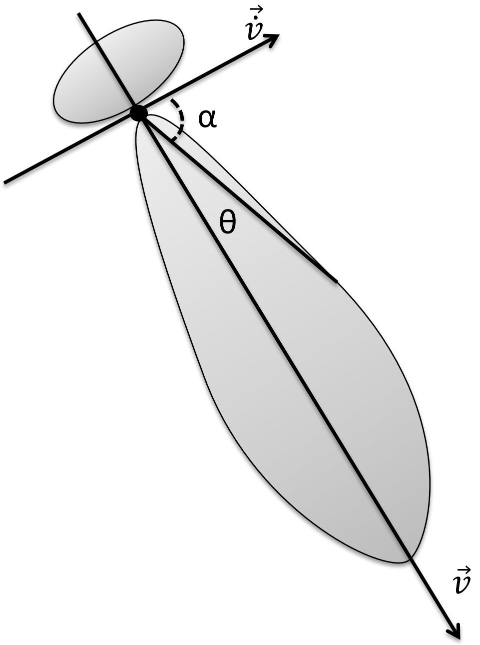

Figure 2.6: Diagaram of a relativist particle radiating. Its dipole pattern becomes asymmetric and extends in the direction of motion because of the forward blueshift and backward redshift caused by the Doppler effect.

with a distance δd is going to be:

$$\Delta T_{obs} = \frac{\Delta T_{emiss}}{2\Gamma^2}$$

where obs refers to the observer frame (Earth) and $emiss$ to the emission frame (GRB). A Lorentz factor of 100, therefore, will imply that a time variability of 10 seconds at the source will appear as few milliseconds for the observer. This means that the size of the source is expanded by a factor Γ^2 ($\delta d \sim 300 \times 10^4$ km). A complete calculation of the constraints on the Lorentz factor requires integration over the angular distribution of the emission and energy dependence of the pair production cross section to be taken into account. A detailed description of these processes is given in (33). Here it is sufficient to note that for an infinitesimal angle of aperture of the emission, all photons regardless of their energy will be free to travel to outer space. Photons are generated by relativistic magnetic Bremsstrahlung emission (synchrotron emission). Relativistic transformation of emission angles causes aberration, which is the responsible for "beaming" the emission. The power $dP_{emiss}/d\Omega_{emiss}$ emitted per solid angle in the emission frame (co-moving with the charged particle) is different to the power $dP_{obs}/d\Omega_{obs}$ as seen in the observer frame, because the two relative emission angles α_{emiss} and α_{obs} are different. The emission power in the observer frame relative to the observation angle α_{obs} is

$$\frac{dP_{obs}}{d\Omega_{obs}} \propto \sin^2 \alpha_{obs}.$$

The Lorentz transformation of the angle $\theta = \pi/2 - \alpha$ is

$$\sin\theta_{obs} = \frac{\sin\theta_{emiss}}{\Gamma(1+\beta\cos\theta_{emiss})}$$

where $\beta = v/c$ is the velocity of the particle in terms of speed of light. Because of the dipole pattern of a relativistic Bremsstrahlung emission (Figure 2.6) the emission tends to be pointing along the motion β. In a relativistic outflow the angle of emission therefore is

$$\sin\theta_{obs} \sim \theta \sim \frac{1}{\Gamma} \tag{2.1}$$

This means that the outflow of the GRB is highly collimated. It can be shown that to have an optically thin medium a $\Gamma \gtrsim 100$ is required. This effect has two more important consequences. The first one is that two observers looking at the same GRB from different angles will measure different light curves. Reversing this argument means that our study on GRBs is biased by the fact that we detect more easily burst that are pointing in our direction.

2.4.2 Relativistic time effects

Besides the variability time, Gamma Ray Bursts are characterised by the duration of the burst, defined for example as the T_{90}. We have just observed in the previous paragraph how to solve the inconsistency of the compactness of the source with the time variability scale by introducing the relativistic motion of the object towards the observer. Another problem arises observing that a typical burst duration is around 100 seconds, while to travel 10^{15} m light would take a month. This aspect cannot be directly explained by the relativistic motion of the flow, but is strictly connected with the beamed emission of the burst. The time difference between the first and the last emitted photon in the observer frame does not only depend on the size of the emitting object, but also on the solid angle of the emission (34). Considering a spherical shell moving away from the inner engine, emission coming from parts of the shell moving at an angle θ from the line of sight of the observer will arrive later than the direct emission. This delay gives the order of the duration of the burst and can be written as

$$\Delta T_{burst} \simeq \frac{R(1-\cos\theta)}{c}$$

If the emission is beamed, θ is going to be small, therefore the delay is just

$$\Delta T_{burst} \simeq \frac{R(1-\theta^2)}{2c}$$

Using equation 2.4.1 we have

$$\Delta T_{burst} \simeq \frac{R}{2c\Gamma^2} \tag{2.2}$$

Therefore with a $\Gamma \sim 100$ a time difference of one month in the co-moving frame will appear as no more than 300 seconds in the observer frame.

The success of this model in explaining the observations is a compelling argument for assuming relativistic effects in the GRB physics. Nowadays we can rely in a even more compelling proof. The Fermi satellite managed to measure the Lorentz boost factor of at least three of the brightest GRBs observed. Knowing the distance (that means having a measured redshift) of the GRB, the total luminosity and the time variability, the highest energy photon put a constraint on the minimum compatible Lorentz factor in order to maintain the optical depth for photon-photon pair production smaller than 1. For example the Fermi collaboration published the limit for $\Gamma_{min} \simeq 900$ for GRB 080916C, $\Gamma_{min} \simeq 1200$ for GRB 090510 and $\Gamma_{min} \simeq 1000$ for GRB 090902B (see (20) and references within).

2.4.3 Internal Shockwaves

Due to the photon density in the jets, one should expect the spectrum emitted by the gamma ray burst to be thermal, in other words should follow a black body emission (35). The observed spectrum, nevertheless, follows a non-thermal behaviour, showing a broken power-law shape. This means that the energy dissipation is in the form of kinetic energy of protons, but this makes the dissipation of the energy very inefficient.

An efficient way to produce a non thermal spectrum is to reconvert the kinetic energy in random energy via shocks (29). The idea is to have a "internal engine" that drives the nearby plasma inside the fireball. This would generate series of waves that propagate in the form of compression waves : this phase is the internal shock phase. Within a short time the waves merge together and form a shock, that is the front of the wave. These shocks are collisionless, which means that the particles scatter off the fluctuations of the magnetic field rather than with other particles. When the compression waves that are travelling faster overtake earlier ones, a shock is generated.

As the later compression waves keep merging into the shock the energy and the pressure behind the shock become stronger and the shock can reach relativistic speeds. The relativistic electrons present in the wave can produce a non thermal radiation via synchrotron and Inverse Compton processes. During the internal shocks pp collisions can occur, leading at the production of high energy gamma rays via the production and decay of π^0 and the production of neutrinos via meson and muon decay. Accelerated protons can also interact with high energy synchrotron photons, giving rise to photomeson production (see Section 3.2).

Once the central engine ceases to feed the shock the deceleration period starts and the fluid gives rise to an expansion wave. Once the fireball runs into the external medium the external shockwaves start, slowing down the relativistic flow.

In principle, both internal shocks and external shocks could contribute to the gamma ray prompt emission. Only internal shocks, on the other hand, succeed in explaining the short time variability of the burst. The reason is that the variation timescale in the internal shocks is limited only by the dynamic timescale of the inner engine. On the other hand, internal shocks can only dissipate a fraction of the kinetic energy, therefore they must be accompanied by the external shocks, that produce a smooth long lasting emission - the afterglow.

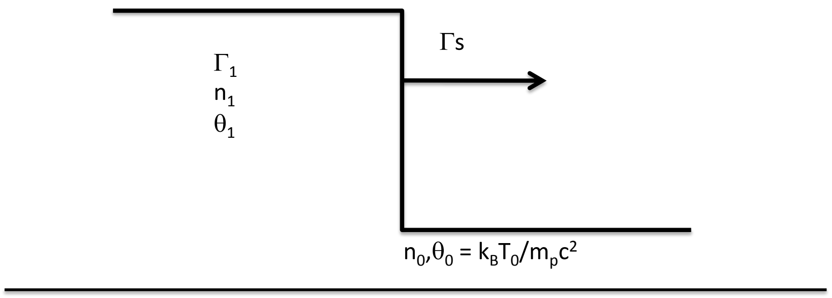

(a) Forward Shock

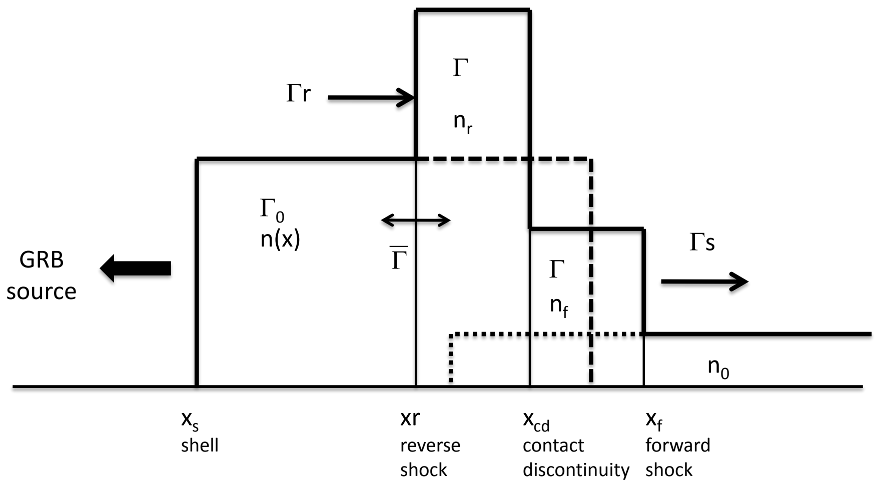

(b) Reverse Shock

Figure 2.7: Diagaram of the relativistic shocks model. (a) Quantities from the basic system consisting of a shocked fluid encountering the stationary external medium (external shock). (b) Quantities for the system consisting of the unshocked shell, the reverse and the forward shocks, and the stationary external medium (36)

2.4.4 Alternative prompt models

The Internal Shock model succeeds very well in reproducing the observed spectra, but remains a phenomenological model, as the physics of the central engine and of the possible progenitors is not known in detail. There are, as a consequence, several other models that can equally well reproduce the observations. In the Poynting or Reconnection model (see, for example, (37)), the internal energy is dissipated via magnetic reconnection. The name Poynting comes from the definition of the Poyinting vector, equal to the cross product of the electric-field strength and the magnetic-field strength. Its normal component, when integrated over a closed surface, gives the outward flow of electromagnetic energy through that surface. In this model the flow dissipates energy via this flux. The very high magnetic field involved leads to a high radiative efficiency and the acceleration of particles is driven by the reconnection. This model leads to a very low neutrino flux (38). Another speculative model is the "Shotgun" model, which considers a scenario similar to the one having only external shock, but to workaround the time variability problem considers an inner engine that "shoots" clumps of dense plasma toward the outer matter with short time intervals. The energy is then dissipated via external shocks, but the short time variability is given by the inner engine (39).

For the development of this work only the Fireball scenario has been used. The Fireball model provides the reference neutrino spectrum from Gamma Ray Bursts (40).

2.4.5 External Shock Scenario and the afterglow emission

When the material accelerated by the fireball jet collides with the external medium, the period of afterglow starts. The external shock scenario can be described as a cold (so with negligible internal energy) relativistic shell in collision with the interstellar medium (ISM). When this happens two different shocks take place. When the shock propagates through the unshocked material in front of the wave, it is referred to as "forward shock". When the collision between the newly generated wave and the previous wave happens, another shock is formed, moving in the opposite direction to the accelerating wave. This shock is defined as the "reverse shock" (see Figure 2.7).

This process can be described separated in four different regions. Two regions are unshocked, and are the interstellar medium at rest, and the material of the shell before colliding with the external medium. There are two regions of shocked materials moving in two opposite directions: the shocked ambient matter, passing through the forward shock, and the shell material, passing through the reverse shock. As the interstellar matter moves across the shock, it is immediately heated to extreme temperatures. The particles in that matter move relativistically. While traversing the strong local magnetic field they are bent perpendicular to the field, causing them to radiate energy via synchrotron radiation. In general, energy of gamma ray emission assumes the form of a power-law with three break points (and therefore four different power-law segments). Each phase of the external shock is characterised by a different photon flux, depending on the hydrodynamic conditions (see, for example (30) and references within). Optical-UV photons are emitted by electrons propagating through the reverse shocks. In the reverse shocks, also protons can be accelerated, and can then produce high energy neutrinos (41) via photo-meson interactions. Although these neutrinos are very interesting as there is, for instance, no or little high energy suppression due to pion synchrotron losses, because the magnetic fields are weak (42)), they are not considered in this thesis, as they are produced several hours to several days after the GRB explosion itself. As the analysis presented in this thesis is based on the time correlation between the prompt photons and the observed neutrinos, it is not sensitive to this afterglow emission.

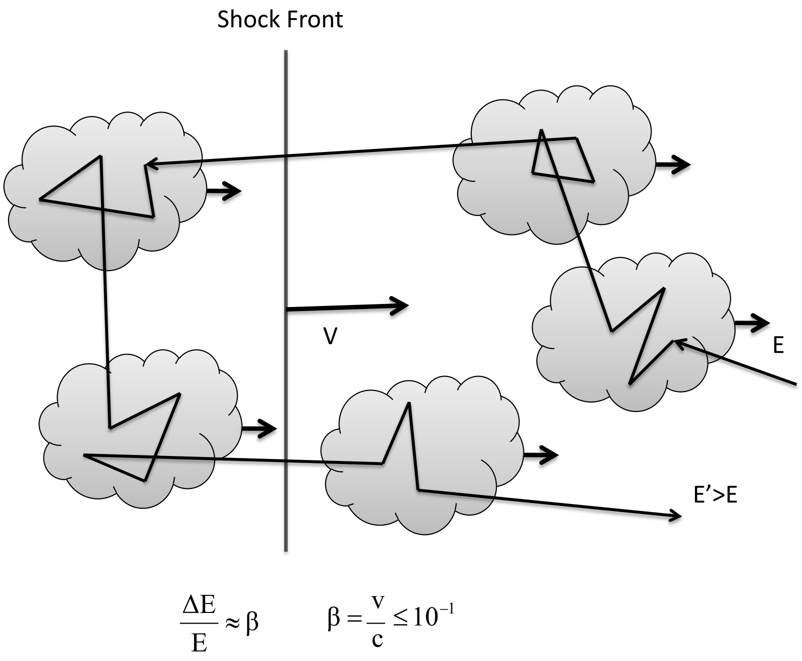

(a) First Order: acceleration in strong shock waves

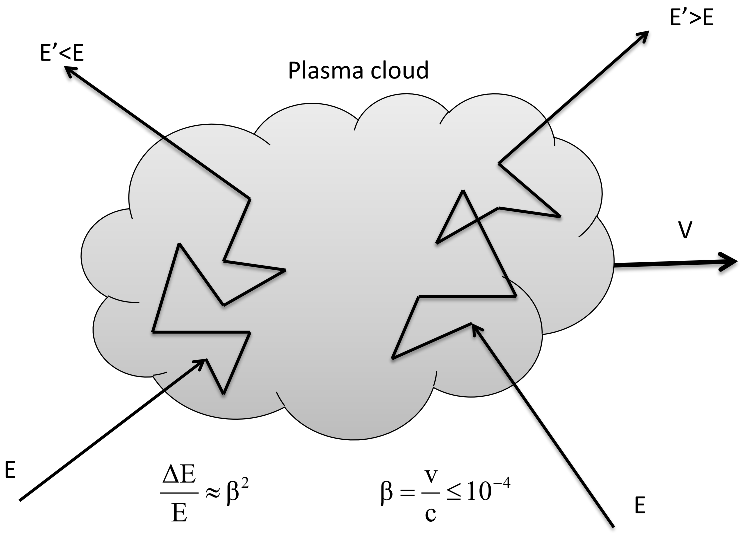

(b) Second Order: randomly distributed magnetic mirrors

Figure 2.8: First and Second order Fermi acceleration Mechanism: stochastic energy gain in collision with plasma clouds.

2.5 Diffuse shock and Fermi acceleration

Particles can be accelerated in two different ways: via stochastic scattering on magnetized medium, or crossing a highly magnetised relativistic plasma wave. Both these mechanisms are known as Fermi acceleration, although only the former has been theorized by Fermi. Fermi was the first to calculate the acceleration of cosmic rays via random scattering off molecular clouds in the interstellar medium (43) (see Figure 2.8(b)). This description is known as Second Order Fermi Mechanism (F2), because the gain in energy of the particle is proportional to the square of the speed of the cloud. In GRBs the scattering takes place off the random fluctuations in the magnetic field (collisionless process) rather than with other particles.

Each time a charged particle cross the shock wave, it gains energy by the conversion of the kinetic energy in the flow (Figure 2.8(a)), proportionally to the fluid speed (F1). Both Fermi accelerations (stochastic and shock) are based on the scattering of charged particles with moving scattering centres. In GRB physics, the Fermi acceleration mechanism is always considered as the most likely method of acceleration, as it succeeds very well in producing a power-law distribution of the accelerated particles. A more detailed and explanatory derivation of the following results can be found in (36).

Diffuse shock or First Order Fermi Mechanism

In the first order acceleration, particles are accelerated when crossing the wave front of a very energetic and magnetized blast wave. How much energy the particle can gain depends on the parameters of the moving fluid, such as the discontinuities in velocity, density and magnetic field at the shock wave front. Each time the particle crosses the shock front, it gains energy at the expense of the shock itself. The more times a particle cross the shock front, the more energy it gains. To know whether a particle can traverse multiple times the shock front, one has to compare its gyroradius[1] with the size of the shock width. When the former is considerably larger than the latter, the particle can be magnetically accelerated up to superthermal limits, cycling upstream and downstream across the shock. If the gyroradius is too large, the particle will fail in turning around the magnetic field lines of the shock and will eventually escape. It is notable how the convective loss downstream balances the energy gain rate and provides the particles with a power law distribution.

Stochastic or Second order Fermi Mechanism

The idea of stochastic or second order Fermi acceleration (43) is a relativistic charged particle colliding with massive magnetized clouds, that move in random directions with mean speed $v = |\vec{v}| = \beta c$. These clouds represent scattering centres. The scattering rate of the particle with the clouds is $(1 - \beta_p \beta \mu)$, where β_p is referred to the particle, β to the clouds, and $\arccos \mu$ is the angle of incidence between the particle and the cloud. This rate has a smaller value for "tail-on" collisions, therefore the energy loss is smaller for this type of collision than for "head-on" collisions. For this reason a particle randomly scattering with the clouds gains energy at the

---

[1] The gyroradius is defined as $r = \frac{mv_\perp}{q|B|}$

expense of the kinetic energy of the clouds This means that it gains enough extra energy to decouple from its original thermal state. At times, these particles can be accelerated reaching a power law distribution with power index down to 1.

2.5.1 Energy gain per cycle

A particle with Lorentz factor γ travelling in a fluid with speed βc and Lorentz factor Γ, in the comoving frame will have a Lorentz factor of (36):

$$\gamma' = \Gamma\gamma(1-\beta\beta_p\mu) \xrightarrow[\beta_p\sim 1]{} \Gamma\gamma(1-\beta\mu) \tag{2.3}$$

after scattering the particle escapes and returns to the original medium (outside the cloud or around the shock front) but with a Lotentz factor of:

$$\gamma_f = \Gamma\gamma'(1+\beta\beta_p\mu'). \tag{2.4}$$

If one considers the particle much faster than the target centre, with $\beta_p \sim 1$ and $\gamma \gg 1$, equation 2.4 can be rewritten as:

$$\gamma_f = \Gamma^2\gamma(1-\beta\mu)(1+\beta\mu) \tag{2.5}$$

The fractional energy gain can be expressed as:

$$\frac{\Delta\gamma(\mu,\mu')}{\gamma} = \frac{\gamma(\mu,\mu')-\gamma}{\gamma} = \Gamma^2(1-\beta\mu+\beta\mu'-\beta^2\mu\mu')-1 \tag{2.6}$$

In the case of second order acceleration, the particles are distributed isotropically both before and after scattering, so the average energy gain per cycle, averaged over entering and exiting angles is:

$$\left(\frac{\Delta\gamma}{\gamma}\right)_{F2} = \frac{4}{3}\beta^2\Gamma^2 \propto \beta^2 \tag{2.7}$$

because of the proportionality to β^2 this mechanism is of second order.

In a GRB particles are assumed to be accelerated via First order Fermi mechanism. They travel along with the blast wave and accelerate crossing the shock front. In the first order acceleration, the geometry is different, and no longer involves the reaction rate factor $(1-\beta_p\beta\mu)$ because there is a fixed velocity discontinuity in the frame of the shock. To average the energy gain, one has to project the isotropic flux of particles on the plane of the shock, as the flux is reduced proportionally to μ and μ'. Weighting the flux by μ results in the following energy gain per cycle:

$$\left(\frac{\Delta\gamma}{\gamma}\right)_{F1} = \frac{4}{3}\beta\Gamma^2 + \frac{13}{9}\beta^2\Gamma^2 \tag{2.8}$$

A summary of the maximum energies reachable in different types of cosmic explosions is given in table 2.1.

Explosion type	Outflow speed ($\mathrm{km\,s^{-1}}$)	$\langle\beta_0\Gamma_0\rangle$	$\frac{E_{\mathrm{max,F1}}(\mathrm{eV})}{Z}$	$\frac{E_{\mathrm{max,F2}}(\mathrm{eV})}{Z}$
SN Ia	$\lesssim 2\times10^4$	0.03	$\sim 10^{15}$	$\sim 2\times10^{14}$
SN II	$\lesssim 10^3 - 2\times10^4$	0.01	$\sim 5\times10^{14}$	$\sim 2\times10^{12}$
SN Ib	$\lesssim 1.5\times10^3 - 10^5$	0.1	$\sim 2\times10^{15}$	$\sim 2\times10^{16}$
SN Ic	$\lesssim 3\times10^4 - 3\times10^5$	0.3	$\sim 4\times10^{15}$	$\sim 2\times10^{18}$
GRBs	3×10^5	~ 300	$\sim 7\times10^{16}$	$\sim 10^{20}$

Table 2.1: Maximum particle energy reached through Fermi acceleration Mechanism in different types of cosmic explosions. Table taken from (36)

2.6 Choked GRBs

A special type of Gamma Ray Bursts can be of particular interest for this analysis. In Section 2.4.1 it has been explained that the compactness problem is automatically solved once the relativistic motion of the jet is accepted. This can only be true if the system is able to transform enough internal energy into kinetic energy to accelerate matter in relativistic jets. Some scenarios could describe a different situation. In the case of short Gamma Ray Bursts, generated by the merging of two compact objects (see Section 2.2) the energy transfer could be slow enough not to generate a relativistic outflow. Also for long Gamma Ray Bursts, associated with a supernova explosion, matter could fail to escape from the central engine area. GRBs are always associated with supernovae of type IB, where the hydrogen shell surrounding the star has already been removed. A supernova of type II, still surrounded with a hydrogen shell, can still possess the inner engine responsible for the Gamma Ray Burst, but the accelerated matter cannot escape from the shell and is trapped inside the inner engine area. Without a relativistic flow, the optical depth of the plasma is extremely high, of the order of $\tau \sim 10^{15} - 10^{16}$, causing all photons to stay trapped inside the shell with a thermal distribution. At temperatures of the order of $\sim 10^{10} K$ the dominating process is electron-positron pair production and neutrino pair annihilation:

$$\gamma + \gamma \longrightarrow e^+ + e^- \longrightarrow \nu + \overline{\nu} \tag{2.9}$$

The interaction length for neutrinos is big enough so that these particles can freely escape from the plasma. These neutrinos are relatively low energy, being only of a few MeV (44), and will carry away a substantial fraction of the total energy of the fireball, but this is not the only process that can happen. In the flow, protons are still accelerated, and can easily interact with the dense plasma, giving rise to mesons like pions and kaons (see Section 3.2), that can then decay in high energy neutrinos (with energy >10 GeV) which can then be detected with an Antares-like telescope. This feature is particularly interesting because very little is known on the existence and the environmental condition of choked gamma ray bursts, and it is only possible to provide information on these objects using neutrinos as probes. The disadvantage is that with this type of GRB the time coincidence with gamma-ray experiments is lost. On the other hand, it is possible to correlate the observed neutrino flux with the initial supernova or with a sort of afterglow emission, that can happen when the plasma becomes transparent after having lost enough energy via neutrino emission. In both choked and successful GRBs, there are theoretical considerations that suggest the production of TeV neutrinos in the early phases of the fireball expansion. At that moment, an internal shock inside the flow itself might be able to accelerate protons up to $\gtrsim 10^5$ GeV, producing high energy neutrinos that would appear before any gamma emission (45). This mechanism is valid for both successful GRBs and for fireballs that do not manage to pass through the stellar envelope. Such an observation would provide a good probe to detect choked GRBs. What is more, as explained in Section 3.5, the flavour ratio of the detected neutrinos from choked GRBs could be different than the one expected for standard GRBs, because effects due to the matter inside the plasma (46).

3

Neutrinos from Gamma-Ray Burst

> *I saw a star explode and send out the building blocks of the Universe. Other stars, other planets and eventually other life. A supernova! Creation itself!*
>
> Number One

Neutrino and photon spectra are strictly related. This is in the case of an hadronic component in the fireball jet. In this scenario, neutrinos are produced by pions created by accelerated protons. The energy of the protons and, as a consequence, the energy of the neutrinos, is linked to the photo production threshold of the Δ resonance.

3.1 GRB photon spectrum

Once one accepts the internal-external shock scenario (see section 2.4.3), and the Fermi acceleration of particles within (see section 2.5), it is a logical step to explain the gamma ray emission mechanism by synchrotron radiation from relativistic electrons. An additional mechanism that has to be considered is the Synchrotron self-Compton (SSC) process (47), that is the scattering of synchrotron photons by relativistic electrons to boost to higher energies. The prompt emission observed from classical GRB has most of its energy concentrated in the range $0.1 - 2\,\mathrm{MeV}$. Using the synchrotron emission to explain the observations, leads to the broken power law observed spectrum. The frequency at which the synchrotron spectrum peaks is given by $\nu_{pk} = \Gamma \frac{3}{8}\pi \frac{eB'}{m_e c}\gamma_{pk}^2$, where Γ is the shock Lorentz factor, B' is the magnetic field in the observer frame and γ_{pk} is the Lorentz factor of the electron in the shock frame. This description agrees with the fit given by Band et al. (17). This is referred to as the Band spectrum and can be written as:

$$F_\gamma = \frac{dN_\gamma}{dE_\gamma}(E_\gamma) = A_\gamma \begin{cases} \left(\frac{E_\gamma}{100\,\mathrm{keV}}\right)^{\alpha_\gamma} \mathrm{e}^{-\frac{E_\gamma(2+\alpha_\gamma)}{E_{pk}}} & E_\gamma < \varepsilon_\gamma^b \\ \left[\frac{\alpha_\gamma-\beta_\gamma}{2+\alpha_\gamma}\,\frac{E_{pk}}{100\,\mathrm{keV}}\right]^{\alpha_\gamma-\beta_\gamma} \mathrm{e}^{\beta_\gamma-\alpha_\gamma} \left(\frac{E_\gamma}{100\,\mathrm{keV}}\right)^{\beta_\gamma} & E_\gamma > \varepsilon_\gamma^b \end{cases} \tag{3.1}$$

where A_γ is the maximum intensity of the spectrum, α_γ the asymptotic low energy spectral index, β_γ the high energy spectral index, E_{pk} is the peak energy of the synchrotron spectrum distribution (correspondent to ν_{pk} given earlier), and $\varepsilon_\gamma^b = (\alpha_\gamma - \beta_\gamma)/(2+\alpha_\gamma)E_{pk}$ is the break energy. This spectrum is often referred to as a fluence (F_γ), that is defined as the spectrum integrated over the duration of the gamma ray burst. Typical values of these parameters are $\alpha_\gamma \simeq -1$, $\beta_\gamma \simeq -2.2$, $\varepsilon_\gamma^b \simeq 300 - 1000\,\mathrm{keV}$, $A_\gamma \simeq 0.001 - 1\ \mathrm{photons\,cm^{-2}\,s^{-1}\,keV^{-1}}$. The synchrotron interpretation of the GRB emission is the most accepted. It must be remarked that the plain synchrotron spectrum is modified at low energies by synchrotron self-absorption, and at high energies due to Inverse Compton effects.

3.2 Neutrino Production

The observation of Ultra High Energy Cosmic Rays (UHECRs) ($E \sim 10^{20} eV$) has posed a problem concerning their origin. The only observational hint as to their origin has been provided by the Auger Observatory (see, for example, (48)) with its measurement of an anisotropic distribution of UHECR. Gamma Ray Bursts are valid candidates for cosmic rays sources (49). The UHECR spectrum is compatible with a power law spectrum E^{-2} that generated by the Fermi acceleration process (see section 2.5). In the model in which GRBs are (one of) the sources of UHECRs, protons are accelerated in the jets as well as electrons. These can be accelerated to the ultra high energies required to explain the observed cosmic ray spectrum and can produce high energy neutrinos via interactions with matter and photons.

3.2.1 Photohadronic processes

Assuming the dissipation of energy via baryons in the Fireball model (sec. 2.4), the main source of high energy neutrinos is the decay of charged pions:

$$\begin{aligned} \pi^+ &\longrightarrow \mu^+ + \nu_\mu \\ &\longrightarrow e^+ + \nu_e + \nu_\mu + \overline{\nu_\mu} \end{aligned}$$

and the conjugate production of π^-. Pions can be generated from photopion production or nucleon-nucleon collisions:

$$\begin{aligned} \text{photopion production:} \gamma + n &\longrightarrow p + \pi^- \\ \gamma + p &\longrightarrow n + \pi^+ \\ \text{nucleon-nucleon:} p + n &\longrightarrow p + p + \text{many}\,\pi \\ p + p &\longrightarrow n + p + \text{many}\,\pi \end{aligned}$$

Although the cross section of nucleon-nucleon collision is around two order of magnitude greater than for photon-nucleon interaction, the photon density in the GRB wind is around four orders of magnitude higher, therefore photopion production will be the dominant process of pion creation in the energy range considered in this work (see figure 3.1). Photopair production ($p + \gamma \rightarrow p + e^+ + e^-$, a specific case of the Bethe-Heitler pair production) is only important at energies below 10^4 GeV. Above this energy it levels off at about 20% of the photopion

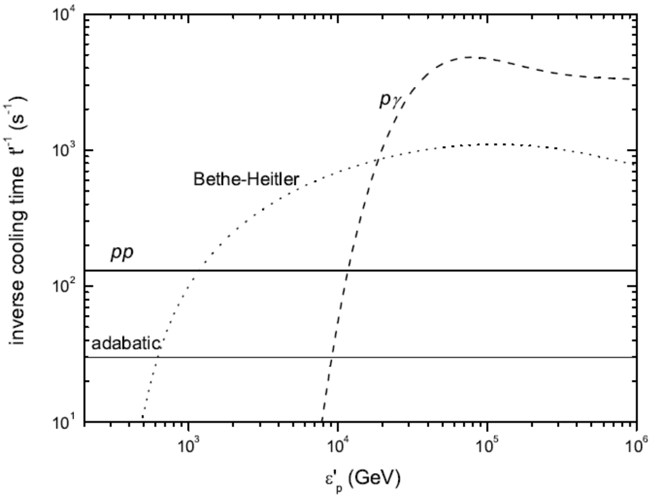

Figure 3.1: Inverse of proton cooling time scales in the comoving frame of the internal shock as functions of proton energy. The straight solid line, dotted line and dashed line are for proton-proton collision, Bethe-Heitler cooling and p processes respectively. Also shown is the cooling time scale due to adiabatic expansion. Figure taken from (50).

production. This process does not have the possibility of producing neutrinos and therefore is neglected. For neutrino production therefore only the $p+\gamma$ process is considered. In this case the dominant channels are:

$$p+\gamma \longrightarrow \Delta^+ \longrightarrow \left\{ \begin{array}{ll} p+\pi^0 & \longrightarrow p+2\gamma \\ n+\pi^+ & \longrightarrow n+e^+ + \nu_e + \nu_\mu + \overline{\nu_\mu} \\ & \longrightarrow p+e^- + e^+ + \overline{\nu_e} + \nu_e + \nu_\mu + \overline{\nu_\mu} \end{array} \right. \tag{3.2}$$

The first channel occurs at a rate twice as large as the second. The second channel generates an extra neutrino from the beta decay of the neutron (decaying after a mean lifetime of $\tau_n \sim 10^3$ s), but this neutrino, besides arriving considerably later than the others, carries around 50 times less energy and, as a consequence, is generally not considered in the computation of the neutrino flux from GRBs.

As a reference neutrino spectrum the one calculated by Waxman and Bahcall in their work (40) is taken. Their description of neutrino production in GRBs is briefly summarized here (36).

To calculate the expected neutrino spectrum, few ingredients are necessary. The interaction cross section of a $p+\gamma$ process is denoted as $\sigma_{p\gamma}(E_r)$. It depends only on the invariant energy of the interaction:

$$E_r = \sqrt{s} = \gamma_p E_\gamma (1-\beta_p \cos\theta) \tag{3.3}$$

Here E_γ is the photon energy, while $\gamma_p = E_p/m_p c^2$ is the Lorentz factor of the accelerated proton. θ is the angle between the directions of the proton and of the photon. With the cross section, it is possible to calculate the interaction rate of a ultra-relativistic proton, travelling in a photon field with number density $n_\gamma(E_\gamma,\Omega) = dN/dE_\gamma d\Omega dN$. This process is important for the conversion of the kinetic energy of the shock in internal energy. The interaction rate can be written as the cross section of the process multiplied by the photon density and integrated over all energies and solid angle. For an inelastic scattering leading to pion production, the proton loses an average fraction of energy $K(E_r)$. The inverse of the photo hadronic energy loss timescale therefore is:

$$t_{\gamma p}^{-1} = \frac{1}{\gamma_p}\left|\frac{d\gamma_p}{dt}\right| = c\int d\Omega \int_0^{\infty} dE_\gamma (1-\beta_p \cos\theta) n_\gamma(E_\gamma, \Omega)\sigma_{\gamma p}(E)r)K_{\gamma p}(E_r) \tag{3.4}$$

To solve this integral, the photon distribution $n_\gamma(E_\gamma)dE$ described in section 3.1 is used. The energy at which this process can take place with the highest rate is given by the energy where the center of mass energy coincides with the Δ mass ($E_{\text{peak}} \simeq 0.3\,\text{GeV}$), where the cross section is maximal ($\sigma_{\text{peak}} = 5\times10^{-28}\,\text{cm}^2$). For low energy protons the target photons must have a very high energy to be able to undergo a photo-meson interaction. But photons with very high energy ($\gg m_e c^2$) will be converted to electron pairs and therefore cannot contribute to pion production. The low energy region of the neutrino spectrum is therefore suppressed with respect to the central region. The neutrino production is however also suppressed at high energy, where the lifetime of high energy pions $\tau_\pi \approx 2.6\times10^{-8}E_\pi/(m_\pi c^2)$ is greater than their characteristic timescale for synchrotron energy loss.

The last ingredient for the calculation of the neutrino spectrum is the fraction f_π of the energy of the proton that gets converted into pion energy. The time available for protons to lose energy via photomeson interaction is comparable to the time for the plasma to reach the radius $r_{int} \simeq \Gamma^2 c\Delta t$, where the collision takes place. Here Γ is the Lorentz factor of the shock and Δt the variability time of the GRB.

So the fraction of proton energy that is given to the pion is the ratio between the expansion time $t_{int} \simeq r_{int}\,\Gamma c$ and the time scale for the photomeson interaction t_π:

$$f_\pi = \frac{t_{int}}{t_\pi} \tag{3.5}$$

One can obtain this quantity substituting the result of equation 3.4 approximated at the peak energy and using the definition of total luminosity of the GRB $L_\gamma = 4\pi r_{int}^2 \Gamma^2 c U_\gamma$, where U_γ is the photon energy density. It is shown (40) that this approximation leads to:

$$f_\pi \approx 0.20\frac{L_{\gamma,52}}{\varepsilon^b_{\gamma,\text{MeV}}\Gamma^4_{300}t_{v,-2}} \gtrsim 20\% \tag{3.6}$$

The notation used indicates the order of magnitude of the interested quantities: $L_{\gamma,52}$ is the total luminosity of the GRB in units of $10^{52}\,\text{erg}\,\text{s}^{-1}$, $\Gamma_{300} = \Gamma/300$ is the scaled Lorentz factor, $t_{v,-2}$ is the variability time of the GRB defined as $t_{v,-2} = t_v/10^2$ and $\varepsilon_{\gamma,b}$, is the break energy of the photon spectrum as defined in equation 3.1 in units of MeVs. This expression is useful to express f_π as a function of the observed GRB parameters. The fact that is close to 20% can also be understood by the observation that when a proton and a photon interact at the resonant energy, the so produced Δ decays in a proton (or neutron) plus a pion. The baryons and the pion will have the same β, as they are produced by the same particle. As their mass difference is about 20%, also the ratio of their momenta will have approximately the same value. This

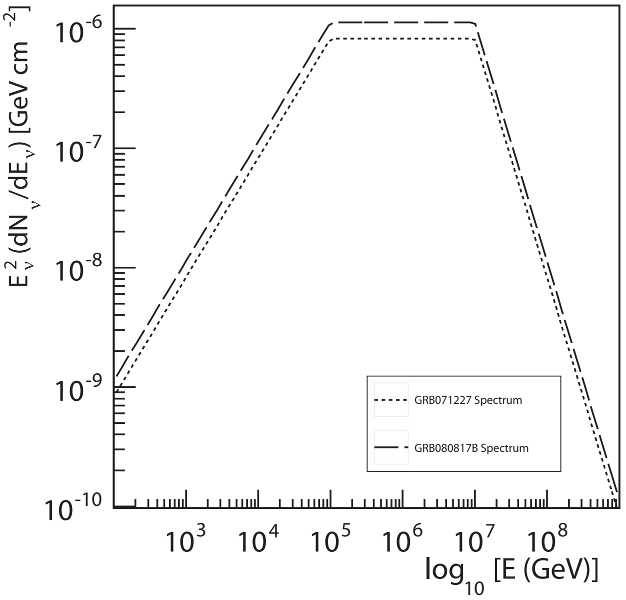

Figure 3.2: Neutrino spectrum from GRBs GRB071227 and GRB080817B calculated using equation 3.3 and inserting the corresponding values for fluence, duration and break energy of these gamma ray bursts.

is why to calculate the neutrino spectrum (40) the fraction of energy lost by the protons into pions is approximated by 20%.

It must be noted, nevertheless, that the value of f_π is strongly dependent on the value of Γ. In (51) the neutrino spectrum for different values of gamma ray burst parameters is calculated. It is remarkable that even without varying the Lorentz factor, but only changing the isotropic GRB energy and the distance, the number of predicted neutrino events per year in a kilometre cube telescope can be enhanced up to a factor 10. This suggests that the fraction f_π can be significantly different from the approximation of 20%. In this case the neutrino flux will be dominated by few bright bursts with $f_\pi \sim 1$. Nevertheless, as shown in (52) the main parameters of the GRBs, such as the Lorentz factor, the total luminosity and the time variability, are correlated and constrained by observations. It is important to note, though, that a single GRB with favourable parameters (for example considerably closer or more energetic) can yield a considerably higher neutrino flux than the one described by the standard values.

3.3 Neutrino Spectrum

The GRB photon fluence, given by formula 3.1, the relative break energy ε_γ^b and the fraction of proton energy that goes into the pion f_π (eq. 3.2.1) are the main ingredients needed to calculate the neutrino spectrum. A precise derivation of the neutrino spectrum, for different GRB models, can be found in (53), but in this paragraph the basic steps to derive it will be presented, considering only the Fireball model. Following the photon spectrum, also the neutrino spectrum results in a broken power law. The neutrino break energy is given, in the observer frame, by:

$$\varepsilon^b_{\nu,\mathrm{obs}} = 7 \times 10^{14} \frac{1}{(1+z)^2} \frac{\Gamma^2_{300}}{\varepsilon^b_{\gamma,\,\mathrm{MeV}}}\,\mathrm{eV} \tag{3.7}$$

As mentioned in the previous paragraph, the neutrino spectrum depends significantly on the GRB parameters. The formula of the break energy is yet another indication that the distance (z, the redshift) and the Lorentz factor of the GRB are important ingredients for the determination of the number of expected events in the detector. Apart from the energy break due to proton synchrotron energy loss, the synchrotron radiation loss of pions and muons prior to their decay also affects the neutrino spectrum. This energy loss becomes important when the synchrotron time scale is comparable to the pion lifetime. It corresponds to a break energy of:

$$\varepsilon^s_{\nu_\mu,\mathrm{obs}} = \frac{10^{17}}{(1+z)^2} \varepsilon_e^{1/2} \varepsilon_B^{-1/2} L_{\gamma,52}^{-1/2} \Gamma^4_{300} t_{v,-2}\,\mathrm{eV} \tag{3.8}$$

where ε_e is the fraction of energy converted into electrons and ε_B is the fraction of energy carried by the magnetic field. For neutrinos produced by muon decay this break energy is ten times lower, as muons have a lifetime 100 times longer than pions.

Supposing that each pion, both charged and neutral, is produced with the same probability, and each neutrino carries 1/4 of the pion energy, the neutrino spectrum can be written as:

$$\frac{dN_\nu}{dE_\nu} E^2_\nu \simeq \frac{1}{8} \frac{1}{\varepsilon_e} \frac{F_\gamma}{ln(10)} f_\pi \tag{3.9}$$

Using the approximation where $f_\pi \sim 0.20$ and deriving the neutrino fluence directly from the photon fluence, the neutrino spectrum can be rewritten as:

$$\frac{dN_\nu}{dE_\nu} E^2_\nu \simeq \frac{0.2}{8\varepsilon_e} \frac{F_\gamma}{ln(10)} \times \begin{cases} (E_\nu/E^b_\nu)^\beta & E_\nu < E^b_\nu, \\ (E_\nu/E^b_\nu)^\alpha & E^b_\nu < E_\nu < E^s_\nu \\ (E_\nu/E^b_\nu)^\alpha (E_\nu/E^s_\nu)^{-2} & E_\nu > E^s_\nu \end{cases} \tag{3.10}$$

The break energies are the ones shown before, with $\beta = -\alpha_\gamma$ and $\alpha = -\beta_\gamma$. The result of this calculation of the spectrum for two example GRBs is shown in Figure 3.2.

3.4 Neutrino flavours from GRBs

The flavour ratio of the neutrinos coming from Gamma Ray Burst is derived from equation 3.2.1. It is nevertheless necessary to consider neutrino oscillation, as neutrinos can change their flavour on their path to Earth. This happens because neutrinos are created at the source as flavour eigenstate ($\nu_\alpha, \alpha = e, \mu, \tau$) but while travelling through space they propagate as mass eigenstates. Neutrino mass eigenstates $\nu_i, i = 1, 2, 3$ are equivalent to the charged leptons mass eigenstates indicated by e, μ, τ and, in contrast to the charged leptons, do not coincide with their flavour eigenstates. Oscillation is a characteristic of the weak interaction and it is manifested by the fact that the weak boson W can couple any lepton mass eigenstate with any neutrino mass eigenstate, analogously to the quark sector, where the quarks d, s and b are coupled with the W boson as weak eigenstates (or flavour eigenstates), and are described as a linear combination of the corresponding mass eigenstates. When a charged lepton of flavour eigenstate α is created, the associated linear combination of neutrino mass eigenstates is defined as its flavour eigenstates, and can be written as:

$$|\nu_\alpha >= \sum_j U^*_{\alpha j} |\nu_j > \tag{3.11}$$

where U is the unitary leptonic mixing matrix that carries the names of Pontecorvo-Maki-Nakagawa-Sakata (PMNS). In the following the oscillations of neutrinos and antineutrinos are considered equal, although some latest evidence shows that there might be some differences (54).

3.4.1 Neutrino Oscillation in vacuum

In standard Gamma Ray Bursts prompt neutrinos are produced in a zone with relatively low density of matter, already quite far from the central engine (see section 2.4.3). In addition to that both the obstacles that neutrinos will find on the way and their trip throughout the Earth can be ignored compared to the distance they cover in empty space. A detailed and clear review of neutrino mixing in vacuum is given in (55), where it is shown that the probability for a neutrino of flavour α to oscillate into a neutrino of flavour β at a distance L is given by:

$$P(\nu_\alpha \longrightarrow \nu_\beta, L) = \delta_{\alpha\beta} - \sum_{j \neq k} U^*_{\alpha j} U_{\beta j} U_{\alpha k} U^*_{\beta k} (1 - e^{-i\Delta E_{ij} L}) \tag{3.12}$$

The formulation of the PMNS matrix given in (55) is:

$$\begin{aligned} U &= \begin{bmatrix} U_{e1} & U_{e2} & U_{e3} \\ U_{\mu 1} & U_{\mu 2} & U_{\mu 3} \\ U_{\tau 1} & U_{\tau 2} & U_{\tau 3} \end{bmatrix} = \qquad\qquad (3.13) \\ &= \begin{bmatrix} c_{12} c_{13} & s_{12} c_{13} & s_{13} e^{i\delta} \\ -s_{12} c_{23} - c_{12} s_{23} s_{13} e^{i\delta} & c_{12} c_{23} - s_{12} s_{23} s_{13} e^{i\delta} & s_{23} c_{13} \\ s_{12} s_{23} - c_{12} c_{23} s_{13} e^{i\delta} & -c_{12} s_{23} - s_{12} c_{23} s_{13} e^{i\delta} & c_{23} c_{13} \end{bmatrix} \begin{bmatrix} e^{i\alpha_1/2} & 0 & 0 \\ 0 & e^{i\alpha_2/2} & 0 \\ 0 & 0 & 1 \end{bmatrix} \end{aligned}$$

where $c_{ij} = \cos\theta_{ij}$, $s_{ij} = \sin\theta_{ij}$ are the mixing angles, α_1 and α_2 are meaningful only if neutrinos are Majorana particles (in which case neutrinos and antineutrinos coincide) and would therefore influence the rate of the neutrinoless double beta decay if such a interaction would take place. The phase factor δ is the leptonic Charge Parity (CP) violation phase and differs from zero only when the symmetry CP is broken. As explained, a neutrino of flavour eigenstate α is described as the linear combination of mass eigenstates ν_j. After a time t, in which the neutrino has travelled trough vacuum, the mass eigenstate can be described as a plane wave:

$$|\nu_j > (t) = |\nu_j > (t) e^{i(px - E_j t)} \tag{3.14}$$

where p is the neutrino momentum and E_j the energy associated to the eigenstate j of mass m_j. The probability of measuring a neutrino of flavour β, when it was produced with flavour α after it has travelled for a time t is therefore:

$$P(\nu_\alpha \to \nu_\beta) =< \nu_\beta|\nu_\alpha > (t) = \sum_j U_{\alpha j} e^{-iE_j t} < \nu_\beta|\nu_\alpha > (0) \tag{3.15}$$

To solve this equation it is necessary to know the parameters for the initial conditions, that are extracted from experimental data, such as:

- $|\Delta m^2_{12}| < |\Delta m^2_{32}| < |\Delta m^2_{31}|$
- From solar neutrino experiments: $\Delta m^2_{21} \simeq \Delta m^2_\odot \simeq 8 \times 10^{-5}\,\mathrm{eV}^2$
- $\theta_\odot \simeq \theta_{12} = 33.83°$
- From atmospheric neutrino experiments: $\Delta m^2_{32} \simeq \Delta m^2_{atm} \simeq 2.4 \times 10^{-3}\,\mathrm{eV}^2$
- $\theta_{atm} \simeq \theta_{23} = 45°$
- $\sin^2(2\theta_{13}) \lesssim 0.15°$

it is then possible to rewrite the oscillation probability as

$$P(\nu_\alpha \longrightarrow \nu_\beta) = \sin^2(2\theta)\sin^2\left(\frac{\Delta m^2 L}{4E}\right) \xrightarrow[L\to\infty]{} \frac{1}{2}\sin^2(2\theta) \tag{3.16}$$

where L can be considered to be very big with respect to the other quantities. A typical GRB takes place at $L \simeq 10^2\,\mathrm{Mpc}$, where $1\,\mathrm{pc} \simeq 3 \times 10^8\,\mathrm{cm}$.

This means that if at the source of the GRB the neutrino fluxes are $\phi^0_{\nu_e}$, $\phi^0_{\nu_\mu}$ and $\phi^0_{\nu_\tau}$, the relative fluxes received at Earth will be:

$$\begin{aligned}
\phi_{\nu_e} &= \phi^0_{\nu_e} - \frac{1}{4}\sin^2 2\theta_{12}(2\phi^0_{\nu_e} - \phi^0_{\nu_\mu} - \phi^0_{\nu_\tau}) \\
\phi_{\nu_\mu} &= \frac{1}{2}(\phi^0_{\nu_\mu} + \phi^0_{\nu_\tau}) + \frac{1}{8}\sin^2 2\theta_{12}(2\phi^0_{\nu_e} - \phi^0_{\nu_\mu} - \phi^0_{\nu_\tau}) \\
\phi_{\nu_\tau} &= \frac{1}{2}(\phi^0_{\nu_\mu} + \phi^0_{\nu_\tau}) + \frac{1}{8}\sin^2 2\theta_{12}(2\phi^0_{\nu_e} - \phi^0_{\nu_\mu} - \phi^0_{\nu_\tau})
\end{aligned}$$

so, for both neutrinos and antineutrinos the oscillation probability leads to:

$$\begin{bmatrix}\phi_{\nu_e}\\ \phi_{\nu_\mu}\\ \phi_{\nu_\tau}\end{bmatrix} = \begin{bmatrix}0.6 & 0.2 & 0.2\\ 0.2 & 0.4 & 0.4\\ 0.2 & 0.4 & 0.4\end{bmatrix}\begin{bmatrix}\phi^0_{\nu_e}\\ \phi^0_{\nu_\mu}\\ \phi^0_{\nu_\tau}\end{bmatrix} \tag{3.17}$$

Considering the production rate at the source, it is possible to calculate the ratio of each flavour at Earth (56) for the photomeson process:

$$p\gamma \longrightarrow \begin{array}{cc} \phi^0_\nu & \phi^0_{\overline{\nu}} \\ \begin{bmatrix}1\\1\\0\end{bmatrix} & \begin{bmatrix}0\\1\\0\end{bmatrix}\end{array} \Rightarrow \begin{array}{cc} \phi_\nu & \phi_{\overline{\nu}} \\ \begin{bmatrix}0.8\\0.6\\0.6\end{bmatrix} & \begin{bmatrix}0.2\\0.4\\0.4\end{bmatrix}\end{array} \tag{3.18}$$

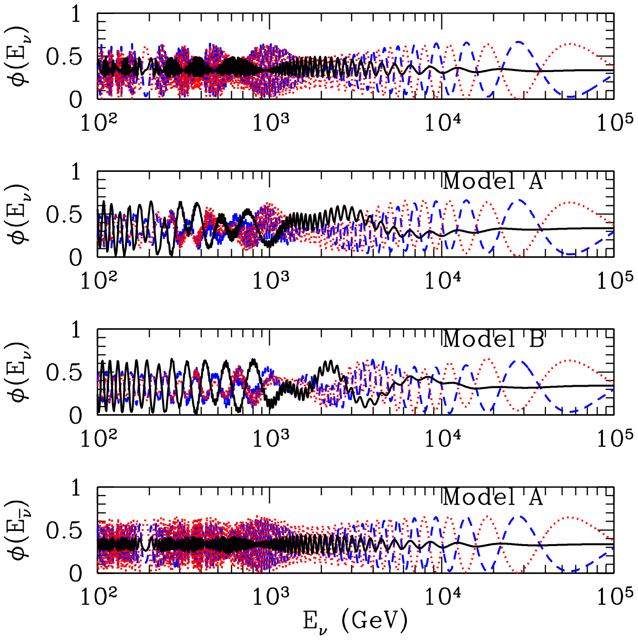

Figure 3.3: This figure shows the neutrino fluxes for different flavours at the surface of the source. The first image refers to the oscillation in vacuum, while the three following models are the fluxes expected for oscillation in matter following three different density profiles. Figure taken from (46)

It is interesting to see that although the final ratio summing neutrinos and antineutrinos is $\nu_e : \nu_\mu : \nu_\tau = 1 : 1 : 1$, because of the maximal $\nu_\mu \leftrightarrow \nu_\tau$ mixing, this is not true if neutrinos and antineutrinos are considered separately. This observation is meaningful for this work, because $\overline{\nu}_e$ detection can be enhanced by the Glashow resonance (see section 4.1.1) at $6.3\,\mathrm{PeV}$.

The average neutrino spectrum from a typical GRB, as calculated in 3.3, refers to the flux of each flavour at the source. To calculate the expected flavour composition on Earth, therefore, one must weight that flux with the flavour ratio calculated above.

3.5 Neutrino flavour change from choked GRBs

The expected neutrino ratio at Earth can be different from the one described in 3.4.1 if the flavour ratio at the source is different from 1:2:0. This can be the case for choked gamma ray bursts (see section 3.5), because of matter effects to which neutrinos are subjected before reaching the surface of the star (46). Analogously to the previous case, to know the flavour at the surface of the astrophysical object one can use the following expressions:

$$\begin{aligned}
\phi^0_{\nu_e} &= \phi^s_{\nu_e} P(\nu_e \to \nu_e) + \phi^s_{\nu_\mu} P(\nu_\mu \to \nu_e) \\
&= \phi^s_{\nu_\mu}(\frac{1}{2}P(\nu_e \to \nu_e) + P(\nu_\mu \to \nu_e)) \\
\phi^0_{\nu_\mu} &= \phi^s_{\nu_\mu}(\frac{1}{2}P(\nu_e \to \nu_\mu) + P(\nu_\mu \to \nu_\mu)) \\
\phi^0_{\nu_\tau} &= \phi^s_{\nu_\mu}(\frac{1}{2}P(\nu_e \to \nu_\tau) + P(\nu_\mu \to \nu_\tau))
\end{aligned}$$

the difference is, of course, that the oscillation probabilities are in this case different. The reason is that when neutrinos propagate trough matter they are differentiated according to their flavour. This happens because matter is almost exclusively composed from particles of the first family or generation (electrons and up-down quarks). As a consequence, electron neutrinos can interact with the surrounding matter with both neutral and charged current interactions. This effect is known as Mikheyev-Smirnov-Wolfenstein (MSW) effect. Neutral current interactions act on all neutrino flavour indistinctly with a potential:

$$V_n(r) = -\frac{1}{\sqrt{2}} G_F N_n(r)$$

where $N_n(r)$ is the neutron density profile as a function of the distance from the center of the star r and G_F is the Fermi constant. Charged current interactions, on the other hand, have a potential only for electron neutrino scattering on matter:

$$V_e(r) = \sqrt{2} G_F N_e(r).$$

In this case the evolution equation 3.14 has also to include this potential. Matter effects could become very large when the electron density is resonant. For a constant electron density these resonances take place in correspondence to the two mass squared differences involved Δm^2_{12} and Δm^2_{13} and with specific neutrino energy ranges. Figure 3.3 shows the expected neutrino fluxes at the surface of the star using three different models for describing the electron density in the source (46).

3.6 Neutrino Event Rates

The calculation of expected neutrino rates in the detector, taking into consideration the calculations explained in the previous paragraphs, is done by means of Monte Carlo simulation, as explained in section 5.2.1.1 of chapter 5. It is nevertheless useful to understand it from a more analytical point of view, as it is done, for example, in reference (53). The number of hadronic showers induced by a Gamma Ray Burst of duration T and happening in a detector with a surface A sensitive to a neutrino flux $d\phi_{\nu_i}/dE_{\nu_i}$ is

$$N_{sh} = \sum_{ij} 2\pi AT \int dE_{\nu_i} \frac{d\phi_{\nu_i}}{dE_{\nu_i}} P_{surv}(E_{\nu_i}, \theta_z) \times \tag{3.19}$$

$$\times \int_{y^{i,j}_{min}}^{y^{i,j}_{max}} dy \frac{1}{\sigma^i(E_{\nu_i})} \frac{d\sigma^j}{dy}(E_{\nu_i,y}) P_{int}(E_{\nu_i}, y, \theta_z)$$

Sums are made over neutrino flavour ($i = e, \mu, \tau$) and type of interaction ($j = CC, NC$, charged current or neutral current). P_{surv} is the survival probability of a neutrino to cross Earth without interacting, and can be written as:

$$P_{surv} = \exp[-X(\theta_z)\sigma(E_{\nu_i})N_A] \tag{3.20}$$

where the exponential is the number density of the column of earth crossed by the neutrino ($X(\theta_z)N_A$) as a function of the direction of the neutrino itself, multiplied by the total cross section ($\sigma = \sigma_{CC} + \sigma_{NC}$) for neutrino interactions. P_{int} is the probability that a neutrino that passes inside the detector will interact there to produce a signal. Figure 3.4 shows the probability that a neutrino of each flavour could generate a signature of any type in the detector. From this plot is possible to see that upgoing neutrinos have a energy cut at around 10^{15} eV (half order of magnitude below for shower events) because of the absorption of the Earth: a neutrino with such energy will most likely interact well before reaching the detector. This is not true for tau neutrinos, as the product of such interaction, a tau lepton, will immediately decay in another tau neutrino, causing a regeneration process that will allow tau neutrinos to reach the detector even at considerably higher energies. As shown in chapter 6, the technique used in this work can also detect tau neutrinos, and is presently the only method in Antares to be able to detect neutrinos with energies above 10^{15} eV from Gamma Ray Burst situated on the other hemisphere in respect to the detector.

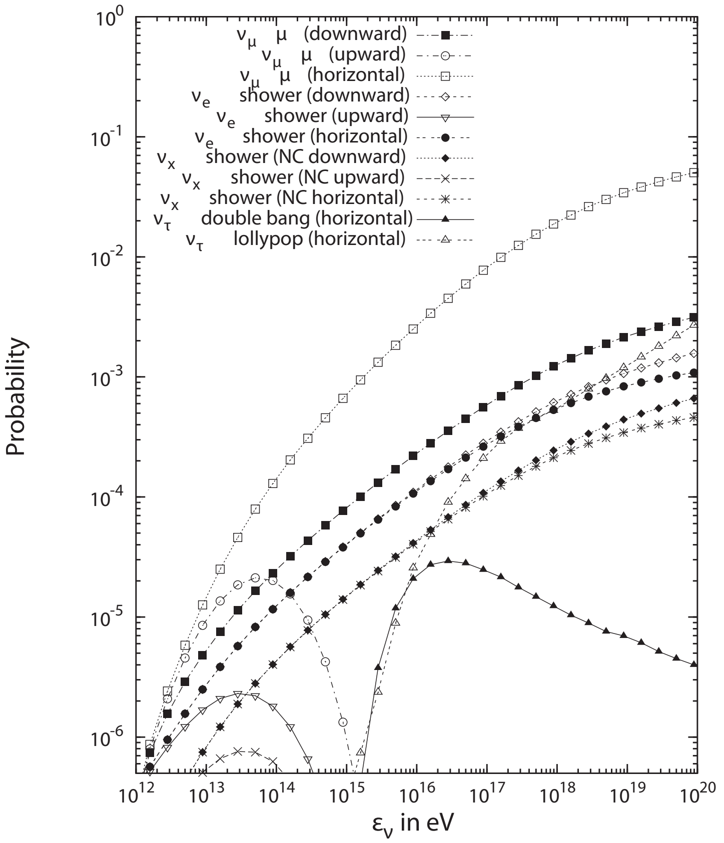

Figure 3.4: This figure shows the neutrino probability of interacting in a neutrino telescope and generating different types of signatures. Figure taken from (53)

4

The Antares Detector

> *I always loved the view. Sunlight on the water. It's my favourite spot in the universe.*
>
> Caprica-Six

4.1 Neutrino Interactions

The majority of neutrinos that reach Earth, will just pass through it, without leaving any detectable trace. However, it is possible for them to undergo a weak interaction with a nucleon or more rarely with an electron. Due to their extremely small cross section, a very large target mass is necessary to attempt detection. The reaction that is used in high energy neutrino detectors to reveal this particle is the neutrino Deep Inelastic Scattering (DIS) off a matter nucleon. The kinematics of this reaction is represented by the Feynman diagram in Figure 4.1. A neutrino of energy E and momentum $\vec{p}$ interacts with a nucleon (with four-momentum P) via the weak interaction (with the exchange of a $W^{\pm}$ or Z^0 boson), generating in the process a lepton with energy E' and momentum $\vec{p}'$. The interaction is described by the kinematics variables Q^2, the exchanged four-momentum squared, the Bjorken scaling variable $x = Q^2/2qP$ and inelasticity y. $Q^2 = -q^2$ is minus the square of the transferred 4-momentum between the interacting neutrino and the nucleon:

$$Q^2 = -q^2 = -(p - p')^2 \tag{4.1}$$

As the incoming neutrino has a very high momentum compared to the scattered nucleon, the latter is considered to be at rest. In this condition the Bjorken variable x represents the fraction of 4-momentum of the proton carried by the struck parton:

$$x = \frac{Q^2}{2qP} = \frac{Q^2}{2M(E - E')} \tag{4.2}$$

For an inelastic interaction the hadronic mass of the final state M' is different from its initial mass M, therefore $Q^2 = 2M(E - E') + M^2 - M'^2$. For a perfectly elastic scattering x would be

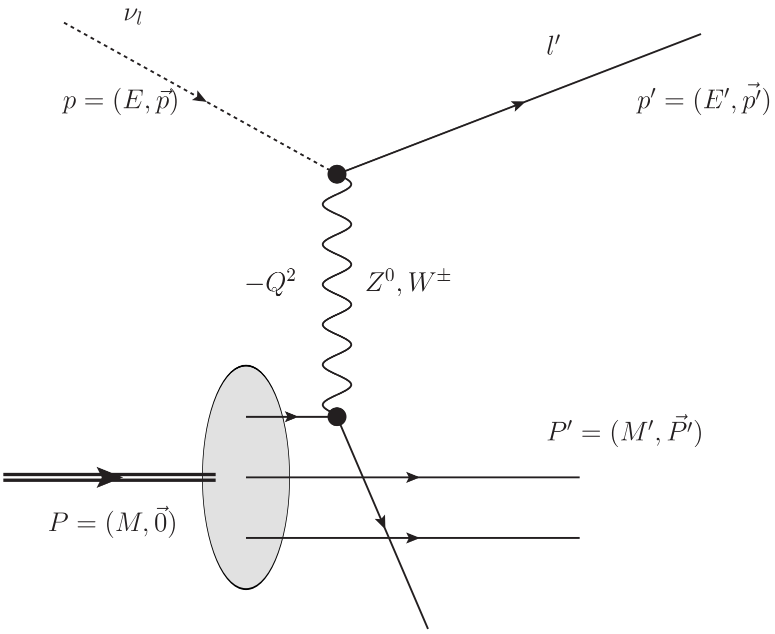

Figure 4.1: Feynmann diagram of the deep inelastic scattering of a neutrino off a nucleon. A neutrino with 4-momentum p interacts with a nucleon with rest mass M, generating a lepton with 4-momentum p'.

equal to 1. The inelasticity parameter y is the fraction of the energy transferred to the hadronic system left after the interaction:

$$y = \frac{qP}{pP} = \frac{E - E'}{E}. \tag{4.3}$$

For perfectly elastic scattering the lepton must scatter off the full nucleon so $x = 1$ and transfer no energy in the nucleon rest frame, therefore $y = 0$.

4.1.1 Interaction Types

When neutrino interactions happen with the exchange of a charged $W^\pm$ boson, the interaction is a CC and the resulting lepton is charged. If the boson exchanged is the neutral boson Z^0, the interaction is a neutral current (NC) and the outgoing lepton is a neutrino. Figure 4.2 shows the cross sections calculated with the SeaTray Monte Carlo package (Chapter 5). CC interaction cross sections are always larger than the corresponding NC interactions (NC cross section is about one third of the CC cross section), and the same holds for neutrinos with respect to antineutrinos.

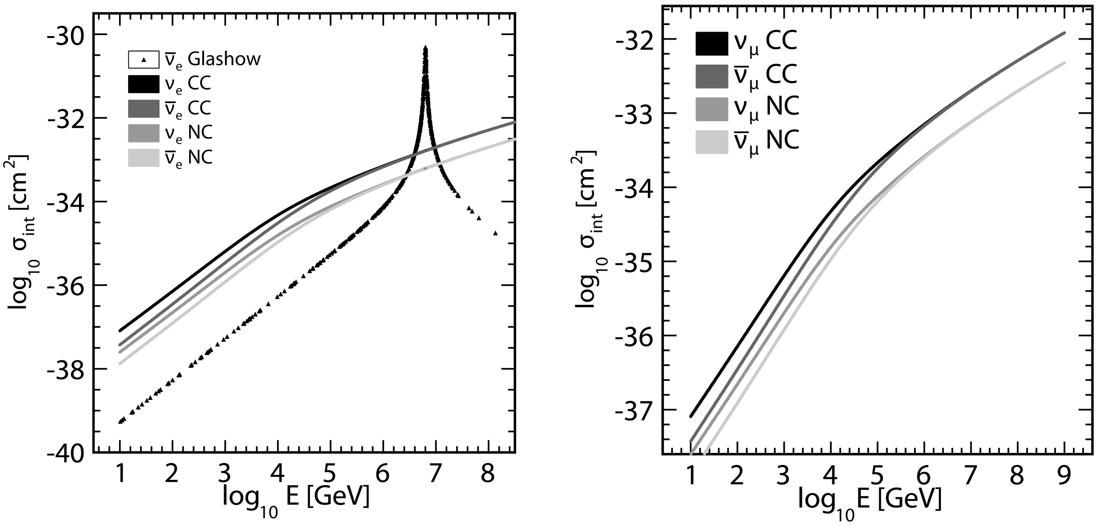

(a) ν_e, $\bar{\nu}_e$ Cross Section

(b) ν_μ, $\bar{\nu}_\mu$ Cross Section

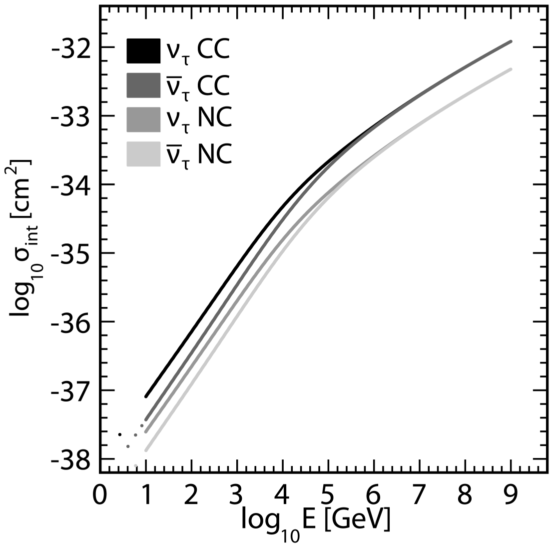

(c) ν_τ, $\bar{\nu}_\tau$ Cross Section

Figure 4.2: Cross sections for neutrino interactions with a nucleon. Each figure shows a different neutrino flavour, and each line correspond to a different neutrino/antinuetrino, CC/NC interaction. The plot was generated using the CTEQ5 parton distribution inside the SeaTray simulation software (Chapter 5). For $\bar{\nu}_e$ the cross section with electrons is also given, showing the effect of resonant W production.

A notable difference is visible in Figure 4.2(a), where the Glashow resonance is shown at about 7 PeV of energy. The Glashow resonance takes place when a $\bar{\nu}_e$ of this energy interacts with one of the electrons in matter, producing a W boson resonantly via a CC interaction. This leads to a significant enhancement in the cross section. In fact at the resonance the interaction cross section with the electron exceeds that with the nucleon by more than an order of magnitude.

4.2 Neutrino Detection

The only way to detect a neutrino is to search for signals produced by the charged particles in a neutrino interaction. The signal searched for is that of Cherenkov radiation. Due to the small interaction cross sections involved, a large target mass is necessary to provide a sufficient interaction rate. Furthermore the detection of Cherenkov light requires the target to be transparent. Therefore the Antares neutrino telescope is equipped with an array of light sensitive Photomultiplier Tubes (PMTs) installed at a large depth in the Mediterranean Sea. This array of PMTs can detect the photons produced by highly energetic charged particles generated by neutrino interactions in the vicinity of the detector.

4.2.1 The Cherenkov Radiation

The main physical effect that allows for the detection of neutrinos is the Cherenkov radiation. When a neutrino interacts in the vicinity of the detector via a CC interaction, it generates a relativistic charged particle that will travel through the sea water in the detector. When the speed of a charged particle exceeds the velocity of light in the medium through which it is travelling it will emit radiation called Cherenkov radiation (57). The light speed v_l in a medium is given by

$$\beta c = v_l = \frac{c}{n} \tag{4.4}$$

where c is the speed of light in vacuum and n is the index of refraction of the medium. When the particle travels faster than light in the medium it will generate a shock wave, as depicted in Figure 4.3.The light emission creates a wave front where the emitted light is coherent. It is easy to show that the wave front forms a cone with its apex at the travelling particle. The opening half-angle of the cone θ_c can be written as

$$\cos\theta_c = \frac{1}{\beta n} \tag{4.5}$$

The sea water at the location of the Antares neutrino telescope, has a value of n of about 1.35 (58), thus the value of the Cherenkov angle is about 42.2°. The number of Cherenkov photons emitted by a particle with a single charge (as a muon or an electron) per unit wavelength, $d\lambda$ and per unit track length (dx) is given by

$$\frac{dN}{dxd\lambda} = 2\pi\alpha\frac{1}{\lambda^2}\left(1 - \frac{1}{\beta^2 n^2}\right) \tag{4.6}$$

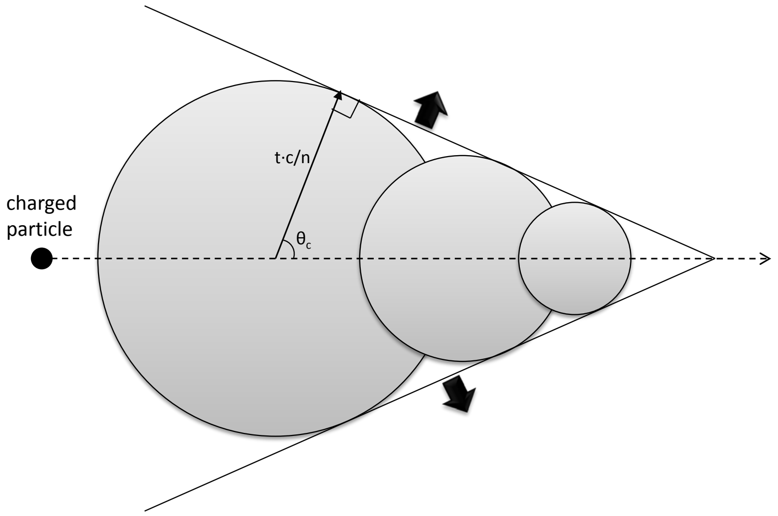

Figure 4.3: Cherenkov cone generated by a charged particle travelling through a medium with a speed superior of that of light in the same medium.

where λ is the emission wavelength of the photon and α is the fine structure constant. Given the refraction index of the Antares sea water, and considering photons with a wavelength between 300 and 600 nm (where the Antares PMTs are most efficient), about 3.5×10^4 detectable photons are emitted per metre of track.

4.2.2 Detection Principle

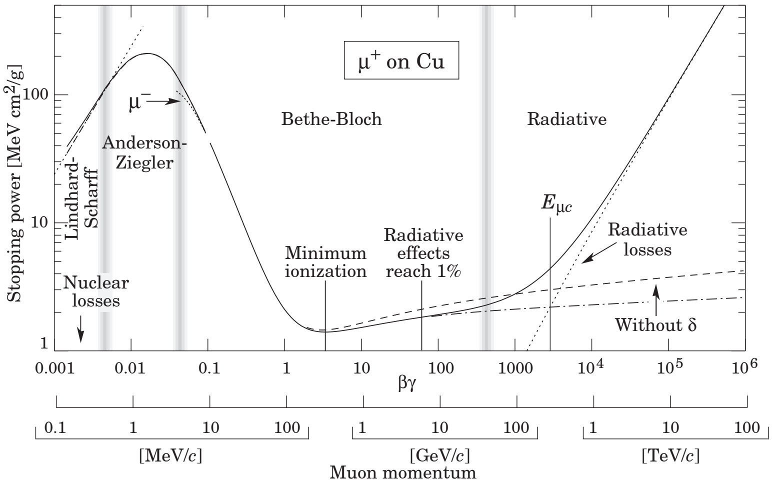

Figure 4.4: Stopping power for positive muons in copper as a function of $\beta\gamma = p/Mc$ over nine orders of magnitude in momentum (12 orders of magnitude in kinetic energy). Solid curves indicate the total stopping power. Figure taken from (59)

Neutrinos of any flavour interacting with a NC will produce a neutrino, which remains undetectable, and an hadronic shower, consisting of many interaction products. These produce Cherenkov light. Due to the small volume where the shower takes place the shower appears in the detector as a point-like light source developing isotropically in time. Electron neutrinos will also produce a luminous shower in the detector, regardless of the interaction. Muon neutrinos with a CC interaction will in addition produce a charged muon, visible in a neutrino telescope as a long track emitting Cherenkov radiation . This last signal is the main one for the Antares detector. The reason is that the muon generated by CC interaction of a high energy muon (anti)neutrino can travel very large distances due to its low energy loss in matter (see Figure 4.4). This increases the effective volume of the detector. Furthermore the produced muon will have approximately the same direction as the incoming neutrino, following the empirical relation:

$$\Delta\theta \leq \frac{1.5^\circ}{\sqrt{E_\nu/[TeV]}} \tag{4.7}$$

where $\Delta\theta$ is the angular difference between the neutrino and the muon direction and E_ν is the neutrino energy. Although the muon is subjected to multiple scattering through matter, it will maintain the same direction to a large extent. Figure 4.5 shows the difference in the direction of the muon with respect to the neutrino and the variation of the muon direction from the interaction vertex point to the moment in which it enters the detector.

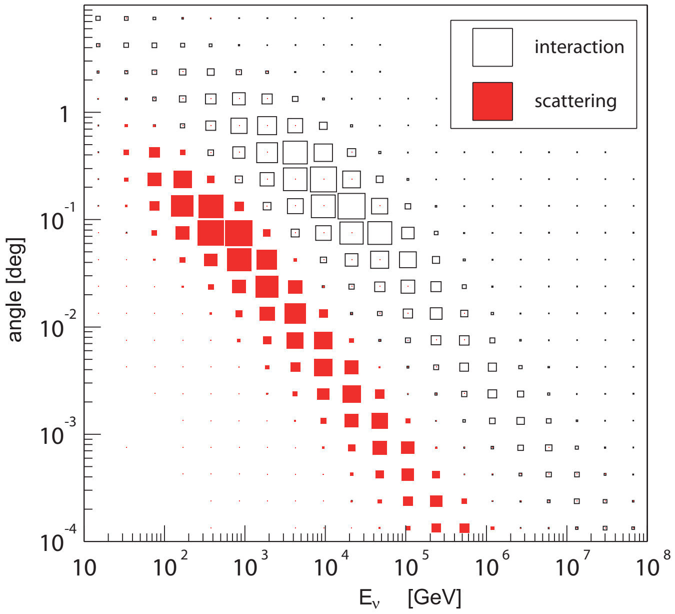

Figure 4.5: Angle between the neutrino direction and the produced muon (labelled as "interaction"), and the variation in direction of the muon due to multiple scattering. Figure taken from (60)

When a charged particle generates Cherenkov radiation, the signal appears in the detector as a "track". The hadronic products of the neutrino interaction can also be detected by Antares.

They appear as a flash of light propagating isotropically in time. An overview of all possible signature in the Antares telescope is given in Figure 4.6.

4.2.3 Track-like Events

Several neutrino interaction channels can produce detectable tracks in the detector. The one that generates the longest track is a muon neutrino or antineutrino that interacts with matter via a CC interaction in or around the detector and produces a charged lepton:

$$\nu_\mu(\overline{\nu}_\mu) + N \rightarrow \mu^\mp + \text{hadronic shower}$$

The charged muon then produces light via Cherenkov radiation. This light is collected by photomultipliers tubes and used to reconstruct the direction of the muon. Both muon neutrino and antineutrino produce the same signature in the detector and are therefore indistinguishable. Both events are represented in Figure 4.6(a).

A CC interaction induced by a tau (anti-)neutrino can also produce a track. The difference, in this case, is the lifetime of the charged lepton: a tau lepton has a decay length of approximately 50 m at a peta electronvolt = 10^{15} eV (PeV). Thus, if it is sufficiently energetic, the tau can emit Cherenkov radiation and be detected as a track, but will eventually decay either leptonically as $\tau \rightarrow e + \nu_e + \nu_\tau$ (with a branching ratio of $\sim$ 17.8%) or $\tau \rightarrow \mu + \nu_\mu + \nu_\tau$ ($\sim$ 17.4%), or hadronically, mainly to charged and neutral pions and kaons ($\sim$ 65%). In the first and in the last case (around 82% of branching ratio) this decay will produce an additional hadronic shower, with no track remaining (because of this peculiar signature, these type of events are also referred to as "double bang" events). In the case of the muonic decay, on the other hand, the muon will emit Cherenkov radiation, so this event will look like a straight track in the detector. Because of the mass difference between the two charged leptons, the muon will emit more light than the tau (from 3 to 7 times more light, depending on the photonuclear energy loss model), making it possible to distinguish this signature (61).

In each of these cases, a hadronic shower is also produced together with a track, as shown in Figure 4.6(b). Nevertheless, very often this shower is far from the detector itself, and only the track is reconstructed. The CC muonic channel is the most used, as it produces a long track that is easier to detect by a neutrino telescope. Using different signatures, nevertheless, allows for flavour recognition and for investigating different physical aspects, such as neutrino oscillation.

4.2.4 Shower-like Events

When the neutrino interaction does not produce a high energy muon, no track is visible in the detector. If the main vertex of the interaction is in the vicinity of the detector, it is possible to see light as if being emitted from a point source. The reconstruction of the primary shower therefore relies on the hits being produced at a time after the occurrence of the shower that is equal to the distance from the shower divided by the velocity of light in water. A neutrino that undergoes a NC interaction will not produce a charged lepton capable of leaving a detectable

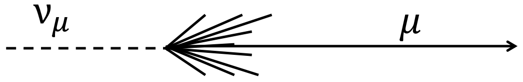

(a) CC interaction of a ν_μ generating an hadronic shower and a charged muon

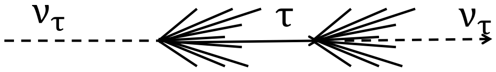

(b) CC interaction of a ν_τ producing an hadronic shower and a charged tau lepton that decays into another ν_τ after some distance, generating another hadronic shower

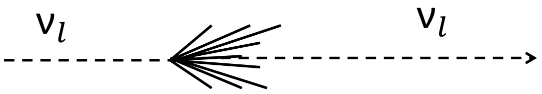

(c) NC interaction of any flavour neutrino, producing only an hadronic shower

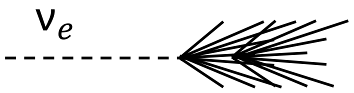

(d) CC interaction of a ν_e producing a charged electron that initiate a electro magnetic shower right after the hadronic shower.

Figure 4.6: Schematic view of a "track" or "shower" like event in the Antares detector.

track:

$$\nu_l(\overline{\nu}_l) + N \rightarrow \nu_l(\overline{\nu}_l) + \text{hadronic shower}$$

where l indicates the neutrino flavour. As shown in Figure 4.6(c), a neutrino having a NC interaction in the detector will create an hadronic shower, identifiable by its large light emission from a single point. A hadronic shower, together with a charged electron, is also produced by an electron neutrino interacting with a CC interaction. Since electrons are considerably lighter in mass than muons or taus they will undergo substantial energy loss via Bremsstrahlung. Therefore instead of leaving a track, the electron generates an electromagnetic shower of particles very close to the primary vertex.

An hadronic shower is physically different from an electromagnetic shower. While the electromagnetic shower is composed exclusively of electrons and photons, a hadronic shower contains several heavier particles, such as mesons (mainly pions) and heavy leptons such as muons. As a result of this different composition, the extension of the shower is larger and much more variable for hadronic showers. An electromagnetic shower appears when a electron neutrino interacts generating an electron. Electrons, having a very light mass, produce a number of photons via Bremsstrahlung. These photons create new electrons via pair production, and electrons and positrons generate again new light via Bremsstrahlung. This chain continues until the electrons energy is such that their rate of Bremsstrahlung and ionization is the same. At this point the remaining energy is dissipated via ionization and the shower finishes. The difficulty in describing an hadronic shower is that the composition may vary considerably event by event. Although they are primarily composed of pions, a fraction of kaons, muons and other charged particles can be present. Muons will most likely leave the shower, and proceed to radiate Cherenkov light along its track. These effects cause the hadronic shower to appear less regular and more oblong. On the other hand, with the increase of the energy of the hadronic shower, the electromagnetic component becomes more and more important, as more π^0 are created. The π^0 have a much shorter life time than their charged companions and decay almost immediately into photons. These photons start an electromagnetic cascade. Due to the difference in composition, hadronic showers emit roughly 20% less light than an electromagnetic shower of the same energy. In a high energy neutrino detector, such as Antares, it is not possible to distinguish electromagnetic and hadronic showers, as the spacing between optical modules (see 4.3.1) is too large to allow for a detailed study of the shower topology.

For an hadronic (or electromagnetic) shower to be measured, it is necessary for the primary vertex to occur in or around the instrumented detector volume. This reduces the probability of production of a reconstructible shower. This results in the effective target volume being equal to the geometrical volume of the detector. For muons this effective volume is much larger due to the large range of muons in matter. Therefore one expects a worse sensitivity for showers than for muon tracks. A shower reconstruction is sensitive to all neutrinos and both CC and NC interaction. Being able to study shower events, is therefore a valuable complementary study to support track reconstruction and analysis and has very different systematics.

First of all it represent a parallel channel, being able to detect neutrinos of flavours not visible via track reconstruction. Coincidences between track and shower measurements can be a useful tool to improve the detection capabilities of a neutrino telescope. What is more, the background reduction for shower analyses, such as the one presented in this thesis, is based on energy and time cuts, and not on the directional information, that is generally not present or not as precise as for tracks. Therefore it is not necessary to select only events caused by neutrinos passing through Earth, but the entire sky can be considered for the analysis.

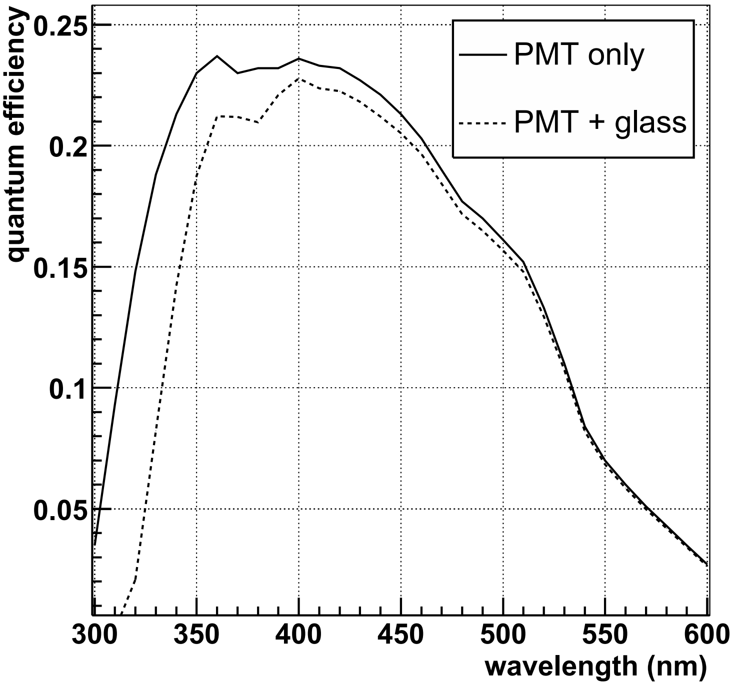

Figure 4.7: Quantum efficiency as a function of the wavelength for a pmt alone and for the pmt enclosed in the glass sphere.

4.3 The Antares Detector

The Antares neutrino telescope (Astronomy with a Neutrino Telescope and Abyss environmental RESearch) is a European project consisting of more than 150 scientists and engineers coming from 22 institutes in seven different nations. The Antares detector is placed at geographical coordinates $42°50'$N and $6°10'$E, around 40 km south of the coast in the gulf of Toulon. It is positioned on the seabed at 2475 m of depth. The choice of location and depth followed several studies into marine conditions, optical backgrounds, sedimentation and bioluminescence rates (62).

The Antares detector consists of a three-dimensional array of photo sensitive devices (photomultipliers) that measure the Cherenkov signal photons. Figure 4.10 shows a schematic view of the detector: it covers an area of about $0.1\,\mathrm{km}^2$. The photosensors are suspended from ~ 450 m long vertical cables. The detector contains twelve such lines and 890 photosensors.

4.3.1 Optical Module

The Optical Module (OM) are the core of the detector itself. They consist of a photomultiplier (PMT) (10" Hamamatsu R7081-20) housed in a pressure-resistant glass sphere with a diameter of around 43 cm and 15 mm of thickness (63). In Figure 4.8 a 3-dimensional view of the optical

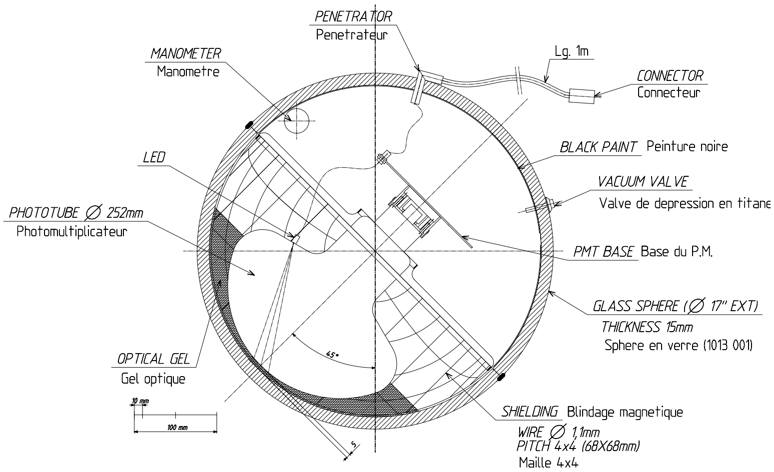

Figure 4.8: A schematic view of the Antares optical module.

module is shown. The PMT has a sensitive area of 440 cm^2 and is glued to the surface of the sphere with a layer of optical silicon gel. The photocathode is of the bi-alkali type and has a Quantum Efficiency (QE) of about 25% at 370 nm. The wavelength dependence of the quantum efficiency is shown in Figure 4.7.

The accuracy with which the arrival time of a photon at the photocathode can be determined is limited by the Transit Time Spread (TTS). The transit time is the time that it takes between the moment in which the photon touches the photo-cathode and the moment in which the anode release the current pulse. The TTS is the full-width-at-half-maximum (FWHM) of the probability distribution of the fluctuations in transit times in response to a single photon. The TTS is inversely proportional to the squared root of the number of photons, $1/\sqrt{n}$. The single photon TTS for the used PMTs is 2.6 ns. To shield the PMT from the magnetic field of the Earth, it is surrounded by a cage of μ-metal, a nickel-iron alloy with a very high magnetic permeability for low intensity magnetic fields. Every OM is read out by the electronics contained in the Local Control Module (LCM), in particular by a pair of Analogue Ring Samplers (ARS), the ASIC chip used for signal processing and digitisation (see Section 4.4). The optical modules (OM, see 4.3.1) are suspended from a titanium frame called Optical Module Frame (OMF). The photomultipliers are directed toward the bottom of the sea, with an inclination from the vertical of 45°. On each OMF there are three optical modules, that are pointing 120° away from each other. This configuration optimises the detection of Cherenkov radiation coming from up-going muons. Having the photomultipliers looking upward would also pose problems because of the deposit of dust on the photosensitive surface. In the chosen conditions, on the other hand, the average transmission loss after one year was measured around 2% (64).

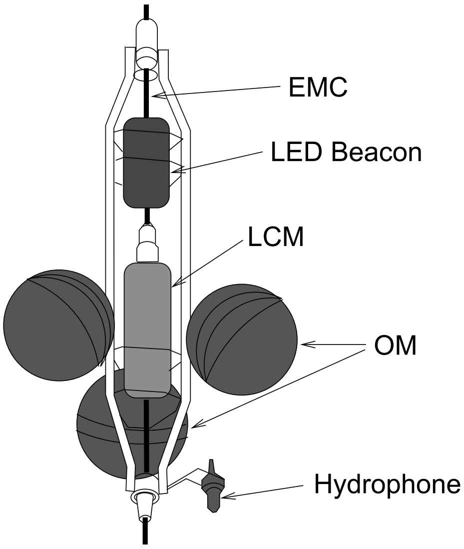

Figure 4.9: Schematic view of the Antares storey

4.3.2 Detector Layout

The OMF holds the electronic and the readout system of the modules, protected within a titanium cylinder referred as local control module (LCM). Some of these structures contain a pressure-resistant glass cylinder, a hydrophone used for acoustic positioning and the LED optical beacon for the time calibration (see 4.5). The collection of the OMF and all the contained devices is defined as a *storey* (Figure 4.9). Five storeys along the same line form a *sector*. Each sector is independent and one of the storey manages the distribution of data and connection with the shore. This module is the master local control module (MLCM). One single vertical line contains five sectors, and each storey is 14.5 m apart from the other.

There are a total of 12 independent lines, corresponding to 900 photomultiplier tubes, kept vertical by a buoy and anchored to the soil via a Bottom String Socket (BSS) (see Figure 4.10). This socket contains also a String Control Module (SCM) and the String Power Module (SPM) to provide data and power connection to the line. A laser beacon is also situated there and its function is to provide the time calibration (Section 4.5). The lines are separated from one another by a distance that varies from 60 to 75 m. The detector has a thirteenth line, called Instrumentation Line (IL), whose function is to constantly monitor the environmental parameters for use of the Antares collaboration and external marine scientists. The Antares detector is placed 40 km away from the shore, but it is connected to the main control room through a Main Electro-Optical Cable (MEOC) that contains the cables needed to transfer the power and the optical fibres for the signal data. The detector is powered the Junction Box (JB), connected to the MEOC and then to the detector itself. The control room is placed close to the beach in La Seyne-sur-mer, in the Institute Michel Pacha. The deployment of the detector took place from March 2006 up to May 2008, line by line. Each line has been deployed by a ship and, eventually, connected by a Remotely Opertated submarine Vehicle (ROV) with a

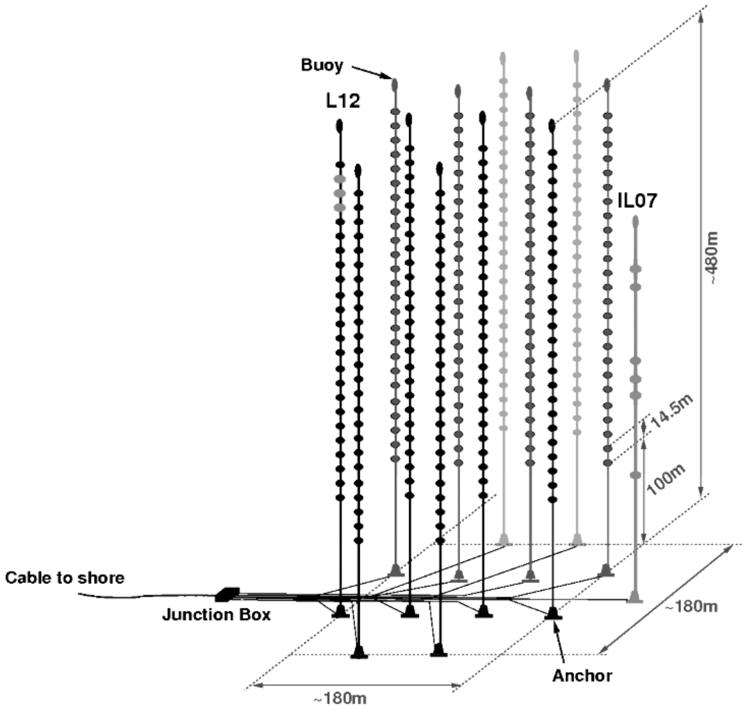

Figure 4.10: Schematic view of the detector layout

interconnecting link cable. The detector layout has been chosen in order to achieve the best compromise between costs, connection and control possibility and volume coverage.

4.4 Data Acquisition System

The data acquisition system of Antares is based on the concept of *all-data-to-shore*, in which all background removal is performed in a software data processing farm on shore. All signals with an amplitude higher than 0.3 photo electrons (p.e.) are digitised at the LCM before being sent to shore. A schematic view of the data acquisition system is shown in Figure 4.11 (65).

The analogue signal of each PMT is read by two integrated circuits called Analogue Ring Sampler (ARS), that digitise the signal when triggered. Once the signal has been digitised, it is sent to the Data Aquisition (DAQ) board, that collects the data and sends it to shore via an Ethernet network. To provide the correct time information for the data acquisition, an internal clock system is used. It is composed of a master clock, on shore, a clock distribution system and a clock signal transceiver placed locally on each LCM. The master clock provides an optical signal with a frequency of 20 MHz (so, each 50 ns) to the ARSs mounted in the LCMs. It is possible to superimpose to the clock signal also data commands, such as *start* and *stop* commands. This signal is then sent to the junction box, where is distributed to the single LCMs. The received optical signal is converted in a data stream and sent to the front-end chips. Each time the PMT registers a signal above threshold (typically 0.3 p.e.), the ARS records the

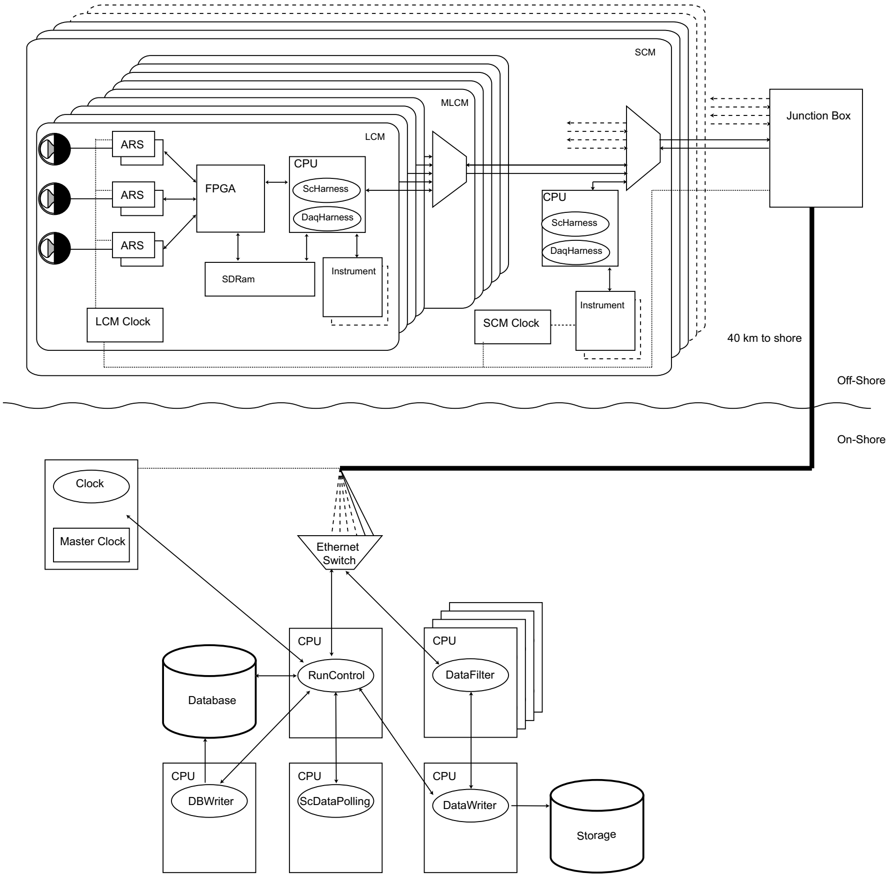

Figure 4.11: Schematic view of the data acquisition system

number of Time Stamp (TS) since the last reset of the master clock. The time stamp is the period of the master clock pulse. In that way, one has the time of the photon reaching the PMT with a 50 ns precision. A high precision Time to Voltage Converter (TVC) interpolates clock pulses. It returns an analogue signal that is directly proportional to the moment in which the PMT signal took place within the TS. The 8 bits resolution of the TVC corresponds to $50\,\mathrm{ns} \times 256^{-1} \simeq 0.2\,\mathrm{ns}$ (66) (see Figure 4.12).

To reconstruct really precisely the arrival moment of the photon it is necessary to know the time offsets introduced by the different optical paths between the local clock board and the PMT photocathodes. For this a time calibration system is used (see Section 4.5).

The process of writing the data in a temporary memory (pipeline) induces a dead time of 250 ns for each ARS. This is the reason for employing two different ARSs for each module, because the alternating use of the two samplers allows dead time to be reduced. The ARS can also work in a waveform mode. In this mode the photomultiplier signal is sampled and then digitised. This function is not used in normal data taking and is applied only for certain

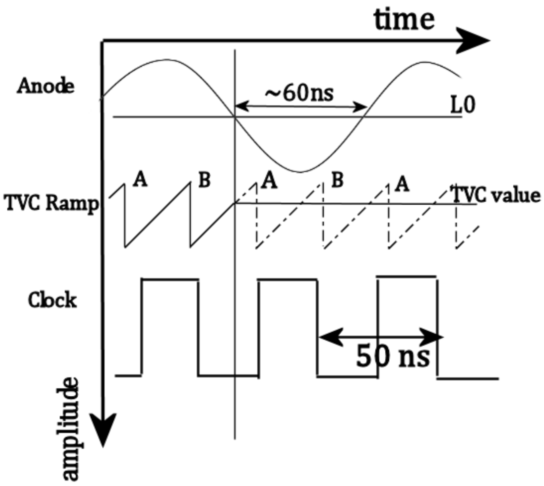

Figure 4.12: Scheme of the internal data acquisition system of the ARS

calibration runs. The ARS integrates the charge from the start where the signal passes the threshold for a period of 40 ns.

After the ARS, the data contains arrival time and charge information of the signals from the PMTs. The combination of these two quantities forms a hit. The read out of the ARS is performed by a Field Programmable Gate Array (FPGA) that organises the hits in frames covering a time period of 104.858 ms. The data from each frame are sent to shore as separate packages. The transmission of the frames is performed by a program called *DaqHarness*, that is run in the CPU of the LCMs. This CPU also runs another program, called *ScHarness*, which controls and reads out the local power supply and the monitoring and calibration devices present in the LCM.

Except for the PMT threshold of 0.3 p.e. there is no selection applied to the PMT signals. The raw data cannot be stored completely because the storage space limitation. Therefore, it is necessary to perform a background suppression before storing the data. In the rooms of the Institute Pacha, in La Seyne-sur-mer, a DataFilter program runs on a computer farm. The DataFilter program performs a fast algorithm, that can be run real time, that suppresses that background and keeps only signals that are compatible with a muon track hypothesis. After filtering, the selected data are sent to one of the PCs in the farm that runs the *DataWriter* program that stores the data on disk.

4.5 Calibration

Calibration in Antares is essential to be able to reconstruct the incoming particle. Two quantities must be know with high precision: time and position. Each of them has a specific calibration technique.

4.5.1 Position Calibration

Knowing the position of each photomultiplier at every moment is very important for the reconstruction. As Antares is subject to sea currents it must be monitored continuously. One method to do so is to use the acoustic positioning system. On the BSS of each line, an acoustic transmitter sends a pulse in the 40-60 kHz range and this pulse is received by the hydrophones situated on each sector along the line. The BSS is also equipped with pressure sensors that determine the depth of the BSS itself. Besides the acoustic system, each LCM is equipped with a bi-axial tilt meter and a compass. These instruments allow a measurement of the pitch, the roll and heading. Through the combination of these systems it is possible to know the position of the optical modules with a precision of 10-20 cm (67).

4.5.2 Time Calibration

As important as the knowledge of the position, is the understanding of the time resolution of the detector. The time resolution is influenced by the transit time spread of the PMT (see 4.3.1) and the scattering and chromatic dispersion of the Cherenkov light in the environment (68). The variation in the delay due to the detector electronics is far less relevant, being no more then 0.5 ns. It is thus in principle possible to reach a time precision better than a nanosecond. To achieve this result, several time calibration systems are implemented.

Internal Optical Module LEDs

Inside each OM there is a blue LED glued to the back of the PMT, that can illuminate the photocathode in the wavelength band where Antares is most sensitive (470 nm). These LEDs are used to measure the relative variation of the PMT transit time and dedicated runs of this LED calibration are taken once per month. This system is used to calibrate delay incurred by the signal when travelling the path starting at the PMT photocathode up to the read-out electronics.

Optical Beacon

This system allows for the relative time calibration of different OMs to be determined by means of independent pulsed light sources. It also makes the monitoring the influence of the water on the light propagation possible.

There are two different Optical Beacons, the LED Beacons and the Laser Beacons. A LED Beacon is composed of 36 LEDs pulsed by dedicated electronic circuits and arranged on the surface of "hexagonal cylinders". The LED Beacons are located uniformly along the lines so that their light can illuminate all storeys on the neighbouring strings. The trigger for LED beacon to fire is provided by a 1.5 V negative square pulse with a duration of around 150 ns superimposed on a negative direct current (DC) bias that can be varied from 0 to 24 V. The amount of light each LED emits can be tuned by varying the DC voltage. Below 8 V the amount of light emitted is below the visibility of the detector. For a DC level of 24 V the energy per pulse emitted is at least 150 pJ, which corresponds to the emission of approximately $4 \cdot 10^8$ photons (66).

The Laser Beacons are much more powerful devices that use a solid state pulsed laser whose light is spread out by a diffuser. They are located in a stationary position at the BSS of the lines 7 and 8 and illuminate mainly the lower part of the detector. The average resolution measured with the Optical Beacon system is about 0.3 ns which is in agreement with the expected value due to the intrinsic electronics resolution (69).

4.6 Background Rate

The Antares telescope is built on the bottom of the sea safe from light sources other than Cherenkov light from muons. Unfortunately, even at two kilometre depth, this complete darkness cannot be reached. Several light sources pass even there.

First of all, the sea water contains 400 part per million (ppm) of potassium. Of this quantity, 0.0117% is the radioactive isotope $^{40}\mathrm{K}$. This decays mainly into ^{40}Ca, emitting a electron. This electron has a maximum energy of 1.311 MeV and can therefore produce Cherenkov light. Simulations (70) show that the background rate caused by $^{40}\mathrm{K}$ in the Antares detector is constant and about $30 \pm 7\,\mathrm{kHz}$ per PMT (71). Another source of light present in the deep sea is bioluminescence. Organisms living in the deep sea can produce light, for different purposes connected with their survival. The amount of light due to this source that is observed the Antares detector varies in time. It is nevertheless possible to define a baseline rate that contains the contributions of the $^{40}\mathrm{K}$ and the bioluminescence and that can vary from about 50 kHz to several hundred kHz. On top of this baseline rate, bursts of bioluminescence may occur, lasting from several milliseconds to minutes. The single rates of the optical modules are monitored to allow for rejection of runs that have excessive background rate from the analysis (see Figure 4.13).

A different background has its origin in cosmic rays. The great majority of muons crossing the Antares detector are atmospheric muons produced by the interaction of cosmic rays in the atmosphere. The deep layer of water above the detector provides a certain amount of shielding from these muons but, if their energy is high enough, they can reach the detector. The number of muons able to do so amounts to a few hundreds per second. To reduce this, the Antares photomultipliers point downward and are so inefficient for signals from downgoing muons while optimising efficiency for upgoing muons. Upgoing muons can only be generated by neutrino interactions in the vicinity of the detector. It is impossible for a muon to travel through the Earth, because it loses all its energy far before reaching the other side. The cosmic interactions in the atmosphere do however also produce neutrinos. These neutrinos, referred as atmospheric neutrinos, can travel to the Antares site even from the other side of the Earth and interact in the vicinity of the detector, inducing the creation of a muon. This kind of background is impossible to be distinguished from the signal, separation of signal from this background can therefore only be done on a statistical basis (see Chapter 7). Around five or six neutrinos per day are detected with the Antares detector, and there is no as yet evidence that any of them is of cosmic rather than atmospheric origin. The total muon flux reaching the detector is shown in Figure 4.14, as a function of the cosine of the zenith angle. The zenith angle is the angle with which the muon cross the detector with respect to the vertical. From the figure it is clear

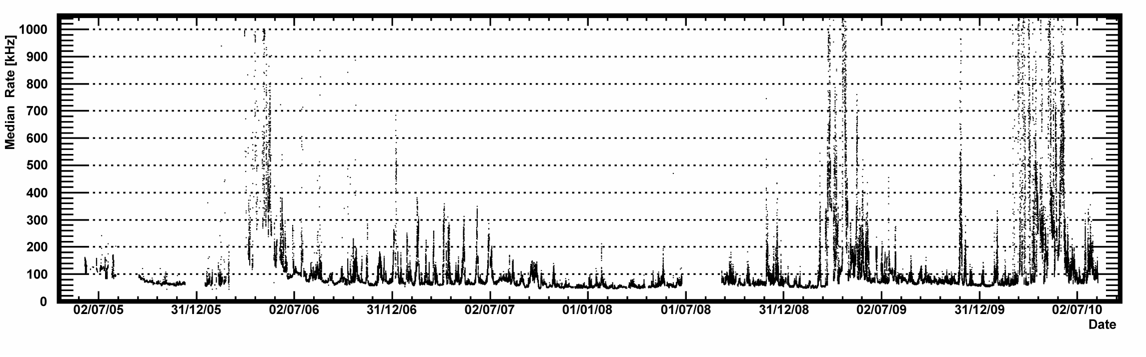

Figure 4.13: This plot shows the median rate (in kHz) of measured single photon counts recorded by the PMT 1 of MILOM up to 25/10/2006, by the OM1 Floor 1 of Line 1 from 25/10/2006 to 01/01/2008, and finally by the IL07 PMT.

how a cut in the incoming direction can prevent mistaking atmospheric muons for neutrinos. The upward event rate is therefore caused by atmospheric neutrinos.

A background handling is therefore of extreme importance, and it is performed at various levels. The first level is the trigger (see Section 4.7). It separates the signals that are correlated in time and position like the signals from a muon track producing Cherenkov radiation are, and uncorrelated signals, due to random background. The triggered data is then processed further to reject remaining background.

4.7 Data Processing and Triggering

The Antares data-taking is organized in data-taking runs, each corresponding to a live-time period of around 3 hours. The duration, starting time, ending time and the trigger condition used are stored in the database via a control program ("RunControl"). During a run, the data frames from the LCMs corresponding to the same time period are sent to a single on-shore PC. The frames of a following time period are then sent to a different PC. The set of frames of a time period of 13 ms are referred to as a "TimeSlice".

The first goal of the filtering is to reduce the background due to $^{40}\mathrm{K}$ and bioluminescence. To do so the properties of the direct Cherenkov light emitted by a single muon track are used. All the signals that produce a charge larger then 0.3 photo electrons in the photomultiplier are available. The transfer of this data is organised such that all data from the full detector occurring within a time window of $\sim 100\,\mathrm{ms}$ is sent to a single computer in the processing farm. The flow of data corresponds to a transmission of 0.5 GB per second from the detector to shore. The majority of this data is composed of optical background. After the first level of filtering, the amount of data is reduced by a factor 10^4. The software that performs the filtering (*DataFilter*) is usually referred to as trigger, in analogy to the hardware trigger used in high energy experiments (72).

The first hypothesis is that hits caused by random background are less likely to appear in

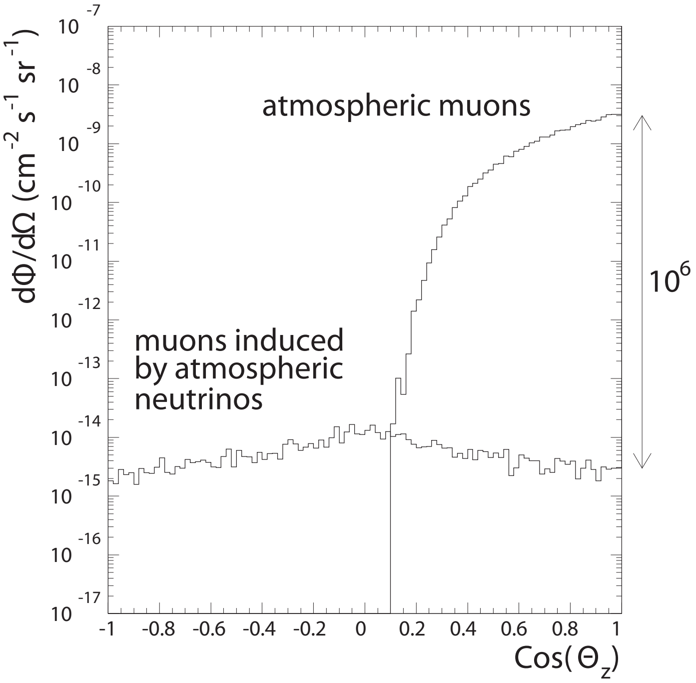

Figure 4.14: Muon flux at a depth of 2.1 km as a function of the zenith angle. A $\cos(\theta) > 0$ indicate downward-going particles.

time coincidence in the same storey. So the first level selection is made searching for hits that happen within 20 ns in different PMTs of the same storey. A single hit can also be accepted if its charge exceeds 3 photo electrons. Hits that satisfy this condition are defined as level 1 hits, or L1. All other hits are defined as L0 hits. The time and amplitude information of the hits are merged. The *DataFilter* looks for hits that are correlated by a causal relation. Two hits in different parts of the detector are causally related if their timing and position satisfy the following condition that parametrizes a light wave propagating from one PMT to another

$$| \Delta t | \leq \frac{n_g}{c} \cdot d \tag{4.8}$$

where Δt is the time difference between two hits, d is the distance between the two hit storeys and $v_g = n_g/c$ is the group velocity of light in the sea water. For the trigger selection an additional 20 ns are added to allow for the uncertainty on the storey position, the time calibration and light scattering.

The set of L1 hits that satisfy this condition are called a *cluster*. Each cluster is considered a candidate *event*. If the cluster is of sufficient size (typically, $N_{L1} \geq 5$) the events are stored on disc. The data contains all the hits that triggered the event, plus all other hits that happened within $2\,\mu$s before the first triggered hit and $2\,\mu$s after the last one. This collection of hits is referred to as a *snapshot*. The data structure in which all these hits are saved is called *PhysicsEvent*. For each timelice, a “SummaryTimeSlice” is generated containing the number of L0 hits that were recorded by each optical module. The SummaryTimeSlices are stored together

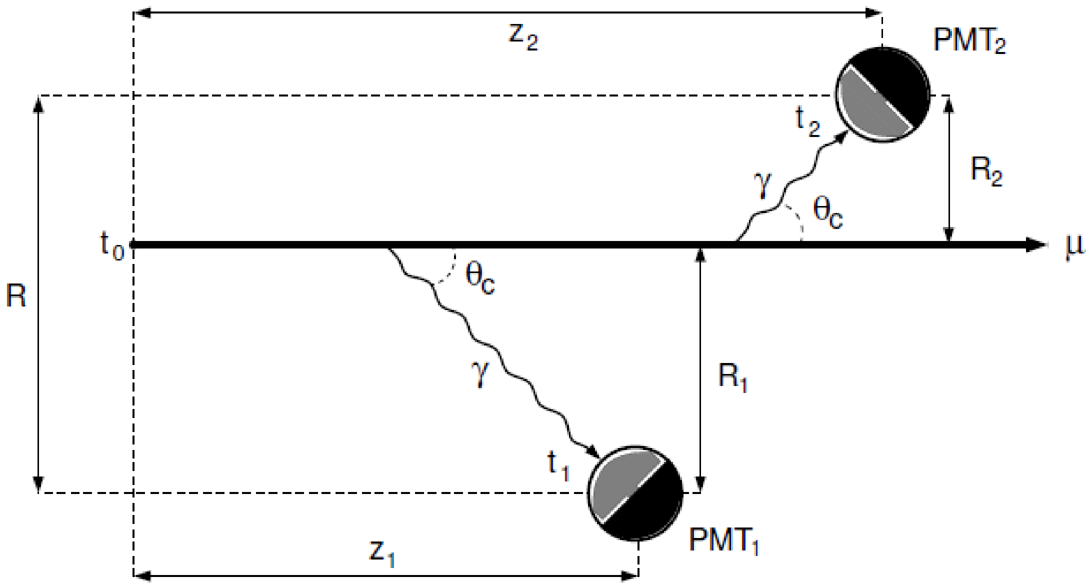

Figure 4.15: Schematic view of the track passing in the detector. The photons (γ) are emitted at the Cherenkov angle θ_c and reach the PMT_i at time t_i. The PMT position is defined in this reference system as the distance between the PMT and the muon position at the time t_0 (z_i), while R_i is the distance of closest approach.

with the PhysicsEvents.

The second level of triggering consists of looping over a certain number of directions to look for coincidences that are consistent with the Cherenkov angle emission. In general, the solid angle is subdivided uniformly with a spacing of approximately $10°$. For each direction one investigates whether the hit times correspond to those expected for Cherenkov photons emitted by a track travelling in that direction. A schematic view of the geometry is shown in Figure 4.15. Note that the reference frame is changed to have the axis of the detector parallel to the muon track. In this geometry, the expected time of a hit caused by a Cherenkov photon from the track is:

$$t_i = t_0 + \frac{1}{c}\left(z_i - \frac{R_i}{\tan\theta_c}\right) + \frac{n_g}{c}\frac{R_i}{\sin\theta_c} \tag{4.9}$$

where t_0 is the initial time of the muon track, the second term represent the time that the muon takes to travel from the initial position to the point where the detected photons are emitted, and the last term is the time required for the photons to reach the PMT. Assuming $\cos\theta_c = 1/n_g$ one can write the time difference between to hits caused by Cherenkov radiation as:

$$t_2 - t_1 \leq \frac{z_2 - z_1}{c} + \frac{R}{c}\tan\theta_c \tag{4.10}$$

where R is defined as the maximum distance between two PMTs perpendicular to the muon track (see Figure 4.15). The condition for pairs of hits to be considered as Cherenkov hits is

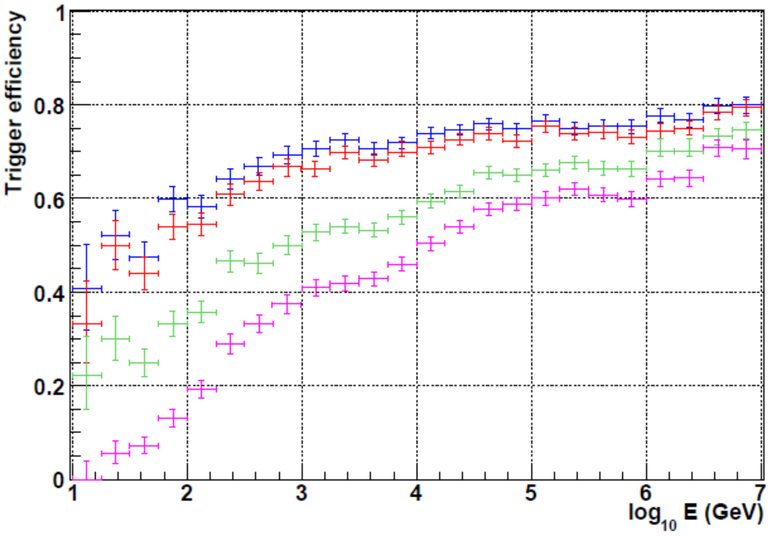

Figure 4.16: Trigger efficiency normalized to events with hits on at least 6 floors and 2 lines, for the 2T3 (above) and 3N (below) triggers, versus neutrino energy.

therefore:

$$|t_2 - t_1| \leq \frac{z_2 - z_1}{c} + \frac{R}{c}\tan\theta_c + 20\,\mathrm{ns} \tag{4.11}$$

New clusters are then formed with all pairs of hits in the cluster obeying 4.11. Requiring a minimum size of this new cluster allows for a more restrictive selection of muon tracks. Performing the trigger in software allows for freedom to choose or modify of the algorithm at any time. Several trigger selections can be performed simultaneously. The standard trigger just explained is specifically designed to select signals from muon tracks. In the work described here the interest in concentrated on shower-like signals. As described in 6.1, hits from photons emitted by showers have a some what different time – position correlation.

4.7.1 The T3Trigger Logic

It is therefore more appropriate to use a different trigger algorithm. This algorithm goes under the name of T3 trigger (73), is more open and therefore accepts more background hits, but allows for more efficient shower recognition. Instead of looking for hits that are causally connected, one searches for a T3 trigger cluster. A T3 trigger cluster is defined as the occurrence of at least two L1 hits in three consecutive storeys within a coincidence time window. This coincidence time window is 100 ns in the case that the two storeys are adjacent, and 200 ns in the case of next to adjacent storeys. Once the T3 clusters are identified, a minimum number of T3s in a predefined time window are required to accept the event. The search for N T3 clusters is done in an exclusive way, so that a single L1 hit cannot belong to more than one T3 cluster. This implies that a 2 T3 trigger requires at least 4 L1 hits. For this analysis a 2T3 trigger was required.

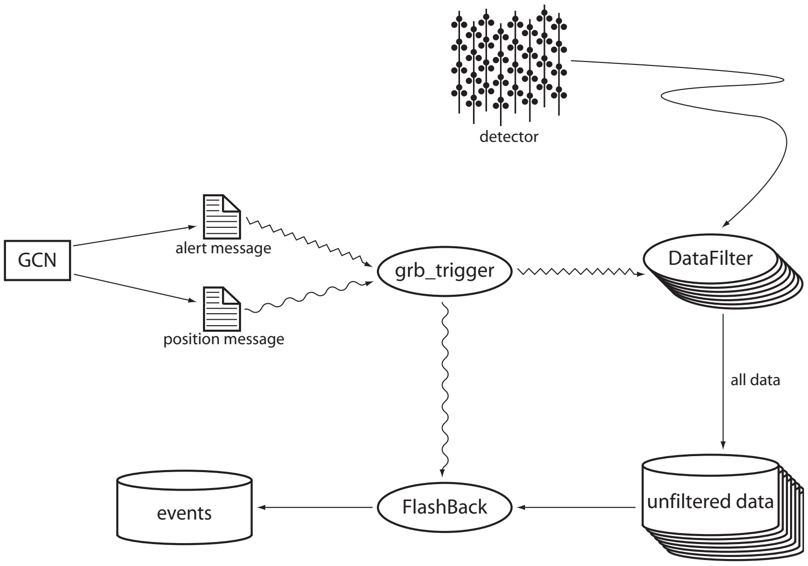

Figure 4.17: Scheme of the special data taking in the case of coincidence with a GRB, from (75).

4.8 Special Data Taking: the GRB Trigger

In the Antares experiment, several other studies on neutrinos from gamma-ray bursts have been performed (67), (74), (75). The main difference between this work and the previous ones is that in the other analyses a search for muon tracks induced by neutrino interaction in time coincidence with a gamma-ray burst was performed. Several satellites (mainly Swift (76) and Fermi (77)) provide almost almost real time alerts of Gamma Ray Burst events. These alerts are distributed over the network to interested experiments. Antares is among these experiments. When a GRB satellite alert is recorded a dedicated program in the Antares data acquisition system (*grb trigger*) notifies the *DataFilter* software. This will immediately start a new process, parallel to the normal data filtering, that saves all the raw data to disc (without applying any selection) (Figure 4.17). It saves raw data for a few minutes. It is then possible to perform a custom data selection and analysis. This special trigger is particularly useful when one wants to detect muon tracks in temporal coincidence with a GRB. The main idea is that, together with the time, also the exact galactic coordinates of the gamma-ray bursts are given. Therefore one can fix the direction of the scanning trigger selection (Section 4.7). Knowing this it is possible to relax the selection criteria and so be much more efficient in the reconstruction (75). The background reduction due to the known direction and the limited time window provides for a lower energy threshold of the detector.

In the analysis presented in this work, this special data taking is not used for two main reasons. First of all the shower reconstruction does not provide a precise determination of the direction of the primary neutrino. It is therefore impossible to use the directional information of the GRB to reduce the background. Secondly, this work focuses on high energy neutrinos, which are already efficiently accepted by the T3 trigger (see Section 4.7.1).

4.9 KM3NeT Detector

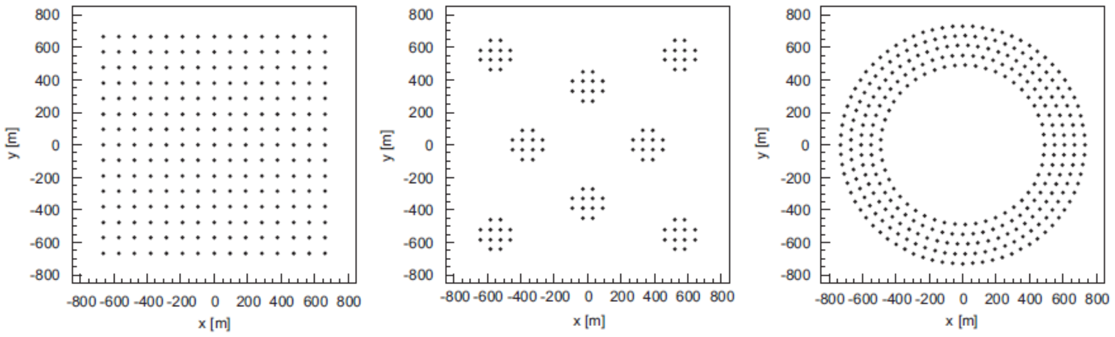

Figure 4.18: An example of a seabed layout for three different KM3NeT configurations

Antares is only the first step toward a much vaster project in the Mediterranean Sea. Antares is one of the three experiments that can be seen as prototypes for the KM3NeT (kilometre cube -KM3- Neutrino Telescope) experiment. The other two experiments that formed a "Mediterranean Sea" consortium are Nestor and NEMO, situated near Pylos, by Kalamata in Greece and off the coast of Capo Passero, in the south of Catania, in Sicily, respectively. The expertise acquired by these pilot experiments is indispensable for the final design of KM3NeT, which Technical Design Report (TDR) was made public in the beginning of 2010. In 2012 the preparatory phase will be terminated,and the decision on the best design and infrastructure for the detector will have been made. Having a volume of a several cubic kilometres will improve the efficiency of neutrino detection. To cover such a big volume it is necessary to leave more space between the structures carrying the optical modules. For this reason the detector is optimised to detect high energy neutrinos, above 10 TeV, where it also reaches the best angular

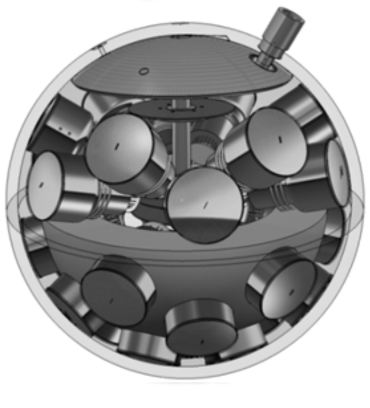

Figure 4.19: Schematic view of the"multipmt" concept in KM3NeT.

resolution. Different geometries are being considered that allow for a lower energy threshold to be achieved, or the detector to be optimised for different energy ranges (corresponding to different sources and signals). Figure 4.18 shows three of the considered configurations of the detector footprint. The ideal situation is achieved when the detector presents a large area in the direction of the source in order to detect high energy neutrinos but, at the same time, has densely packed lines to improve sensitivity for neutrinos in the lower end of the energy spectrum. It has been proposed to use optical modules containing many small photomultipliers. This contrasts with the single big PMT used in Antares 4.3.1. This provides for a more uniform angular coverage and minimises the number of high pressure feed through needed in the detector. A schematic view of the proposed PMT design is shown in Figure 4.19. Studies with a reference detector show that the sensitivity of a KM3NeT detector to point sources will improve very significantly with respect to the Antares sensitivity (see Figure 4.20). The geographical location of KM3NeT, in the Mediterranean Sea, makes it possible to investigate Galactic sources with unparalleled sensitivity. It will be the next generation telescope after the other kilometre cube detector IceCube. This, together with the choice of a common software framework for the data analysis (see chapter 5) provide the perfect ground to join forces and answer many of the still open questions on neutrino astrophysics in the following years.

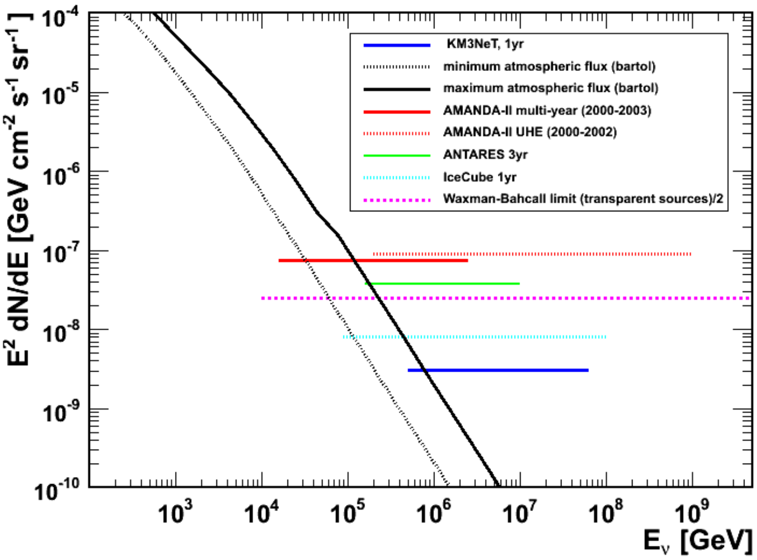

Figure 4.20: Average flux limit for diffuse fluxes for the KM3NeT reference detector. For comparison, the experimental results from AMANDA are plotted together with expected limits from the ANTARES and IceCube neutrino telescopes.

5

SeaTray and Monte Carlo Simulation

Sometimes, you have to roll a hard six.

Commander William Adama

5.1 SeaTray: a Software Framework

Antares, like the majority of high energy physics experiments, deals with a huge amount of data on a daily basis. The raw data after triggering are more then 30 gigabytes per day, and all these data must be stored and processed. To do so, a complex system of computer software is needed. To simplify the task of the scientist, that most likely will need to develop extra software to perform his personal analysis, it is desirable to have the entire software package organised in a modular way, so that the user can modify or add a single module, to perform a specific task, taking advantage of the simplicity of a fixed programming scheme. To achieve this organizational goal, the Antares and KM3NeT collaborations have adopted IceTray, the software framework used in the IceCube collaboration, detached from the IceCube version and modified in order to suit the seawater detectors (78). This new framework is named SeaTray. The use of this software framework forces the user to follow a certain logic while developing software, so that the entire code remains readable by anyone who is familiar with this logic. At the same time it provides a large set of object classes and services that can be employed by the user in his own code.

This framework supplies a set of "*dataclasses*": C++ classes that describe how to store quantities such positions, directions, particles, hits, a detector geometry and other data needed for the simulation, reconstruction and analysis of neutrino telescope events. The user can write SeaTray "modules", objects dynamically linked into the framework which perform the actual data processing, i.e. for reconstruction, analysis, etc. Data is passed between modules in containers called "*frames*", collections of dataclasses that can be written to disc or stored in memory. These frames can be associated with different "*streams*", each corresponding to a different aspect of the analysis. "Calibration frames" contain the calibration data of the detector, while "Geometry frames" describe the geometry of the detector, including the descriptions of optical

Order	Program	Description
1	Neutrino Generator	Neutrino flux and primary interaction generator
2	MMC	Lepton propagator
3	HitConstructor	Photon propagator and MC hit constructor
4	Root Writer	Converts SeaTray format into a TriggerEfficiciency readable format
5	Trigger Efficiency	Detector and trigger simulator
6	Antares Reader	Reads Antares root files back to SeaTray
7	Shower Reconstruction	Shower reconstruction (Chapter 6)

Table 5.1: Scheme depicting the Monte Carlo chain used for the signal simulation.

modules and photomultipliers. The "Detector Status frames" store the status (on or off) of the detector components at the time of the data. The "Physics Frame" stores all the typical event information, such as simulated particles, simulated or real hits and reconstructed tracks. SeaTray contains a set of classes that define its standard data format. By default it uses Boost libraries (79) for the I/O, but other methods and file types can be used, such as Root (80).

5.2 A Neutrino Telescope simulation chain

In order to successfully detect cosmic high energy neutrinos, the neutrino signal must be separated from a background that initially is up to 10 orders of magnitude above the signal. Monte Carlo simulations are important for studying such separation methods, as they allow the separate exploration of the neutrino signal and the background. The simulation of a signal in a neutrino telescope is generally divided in three parts: the generation of the cosmic neutrino flux and its propagation from the top of the atmosphere down through the Earth (with the assumption that the matter encountered by a cosmic neutrino during its trip to Earth is negligible in comparison to the propagation through the Earth); the generation of secondary particles such as muons and their propagation in the vicinity of the detector, and the propagation of secondary or tertiary particles such as electrons and Cherenkov photons in the vicinity of the detector and their interaction with the detector components. The *generator* generates a flux of cosmic neutrinos at the top of the atmosphere and propagates it until the neutrino interaction with a Earth nucleus. A this point secondary particles are created and their propagation is done by the *propagator*. A selection of secondary particles, able to produce light, is selected and the light is propagated to the detector. Finally the detector response to charged particle induced photons is simulated. A schematic view of the software chain used is shown in Table 5.1. The neutrino generator and the propagator are the same programs used in the IceCube collaboration (81, 82, 83), although

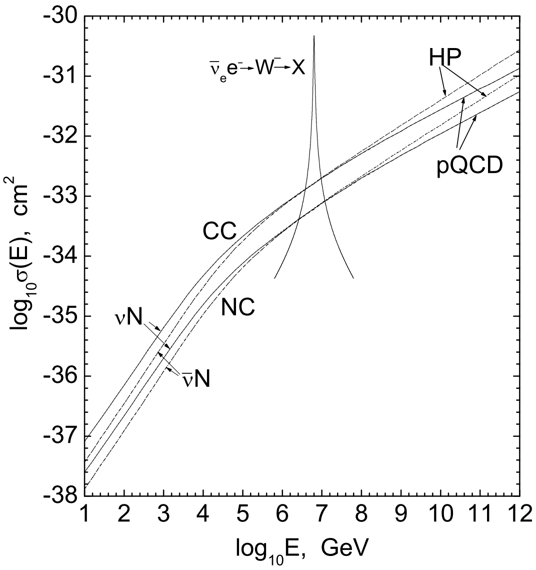

Figure 5.1: Cross sections for $\nu - N$, both CC and NC interaction, and resonance of $\bar{\nu}_e - e^-$. Solid lines indicated the cross sections calculated with perturbative QCD, while dashed lines are calculated with the Hard Pomeron approximation. Figure taken from (81)

they have been adapted to work for a water detector. Neutrino Generator (NuG), a version of Anis (81) implemented in the SeaTray and IceTray frameworks, has been used, while MMC (Muon Monte Carlo) (82) has been used as lepton propagator. A detailed comparison between this software and the simulation chain used in Antares prior to the introduction of SeaTray can be found in (84) and in Section 5.4.

5.2.1 Neutrino Generator

In SeaTray the neutrino event generator is called, quite logically, Neutrino Generator, or NuG for short. It randomly generates primary neutrinos at the surface of the Earth's atmosphere according to a power law spectrum $\phi_\nu(e) \propto E^{-\alpha}$, and then performs a complete propagation through Earth, taking into account absorption due to CC interactions and regeneration due to NC interactions. The user can choose several parameters for the generated flux, such as the neutrino flavour, the energy range and the spectral index of the generated power law.

The physics processes implemented in the program are directly derived from the program Anis (81). Anis focuses on the medium/high energy range, reaching the ZeV region. As shown in Figure 5.1, the $\nu - N$ cross section implemented is valid in the energy range from 10^1GeV to about 10^{12}GeV. NuG is able to simulate all three flavours of neutrino: ν_e, ν_μ, ν_τ.

In order to simulate neutrino - nucleon interactions, NuG parametrizes the interaction cross section using structure functions $F_i^{\nu N}(x, Q^2)$ according to a modified version of CTEQ5 DIS (85). At very high energies, the $\nu - N$ cross section is predominantly driven by scattering off sea-quarks at small x. Because the behaviour of the structure functions at $x \lesssim 10^{-6}$ is not well understood, the resulting simulation depends heavily on the model chosen. In

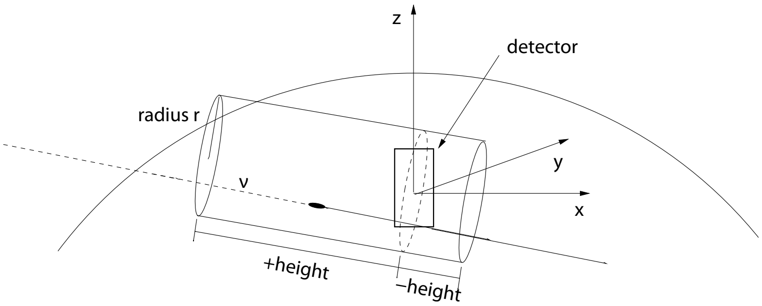

Figure 5.2: Detector geometry used in neutrino-generator: the detection volume is a cylinder coaxial with the direction of the incoming muon. The size of this volume is defined by the user fixing its radius and the two heights before and after the detector centre. The actual detector is represented by a rectangle at the center of the reference system.

neutrino-generator, it is possible to choose between two small-x models: the pQCD CTEQ5 parametrization to small x and large Q^2, or a hard-pomeron enhanced extrapolation from HERA data (86). Both models are shown in Figure 5.1, as a function of the neutrino energy (81). The invariant transferred momentum Q^2 and the Bjorken scaling variable x have been defined in Section 4.1.

Once the neutrino has been propagated through the Earth and reaches the detector depth, the neutrino is forced to interact creating either another neutrino (NC) or a charged lepton (CC) along with hadrons. A weight is assigned to each event, as described in Section 5.2.1.1 which takes into account the interaction probability. A schematic view of the entrance of a neutrino into the detection volume is shown in Figure 5.2. The detector itself is represented by a rectangle that covers the instrumented volume. The detection volume is defined as a cylinder coaxial to the incoming neutrino and fully containing the instrumented volume. When a muon passes within this cylinder the Cherenkov radiation produced will reach the detector and, therefore, can be detected.

The description of the Monte Carlo generation parameters and the software options used for this thesis is found in Appendix A.1

5.2.1.1 Neutrino fluxes and weights

NuG chooses the energy of a neutrino interaction according to a power law spectrum. In order to obtain a collection of neutrino interactions that corresponds to some physical flux, neutrino events must be weighted using weights provided by the generator itself.

The neutrino event rate $R_\nu^{gen}(E_\nu)$ corresponding to a generated flux $J_\nu^{gen}(E_\nu)$ is a function of the neutrino energy E_ν. The resulting rate of neutrino interactions in the proximity of the detector, N_ν^{det}, that can lead to a detectable signal, depends on the probability for a neutrino to survive the propagation through the Earth P_ν^{surv}, the probability P_{int} for it to interact and create a charged lepton of energy E_l, and the probability P_{det} that the detector performs a successful detection of this lepton:

$$R_\nu^{det}(E_l, E_\nu) = \sum_j \int \left[J_\nu^{gen}(E_\nu) P_\nu^{surv}(E_\nu \to E'_\nu) P_{int}(E_\nu; E_l) P_{det}(E_l)\right]_j dx dE d\Omega \quad (5.1)$$

where j represents the sum over neutrino flavours and the integral is performed over the travelled path x, the energy E and the solid angle Ω. Assume a cylinder of length L coaxial with the incoming neutrino and fully containing the detector. The probability of a neutrino of interacting at a point x along the axis of this cylinder is given by:

$$P_{int} = N_A \rho \sigma_{tot}(E_\nu) \cdot e^{-N_A \rho \sigma x} \quad (5.2)$$

where $N_A\rho$ is the number density of target nucleons in the Earth and σ_{tot} is the total neutrino-nucleon cross section. The exponential takes into account the probability that a neutrino reaches the point x insider the cylinder.

This probability is very small and, as a consequence, most of the generated neutrinos are not interacting and producing a signal in the detector. This makes the generation process very slow and inefficient. To optimize the speed of the generator, each neutrino is forced to interact within a user-defined cylindrical volume surrounding the detector. The interaction vertex point, x, is randomly sampled along the cylinder length, L ("TotalDetectionlength" in the SeaTray jargon). The interaction probability at the point x is then $P_{int}(x) = 1/L$. As this is not the real interacting probability, as calculated in Equation 5.2, each event is assigned a weight ("InteractionProbabilityWeight" in SeaTray, shown in Figure 5.3(a)) that re-weights each event with the real probability of happening:

$$W_{int}(x, E_\nu) = \frac{N_A \rho \sigma(E_\nu) \exp^{-N_A \rho \sigma(E_\nu) x}}{1/L}. \quad (5.3)$$

The same concept must be applied to the flux. The generated flux $J_\nu^{gen}(E_\nu)$ is a simple power law and does not always correspond to the physical flux one wants to simulate. In order to get the flux $J_\nu^{model}(E_\nu)$ for a certain physical model, it is necessary to assign a weight to each event.

To aid the user in this calculation, NuG provides a quantity called "OneWeight" that includes not only the interaction weight of Eq. 5.3, but also the generation volume information, the detection probability and the generation parameters, such as the initial spectral index γ, the energy range and the solid angle range Ω. OneWeight (OW), shown in Figure 5.3(b) for electron neutrinos, is defined as:

$$OW = \frac{W_{int}}{E_\nu^{-\gamma}} \int_{E_{min}}^{E_{max}} E^{-\gamma} dE A \cdot \Omega \cdot T \; [\mathrm{GeV\,cm^2\,s\,sr}] \quad (5.4)$$

where T is the time period covered, by default 1 second. The weight w_i for each event i, applicable to a generic flux J_ν^{model} for a live time of observation T_l is then:

$$w_i = \frac{OW_i}{\sum_j N_{ev}^j} J_\nu^{model}(E_\nu) \frac{T_l}{T} \quad (5.5)$$

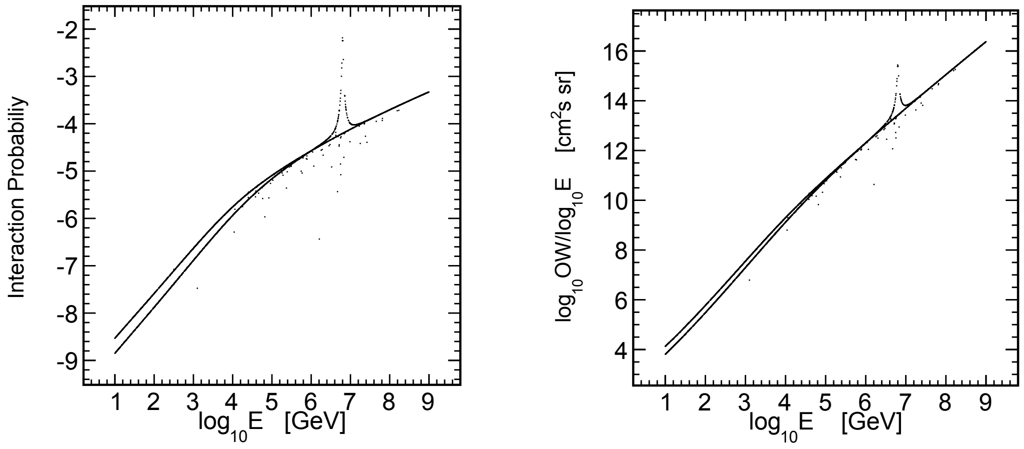

(a) Interaction Probability weight

(b) One Weight

Figure 5.3: Weights calculated by NuG for a E^{-1} electron neutrino and antineutrino spectrum. Both figures have the y and x axis expressed as the logarithm of the presented quantity. In both figures is clear the electron antineutrino Glashow resonance at 10^7 GeV. Figure (a) shows the interaction probability weight $W_{int,j}$, while (b) shows One Weight.

where the sum over j is made over all neutrino flavours. Note that the total number of generated events is not included in the OneWeight, as if multiple files are used for the analysis, the sum of all generated events on all files must be used. NuG generates by default half of the events as neutrinos and half as antineutrinos, therefore if one wants to calculate the expected flux for neutrinos and antineutrinos separately this must be taken into account:

$$w_i = \begin{cases} \frac{OW_i}{\sum_j N^j_{ev}/2} J^{model}_{\nu}(E_\nu) T_l, & \text{for } \nu \\ \frac{OW_i}{\sum_j N^j_{ev}/2} J^{model}_{\bar{\nu}}(E_{\bar{\nu}}) T_l, & \text{for } \bar{\nu} \end{cases} \tag{5.6}$$

5.2.2 Muon Monte Carlo (MMC)

The task of propagating muons and other charged leptons trough matter is performed by MMC. The detector response and the entire analysis results are strongly dependent on the estimation of the amount of light generating particles and the type of interactions that are simulated. Such simulation must include a precise description of the medium in which the lepton is travelling. The medium is defined by a set of values, such as the atomic number, the atomic mass, the density, the ionization potential, the ionization formula constants and other parameters. MMC allows for many choices such as rock, ice, salt, water and some specific media, such as Frejus rock (properties of rock measured in the Frejus site) and the Antares water. The values for the Antares water differ from the standard water as it is salt water from the Antares site.

When a muon travels through matter, it loses energy due to ionization, Bremsstrahlung, photo-nuclear interactions, and pair production. To simulate the behaviour of a charged lepton in matter, MMC evaluates each interaction probability via tracking integrals. The energy loss of a particle is divided in a continuous part, described by a function of its energy, and a stochastic part, defined as the probability for any energy loss event to occur along the path of 1cm (82). This description leads to three integrals to be solved. The first is the *energy integral*, that is used to find the final energy of the particle after each step. The second is the *tracking integral*, that computes the displacement of the particle after its energy is completely depleted, and the last one is the *time integral* that calculates the total elapsed time.

In order to control the CPU time needed to run the program, it is possible to choose to solve these integral using a parametrization called *continuous randomization* (82). This assumes that if the tracking intervals are small enough, also the the average energy loss for each interval is very small. Therefore one can assume that for each interval the same amount of energy is lost and the final energy loss distribution will be a Gaussian, and it is possible to parametrise the previous integrals. This will reduce the computational time, but also the precision of the results. Parametrizations can be turned on or off for each integral separately. The default energy range in which parametrized formulae will work has been chosen to be from 105.7 MeV (the muon rest mass; 1777 MeV for taus) to $E_{big} = 1014\,\mathrm{MeV}$. The program has been tested to work with much higher settings for E_{big} (87). The energy losses that are considered in MMC are ionization (with the Bethe Bloch equation modified for muon and tau leptons), Bremsstrahlung, photonuclear interaction, electron pair production, Molière scattering and other effects that can be turned off or on by the user (82).

All software parameters used for running MMC are described in Appendix A.2

5.2.3 Hit Constructor

The Hit Constructor module uses the tracks provided by MMC, selects the ones that can produce light, generates Cherenkov photons and propagates them to the PMT surface, and then may generate a hit, taking into account the quantum efficiency and the angular acceptance of the PMT. Other parameters that contribute to the digitization of the signal, such as the TTS and the gain of the PMT are not taken into account, as they are handled by the detector response simulations (see Section 5.3). Hit-Constructor stores a list of hits for each optical module. For very high energy neutrinos, the amount of light reaching the photomultiplier and, thus, the number of photoelectrons, can be very high, up to the saturation level of the PMT. Sometimes, in case the PMT is close to saturation, it is desirable to reduce the number of p.e. on the PMT, in order not to waste computing resources. A parameter ("MaxPEs") forces the hit generation for any PMT to be stopped when this limit is reached. If this happens, Hit Constructor will stop looking for further tracks that can generate light, but only for that specific PMT. It is also possible to scale the photon density by any chosen factor. In this case the hit will not correspond to a single photo electron, but will have an enhancement factor to be taken into account.

The propagation of the photons is done using the program Photonics (88), which calculates photon flux and time distributions in a medium with given properties (the scattering and absorption lengths as functions of wavelength and depth). The medium properties are defined by the user and stored in a text file that is read by the program. The resulting photon flux and

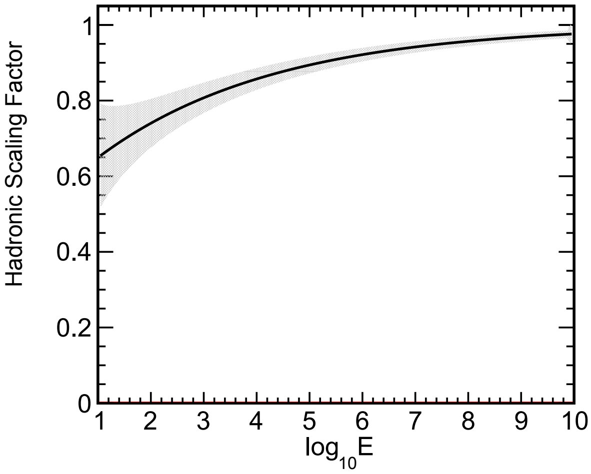

Figure 5.4: Ratio of hadronic to electro-magnetic light emitted from protons at different energies. The shaded area exhibits the spread, which is used to account for fluctuations.

time distributions can be tabulated in binary tables for an arbitrarily large volume of the chosen medium, and for a number of light sources and detector properties. In this way a higher level analysis can be performed acquiring the light yield and time distributions from these tables, without a real time photon propagation.

Typically, the parameters describing the optical medium, such as group and phase indexes and optical depth are dependent on the wavelength and the spatial dimension. For this reason the propagation medium can be divided into horizontal regions. In the Antares detector only one zone is used, as the sea water presents the same properties in the entire detector. Cherenkov emission is simulated as a point-like emitter that emits symmetrically in azimuth around its principal axis. After the emission it is propagated until the next scattering point. Electromagnetic cascades are considered as many short Cherenkov emitting tracks. Photonics calculates photon densities by tracking the photons from their origin and assigning them survival probability weights at each point they pass through. The sum of all weights is the photon density in a certain position of space time. Photons are then tracked dividing the surrounding volume into small cells, over which the photon density is averaged. Two possible modes for the light propagation can be chosen. In the volume-density mode, photons are recorded at equidistant points along their path. In the area-crossing mode, photons are recorded into a cell every time they cross a predefined surface around the emitter. When a scattering point is reached, the photon's direction changes by an angle randomly chosen from the phase function (88). For the Antares production the area-crossing mode is used.

In SeaTray the so called "Photonics tables" have two different formats. The first one is relative to the propagation of shower light, while the second is used for light from muons. The description of the tables and other parameters used for this thesis can be found in Appendix A.3 and in the user manual (89). This software only generates light produced by electromagnetic interactions. When an hadronic shower is generated, Hit Constructor finds a scaling factor derived in (90) and shown in Figure 5.4. It then generates an electromagnetic shower with an energy equal to the hadronic shower energy multiplied for this scaling factor. As this factor has been derived experimentally it has a fluctuation. The value chosen is a random number sampled from a Gaussian distribution around the scaling factor value with a width as indicated in the figure.

5.3 Detector simulation

The simulation of the electronics of the Antares detector is performed by the programme "TriggerEfficiency". Through this program it is possible to apply to Monte Carlo events the same trigger(s) that are applied to data, reproducing with the best possible accuracy the real detector response (see Section 4.7). To achieve this goal, the program reproduces the detector status, such as the number of active lines and OMs, and adds the optical background before applying the trigger selection (see Section 4.6). In the detector data acquisition, for each TimeSlice, a SummaryTimeSlice is recorded (see Section 4.7), containing the rate for each optical module. This information is not stored in the normal data, as only triggered events are saved. But for each TimeSlice it is possible to know the average rate in the entire detector. SummaryTimeSlice are sampled during a user defined data taking period, covering all data runs in that period. To have a Monte Carlo production that covers the same period of time, this set of SummaryTimeSlice is used to force PMTs to have the same rate as the measured one.

The first step to generate the optical background and add it to each event. One option available in TriggerEfficiency is to generate background hits according to a Poisson probability distribution, with the mean rate being specified by the user. For this work, Trigger Efficiency was allowed to determine the background rate of each PMT from the measured rates, with these measured rates being supplied by the user. In this way it is possible to reproduce the data-taking conditions very precisely, from the amount of optical background present during the selected period, such as bioluminecence, to the electronics conditions of the detector, such as the malfunction of a single PMT or an entire line.

In the actual data taking, the generated analogue signals are integrated by the ARS chips (see Section 4.3 for a more detailed description) in a time window of approximately 25 ns. To build a single hit simulating the integration efficiency of the front-end chip, that leads to a time resolution of 1.3 ns (see Section 4.5), all hit times are smeared using a Gaussian distribution with a $\sigma = 1.6ns/\sqrt{N_\gamma}$, with N_γ being the total number of photons detected at a given time.

From this point on, the triggering proceeds in the same way as in the real data taking, as explained in Section 4.7. The first level trigger is the selection of the so-called L1 hits, defined as a cluster of hits that occur within 20 ns in different PMTs of the same storey, or a single hit with a charge greater than 3 photo electrons. The physics triggers applied for the Monte Carlo productions used in this thesis are the same as the ones used in the Antares standard data taking during the year 2008, and go under the name of 2T3 and 3N.

5.3.1 “3N” and “2T3” Trigger Logics

The “3N” trigger is designed for triggering on muon tracks by looking for causally connected hits along the same trajectory. As a first step it applies a three-dimensional triggering, searching for causally related hits. To do that, it checks for a minimum number (usually set to 5) of L1 hits within 2.2μs of each other (this time corresponds approximately to the time the light will take to travel through the full detector). Each pair of these selected hits, i, j must satisfy the following causal relation:

$$\Delta t_{ij} \leq \frac{n_g}{c} \cdot d_{ij} + 20\,\mathrm{ns} \tag{5.7}$$

where Δt_{ij} is the time difference between hit i and hit j, d_{ij} is the geometrical distance between the two hits and $v_g = n_g/c$ is the (group) velocity of light in sea water. In addition, it performs a scan over all directions to search for the most likely direction of the incoming muon (1D trigger).

The 2T3 trigger logic is based on T3 trigger clusters, defined in Section 4.7.1 and 6.2 as the occurrence of at least two L1 hits on three consecutive storeys within a coincidence time window of 100 ns, in the case the two storeys are adjacent, or 200 ns for next-to-adjacent storeys. The 2T3 trigger requires at least 2 T3 clusters to be found within 2.2μs.

5.3.2 Use of Trigger Efficiency for a Seatray Production

TriggerEfficiency has not been designed to run within the SeaTray framework, as it was written before the introduction of this framework in the Antares collaboration. It has therefore been necessary to write an interface that transforms the output of Hit Constructor into a format readable by TriggerEfficiency. The entire Monte Carlo production, generated with Neutrino Generator, propagated with MMC and Hit Constructor has therefore been transformed via an external program into the file format used by Trigger Efficiency. In this way, Trigger Efficiency could be used to perform the detector and trigger simulation. The TriggerEfficiency output is then converted back into SeaTray, and used for reconstruction (Chapter 6). A description of the parameters used for the detector simulation software during the development of this analysis can be found in Appendix A.4.

5.3.3 Detector Efficiency and Effective Area

Not all the events that reach the detector can be successfully measured. A parameter that describes the detection efficiency of the detector is the effective area. It is defined as the area covered by a 100% efficient detector that measures the same number of events as the Antares detector. Depending on the focus of the analysis, one can express the effective area in terms of the detected muons or the neutrinos. The neutrino effective area is the ratio of the rate of selected events (where the selection can be the trigger, the reconstruction or the quality selection) to the total incident neutrino flux arriving at the Earth:

$$A_\nu^{Eff}(E,\nu) = \frac{R_\nu^{det}(E_\nu)}{J_\nu(E_\nu)} \tag{5.8}$$

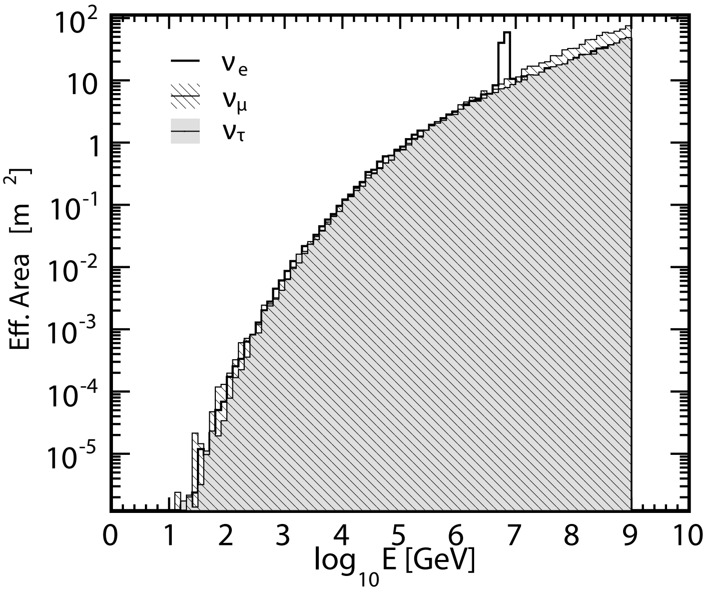

Figure 5.5: Antares $\nu-$effective area at trigger (3N+2T3) level for muon, electron and tau neutrinos and antineutrinos. Both upgoing and downgoing events are considered, and no further cuts on the goodness of these events is applied.

The rate of detected neutrinos is the same expressed in Formula 5.1, and therefore depends on the neutrino cross section, the probability of a neutrino crossing the Earth and the probability of a neutrino producing a detectable signal.

To understand the efficiency of the detector in triggering signal events, the effective area for triggered events that passed the trigger 3N or 2T3 is shown in Figure 5.5. This plot shows the effective areas for each of the three neutrino flavours, for both upgoing and downgoing neutrinos, weighted with a GRB flux (Section 5.2.1.1). The efficiency of the trigger is defined as the ratio of the triggered events to the total number of events that would be detected in a perfect detector. The trigger efficiency, integrated over the energy range considered, can be written as:

$$\varepsilon = \frac{N_{\text{trig}}}{N_{\text{tot}}} = \frac{\int J_\nu(E)\varepsilon(E)dE}{\int \phi(E)dE} \tag{5.9}$$

where $J_\nu(E)$ is the neutrino flux and $\varepsilon(E)$ is the trigger efficiency depending of the initial neutrino energy E. The values of the trigger efficiency normalized to events with hits on at least 6 floors and 2 lines, as a function of the energy, are shown in figure 4.16 (91).

5.4 Monte Carlo chain comparison

The Monte Carlo chain just described is not the only simulation chain that can be used to study neutrinos in Antares. While the Antares standard Monte Carlo chains have been tested and proved to be in good agreement with data (92, 93), the analysis presented in this thesis is the

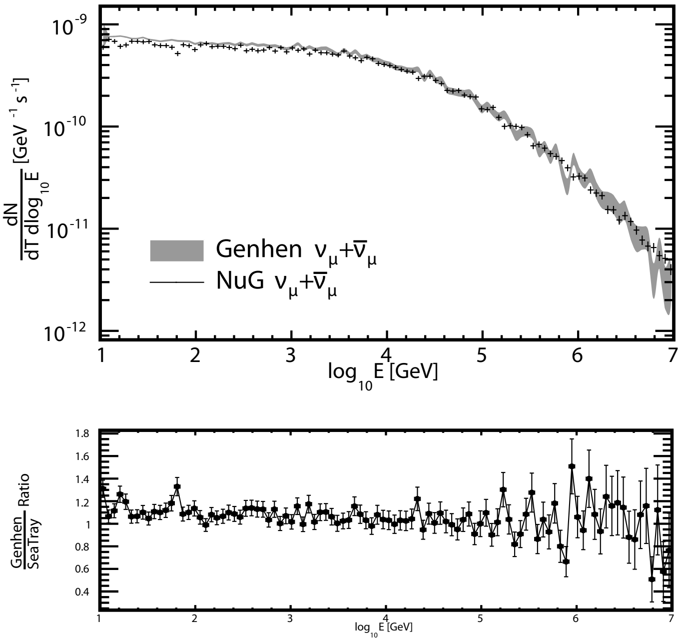

Figure 5.6: Upward-going muon neutrino rates simulated with Genhen (grey shaded area) and NuG (solid line), assuming a diffuse $10^{-8}(E/\,\text{GeV})^{-2}\,\text{GeV}^{-1}\,\text{cm}^{-2}\,\text{s}^{-1}\,\text{sr}^{-1}$ spectrum, for energies between 10 and 10^7 GeV. The statistical errors are shown for both Genhen (shaded area) and NuG (error bars). Systematic errors are not included. The uncertainty on the cross section is the biggest systematics for these simulations and can reach up to 10% above 10^6 GeV (96). All events in which the muon vertex is closer than 200 m to the detector center have been plotted (even if they did not produce any detectable hit).

first Antares analysis which applies the SeaTray Monte Carlo chain. A comparison between the two chains has therefore been performed. As muon neutrinos are the most studied and best understood, the comparison is focused on upgoing muon neutrino events.

5.4.1 Generators

For this work Neutrino Generator, NuG, was chosen rather than the simulation program Genhen, described in (94). The reason for this choice is based on several considerations. First, NuG is already included in the SeaTray software, making it convenient to use. Second, Genhen is particularly focused on the energy range below 10^9 GeV, while neutrino-generator has been tested up to 10^{12} GeV. Finally, in order to take into account the regeneration process of tau neutrinos within Earth, in Genhen it is necessary to use an extension of the software which includes TAUOLA (95). As it is important for this work to treat electron and tau neutrinos as precisely as muon neutrinos, neutrino-generator has proven to be a better choice. As a first step, the generator NuG and Genhen were compared. Genhen is a Fortran code that uses external programs to perform the neutrino propagation through the Earth. A few differences in the generation process between the two programs must be considered. First, Genhen simulates only one neutrino interaction at the time, in order to save CPU power. It becomes necessary, then, to merge several Monte Carlo productions in order to have both neutrinos and antineutrinos, as well as NC and CC events. This must be taken into account when merging the entire production, because the weights must be normalized to the total number of generated events.

Both generators have a reference system centred at the Center Of Gravity (COG) of the detector. The definitions of the zenith and azimuthal angles are, on the other hand, different for the two programs. In the Antares chain, vertically upward-going events have, by convention, a zenith angle $\theta = 0$. Up-going events, that traverse the Earth before reaching the detector, will therefore have a zenith angle such that $0 \leq \cos(\theta) \leq 1$. NuG, on the contrary, defines the zenith angle in the opposite direction, so up-going events have a zenith angle such that $-1 \leq \cos(\theta) \leq 0$.
For both generators, a "can" is defined as a cylindrical volume that fully contains the instrumented volume of Antares. Genhen defines two can, one in which neutrino interactions are generated and a smaller one in which particles are propagated. By contrast, NuG defines only one can, in which the interaction vertex takes place (see Section 5.2.1.1). As described in Section 5.2.1, in NuG this can is coaxial with the incoming neutrino. In Genhen the surrounding volume is coaxial with the detector itself. A default option of Genhen throws away neutrinos that do not reach the can. This differs from NuG, where all neutrinos are forced to interact. Because NuG has been optimized at very high energy interactions, it neglects quasi-elastic (QE) and resonant (RES) interactions, that are only important al lower energies.

The Genhen production used for this comparison has already been compared to real data (93).This production contains both neutrino and antineutrino events and it is focused on medium energies, between 10 and 10^7 GeV. The generated spectrum has a power index of -1.4 and only upgoing events (with direction from below the horizon) were generated. The generation parameters used in the SeaTray are different than the ones in Genhen: the energy range is 10 to 10^9 GeV, and the generated spectrum follows a power law of E^{-1}, in order to have more statistics at higher energies, where the presented analysis is focused. Because the GRB analysis is not limited to upgoing events, the SeaTray production covers the entire solid angle.

In order to compare the two chains, both spectra have been weighted to the same physical flux $J_\nu = 10^{-8} E^{-2}\,\mathrm{GeV}^{-1}\,\mathrm{cm}^{-2}\,\mathrm{s}^{-1}\,\mathrm{sr}^{-1}$. Only events that generated a muon track were considered (CC events). Because of the different definitions of the cans in the two generators, some geometrical cuts were applied in order to select only common events. The distance between the point of closest approach and the detector centre (defined as the orthogonal distance between the muon track, assumed to be infinite, and the detector centre)is required to be smaller than 150 m, and the muon vertex must be closer to the detector centre than 200 m. The comparison between the two generators is shown in Figure 5.6: at high energies Genhen suffers from a lack of statistics that makes it more difficult to perform a good comparison. The difference between the two generations influence for around 1%. The results of the analysis are presented in Chapter 7.

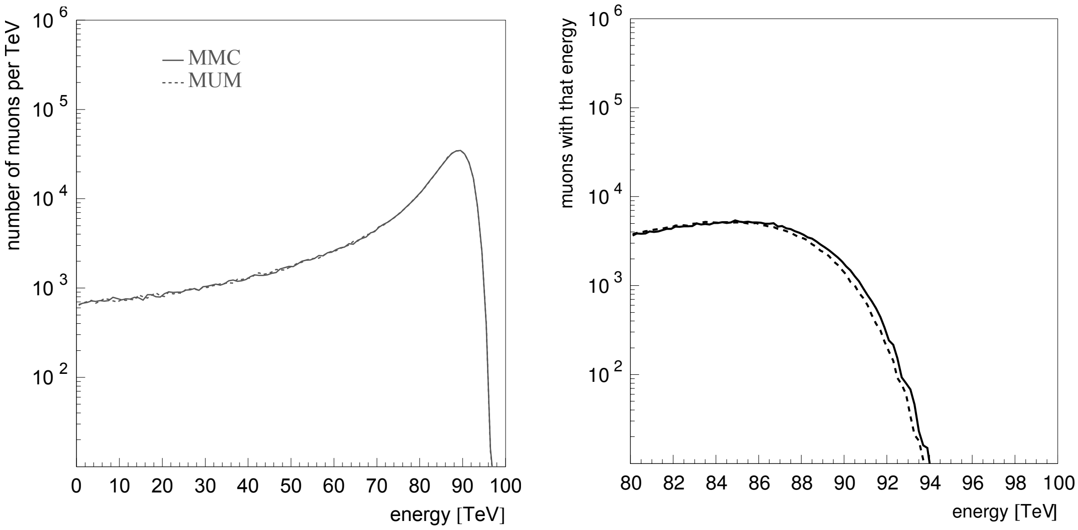

(a) MUM-MMC comparison (b) Zoom of Fig. (a)

Figure 5.7: Comparison of muon propagation through 800 m of Ice with MMC and MUM. As visible from Fig. (a), MUM lies almost always under MMC. Figures taken from (87)

5.4.2 Propagator and triggering

The propagation process in the Antares simulation chain outside SeaTray is handled by the program KM3. To perform the propagation, KM3 uses another software package called MUSIC. In Antares it is also possible to use MUM, a propagation software similar to MUSIC, but that neglects muon scattering. MUSIC is in slightly better agreement with data, but MUM is a much faster software and is often used for this reason. This latter propagator has been compared with MMC by its author (87). In Figure 5.7 the number of muons surviving a propagation through 800 meters of ice with both MUM and MMC is shown. The difference visible at higher energies in Figure 5.7(b) disappears when the comparison is made with MUSIC, as MUM underestimates the survival probability by around 1 ‰with respect to the other two propagators.

The parameters used for the propagation and the tables used in the photon propagation (Section 5.2.3) influence the output of the simulation. For this reason, the two spectra, with the same applied cuts used in Figure 5.6, have been compared after triggering. TriggerEfficiency has been used with the exact same parameters in both cases (see Appendix A.4). Optical background has been added reproducing the same time period of year 2008 in both chains. The result of the comparison is shown in Figure 5.8. Figure 5.8(a) is made with the old Photonics tables, while Figure 5.8(b) is produced with the last available version of the Antares Photonics Tables. The difference is not very big, as the optical background introduced by TriggerEfficiency plays a much more important role. Still, they cause a discrepancy up to around few TeV. The difference at higher energies is introduced by differences in the light propagation between HitConstructor and KM3. Further studies are needed to understand this discrepancy, but for this thesis it is sufficient to introduce an uncertainty in the final result due to the differences in the Monte Carlo (see Section 7.8.3).

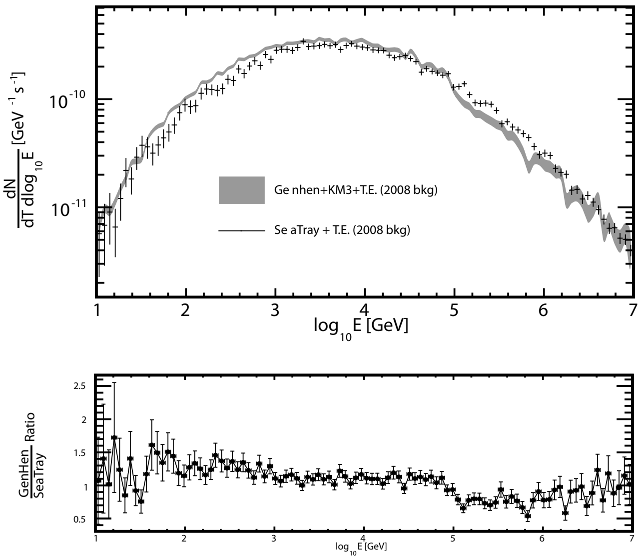

(a) Old Photonics tables

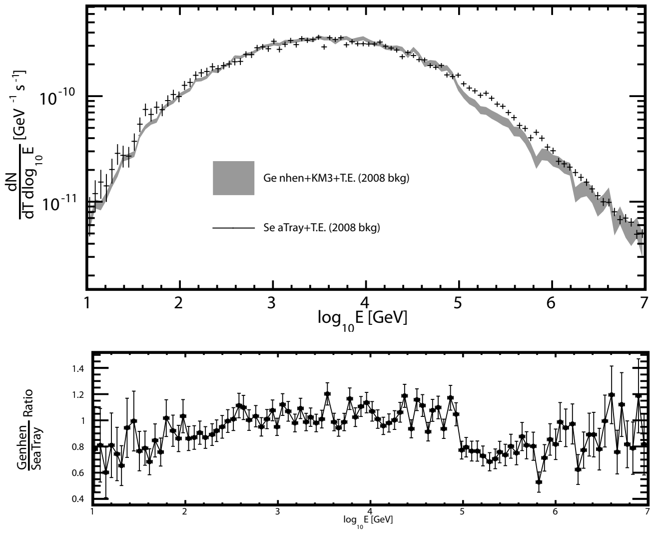

(b) New Photonics tables

Figure 5.8: Upward-going muon neutrino rates simulated with Genhen (grey shaded area, representing the statistical error) and NuG (solid line with error bars for the statistical error), assuming a diffuse $10^{-8}(E/\,\mathrm{GeV})^{-2}\,\mathrm{GeV}^{-1}\,\mathrm{cm}^{-2}\,\mathrm{s}^{-1}\,\mathrm{sr}^{-1}$ spectrum, for energies between 10 and 10^7 GeV. In both cases Trigger Efficiency has been used to perform the triggering and detector simulation. In Figure (a) the old Photonics tables were used, while in Figure (b) the updated version is shown. It is interesting to notice that the difference is not very important. This is because the optical background plays a even more important role.

6

Shower Reconstruction

> *So the fate... of the entire human race depends upon my wild guess.*
>
> Doctor Gaius Baltar

6.1 Physical Motivation

A shower is the main signature of several types of events. One candidate of such an event is a neutrino undergoing a NC interaction without directly producing a charged lepton:

$$\nu_l(\overline{\nu}_l) + N \rightarrow \nu_l(\overline{\nu}_l) + \text{hadronic shower}$$

where l indicates the neutrino flavour. A neutrino undergoing such a NC interaction in the detector will create a hadronic shower, identifiable thanks to its large light emission.

Another candidate of a shower event is an electron neutrino interacting through a CC interaction, producing a hadronic shower and a high energy electron. Since electrons are considerably lighter in mass than muons or taus, they will undergo substantial energy loss via Bremsstrahlung. Thus instead of leaving a track, the electron generates an electromagnetic shower very close to the primary vertex.

An electromagnetic shower is physically different from a hadronic shower. While an electromagnetic shower is composed exclusively of electrons, positrons and photons, a hadronic shower contains heavier particles, such as mesons (mainly pions) and muons. As a result of this different composition, the extent of a hadronic shower is much more variable, but typically larger.

In a high energy neutrino detector, such as Antares, distinguishing electromagnetic and hadronic showers is very difficult. Because the spacing between optical modules is large compared the shower extent, showers of either type appear to emit photons from a single vertex.

For a shower to be measured, it is necessary for the vertex to occur in or near to the instrumented detector volume. This reduces the volume in which neutrino interactions can be detected using shower signatures compared to that using track signatures. However, the ability to study shower events is a valuable complement to track based analyses.

6.2 Hit Selection

Not all the light measurable in the Antares detector originates from neutrino interactions. The majority of the photons measured in Antares are due to optical background and light induced by down-going atmospheric muons. Besides the trigger (see (72) for a review of the trigger software), other methods can be used to distinguish between background and signal hits. One method consists of accurately modelling the signature of signal and background hits and applying a maximum likelihood fit (see, for example, (60)). This is done using a Probability Density Function (PDF) to describe the estimated distribution of measured observable(s) (i.e. hit time residuals with respect to the straight line arrival time of the Cherenkov light).

The method chosen for this reconstruction is to employ a strict hit selection that reduces the number of background hits used during the reconstruction and then to use a simple minimization of hit time residuals.

The topology of a shower in the Antares detector suggests that the hypothesis of the signal shape can be simple, i.e. a point source photon emission leading to a time difference that depends only on the distance, referred to as isotropic time distribution. As this assumption does not account at all for background hits, it is essential to reduce the number of photons included in the fitting procedure for which the assumption cannot hold, such as scattered photons or photons emitted during $^{40}\mathrm{K}$ decays. The hit selection employed for this reconstruction has been designed to reject, as much as possible, such background hits.

The hit selection begins with a search for clusters of hits in time, under the assumption that this is more likely to be due to a signal rather than background. During the hit selection, the geometry of a single storey is ignored and all hits on a floor are considered together.

First, all hits in a time snapshot are calibrated (see Section 4.7). At this point, each hit has a position, given in metres, with respect to the centre of gravity of the detector, a time, given in nanoseconds from the first triggered hit, and an amplitude, defined as the equivalent number of p.e. which produced the hit.

For each event, all hits on one storey are time ordered, even if they came from different optical modules. All hits that occur within 20 ns of each other are merged together: the merged hit will have the time of the first hit in the cluster but the aggregate amplitude of all hits in the cluster. A time window of 20 ns has been chosen to account for the expected background rate in the Antares detector (see Section 4.6). An additional 1.5 p.e. is added to the final merged hit if hits coming from different optical modules have been used. Note that, while the charge of a hit is currently not used during the shower fit procedure, it is used during the hit selection procedure. The position of the newly merged hit is then translated to the geometric centre of the three optical modules in the storey, so that the hit lies on the line itself.

At this point, a first selection is applied: only the merged hits with an amplitude larger than 2.5 p.e. are considered. This first selection defines an L1 hit (note that this definition is different than the one used for the online T3 trigger (91) given in Section 4.7.1). The L1 hits are then clustered using the T3 clustering algorithm, which searches for two L1 hits within 80 ns in adjacent floors, or 160 ns in next-to-adjacent floors.

Using the T3 clusters as seeds, all L0 hits that are causally connected to the T3 cluster are kept. To be sure that only signal hits are selected, only hits compatible with being generated by the same particle are selected. This method, has been developed to be valid for both shower and track photons selection (97).

The algorithm proceeds as follows. Hits are selected in an iterative manner; for a given selected hit, a time window is established in which subsequent hits can be sought on neighbouring floors. This procedure begins with the hits in the T3 cluster. Considering a selected hit on floor i with time t_i, the expected arrival time $t_{i\pm j}$ of a photon on the storey $i \pm j$ can be calculated. The hits selected with the T3 algorithm are used to calculate the time interval in which other hits can be caused by the same source. This time window is defined as:

$$\Delta t < j\Delta z\frac{n}{c} + t_s \tag{6.1}$$

where j is the number of floors that separates the measured hits from the first selected hit (can be 1 or 2), Δz is the spatial vertical distance between two floors (in Antares it is 14.5 m), n is the water refraction index and t_s is a time window allowed for uncertainties on the time resolution of the PMT and the spatial shifting due to the T3 trigger algorithm, and chosen to be 10 ns. The earliest and latest hits acceptable are then defined as:

$$t_{i\pm j}^{early} = t_{i\pm j} - jt_s \tag{6.2}$$

$$t_{i\pm j}^{late} = \max\{t_i + j\Delta z\frac{n}{c} + t_s, t_{i\pm j} + jt_s\} \tag{6.3}$$

The asymmetry in the time window is due the speed of light in water (term $j\Delta zn/c$). The two extreme cases are a plane wave front which propagates horizontally (i.e. the hits in two storeys have the same times, except for the uncertainty t_s), versus a plane wave which propagates vertically (i.e. the time differences are $j\Delta zn/c$). Both conditions are defined in the same way for track and shower photons (97). For the Antares detector, the minimum acceptable time for a hit is $t_{i\pm j}^{\mathrm{early}} = t_j - j * 10\,\mathrm{ns}$ and the maximum time is $t_{i\pm j}^{\mathrm{late}} = t_j + j * 80\,\mathrm{ns}$. If another hit is found in this time interval, it can be considered causally related to the seed hit.

Only adjacent or next-to-adjacent storeys are considered, therefore j can assume the values of 1 or 2. If the T3 cluster is composed of only 2 hits, these two hits are either in adjacent storeys, or they are in next-to-adjacent. If the two hits are next to each other and have the times t_i and $t_{i\mp 1}$ respectively, then the expected time $t_{i\pm j}$ is

$$t_{i\pm j} = t_i + j(t_i - t_{i\mp 1}) \tag{6.4}$$

if the two hits are on next-to-adjacent floors with times t_i and $t_{i\mp 2}$, then the expected time $t_{i\pm j}$ is

$$t_{i\pm j} = t_i + j(t_i - t_{i\mp 2})/2. \tag{6.5}$$

If three hits are present in the three floors ($j = 0, 1, 2$) another Equation can be added, that relates the expected time t_j with the two times $t_{i\mp 1}$ and $t_{i\mp 2}$:

$$t_{i\pm j} = t_{i\mp 1} + (j+1)(t_{i\mp 1} - t_{i\mp 2}). \tag{6.6}$$

All hits that fall within the time window between $t_{i\pm j}^{\mathrm{early}}$ and $t_{i\pm j}^{\mathrm{late}}$ are added to the list of the hits that will be used in the fitting procedure. The hit selection applied for this work has also been used in other reconstruction algorithms in Antares (97, 98).

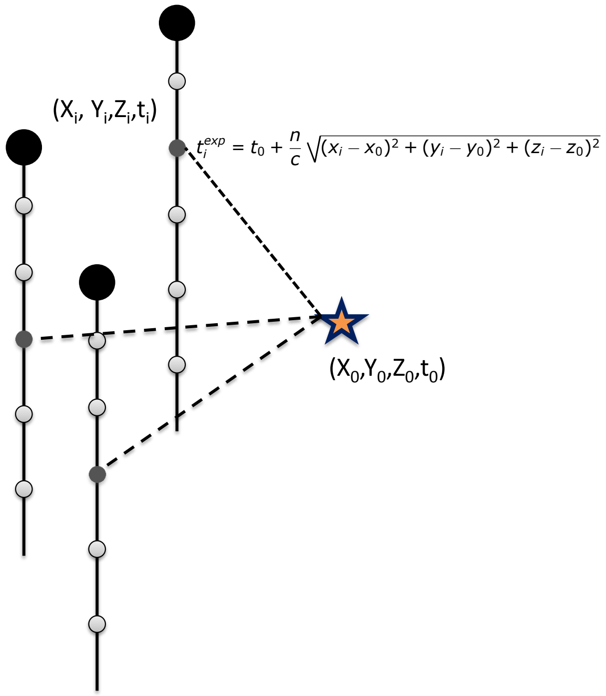

Figure 6.1: Diagram illustrating shower reconstruction: the expected time of the hit and the real measured time of the hit are compared. The expected time is calculated following geometrical considerations on the distance of the shower, as in the picture.

6.3 Shower Reconstruction in Antares

Several algorithms have been developed to perform a track or shower reconstruction in the Antares experiment. For the track reconstruction, a prefit is performed before applying of a likelihood fit that uses a PDF hypothesis (see (60)). The reconstruction described in this note aims to identify showers induced by cosmic neutrinos; in particular, those in coincidence with a GRB alert (see chapter 7). It must therefore be efficient in identifying a shower, but it does not need to reconstruct the direction of the incoming neutrino nor its energy, since the time coincidence between a neutrino-induced shower and a GRB alert from a satellite provides a significant reduction in the dominant background from atmospheric muons.

6.3.1 Prefit: Center of Gravity of the Shower

The first estimate of the position of the shower is obtained by calculating the centre of gravity (COG) of the selected hits. This is just the average position of all selected hits weighted by

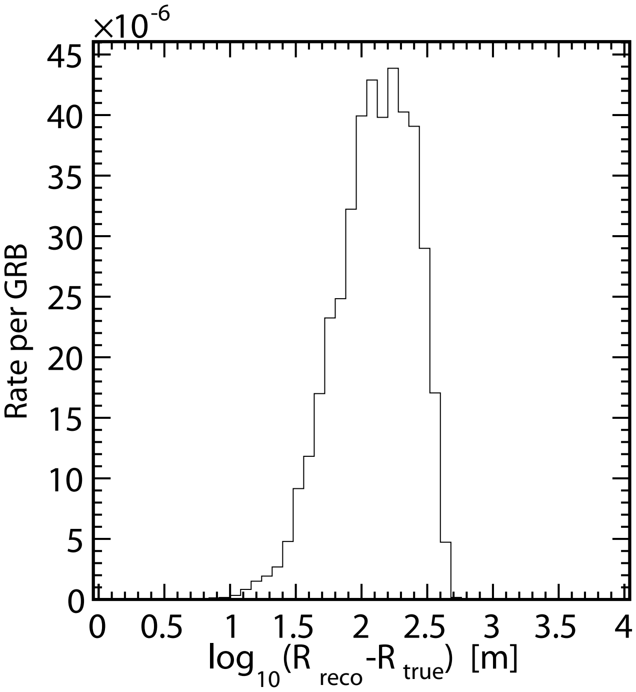

Figure 6.2: Performance of the center of gravity prefit. The position of the shower is reconstructed with a resolution of approximately 80 m. Such a resolution would be unsatisfactory by itself, but it serves well as a starting value for the subsequent fit routines. The y-axis indicates the number of events during the length of a single GRB (assumed to be 50 seconds).

their amplitudes:

$$
\begin{aligned}
COG_x &= \frac{\sum_i X_i * A_i}{N_{hits} \sum_i A_i} \\
COG_y &= \frac{\sum_i Y_i * A_i}{N_{hits} \sum_i A_i} \\
COG_z &= \frac{\sum_i Z_i * A_i}{N_{hits} \sum_i A_i} \\
COG_t &= \frac{\sum_i T_i * A_i}{N_{hits} \sum_i A_i}
\end{aligned}
\tag{6.7}
$$

where N_{hits} is the total number of hits used in the fit and A_i is the amplitude (in p.e.) of each hit. Although the performance of this prefit (Figure 6.2) is not by itself sufficient to be used for an analysis, it does provide a good starting point for a subsequent fit.

The reconstruction begins by calculating the expected arrival time of a photon generated by a shower on a PMT (see Figure 6.1). Given a shower occurring at a position $(X_{true}, Y_{true}, Z_{true})$ and time t_{true}, the expected arrival time of photons coming from the shower is defined as:

$$t_{exp} = t_{true} + \frac{n}{c}\sqrt{(X_i - X_{true})^2 + (Y_i - Y_{true})^2 + (Y_i - Y_{true})^2} \tag{6.8}$$

where n is the group refractive index of sea water ($n = 1.3797$) and c is the speed of light in vacuum. To reconstruct the time t_{reco} and position $(X_{reco}, Y_{reco}, Z_{reco})$ of the shower, these unknown parameters are varied until the difference between the expected time and the measured time of each selected hit is minimised.

Although the hit selection explained in Section 6.2 is strict and allows for a significant background reduction, a small fraction of the surviving hits is nonetheless caused by some sort of background. An example source of such a selected background hit is light due to a $^{40}\mathrm{K}$ decay producing a hit with a large p.e. deposit. Since the hit selection is not perfect, steps have been taken to optimize the reconstruction in order to avoid being affected by these hits.

In 1967, P. Huber (99) proposed a generalization of the maximum likelihood method (see, for example, (100) for a review), minimizing the function

$$L = \sum_{i=1}^{N} \rho(x_i, \vec{\theta}) \tag{6.9}$$

where x_i are the measurements and $\vec{\theta}$ the fit parameters. The solutions are the values $\widehat{\theta}$ that bring Equation 6.9 to its extreme value, and the function ρ is the estimator. When the minimization is performed directly on the $\rho(x_i, \vec{\theta})$ function, the estimator is defined as "ρ-type", while if a derivative is performed prior the minimization, the estimator is defined as "ψ-type". In this reconstruction, a ρ-type estimator is used.

For the purposes of shower reconstruction, the measurements x_i are the measured times of the hits t_i and $\vec{\theta}$ is the set of shower parameters (X, Y, Z, t). Several functions for ρ can be chosen to perform the minimization, and the ideal choice depends on the observed time residual distribution.

The time residuals of selected hits with respect to the true time of the shower in neutrino simulations (see Section 5 for an overview of the Monte Carlo package that has been used) are displayed in Figure 6.3. This plot shows the time difference between each selected hit and the expected time of that hit as calculated by Equation 6.8 using the true position of the shower $(X_{true}, Y_{true}, Z_{true}, t_{true})$. This plot shows how the main peak, very close to zero, is not exactly centred at zero. The reason for this is that the applied hits selection assigns the time of the first hit to the selected cluster. This effect pulls slightly the time residuals to negative values. What is more, the tail of late hits is not negligible. It is therefore important to choose a minimizing function ρ which assigns a smaller weight to these late hits.

6.3.2 M-estimator fit

In Figure 6.4, two possible minimizing functions are shown. The dashed line represents the conventional chi-squared (χ^2) distribution:

$$\rho(t_i, t_{exp}) = \chi^2(t_i, t_{exp}) = \sqrt{\frac{(t_i - t_{exp})^2}{\sigma_i^2}} \tag{6.10}$$

where σ_i represents the error on the measurement of t_i. This error could in principle be different for each data point. This function would be ideal if the time residuals shown in Figure 6.3 were

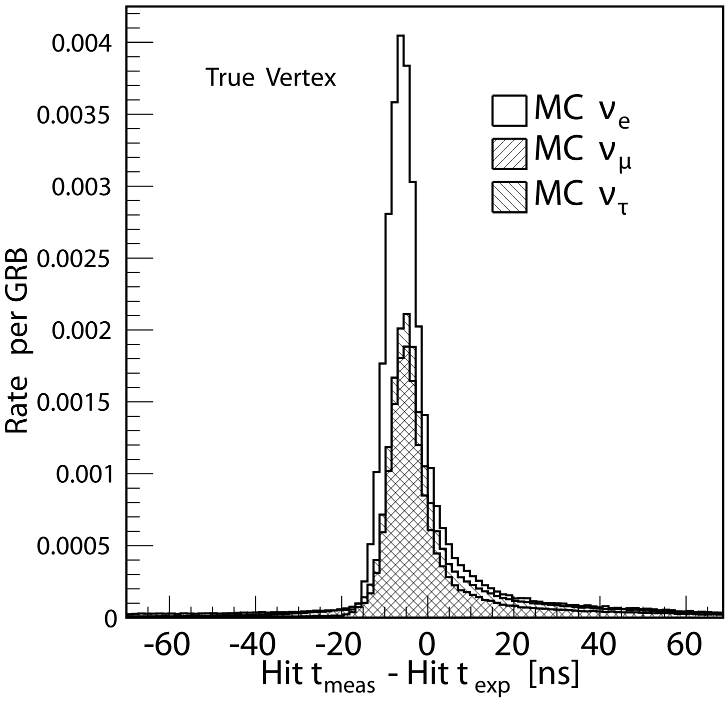

Figure 6.3: Hit time residuals of the selected hits with respect with the true position of the shower.

normally distributed. This hypothesis is not a particularly good one, and a χ^2 fit can be heavily distorted by late hits.

The so called M-estimator function has been used for this analysis, and is defined as:

$$\rho(t_i, t_{exp}) = M(t_i, t_{exp}) = 2 * \sqrt{1 + \frac{(t_i - t_{exp})^2}{2\sigma_i^2}} - 2 \tag{6.11}$$

The minimization itself was performed using the minimizer Minuit (101), a tool that finds the minimum of a multiparameter function and offers several methods for developing a statistical analysis of the results.

As shown in Figure 6.4, the M-estimator function (solid line) becomes linear at large time residuals, and thus the fit is not pulled by late hits as strongly as a χ^2 fit would be. The errors σ_i could in principle be different for each hit. In the Antares experiment, all optical modules are observed to have a similar resolutions and, therefore, the same value of $\sigma_i = \sigma$ is used for each hit. The exact value of this error can be estimated from calibration data; an estimate of 1 ns has been chosen here.

A study on the dependence of the reconstruction on the value of σ has been performed. The reconstruction has been applied to electron neutrino simulations with different values of σ (see Figure 6.5) to observe the effect of a significantly different choice for this parameter on the results of the reconstruction. As shown in Figure 6.6, the number of well reconstructed

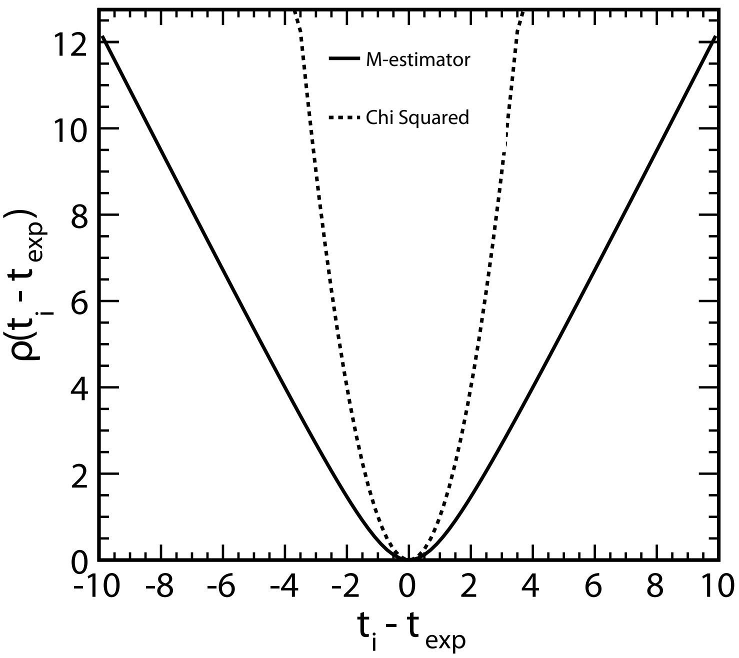

Figure 6.4: Two example functions that may be used for the shower fit minimization. The solid line shows the so-called "M-estimator" function, while the dashed line represents the chi squared (χ^2) function.

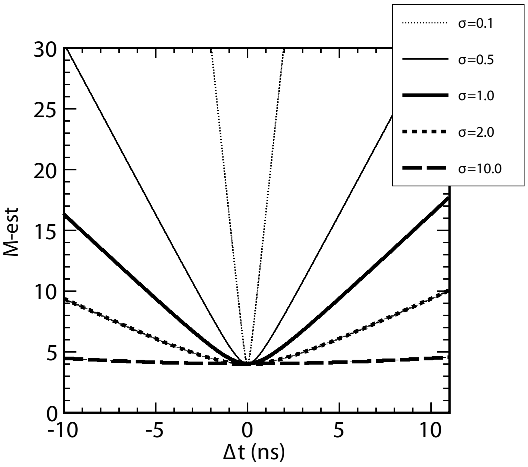

Figure 6.5: M-estimator distributions for different values of *sigma*, from 0.1 to 10 ns. The thick solid line shows the function for $\sigma = 1$ ns, which has been used in the analysis.

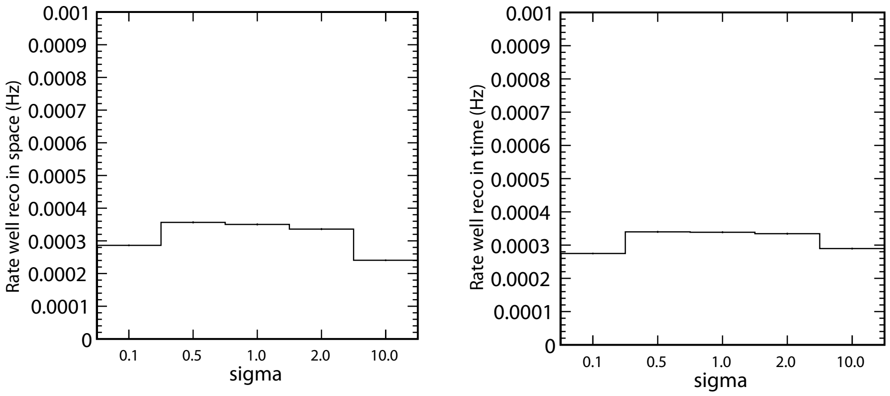

(a) Well reconstructed events in space

(b) Well reconstructed events in time

Figure 6.6: Number of well reconstructed events as a function of the chosen value of σ. The neutrino spectrum has been weighted with an average Waxman-Bachall GRB flux (40). (a) shows the rate of events reconstructed within 2 m of the true position of the shower, while (b) shows the rate of showers reconstructed with a time resolution better than 5 ns.

events is approximately constant when σ is within a factor of 2 of 1 ns. The timing resolution of a single Antares photomultiplier is determined by its TTS, which is about 2.6 ns. When multiple photons are detected at the same time, the time resolution of the PMT improves, because the transit time is determined by the photoelectron with the smallest transit time. After these considerations, the use of $\sigma_i = 1$ ns for each hit seems reasonable and the final fit is not particularly sensitive to the exact value used.

6.3.3 Reconstruction Performance

The performance of the M-estimator shower fit procedure has been studied using neutrino simulations. That the fit procedure finds reasonable values for the time and location of the shower vertex can already be seen from the similarity of the hit time residual distributions calculated using the fitted and the true shower positions, as shown in Figure 6.7.

A measure of the quality of the reconstruction is given by the M-estimator parameter (the value of Equation 6.3.2), whose distribution is shown in Figure 6.8. This value alone may not be enough for a precise quality selection, depending on the analysis that one is interested in performing.

One possible additional cut could be applied to the errors given by minimizer. To determine whether these errors are reliable, the pull distributions for each of the reconstructed parameters have been studied. Pulls are defined as the difference between the reconstructed parameter and the true value of that parameter, divided by the estimated error on the parameter itself:

$$P = \frac{X_{reco} - X_{true}}{\sigma_X} \tag{6.12}$$

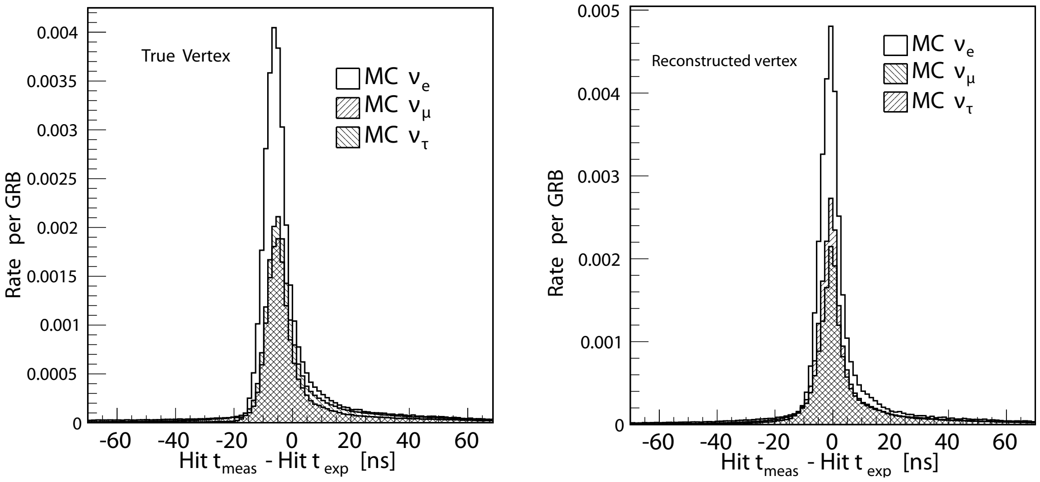

(a) Time residuals true shower

(b) Time residuals reconstructed shower

Figure 6.7: The hit time residual distribution of selected hits (see Section 6.2) calculated using the true time and position of the shower (Figure (a)) and the reconstructed time and position of the shower (Figure (b)).

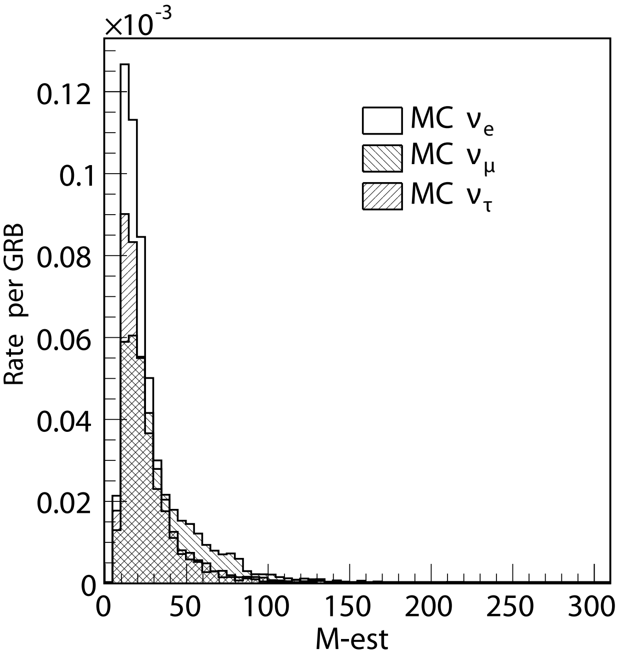

Figure 6.8: The M-estimator fit quality parameter distribution of the reconstructed shower from a neutrino simulation sample. Low values of the M-estimator indicate a better reconstructed shower.

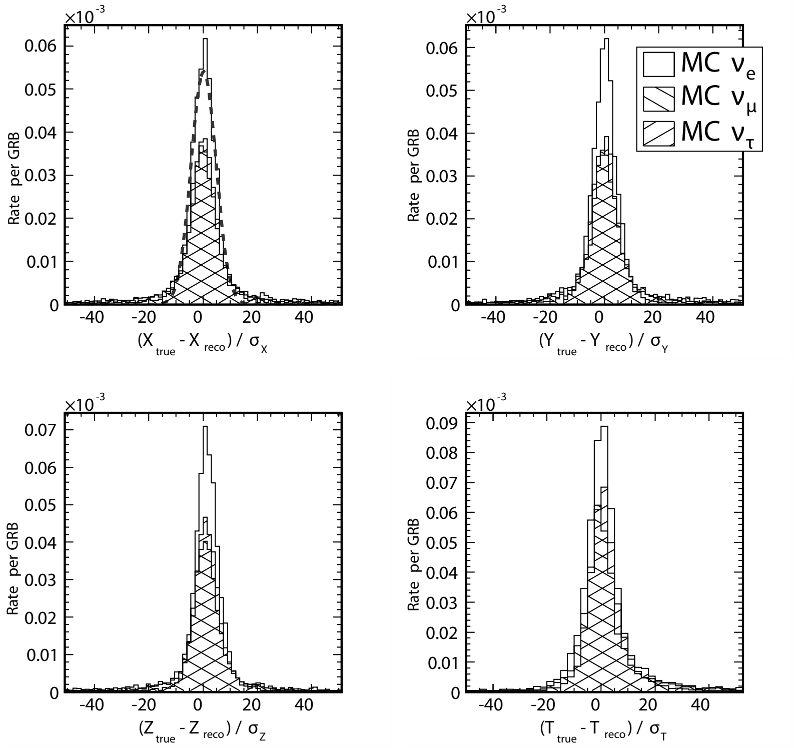

Figure 6.9: Pull distributions for the four reconstructed parameters ($X_{reco}, Y_{reco}, Z_{reco}, t_{reco}$) are centred at 0 and normally distributed. To guide the eye, the pull of the X parameter for ν_e has been fit with a Gaussian, shown by the grey dashed line.

The errors σ_X are given by the minimizer used for the reconstruction (in the work presented here, Minuit (101) has been used). The pull distributions for the M-estimator shower fit are normally distributed around zero, as seen in Figure 6.9. This implies that the fit is not systematically pulled into a narrow local minimum far from the true minimum.

The standard deviation of the pull distribution should give an indication of the reliability of the reconstruction parameter error estimates. However, for this reconstruction, a default value of the Minuit parameter ERR=1.0 has been used. Minuit calculates the error on a parameter as the amount by which the parameter must be changed in order for the value of $\rho(x_i, \vec{\theta})$ to change by ERR. While ERR=1.0 yields proper 1σ errors for $\rho = \chi^2$, it does not give 1σ errors for the M-estimator. For the analysis presented in this thesis, the parameters errors have not been used as quality parameters, as other parameters proved to be a more efficient choice, therefore no attempt has been made to obtain the true 1σ errors. If a future user needs to use the error on the reconstruction as a discriminating parameter, the minimiser options must be changed.

The resolution of the reconstruction is shown in Figure 6.10. The time resolution of the reconstruction taken to be the RMS of the distribution in Figure 6.10(a), 5.1 ns. This value is well within the requirement for the analysis presented in this thesis, as the time window for the search of neutrinos in coincidence with GRBs is of the order of a minute. Figure 6.10(b) shows the logarithm of the three dimensional distance between the true and reconstructed shower. The

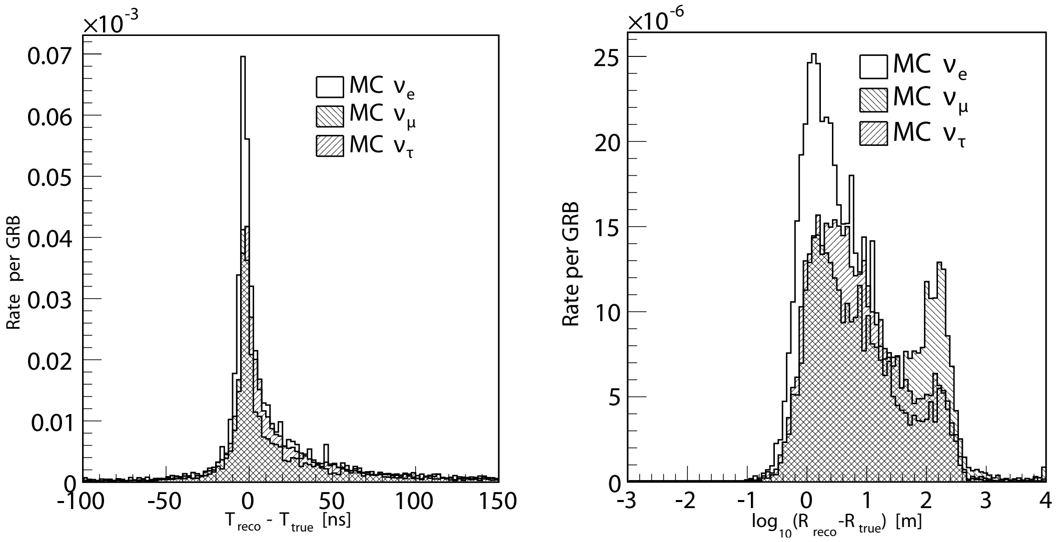

(a) Timing resolution

(b) Spatial resolution

Figure 6.10: Time and spatial resolution of the reconstruction. Figure (a) shows the difference between the reconstructed and the true time of the shower. The time resolution of the reconstruction taken to be the RMS of the distribution, 5.1 ns. Figure (b) shows the logarithm of the three dimensional distance between the true and reconstructed shower. The spatial resolution of the reconstruction is given by the median of this distribution. It is best for electron neutrinos, with a value of 3.0 m, and worst for muon neutrinos, with a value of 9.28 m.

spatial resolution of the reconstruction is given by the median of this distribution. It is best for electron neutrinos, with a value of 3.0 m, and worst for muon neutrinos, with a value of 9.28 m. The reason for this difference is that electron neutrinos always produce a shower-like signal. On the other hand, only muon neutrinos that undergo a NC interaction will produce a pure shower signature. The second peak, especially visible for muon neutrino induced events, is due to Bremsstrahlung and electromagnetic showers generated along the track that are reconstructed far away from the interaction vertex. While the three spatial parameters (X, Y, Z) are fitted separately, Figure 6.10(b) shows only the three-dimensional distance of the reconstructed shower vertex from the true shower vertex:

$$R_{reco} - R_{true} = \sqrt{(X_{reco} - X_{true})^2 + (Y_{reco} - Y_{true})^2 + (Z_{reco} - Z_{true})^2}$$

For the expected neutrino energy spectrum of single gamma-ray burst (40), a resolution of 5.1 ns in time and 5.7 m in space is reached averaging over the three flavours.

The efficiency of the reconstruction has also been studied. Several efficiencies are involved in the analysis. First is the trigger efficiency, which represents the efficiency of the detector to trigger on an event that takes place within the detectable volume. A study on the efficiency of the T3 trigger is presented in (91). As the hit selection (see Section 6.2) uses nearly the same algorithm applied in the Antares trigger (73), the hit selection coincides with the trigger selection.

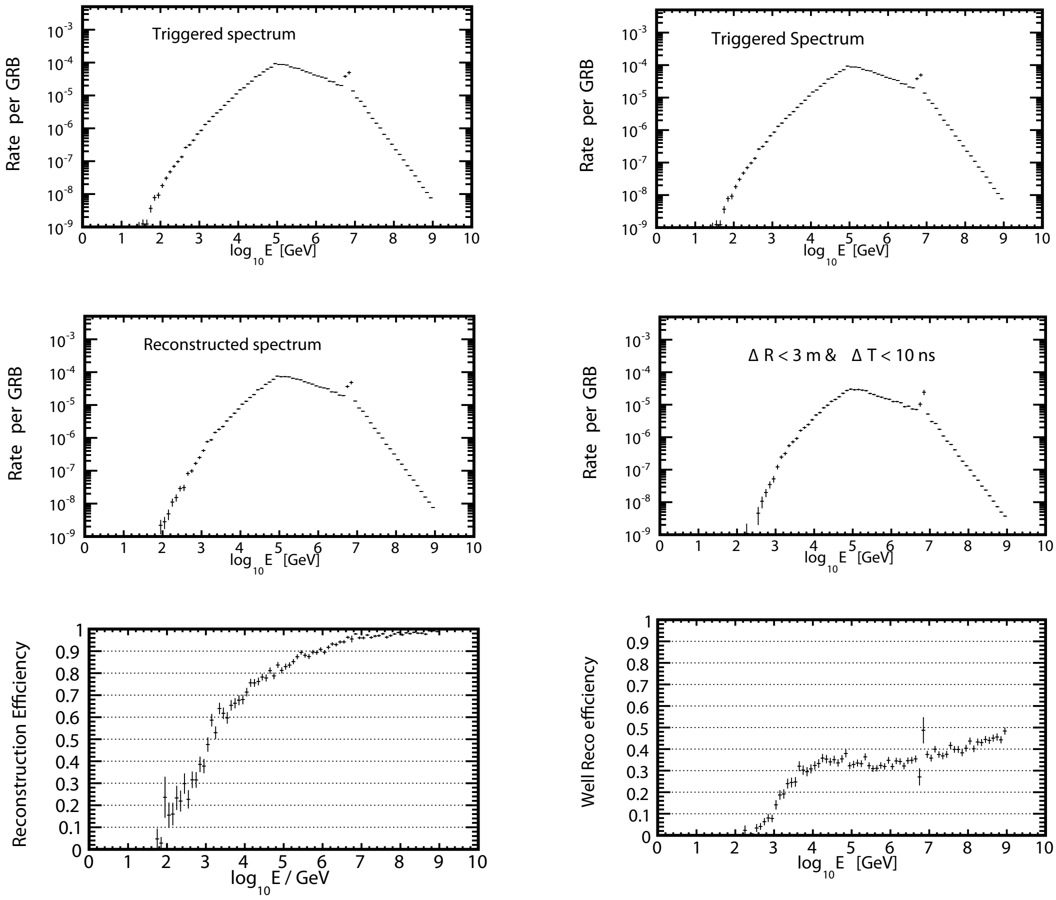

(a) Min-bias Reconstruction Efficiency

(b) Very Well Reconstructed Efficiency

Figure 6.11: Reconstruction efficiency as a function of neutrino energy for an average GRB flux. See text for details.

The efficiency of the shower reconstruction itself depends on the criteria used to select reconstructed showers. A minimally biased reconstruction efficiency can be determined by keeping all events in which the reconstruction successfully found a minimum. For this purpose, two parameters must be set in the reconstruction software: the minimum required number of selected hits and the minimum number of lines with selected hits on them. Events not meeting these criteria will not be reconstructed. For the work presented in this thesis, values of 5 selected hits on at least 2 lines have been chosen. The efficiency of the reconstruction as a function of the neutrino energy after this first selection is shown in Figure 6.11(a). The spectrum is generated weighting the events with a Waxman-Bachall spectrum, which explains the drops at very low and very high energies. The reconstruction is considerably less efficient at low energies, where showers produce fainter light and less hits. At high energy practically all triggered events are reconstructed. This is a wanted feature of the reconstruction, as for this analysis a higher efficiency is more important than a very precise reconstruction. Figure 6.11(b) shows the efficiency with which the shower fit procedure determines very accurately the position and time of the shower. Only events for which the reconstructed shower was within 3 m and 10 ns of the true shower vertex are used for calculating this efficiency. Even with these strict cuts on the quality of the reconstruction, the efficiency stays between 30% and 50%, especially in the energy range on which the analysis is focused.

6.4 Reconstruction of LED Beacon Data

The Antares detector is equipped with a set of LED beacons used to perform timing calibration. These LEDs can be tuned to fire at a given time and to emit light of different colours (wavelengths). This system provides an excellent opportunity with which to test the shower reconstruction without using Monte Carlo simulations, as a flashing LED produces an isotropic light distribution and therefore a good simulation of a shower.

The trigger for a LED beacon to fire is provided by a 1.5 V negative square pulse with a duration of around 150 ns superimposed on a negative direct current (DC) bias that can be varied from 0 to 24 V. The amount of light each LED emits can be tuned by varying the DC voltage. For a DC level of 24 V, the energy per pulse emitted is at least 150 pJ, which corresponds to the emission of approximately $4 \cdot 10^8$ photons (66).

A run with only one LED firing beacon, situated at a central position in the detector (on line 8, floor 9) and flashing with the highest voltage (corresponding to a shower induced by a neutrino of about 100 TeV), has been used to test the shower reconstruction.

As a first step, the hit selection described in Section 6.2 is applied to the LED beacon data. The COG of these hits is then calculated and used as a starting point for the M-estimator fit. The resulting hit time residuals are shown in Figure 6.12. These residuals are calculated according to Equation 6.8 using the reconstructed position of the shower $(X_{reco}, Y_{reco}, Z_{reco}, t_{reco})$. A resolution of 2.4 ns and 1.04 m is observed in the reconstruction of LED beacon events, as shown in Figure 6.13. The time distribution in Figure 6.13(b) is not centred at zero. The reason for this lies in the choice of the clustering algorithm. For each T3 trigger cluster, the time assigned is the time of the very first hit that takes part in the cluster. The more hits are selected in the cluster, the earlier the cluster time is in relation to the time of each hit. This effect is more visible for LED beacon data as more hits are produced. The effect is very small compared to the resolution needed for the analysis presented in this thesis, and therefore no corrections are applied. This resolution shows that the reconstruction is performing very well on real data. The regularity of the LED beacon signal, both in energy and in shape, is the prime reason for the better resolution achieved here in comparison to the signal Monte Carlo events shown in Figure 6.10.

6.5 Identification of Sparking Photomultipliers

Some Antares PMTs suffer from a known effect of high voltage surges that cause the PMT to spark. It is a very rare event, but in a large data set, it is possible to find a handful of runs that

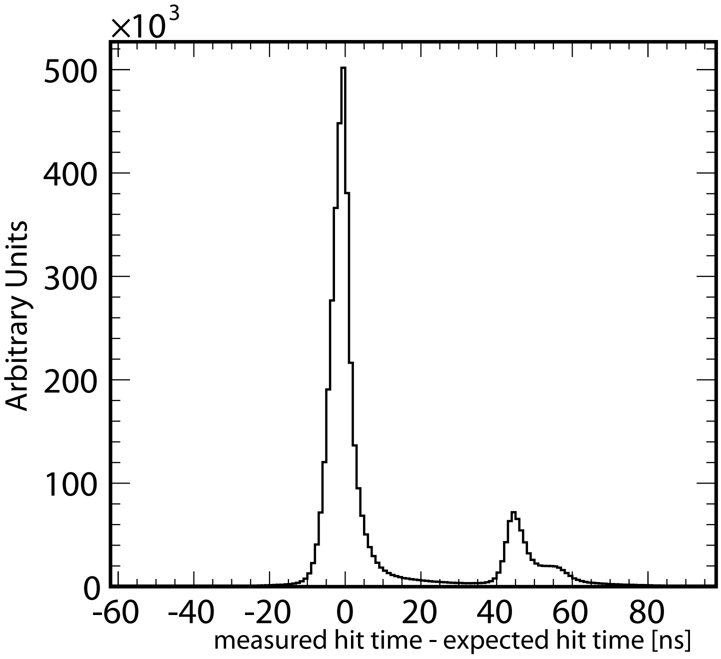

Figure 6.12: Hit time residual of selected hits (see Section 6.2) for LED beacon data. The second peak at 40 ns is due to the dead time of each ARS chip: after 40 ns, the second ARS begins taking data. The peak at values smaller than zero is due to the hit selection method, that assign the the selected cluster the time of the fist hit.

contain such "sparking events". Although rare, it is important to be able to identify and filter out these events when they occur, as they could be misinterpreted as neutrino-induced signal. One method by which runs containing these events can be identified is to look for many events all having a large number of triggering hits, as shown in Figure 6.14.

This method is helpful in identifying runs containing sparking events, but it may not be sufficient to find all sparking events. The shower reconstruction can also be a useful tool in locating these events, as a spark should emit light isotropically in time and be easily reconstructible. It was initially thought that all sparking events would have a reconstructed vertex on or extremely close to a single OM. However, as shown in Figure 6.15(a), the distance to an OM is not by itself sufficient to clearly identify sparking events.

To more accurately locate the sparking events, both the distance of the shower to an OM as well as the number of hits employed in the shower reconstruction should be used. Figure 6.15(b) shows the distance of the reconstructed shower vertex for events in run 34663 that have more than 100 selected hits; all of these events can be identified as coming from a sparking OM. The combination of the distance information and the number of hits allows for an efficient rejection of these events. This therefore represents a useful set of criteria by which to reject (possibly isolated) sparking events.

Further, it is interesting to study the timing of these events, to understand if a PMT suffers

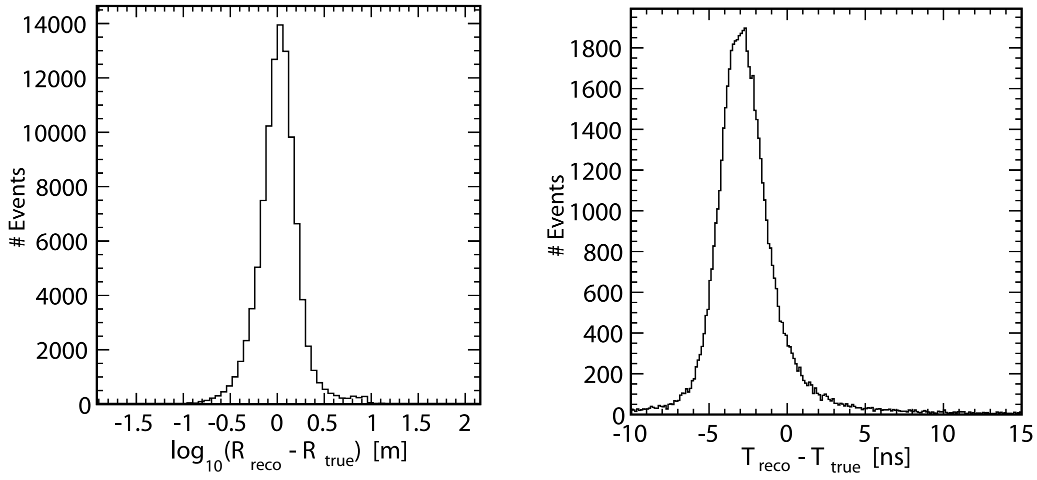

(a) Position Resolution

(b) Timing Resolution

Figure 6.13: Performance of the reconstruction on LED beacon data. Spatial resolution is calculated as the median of the logarithmic three dimensional position error to be 1.04 m. Timing resolution is the RMS of the error of the reconstruction time, 2.4 ns. The time distribution is not centred at zero, but is pulled towards earlier hits, due to the clustering algorithm.

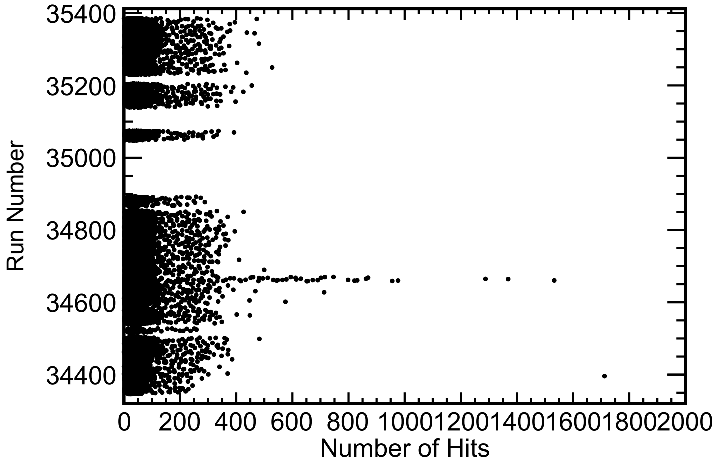

Figure 6.14: Number of triggered hits for each run. Each run contains approximately 3 hours of data taking. Rarely, a run contains many events with an extremely large number of hits, such as run number 34663 seen here. Such runs are thought to contain “sparking events”.

these sparks only for a short duration or if it remains unusable for a long period of time once it starts to spark. This is important to avoid excluding an entire run (around 3 hours of data taking) due to potentially only a handful of sparking events. For example, if all the sparking events in a particular data run occur very close together in time, it should be possible to exclude

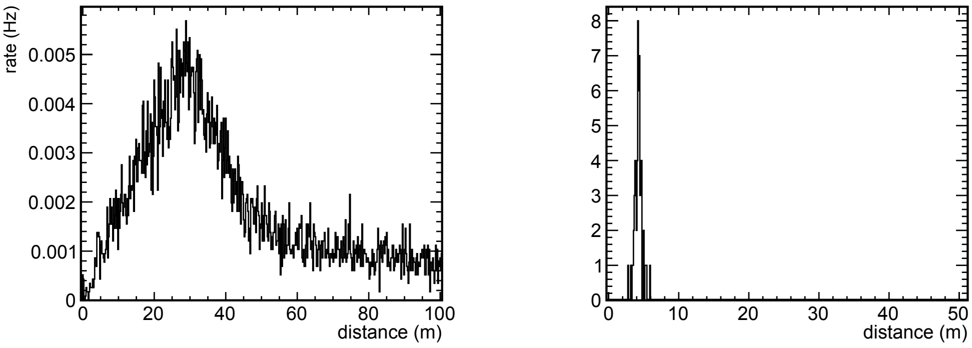

(a) Shower to OM Distance

(b) Same, for large events

Figure 6.15: Number of reconstructed events as a function of the distance of the closest optical module. (a) The number of events as a function of distance from the closest OM to the reconstructed shower vertex. Although sparking events are present, it is difficult to identify them using only the distance (i.e. no clear peak at 0). (b) The same distance is again plotted, but only for showers reconstructed using at least 100 selected hits. The close distance to an OM and the large number of hits together identify these events as coming from a sparking OM.

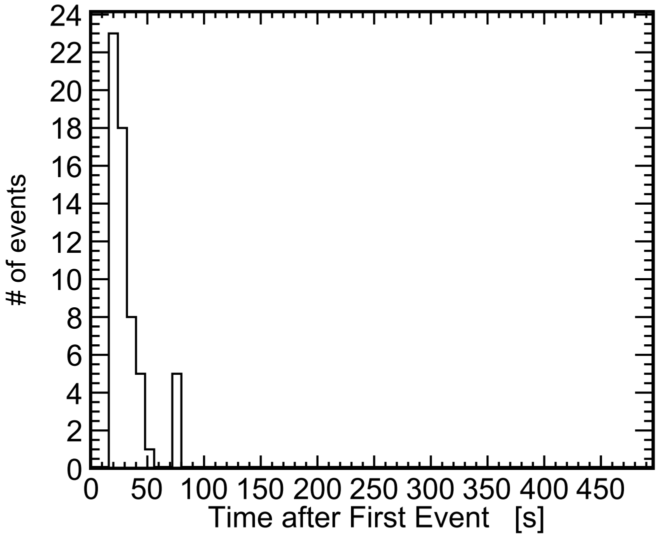

Figure 6.16: Time difference between the first sparking event and all other events having more than 100 selected hits and a reconstructed vertex closer than 10 m to an OM.

only a few minutes of data taking during which the sparking took place.

Figure 6.16 shows the time difference, in seconds, between the first sparking event and all the other sparking events, identified using the above criteria. All sparking events occur within a time range of less than 2 minutes. As an average Antares run lasts around three hours, it should be possible to use the vast majority of such a run while excluding only a few minutes of data taken around the sparking events.

7

Neutrino-Induced Showers Analysis

> *Which leads me to the inescapable conclusion that Cylons are, in the final analysis, little more than toasters... with great-looking legs.*
>
> Dr. Gaius Baltar

7.1 Time Correlated Shower Analysis

The concept of a binned time-correlation analysis is very simple: events are sought occurring in a given time window, within which such events can be considered time-correlated. For the analysis presented in this thesis, the time window should correspond to the duration of neutrinos arriving from a GRB, and an event should be a neutrino induced shower. The choice of the duration of the time window is made considering the physics of GRBs and the amount of background that will be included in the window, assuming the background is a stochastic, i.e. Poissonian, process.

The main advantage of using a time correlated search, compared to an analysis that does not use the timing information, is the efficient background rejection. In addition to the background reduction made with quality cuts on the reconstructed events (see Chapter 6 for a detailed description of the reconstruction), observing only a small time window increase the signal to noise ratio. In addition, the fact that most of the GRB parameters have been measured by satellite experiments, makes it possible to use these specific values, as the GRB duration T_{90}, in order to estimate more accurately the flux limit for each GRB.

Conversely, only those GRBs that have been triggered by one of the satellites can be considered in the analysis. This excludes the so-called choked GRBs (see Section 2.6) and any normal GRBs that were not in the field of view of a satellite.

Using the shower channel for the analysis can also provide some advantages. First of all, neutrinos of all flavours can be measured, in contrast to the track search, where only muon neutrinos that underwent a CC interaction can be detected. The lack of a directional reconstruction reduces the sensitivity for a single GRB, but on the other hand, in this channel

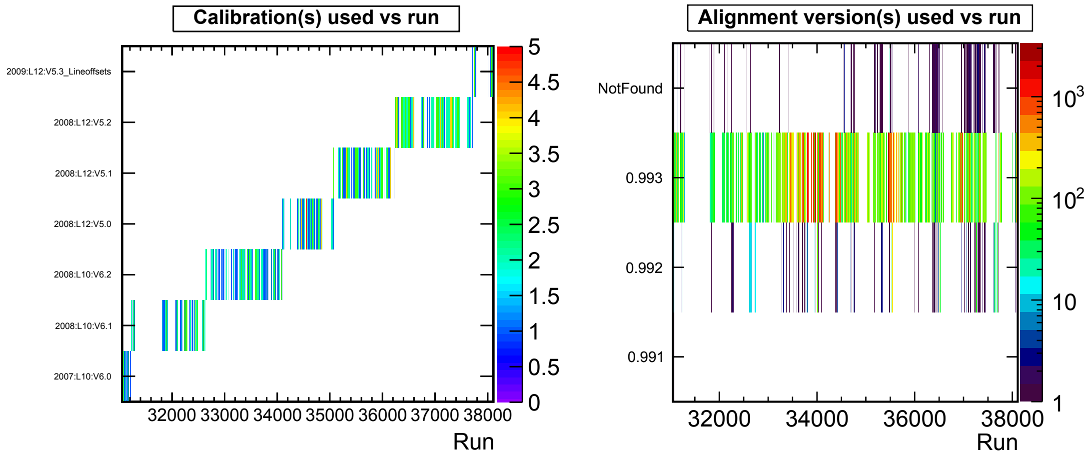

(a) Calibration

(b) Alignment

Figure 7.1: Figure (a) shows the calibration set used for each run in the 2008 data set. Figure (b) shows the alignment version used for each run. During each run the database is accessed several times in order to keep the calibration and alignment information always up to date. The colour scale indicates the number of calibration/alignment sets used for each run.

the detector is sensitive to any given direction. The shower analysis can therefore be seen as a useful complement to the track search.

7.2 Data Selection

In order to obtain an accurate background estimate, the choice was made to use real data as background, without using any Monte Carlo simulation. This method has the advantage that rare event types in data are encountered which may not be simulated properly. Even very rare backgrounds can in this way be identified as the livetime for the background studies is very significantly larger than the signal livetime. Some events that occur in data, such as sparking PMTs, are not included in the Monte Carlo simulation and can be misinterpreted as signal. Data has also been used to study and identify such events.

All physics data runs from the year 2008 have been selected for the analysis. Each run corresponds to about 3 hours of continuous data taking. The live time of the data taking is defined as the time during which the detector is actively recording data. To calculate this live time, the sum of the number of recorded frames multiplied by the duration of each frame (104.858 ms) is performed. Some of the selected physics runs are flagged as “SCAN”, which means that the high voltage conditions for some channels could have been changed from one run to the next. This makes it very difficult to correctly calibrate the detector and therefore these runs were removed from the selection.

Each selected run is then associated with the calibration information that provides the correct position and orientation, as well as the time and charge calibration parameters of each

PMT (see Section 4.5.1). The alignment procedure is performed using a standard calibration package which is continually being refined. In Figure 7.1(b), the version of the alignment program versus the run number is shown. Most of the selected runs are aligned with version 0.993. This version is the latest available and the most correct (93). Data with an unknown alignment or a different version represent only few percent of the total dataset and were not eliminated from the dataset. Figure 7.1(a) shows the calibration version used for each run. Also in this case, the calibration set used is the most correct available at the time of writing (93).

7.2.1 Detector Configuration

The configuration of the Antares detector varied during 2008. At the beginning of the year, 10 lines were installed and taking data. For the period between the 3rd of March 2008 and 25th of May, line 4 suffered problems with its connection to the JB, and data taking continued with 9 active lines. On May 25th, line 11 was connected and data taking began with a new 10-line configuration. On the 30th of May, line 4 was connected together with line 12 in a different JB plug, and the data taking began with the completed 12-line detector. The first run in the 2008 selection is run number 30799, taken on the 18th of December 2007 at 21:05:58. This date precedes the beginning of year 2008, but corresponds to the beginning of 10-line physics data taking. The last run considered is 38215, taken on the 30th of December, 2008 at 18:17:57. From run number 31221 to 34088, the detector had 10 active lines, while from run 34091 to 37716 the detector was in the full 12-line configuration. An overview of the different detector configurations is given in Table 7.1.

From date	To date	Detector Configuration	% of livetime
1st January 2008	3rd March	10-Line	49 %
3rd March	25th May	9-Line	1%
25th May	30th May	10-Line	-
30th May	31st December	12-Line	51 %

Table 7.1: Different detector configurations during the year 2008.

The 2008 data selection contains 1400 runs, corresponding to a livetime of 129.9 days. This data has been used for the background estimation, with the exception of 92 runs containing a GRB alert; of these 92 satellite triggers, 65 correspond to true gamma-ray bursts. Both T3 and 3N triggers (see Section 4.7) were active during the 2008 data taking.

An important condition to be able to correctly estimate the expected background from data is that the detector conditions be consistent during the entire considered live time of the background dataset. If this would not be the case, the chosen background may not represent properly the expected background in the GRB runs. Several quantities are used to quantify the quality of the background conditions of the selected data. The baseline rate is defined as the value of the mean over time of the Gaussian distribution fitted on the measured L0 rate of each photomultiplier (see Section 4.6) and then averaged over all PMTs. The burst fraction is calculated over the entire run and is the average value over all PMTs of the fraction of the

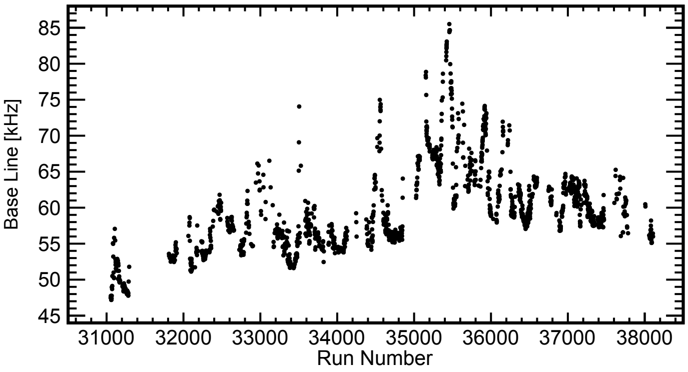

(a) Base line

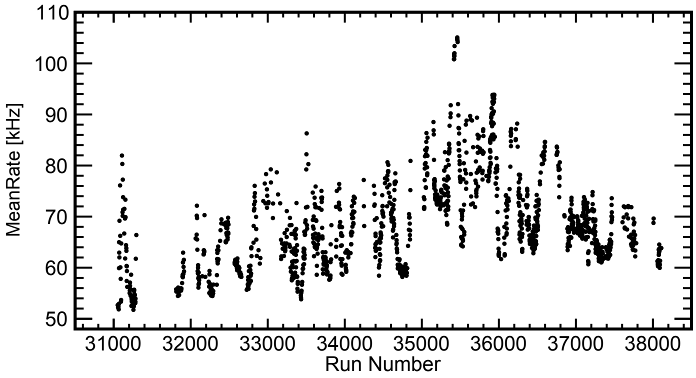

(b) Mean rate

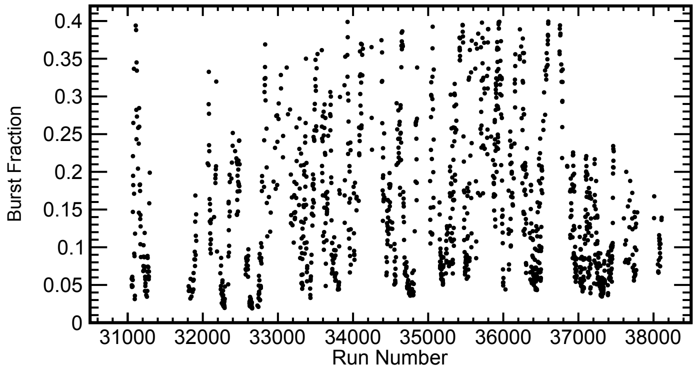

(c) Burst fraction

Figure 7.2: Figure (a) shows the baseline measured for each run in the 2008 selection. Figures (b) and (c) show the mean rate and the burst fraction for the same period. See text for a discussion of these quality parameters.

number of TimeSlices where the rate was higher than the baseline plus 20%. The mean rate is defined as the average rate of all ARSs that measured a rate higher than 10 kHz.

Figure 7.2 shows the distribution of these quality parameters for the selected background runs. The baseline rate is always below 85 kHz, therefore the quality of the selected data is very good.

The mean rate stays below 90 kHz for the majority of the time. The burst fraction varies considerably during the data taking period, and reaches peaks of 0.4, which is a quite high value. It is important to include such runs in the background studies in order to be able to treat these background condition in a GRB run with similar values.

7.2.2 Blinding Strategy

To avoid experimenter biasing in the analysis, a blinding strategy has been followed. The strategy employed applies the standard rules chosen for Antares GRB analyses (102). The GRB triggers are provided by satellites subscribed to the IPN network (103) and are recorded in the Antares database, but not all alerts correspond to a true GRB signal. The information on the true parameters of these alerts, as well as which alerts may be from an actual GRB, is kept hidden while the analysis is developed. That is, while background is studied, cuts are optimized and the detector sensitivity is calculated. Concealing the nature of the alert implies that parameters of the GRB, such as the fluence or the redshift, cannot be used before the data is unblinded. For this reason, an average flux has been used for the optimization of the quality cuts.

From the dataset chosen for the analysis (2008 data), all runs containing a GRB alert registered by the Antares system (therefore both true and false alerts) were eliminated from the background dataset. The remaining runs were used for the optimization of the cuts and for background studies. Thus the background estimates have been obtained exclusively using real data, without any reliance on simulations. During the study of the background and the optimization of the cuts, correlations between shower events on time scales smaller than 120 s were explicitly not explored. This was done to preserve a blinded data set for any future GRBs analyses that might use an un-triggered search method.

7.3 Signal Neutrino Flux Simulation

The software module "NeutrinoFlux" was used to estimate the physical flux, J_{ν}^{model} (see Appendix A.5). The Waxman-Bahcall flux for a single average Gamma-Ray Bursts (40) was used for the shape and normalization of the flux distribution. NeutrinoFlux was used to obtain the diffuse Waxman-Bahcall flux (104), as discussed in Chapter 3. As the work of this thesis is focused on the analysis of individual GRBs, it is necessary to derive the flux of a single, average GRB from this general flux. This procedure relies on a number of assumptions: that the average duration of each GRB is given by T_{90}=50 s and that 667 GRBs are on average detected per year by satellites. The average T_{90} is justified by the measured GRB durations discussed in Section 2.2. The number of GRBs per year is taken from the observations of the CGRO mission (105). It must also be taken into account that a single GRB emits neutrinos from a particular

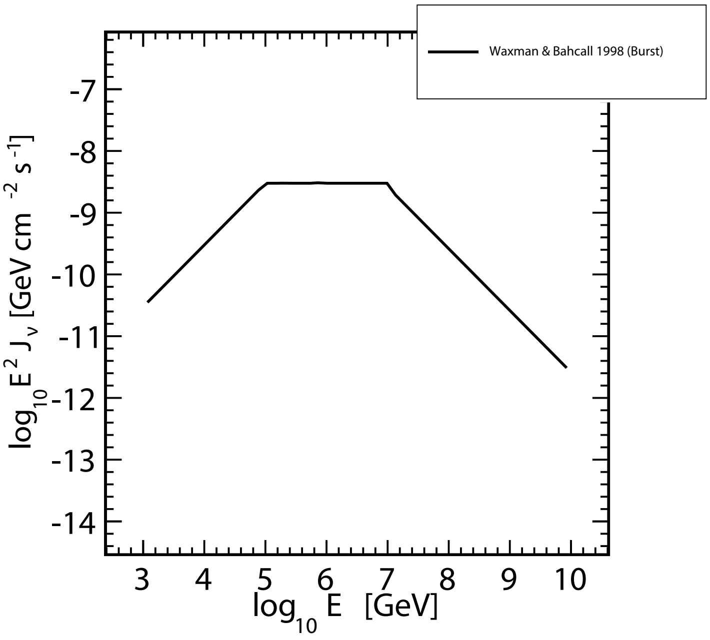

Figure 7.3: Average flux of a single GRB following the Waxman-Bachall spectrum.

direction. The resulting flux of a single, average GRB can be expressed as:

$$J_{WB}^{single} = J_{WB}^{diff} \cdot 4\pi \frac{N_{sec}^{year}}{T_{90}^{avg} 667} \tag{7.1}$$

where the 4π takes into account the solid angle over which the diffuse flux is spread, $N_{sec}^{year} = 31536000$ is the number of seconds in a year, and the denominator represents the average number of GRBs in a year multiplied by their average duration. This is an average flux from any direction in the sky. This is the flux used for the optimization of the quality cuts and is shown in Figure 7.3. A limit on the normalization of this flux for a single GRB can, after the unblinding, be determined using the actual T_{90} of the GRB.

7.3.1 Optical Background and Detector State

To reproduce a realistic optical background and detector status (the fraction of dead channels, which optical modules may be temporarily not functioning, etc.), the signal Monte Carlo uses a list of runs that cover the entire 2008 period (see Section 5.3 for details). However, this list is broader than the background data set, as it includes all basic runs. This could give rise to two possible issues. First, the average detector composition used in the signal Monte Carlo might not be representative of the actual average configuration of the background data set. The second possible concern is about the estimation of the optical background and the number of dead channels in the detector. During the runs used for the 2008 background data set, the detector had a 12-line configuration 54.9% of the time (and 10-line configuration otherwise),

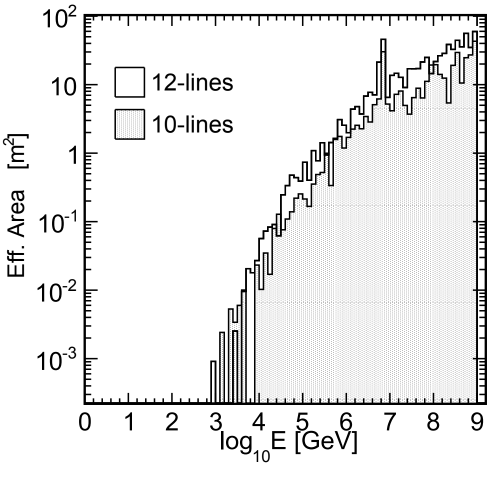

Figure 7.4: Effective area for 2008 dataset after optimized cuts. Different effective areas for different detector configurations: the black empty histogram is relative to the 12-line detector. The filled histogram show the effective area for a 10-line detector.

and in the runs used as background for the signal Monte Carlo, the detector was in a 12-line configuration 55.7% of the time. Thus the average configuration of the detector is well represented in the signal Monte Carlo. When a real GRB is analysed, the correct detector configuration and background conditions will be known, and the expected signal flux can be estimated using the corresponding effective area. The largest effect on the expected neutrino event rate is expected to be the detector configuration. Figure 7.4 shows the effective areas for the 10 and 12-Line configurations averaged over the full data taking period. The optimization of cuts has been performed using the average detector configuration.

To quantify the dependence of the analysis on parameters such as the fraction of dead channels and the optical background, a study has been performed to compare two extreme situations: a perfect 12-line detector with no dead channels and a flat, but large, optical background of 100 kHz, and a realistic 12-line detector with optical backgrounds and dead channels taken from data. This comparison showed that the difference between these two situations influence by less than 2% the expected neutrino rate.

Although the presented search method does not depend on the direction of the incoming neutrino, the detector response does. Figure 7.5, shows the event rate calculated as a function of the zenith angle θ of the incoming neutrino, and that therefore correspond to 180° minus the angle of observation of the GRB. As seen in Figure 7.5, upgoing neutrinos are suppressed relative to downgoing neutrinos. This is due to high energy neutrinos interacting within the Earth before reaching the detector. A partial exception is found with tau neutrinos which, after interacting, create a tau lepton that can immediately decay onto another tau neutrino, causing a regeneration process that increases the probability of tau neutrinos to reach the detector. Because of this dependence on the direction of the GRB, when a specific GRB is observed, the expected neutrino rate is taken relative to that position in the sky.

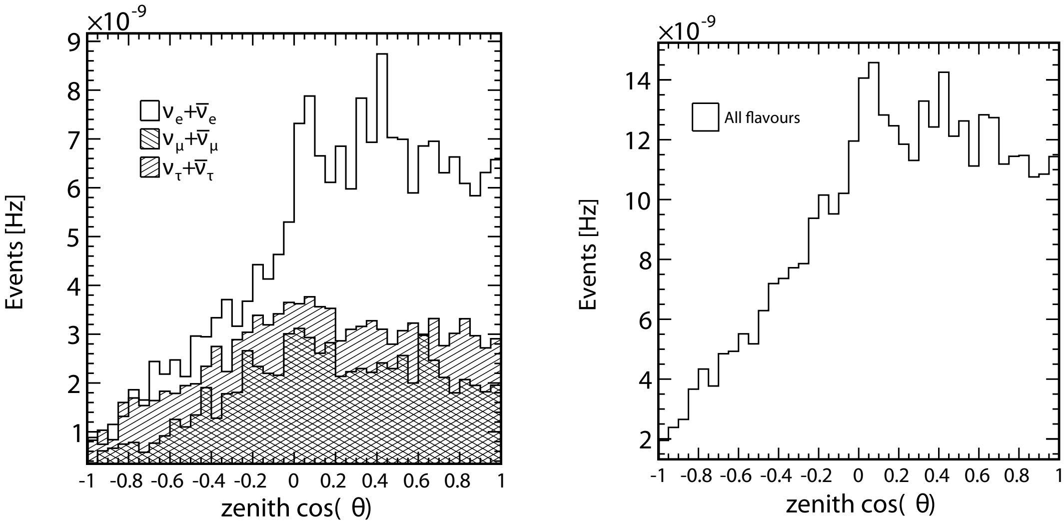

(a) Event Rate for each flavour

(b) Event Rate for all flavours

Figure 7.5: Neutrino event rate as a function of the observed GRB zenith direction. Figure (a) shows the event rates expected for each flavour, while Figure (b) shows the sum of all three flavours.

7.4 Frequentist Confidence Intervals

In order to understand the significance of this analysis and to optimize it for best results, some statistical considerations must be taken into account beforehand.

When a measurement of a random variable is performed, a statistical uncertainty can be assigned to that measurement. The estimator of this variable will have a certain distribution, and its variance is a measure of how widely the measurements (or estimates) of the variable are distributed (100). In the case of a normally distributed variable, the standard deviation, σ, represents, by convention, the statistical uncertainty of the measurement.

In general, the statistical error of a measurement can be determined by defining confidence intervals. The first to develop the concept of confidence intervals was Neyman in 1937 (106). One sigma, σ, represents a Confidence Level (CL) of 68%. This means that in $(100-68)\%$ of similar experiments, a result outside the interval can be measured. One is free to choose the CL with which the measurement interval is made. Traditionally, this choice is represented by the confidence level $1-\alpha$, so that a 1σ CL has $\alpha = 0.32$.

Suppose that one wishes to measure the value of a variable θ. The real value of θ is not known, but it is always possible to define a probability density function, PDF, $f(x;\theta)$ as a function of the estimator of θ, x. A PDF is a function that describes the relative likelihood for a random variable to occur given some conditions (quantified by its independent variables). After measurements are performed, a value x_{obs} is obtained. From the PDF, one can find the values of $x_1(\theta_{true})$, a lower limit, and of $x_2(\theta_{true})$, a upper limit, such that the probability of

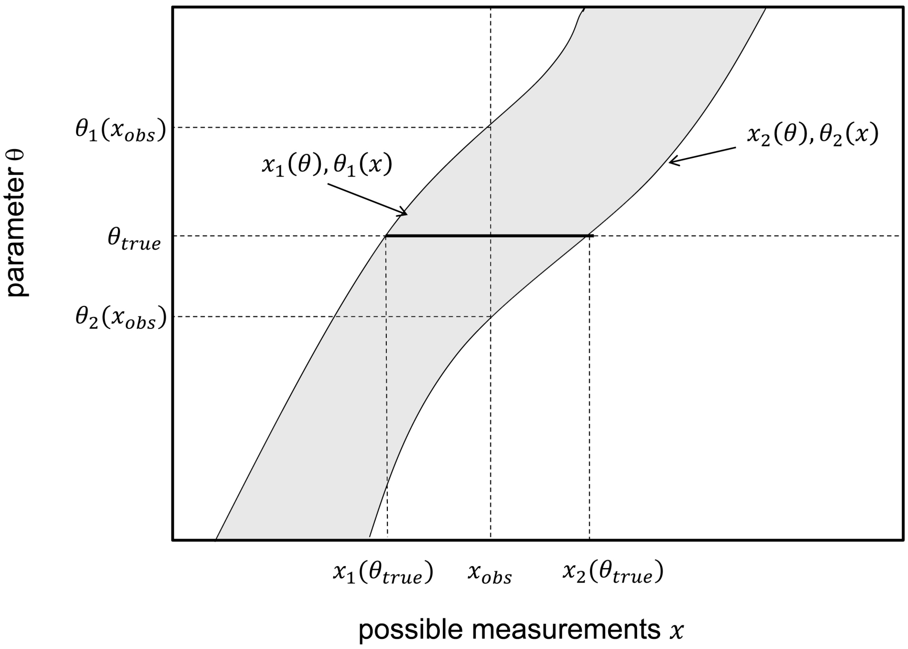

Figure 7.6: Construction of the confidence interval $[u_\alpha, v_\alpha]$, given the observed value $\hat{\theta}_{obs}$ of the estimator $\hat{\theta}$ of the parameter θ with true value θ_{true}

observing $x \geq x_1$ and $x \leq x_2$ is α:

$$P(x_1 \leq x \leq x_2; \theta) = 1 - \alpha = \int_{x_1}^{x_2} f(x; \theta) dx \tag{7.2}$$

Typically the functions $x_1(\theta)$ and $x_2(\theta)$ are monotonic functions of θ. The confidence interval for θ is the set of all values in the line segment $[x_1(\theta, \alpha), x_2(\theta, \alpha)]$ for all values of the unknown parameter θ, shown in Figure 7.6 as the shaded area. When an experiment is performed and a measurement of x gives the observed value x_{obs}, one draws a vertical line that intercepts these upper and lower boundary functions, as shown in Figure 7.6. By definition, with these conditions the chosen interval is said to have a CL of $1 - \alpha$. This implies that the boundaries $[\theta_1(x_{obs}), \theta_2(x_ons)]$ will contain the true value θ_{true} with a probability of $1 - \alpha$. With this approach, the confidence interval $[x_1(\theta, \alpha), x_2(\theta, \alpha)]$ is not uniquely defined by Equation 7.2, but an additional criterion is needed. Often the so called "central intervals" are chosen, so that the probabilities of making a measurement below x_1 or above x_2 are the same, and equal to $\alpha/2$. A problem with this approach arises when the quantity that is measured is very small and close to its physical limit. An example would be counting neutrinos from a signal flux that is lower than the background. In such a situation, the confidence interval may extend beyond the physical boundaries of the system (i.e. counting a negative number of neutrinos). This does not mean that the experiment has a flaw, but that the way the intervals are defined does not cover a physical zone for this specific situation.

To avoid this problem, Feldman and Cousins (107) proposed a different method to define the boundaries of the confidence interval. The idea is to calculate, for each possible value of θ the likelihood of measuring $x(\theta)$. The values of $x(\theta)$ are then ordered with increasing likelihood ratio in relation to the maximum likelihood. Successive values of $x(\theta)$ are added to the interval in order of decreasing likelihood ratio, until the sum of the likelihoods in $1-\alpha$. This approach is repeated for all possible values of θ. If the maximum value is found while θ exists in the physical region, then $x(\theta) = x(\theta_{best})$, the best estimate, otherwise θ_{best} is the limit of the physical region. The PDF for that value is defined as $f(x, \theta_{best})$. The ratio of likelihoods, for each other $x(\theta)$ is then:

$$R(x) = \frac{f(x;\theta)}{f(x;\theta_{best})} \tag{7.3}$$

For a given value of θ, ordered by growing values of $R(x)$, the values of x_1 and x_2 are chosen such that Equation 7.2 is valid.

For this analysis, the upper limit is placed following the Feldman and Cousins approach.

7.5 Discovery Potential and Sensitivity

The best set of cuts is not always the one that minimizes the background. When cutting away background, it is inevitable to cut also part of the signal. To find the right compromise between cutting background away and keeping the signal, different approaches can be taken. In order to optimize the quality cuts one should first decide whether to maximize the discovery potential, that is, to maximize the probability of making a discovery with some chosen significance, or to optimize the cuts in order to place the most restrictive limits on theoretical signal models, in the case that no signal is measured.

The initial considerations are the same for both cases. Assuming that after some cuts, the number of surviving background events is n_{bk} and that they are time distributed with a Poisson probability, one can say that the probability of measuring n events is

$$P(n|n_{bk}) = \sum_{k=n}^{\infty} \frac{n_{bk}^{k} e^{-n_{bk}}}{k!} \tag{7.4}$$

When this probability is smaller than 2.7×10^{-4}, in analogy with the normal distribution, it is said that the probability that the background n_{bk} will fluctuate to n is smaller than 3σ. Analogously, for a 5σ fluctuation, the probability of measuring n events coming only from background must be smaller than 5.7×10^{-7}.

To claim a discovery, one can demand that a critical number of events, n_c, be measured, so that there is only a $5\sigma(5.7 \times 10^{-7})$ probability that the measurement is due only to fluctuation of the background. It is then possible to calculate the number of signal events that the source should emit in order to measure at least $n_{obs} = n_c$ events in the detector, in at least 50% of the experiments:

$$P(n_c|(n_{bk}+n_s)) = \sum_{k=n_c}^{\infty} \frac{(n_{bk}+n_s)^{k} e^{-(n_{bk}+n_s)}}{k!} > 50\% \tag{7.5}$$

Assuming that the expected signal follows a flux of the type $A\phi(E)$, where A is some normalization constant and $\phi(E)$ represents the energy dependence of the modelled flux, it is then possible to put a limit on the maximum value of the normalization constant A, thereby putting a constraint on the upper limit of the neutrino flux. If the goal of the analysis is to verify the validity of a certain flux model, a set of cuts can be tuned to maximize the sensitivity to place the most restrictive upper limit. It is also possible to tune the cuts in order to minimize the number of signal events n_s necessary to make a discovery, as described below. Both procedures, commonly used in neutrino telescopes (108, 109), are described below.

7.5.1 Upper Limit and Sensitivity

The Model Rejection Potential (MRP) technique (108) aims to set the best upper limit for a chosen model, when no discovery is made. One can fix a CL (e.g 5σ) with which to define a confidence interval $\mu_{5\sigma} = (\mu_1, \mu_2)$ that depends on the number of observed events n_{obs} and the number of expected background events μ_{bk} (for this analysis retrieved directly from data): $\mu_{5\sigma}(n_{obs}, \mu_{bk})$. As the minimal number of observed neutrinos is always $\mu_1 = 0$ (one cannot measure a negative number of neutrinos), only the upper limit is interesting, and $\mu_{5\sigma}$ can be taken to imply the one sided CL, $\mu_{5\sigma} = \mu_2$. From this limit on the measured number of neutrinos, one can determine the corresponding upper limit on the source spectrum $\phi(E_\nu)$, scaling the limit on the number of events with the number of expected signal events from this flux, determined by Monte Carlo simulations:

$$\phi_{5\sigma}(E_\nu) = \mu_{5\sigma}(n_{obs}, \mu_{bk})\frac{\phi(E_\nu)}{\mu_s} \tag{7.6}$$

A low value of the ratio $\mu_{5\sigma}(n_{obs}, \mu_{bk})/\mu_s$ leads to a more restrictive limit. The caveat here is that the limit depends on n_{obs}, which is not known until the cuts are performed and the data analysed. In order to proceed with the cut optimization and/or to the calculation of the sensitivity of the analysis before the data has been unblinded and analysed, an average upper limit can be used. This average upper limit (also called sensitivity) is defined as the sum of all possible values of n_{obs}, weighted with their Poissonian probability of being measured:

$$\bar{\mu}_{5\sigma}(\mu_{bk}) = \sum_{n_{obs}=0}^{\infty} \mu_{5\sigma}(n_{obs}, \mu_{bk})\frac{(\mu_{bk})^{n_{obs}}}{(n_{obs})!}e^{-\mu_{bk}}. \tag{7.7}$$

The expected flux limit is then calculated as:

$$\bar{\phi}_{5\sigma}(E_\nu) = \phi(E_\nu)\frac{\bar{\mu}_{5\sigma}}{\mu_s} \tag{7.8}$$

In order to optimize the analysis for best limit, the strongest constraints on the expected signal flux are given when the MRP is minimized:

$$MRP = \frac{\bar{\mu}_{5\sigma}(\mu_{bk})}{\mu_s} \tag{7.9}$$

7.5.2 Discovery Potential

Optimizing for the best limit for a theoretical model does not necessarily mean that the analysis has the best chance of making a discovery. First of all, it is necessary to clarify what a discovery is. With the frequentist statistics, an effect is discovered when the probability of observing of the measured number of events coming only from background, given a certain background rate, is very small. For example, a 5σ discovery may be claimed when the probability of measuring a number of events higher than observed is smaller than 5.7×10^{-7}, in the null hypothesis (i.e. background only).

The optimization of the quality cuts is, in this case, done on a different quantity, the Model Discovery Potential (MDP). Analogous to the average upper limit in the MRP, one determines the value of a signal of strength, μ_s, necessary to measure a sufficient number of events to make a, say, 5σ discovery in 50% of the experiments, as expressed similarly to Equation 7.5:

$$P(n_c|(\mu_{bk} + \mu_s)) = \sum_{k=n_c}^{\infty} \frac{(\mu_{bk} + \mu_s)^k e^{-(\mu_{bk}+\mu_s)}}{k!} > 50\% \tag{7.10}$$

The smallest detectable signal, μ_{sds} ,is defined as the as the minimal value of a signal μ_s such that this inequality is satisfied. The minimum flux that the source must generated to make a discovery in 50% of the observations, is then:

$$\bar{\phi}_{50}(E_\nu) = \bar{\mu}_{sds} \frac{\phi(E_\nu)}{\mu_s} \tag{7.11}$$

The quantity to be minimized in order to optimize the discovery potential of the analysis is the MDP:

$$MDP = \frac{\mu_{sds}(\mu_{bk})}{\mu_s} \tag{7.12}$$

Given both techniques, the choice must be made whether to optimise the analysis for discovery potential or for the best limit. For this analysis, optimization of the discovery potential was chosen, although the method explained in Section 7.5.1 is used to place a limit when the analysis of the signal windows is performed. This choice is motivated by the fact that the sensitivity of the Antares telescope for neutrino induced showers from GRBs is not high enough to reject any of the most common GRB flux models (see Chapter 8).

7.6 Quality Cuts Optimization

The cuts have been optimized using an expected number of signal events, μ_s, calculated using Monte Carlo simulations. The background estimates, μ_{bk}, have been calculated using the full background data set described in Section 7.2. Upon unblinding the signal data, a signal intensity or a flux limit can be calculated using the real measured value n_{obs}.

7.6.1 Search Time Window Optimization

The correlation between a neutrino event and a triggered gamma-ray burst is sought by searching for neutrino induced events happening in a time window around the GRB. The natural time

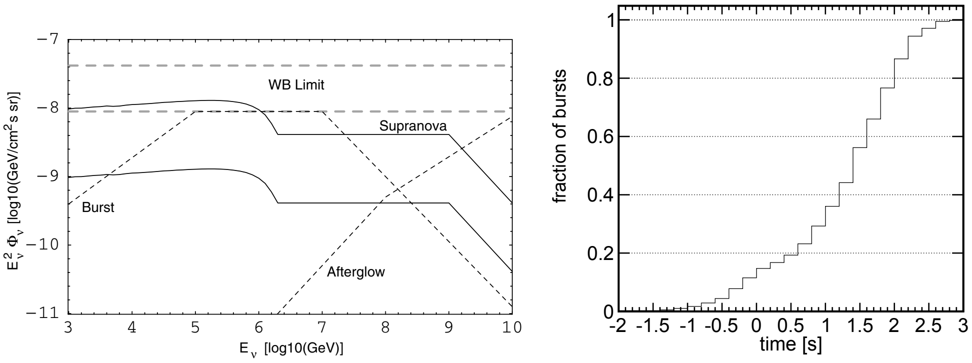

(a) GRB neutrino fluxes

(b) GRB duration cumulative distribution

Figure 7.7: Figure (a) shows the diffuse neutrino flux from postsupernova (supranova) models of GRBs (solid curves), assuming either that all GRBs have an SNR shell (top curve), or that 10% of all GRBs have an SNR shell (bottom), and that 10% of the fireball protons reach the shells. Long dashed lines correspond to the Waxman-Bahcall cosmic-ray limit; short dashed curves are the average diffuse neutrino flux from GRB internal shocks and afterglows. Figure taken from (110). Figure (b) shows the cumulative distribution of 2008/2009 Gamma-Ray Bursts in terms of T90. The time is expressed in seconds and is shown on logarithmic scale. The majority of the observed GRBs are longer than 2 seconds, and a time window of 100 seconds will include most of the GRBs.

window to use for the detection is the T_{90} of the observed GRB. For the optimization of the cuts, it is not reasonable to choose a different time window for each GRB. Furthermore, the blinding strategy applied (Section 7.2.2) does not allow the use of the specific parameters of the GRB for the development of the analysis. The cut optimization is therefore done using a unique time window, determined from statistical considerations. On the one hand, a small time window is preferable, as it reduces the background, while on the other hand, the window must be large enough to contain (most of) the signal produced by a GRB.

Three main periods of neutrino emissions can be selected around a GRB. Before the actual GRB explosion, neutrinos can be produced by the initial precursor supernova. These neutrinos are thought have a maximum flux at low energies (from few GeV to few TeV) and are called precursor neutrinos. They are expected to arrive from a few days to a few minutes before the gamma-rays from the burst. Neutrinos produced in coincidence with the GRB explosion are defined as prompt neutrinos. The last period of a GRB is the afterglow, which continues up to a few hours or even weeks after the prompt emission. A description of different phases of neutrino emission during a gamma-ray burst can be found in (110), from which figure 7.7(a) is taken.

In order to take advantage of the GRB trigger given by the GCN it has been decided to search only for neutrinos from the prompt emission (burst spectrum in figure 7.7(a)). Gamma ray bursts can be divided into two types: so called short GRBs (with a duration shorter than 2 seconds) and long GRBs, that last longer than 2 seconds. From Figure 7.7(b), it is also

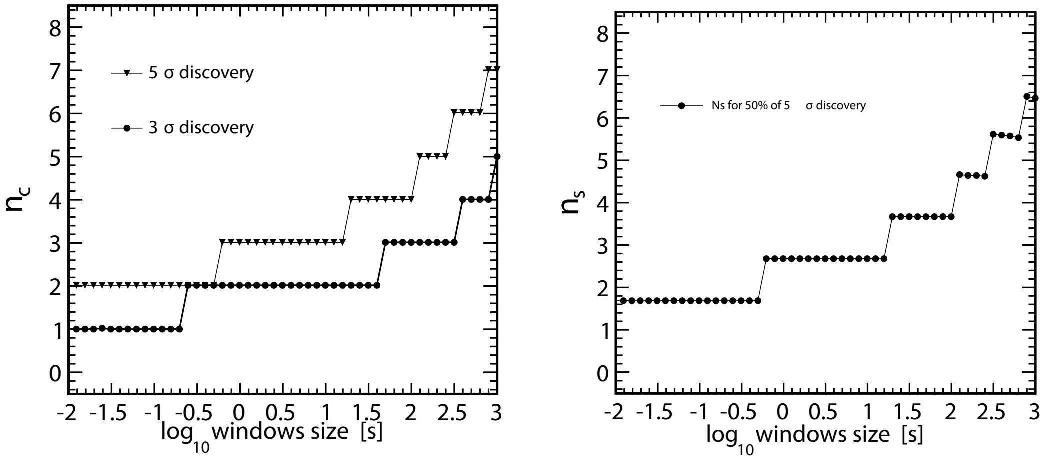

(a) Number of critical events

(b) Number of needed events

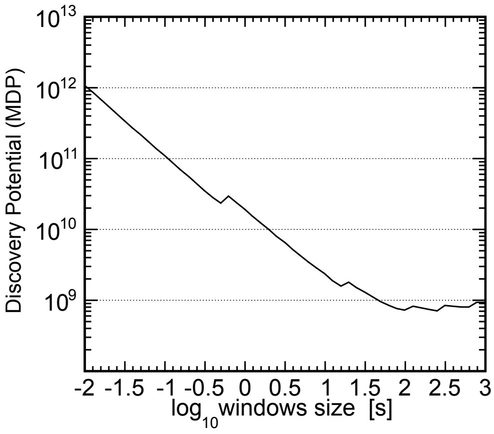

(c) Discovery potential

Figure 7.8: Number of critical measured events N_c given a background rate $N_{bk} = 2.3 \times 10^{-4}$ Hz (Figure (a)) and corresponding number of events needed to make a discovery in 50% of the observations (Figure (b)). In Fig. 7.8(c) the discovery potential is shown as a function of the search window size.

clear that the long gamma-ray bursts are more common than short GRBs. The duration of a GRB, its T_{90}, does not necessarily correspond to the period in which 90% of the neutrinos are emitted. For the sake of this discussion, it is nevertheless assumed that neutrinos are produced together with photons during the internal shocks of the GRB. This assumption is valid as long as photons are generated by synchrotron emission of accelerated electrons and that an hadronic component is present in the flow, together with the electrons. The following optimization of the discovery potential has been performed on 2008 data.

Although GRB data remained blinded, it is known that, within the selected runs, 65 real GRB took place. This number has been used to calculate the "p-value" (the probability previously compared to the number of σ of the normal distribution) for the optimization: that is, the probability that a fluctuation of the background would result in some number of observed events after 65 trials. The number of events required to be above the background at a level of 3σ or 5σ (for 65 GRBs) is shown in Figure 7.8(a).

For this optimization, the background rate has been calculated with a set of quality cuts, not yet optimized, but close to the expected values. After the optimization of the quality cuts (see Section 7.6) the result of the time window optimization has been checked and resulted compatible with the previous value. The background rate used for the optimization of the window is 2.3×10^{-4} Hz.

The discovery potential can be calculated as the ratio between the required number of signal events n_s and the signal rate surviving the cuts integrated over the chosen time window. The optimal time window is that which minimizes this quantity, as shown in figure 7.8(c). This last figure takes into account the fact that increasing the time windows does not mean that the signal will last longer. It takes into account the probability of having a GRB of a certain duration contained in the selected time window, using the dataset shown in figure 7.7(b). This plot shows that a time window of 100 seconds (10^2 s) will minimize the flux required for a discovery. It is also longer than the T_{90} of 70% of all GRBs. Therefore, for an observation of 65 GRBs, the optimal window size with which to perform cut optimization has been set at 100 seconds.

7.6.2 Choice of the Cut Parameters

The procedure of optimising the cuts can be approached in several ways. This analysis could involve many parameters, such as the position of the reconstructed shower, the reconstruction quality parameter M-estimator, the duration of the event, the number of hits, the charge of the hits, and many more. The parameters upon which cuts have been made have been chosen to be those that most effectively reduce the number of background events while preserving the number of signal events. One way of choosing the correct cut for each of these parameters would be to use a neural network algorithm, such as TMVA (111) that, by means of a selection of tools, determines the best cuts for set of parameters. The disadvantage of this approach is that requires a deep understanding of the algorithms used, often not trivial. It is preferable, when possible, to find a set of parameters that allows for a simple, straight forward optimization. Three such parameters have been found for this analysis: the fit quality parameter, $Mest$, (the M-estimator of the reconstruction), the number of direct hits from the shower, $DirHits$, and the number of lines used in the reconstruction of the shower, $Lines$.

The choice of these parameters has been motivated by physical considerations. It is important to have a well-reconstructed shower, to obtain accurate the reconstruction parameters, therefore the quality parameter $Mest$ is very significant. The direct shower hits, $DirHits$, are the set of all the selected hits (see Section 6.2) that have a time residual smaller than 15 ns. That is, direct hits do not arrive later or earlier than 15 ns with respect to the expected time of the hit, calculated using the reconstructed position of the shower. This parameter is important as it gives information on how good the shower hypothesis is for that event. Track signals induced by muons does not follow the shower hypothesis and therefore they do not produce many direct hits. The last parameter used, *Lines*, is the number of detector lines upon which hits were selected for use in the reconstruction, and gives information on how energetic the shower is. As this analysis does not use any energy reconstruction, it is important to have a parameter that can be used to cut away low energy events.

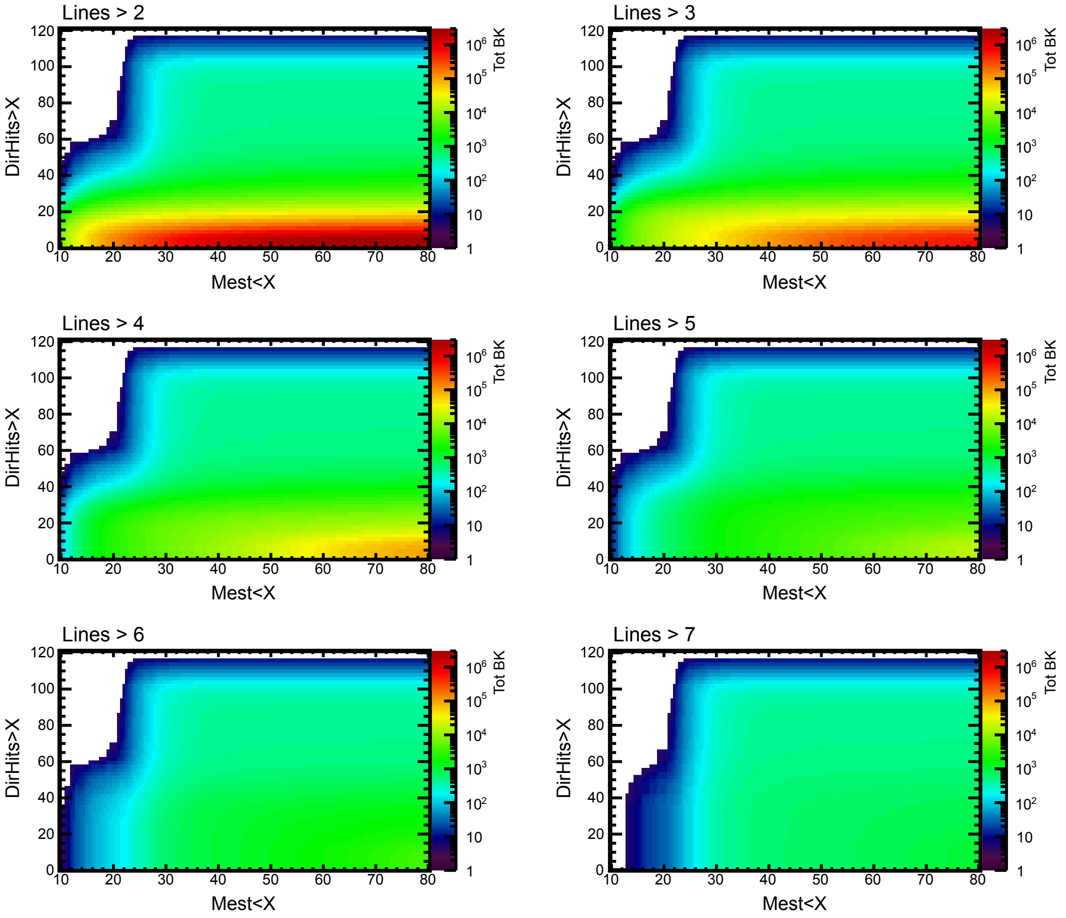

Figure 7.9: Total number of surviving background events in the entire data-taking period (1.12×10^7 s). Each plot corresponds to a cut on the number lines used in reconstruction. The x-axis shows the cut on the M-estimator, accepting only events with a value lower than the selected value. The y axis is the cut value on the number of direct hits. Each point in the space represents the surviving background after the three cuts are applied.

The choice of these three parameters gives an additional advantage. As the number of used lines is a discrete number which can assume only a few values (at most, from 1 to 12), it is possible to divide up the three-parameter space into bins of the number of lines hit. This simplification makes it possible to visualize the entire parameter space as a set of 2-dimensional $MestvsDirHits$ plots.

Other parameters had been considered during the development of the analysis. First of all, the charge of the hits. Both the total charge of all the hits taking part in an event and the average charge of each hit in an event had been considered. The use of these parameters did not increase the capability of distinguish signal from background. The reason for this is that the hit selection used for the reconstruction (Section 6.2) already takes into account the charge of the hits. Therefore this parameter is already included in the analysis at a different stage. Other event parameters such as the duration of the event or the total number of hits had also been studied. They have been excluded from the minimization process as they correlated strongly with the selected parameters (i.e. the number of direct hits), and therefore did not provide additional information.

Further selection criteria had been studied, including the application of a track reconstruction on each event (97), together with a veto of the event in the case of a track-like topology. This method also showed no improvement on the minimization of the discovery potential. The reason for this is that the strict constraints on the shower model already exclude track-like events. Cutting on the number of direct hits that are consistent with a shower hypothesis and including only events that are well reconstructed according to the M-estimator fit is sufficient to cut away the vast majority of background events.

7.6.3 Quality Cuts Optimization

The optimization of the quality cuts is made in order to maximize the discovery potential of the analysis. It has been performed using 1400 runs (129.9 days of live time) taken during the year 2008, to obtain background rates. Figure 7.9 shows the total number of surviving background events from the entire considered live time as a function of the cuts on $Mest$ and $DirHits$, for different values of the $Lines$ parameter. In order obtain an accurate estimate of the background rate, used for calculating the Discovery Potential (DP), regions of the cut-parameter-space having fewer than 3 surviving background events have been excluded. Thus, the white areas in Figure 7.9 have not been used in the cut optimization procedure. For each combination of the cuts, the discovery potential was calculated using Equation 7.12. The result is shown in Figure 7.10. The white area is the part that has been excluded due to low statistics and, although the loop over the parameter space has been made for $Lines$ up to 12, only the cut until 7 has been shown for clarity. The optimal value of the cuts is the set for which the MDP reaches its minimum value.

Scanning the parameter space in Figure 7.10 leads to the conclusion that the best set of cuts is:

- $Lines > 2$
- $DirHits > 35$
- $Mest < 62.$

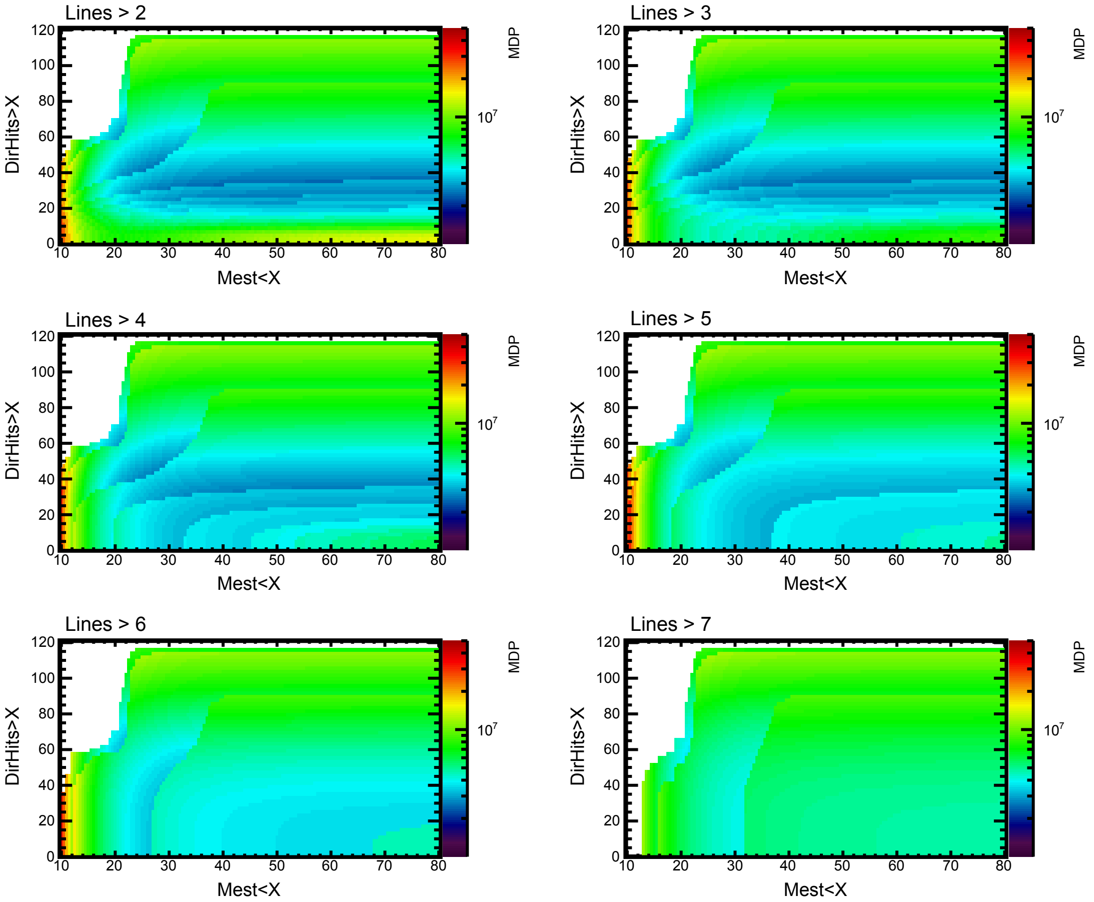

Figure 7.10: MDP as a function of the cuts on the number of direct hits (*DirHits*), the M-estimator (*Mest*) and the number of lines (*Lines*). The white zones have been excluded due to low statistics.

These values lead to a 5σ discovery if 4 events are measured within a time window of 100 s, or a 3σ discovery when 3 events are measured.

These values can be checked with plots that freeze all but one parameter to their optimal values. Figure 7.11 shows the MDP as a function of the cut on one parameter, fixing the other two to their optimal values. For each plot, multiple histograms represent different cuts on the number of lines. The vertical line indicates the value for which the MDP reaches its optimal value. Although these cuts are not optimized for separating signal from background, but for maximize the discovery potential, the efficiency of separating signal from background is shown in Figure 7.12, where the cumulative distributions of signal and background rates are shown as a function of each cut, freezing the other two to their optimal value. The cut that is most effective in reducing the background is the cut on the number of direct hits.

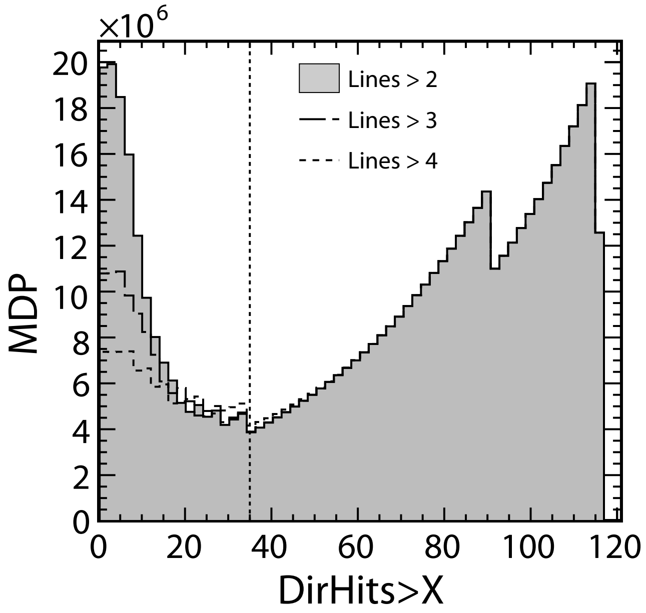

(a) MDP vs DirHits cut

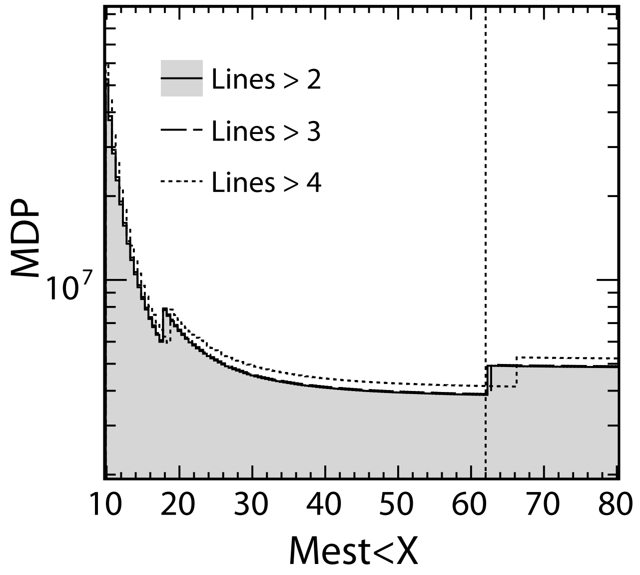

(b) MDP vs mest cut

Figure 7.11: Figure (a) shows the MDP as a function of the cut on the number of direct hits, with the value of the *Mest* cut fixed at 62. Figure (b) shows the cut on the M-estimator, with the cut on the *DirHits* fixed at 35. The vertical line shows the selected optimal cut. The shaded histogram shows to the optimal line cut.

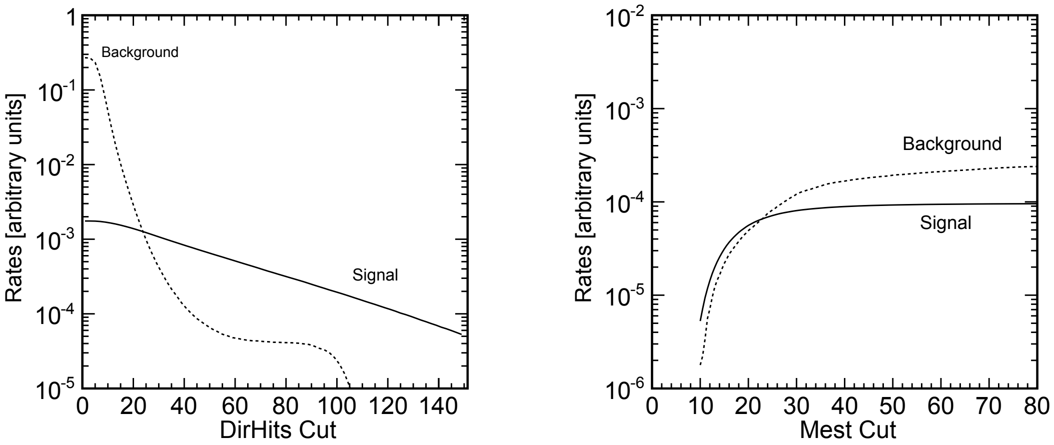

(a) DirHits cut

(b) Mest cut

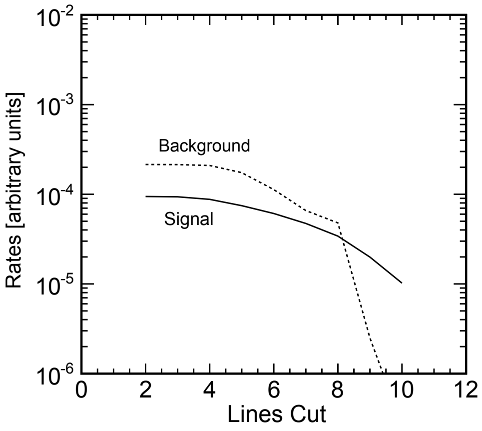

(c) Lines cut

Figure 7.12: Cumulative distributions of signal and background rates as a function of the cut. The signal rate distribution has been normalized to be comparable with the background distribution. Figure (a) shows the distributions as a function of the *DirHits* cut, with the *Mest* cut fixed at 62 and *Lines* at 2. Figure (b) shows the cut on the M-estimator, with the cut on the *DirHits* fixed at 35 and *Lines* at 2. Figure (c) shows the distributions as a function of the cut on the number of lines.

7.7 Sparking Optical Modules

As discussed in Section 6.5, on rare occasions a PMT in the Antares detector sparks, emitting light in a manner that is very similar to an hadronic or electromagnetic shower. These events are rare (less than 10^{-5} Hz) but must be studied for this specific analysis as they could easily be misinterpreted as a signal.

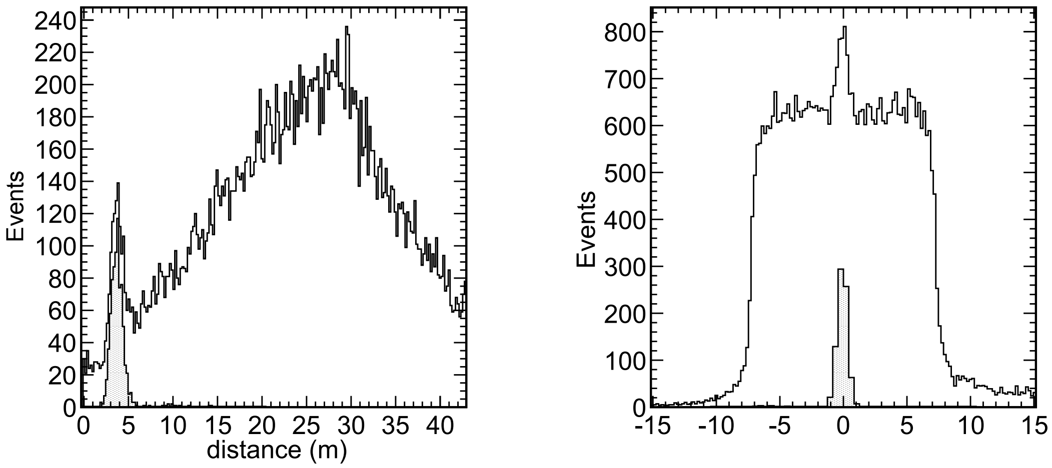

(a) 2D distance

(b) Z distance

Figure 7.13: Distributions of the distance between the reconstructed shower and the OM that happens to be closest to it. Figure (a) shows the distance, ρ, in the X-Y plane, and Figure (c) shows the distance along the Z axis. The shaded areas refer to events that produced more than 100 selected hits.

Some Antares data runs are known containing sparking events because many events with more than 100 hits repeats in a very short time (few minutes). Until now, this repetition of big events was the only method to identify sparking events. This criteria cannot be applied for this analysis, because even if a PMT would produce a single spark, this could be misinterpreted as a neutrino induced shower. To develop an identification method which does not rely on the repetition of many events, a set of four runs equivalent to a total livetime of 12.13 hours, and known to contain sparking PMTs, has been used.

It is reasonable to assume that a shower caused by a sparking PMT will be reconstructed very close to the OM which caused it. To check this assumption, Figure 7.13 shows the distribution of the distance between the reconstructed shower and the closest OM. The shaded histogram shows the same quantity but for events that produced more than 100 hits selected in the reconstruction. As the distinction of sparking events is better on the Z axis than in the XY axes, two distances are shown: the distance along the Z axis (Figure 7.13(b)) and the two dimensional X-Y distance ρ (Figure 7.13(a)). As shown in these Figures, all events suspected

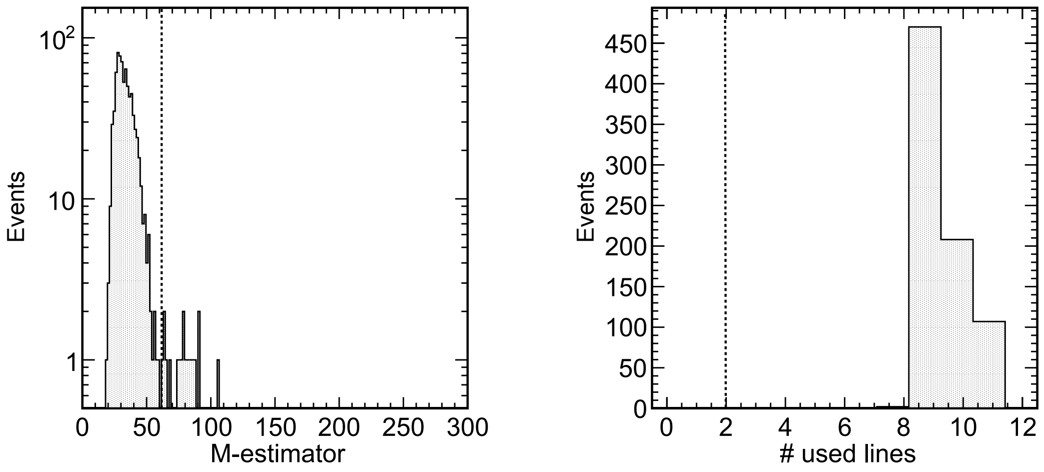

(a) M-est distribution

(b) Used Lines distribution

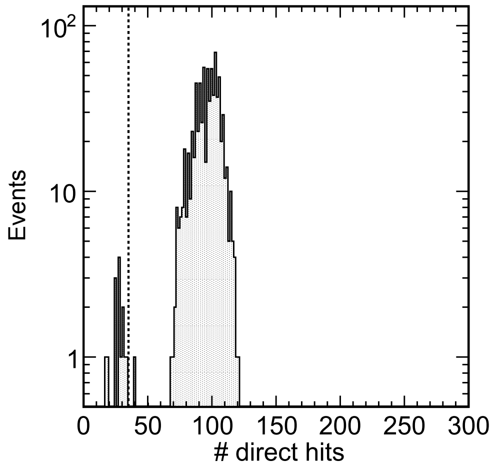

(c) Direct Hits distribution

Figure 7.14: DNumber of events during four sparking runs of the quality parameters for events caused by sparking PMTs. Figure (a) shows the M-est distribution, Figure (b) shows the number of lines used for the reconstruction and (c) shows the number of direct hits. It is easy to see that nearly all the "sparking events" pass the optimized quality cuts.

to be sparking because of their high number of hits, lay very close to a OM. In Figure 7.14 it is shown that nearly all the events considered to be from a sparking PMT would pass the optimized quality cuts of this analysis. For this reason, it is necessary to introduce a further selection criterion that identify and exclude these events. From the plots in Figure 7.13, a set of cuts was chosen that cuts away 99% of the events caused by sparking PMTs, leaving only signal, and that adds to the previous quality cuts:

- $Lines > 2$
- $DirHits > 35$
- $Mest < 62$
- $\rho > 6\,\mathrm{m}$
- $|z| > 1\,\mathrm{m}$

Around 17% of the background events that survived the quality cuts in Section 7.6 are recognised as sparking events and therefore excluded after these cuts were applied. The background rate is therefore reduced from 2.148×10^{-4} Hz to 1.782×10^{-4} Hz. Only less than a percent of the signal events pass this selection. The effect of this additional cut on the discovery potential is less than 0.1%.

7.8 Performance and Systematic Studies

Although the Antares detector performance is well understood through calibration processes, and the dataset for the analysis has been selected in order to maintain control over the detector status, it is necessary to understand how uncertainties in the analysis can affect the results. As shown in Section 7.7, the reconstruction algorithm implemented for this work can be used to identify sparking PMTs and, therefore, it is possible to understand and remove their effect on the analysis. Two more effects have an impact on the analysis: an inaccuracy of the measured time of each hit, and an unaccounted for inefficiency in some PMTs. The impact of these uncertainties on the analysis can be quantified as a systematic error, derived using Monte Carlo simulations.

7.8.1 Hit Time Smearing

In order to account for an uncertainty in the knowledge of the exact time of each hit, a systematic study has been performed by smearing the time of each hit according to a Gaussian distribution with a standard deviation of 2 ns. This procedure can be understood looking at Figure 7.15, where the time difference between the measured hit time and the smeared hit time is shown. This distribution is a Gaussian centred at zero and with a sigma of 2 ns, as expected.

To understand the effect of this smearing on the final result of the analysis, the signal event rate for the average 2008 detector configuration has been computed and compared to the event rate obtained without smearing. The two rates are shown in Figure 7.16. With this new event rate, it is possible to calculate the corresponding Model Discovery Potential. This number differs from the one calculated without smearing by only 0.3%. The uncertainty on the hit time is therefore not important for this analysis (see Table 7.2).

While the effect of an inaccuracy of 2 ns is negligible for this analysis, higher values of time smearing have not been explored, as other studies (93) have shown that an inaccuracy on the

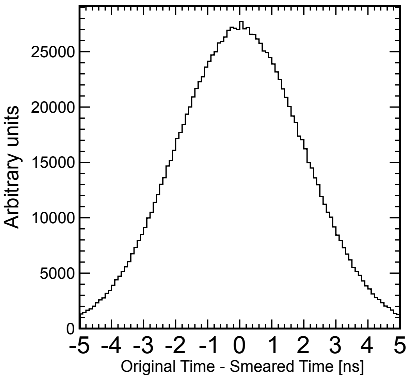

Figure 7.15: Time difference between the measured hit and the smeared hit times.

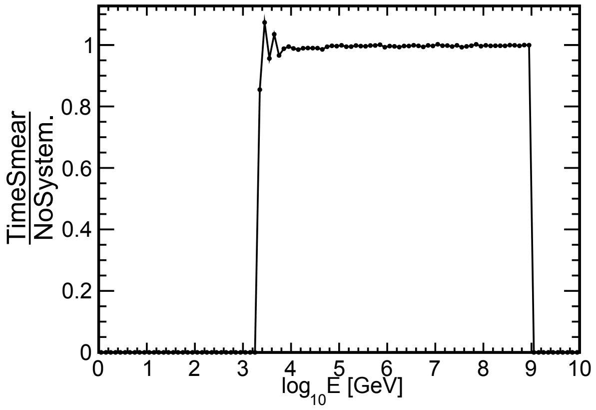

Figure 7.16: Ratio between the event rate without any systematics and with hit time smearing, as a function of the neutrino energy. From this plot, it is already easy to see that a hit time inaccuracy of 2 ns is not important for the final result of the analysis.

hit times of 3 ns can be excluded at 2σ CL by comparing the atmospheric neutrino Monte Carlo to data. To perform this study, a muon track reconstruction based on the PDF of the time residuals was employed. The fit quality parameter, with this method, is very sensitive to the timing precision. Comparing the fit quality parameter of atmospheric muons from Monte Carlo and data constraints the precision with which the time of the hit is known.

7.8.2 Reduced OM Efficiency

An additional effect that has been taken into account is the possibility that the actual efficiency of the OMs is lower than that obtained from calibration. Studies have been performed (93), showing that the actual efficiency cannot be much lower than 85% of the expected efficiency. For this reason, a systematic study was performed by reducing the efficiency of all PMT by 15%. To this end, 15% of the L0 hits have been randomly eliminated, before triggering but after the optical background simulation. The remaining hits were then passed through the trigger, as

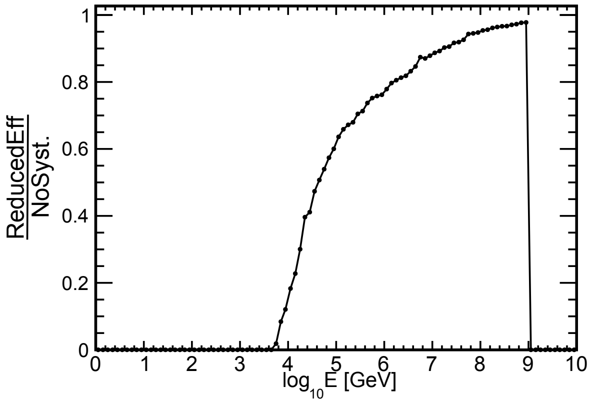

Figure 7.17: Ratio between event rates calculated with and without reducing the efficiency of each PMT as a function of the neutrino energy. From this plot it is clear that an unknown inefficiency in a large number of OM's will strongly reduce the rate of low energy neutrino observed

described in Section 5.3. The hit selection, reconstruction and finally the quality cut selection were then applied. The resulting event rate was used to calculate the Discovery Potential that can be reached after reducing the efficiency. The effect is quite important, especially at lower energies. As shown in Figure 7.17, the event rate below 10^5 GeV is reduced considerably. This is easy to explain considering that a neutrino with a lower energy produces less light and, therefore, fewer hits. If a fraction of these hits is thrown away, it is less likely for that event to pass all selections. On the other hand, at higher energies, neutrinos generate enough light such that throwing away a fraction of the hits has little effect on the final event selection.

7.8.3 Monte Carlo Uncertainties

The analysis presented in this thesis is the first, in the Antares collaboration to use the Monte Carlo chain of SeaTray (see Chapter 5). To explore the degree to which the analysis depends on the details of the simulation, the comparison described in Section 5.4 was done. It is very difficult to make a reliable comparison between simulation and data regarding electromagnetic or hadronic showers in Antares. The standard Antares chain, though, has been proved to be in good agreement with data on muon tracks (93).

Using the SeaTray chain with older tables for the PMT parameters (see Appendix A.3) causes the expected signal to be around 50% smaller in comparison to the expected signal calculated with the Antares chain (see Figure 7.18). The reason is that the angular acceptance of the PMTs is smaller in this version of the SeaTray Monte Carlo, therefore less photons manage to produce a hit. The difference at higher energies is due to differences in the muon tracking and light production of the two chains, and further studies are needed to completely understand this effect.

To account for this discrepancy, the ratio between the rates calculated with the two simulation chains was used to calculate the effect on the discovery potential. The ratio between the Antares chain spectrum and the SeaTray spectrum is used to scale the entire neutrino induced

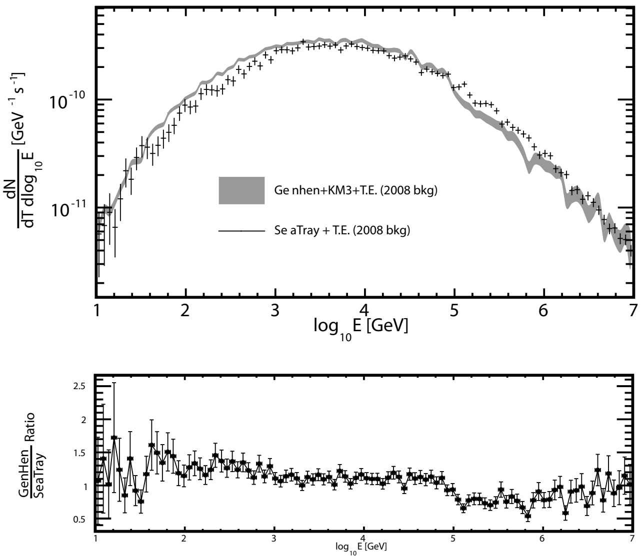

Figure 7.18: Upward-going muon neutrino rates simulated with Genhen (dashed) and NuG (solid line), assuming a diffuse $10^{-8}(E/\,\mathrm{GeV})^{-2}\,\mathrm{GeV}^{-1}\,\mathrm{cm}^{-2}\,\mathrm{s}^{-1}\,\mathrm{sr}^{-1}$ spectrum, for energies between 10 and 10^7 GeV. The relation of the ratio between the two spectra is $Ratio = -0.08 * E + 1.22$. All events in which the muon vertex is closer than 200 m to the detector center have been plotted.

shower event rate, and the resulting discovery potential is used to add a systematic uncertainty to the final value. As shown in Table 7.2, an underestimate of the sensitivity of about of 7% is caused by this discrepancy.

7.8.4 Systematics Summary

Four systematic effects have been considered for this analysis: an inaccuracy of the hit times, an unknown reduction of the OM efficiency, the dependence upon the choice of the Monte Carlo chain and the dependence upon the optical background (Section 7.3.1). The hit time smearing has an effect of a fraction of a percent (see Table 7.2). The reduction of the OM efficiency is known to be an overestimate, but as an upper limit implies its effect on the measured limits should be less than 28%. It represents the biggest uncertainty in this analysis. The choice of the Monte Carlo simulation can change the sensitivity by around 7%. However, this effect acts in the opposite direction, as the SeaTray chain underestimates the expected signal compared to the Antares chain. As these two effects act in different directions, they have not been summed together, but are considered separately in the two directions.

Quality Cuts and Systematic Effects			
Type	Amount	MDP	Effect
Only Quality Cuts	$Mest < 62$, $DirHits > 35$, $Lines > 2$	-	-
Sparking Cuts	$\rho > 6\,\mathrm{m}$, $\lvert z \rvert > 1\,\mathrm{m}$	-	-
Hit time smearing	2 ns	3.878×10^6	0.3%
Reduced OM efficiency	85%	5.34×10^6	28%
Monte Carlo	Seatray VS Antares chain	3.592×10^6	-7.1 %
Optical background	Realistic VS 100 kHz	3.948×10^6	<2%

Table 7.2: Summary of the effects of the uncertainties on the discovery potential reached by the neutrino induced shower analysis.

8

Results

Spins and turns, angles and curves. The shape of dreams, half remembered. Slip the surly bonds of earth and touch the face of perfection - a perfect face, perfect lace. Find the perfect world for the end of Kara Thrace. End of line.

Samuel T. Anders

8.1 Antares Sensitivity for Neutrino-Induced Showers from Gamma-Ray Bursts

With the analysis presented in this thesis, the Antares experiment is sensitive to electromagnetic and hadronic showers induced in the detector by the interaction of neutrinos generated from Gamma-Ray Bursts.

For the development of this analysis, the Fireball model for the description of the physics of GRBs was used. Following this model, neutrinos are produced during the GRB explosion via photopion production from collisions of ultra-relativistic protons with photons in the jet of the GRB. Although the production mechanism favours the muon neutrino, due to neutrino oscillation, it can safely be assumed that the flavour ratio at Earth is $\nu_e : \nu_\mu : \nu_\tau = 1 : 1 : 1$ (see Section 3.4).

Whereas the standard track search is sensitive only to muon neutrinos interacting via charged current interaction with nuclei in or around the detector, a shower analysis is sensitive to all flavours. In order to deal with the high background introduced by atmospheric muons, a track search is generally limited to upgoing neutrinos, i.e. neutrinos that traversed the Earth and interacted near the detector. This limits the field of view of the experiment and also the energy range. The Earth becomes opaque for muon (and electron) neutrinos at energies of the order of a PeV and above, as the neutrino cross section becomes high enough that the mean free path of a neutrino is shorter than the diameter of the Earth. Tau neutrinos are able to cross the Earth at these energies, however, thanks to the regeneration process, by which the immediate decay of the tau lepton produces another tau neutrino.

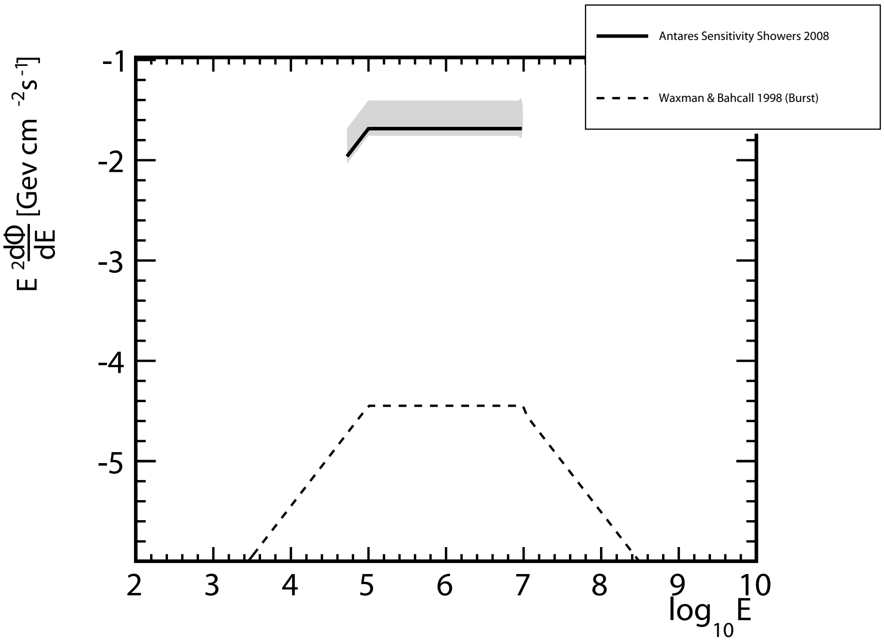

Figure 8.1: Sensitivity of the Antares detector for neutrino induced showers from GRBs. The dashed line shows the flux model used to calculate the expected neutrino rates from GRBs and is taken from (40). The black thick line shows the Antares sensitivity for neutrino-induced showers for the observation of 65 GRBs during the year 2008. The shaded area represents the systematic uncertainties described in Section 7.8.

This shower analysis takes advantage of the time coincidence with a satellite-triggered GRB in order to reduce the background and since showers have a different signal topology in the Antares detector with respect to the main down-going background, the atmospheric muons, it is not necessary to use the Earth as a filter as in the case of tracks, and no directional cut is applied.

To estimate the discovery potential and the sensitivity of the detector, a Waxman-Bahcall flux, averaged for a single GRB, was assumed, as explained in Section 7.3. The analysis consists of the search for coincidences between well reconstructed showers in Antares and photons triggered in one of the satellites which subscribes to the IPN (Interplanetary Gamma-Ray Burst Timing Network) (103).

Following the procedure described in Section 7.6, a set of quality cuts was applied in order to optimize the analysis for the best discovery potential. These cuts and systematic uncertainties are summarized in Table 7.2. This method is then applied to each observed GRB. Before the unblinding of the GRBs, the sensitivity of Antares can be calculated using the method explained in Section 7.5. The average upper limit of Antares (or the sensitivity) for a neutrino-induced shower in coincidence with GRB trigger is shown in Figure 8.1. The dashed black line shows the model used for the estimate of the neutrino rates (40). The thick black line is the average upper limit on the neutrino flux for 2008 data, calculated using the Feldman-Cousins method

(107). The sensitivity of Antares for showers in coincidence with a GRB is:

$$E_\nu^2 \frac{d\Phi}{dE_\nu} \leq 1.67 \times 10^{-2}\,\mathrm{GeV\,cm^{-2}\,s^{-1}} \text{ for } 10^5 < E_\nu < 10^7. \tag{8.1}$$

This is the sensitivity corresponding to the 2008 data set, during which the detector had 10-lines for around 50% of the time, and 12-lines for the other 50% of the time, and during which the average background rate was 1.782×10^{-4} Hz.

In this thesis, a search on each GRB was performed separately. As the sensitivity is far poorer than the expected mean flux, it is appropriate to search for a single extremely powerful GRB, rather than stacking multiple GRBs that all produce a signal flux below the expected sensitivity. Therefore, comparing this analysis with other experiments requires some assumptions on the average number of GRBs observed per year and the average duration of each GRB. The Amanda experiment published a limit for the Waxman-Bahcall diffuse flux for the triggered search (112) of :

$$E_\nu^2 \frac{d\Phi}{dE_\nu} \leq 1.5 \times 10^{-6}\,\mathrm{GeV\,cm^{-2}\,s^{-1}\,sr^{-1}} \text{ for } 10^5 < E_\nu < 10^7.$$

To compare this result with the one presented in this thesis, it is necessary to translate the Antares sensitivity into a comparable sensitivity for a stacking analysis. This consists of correcting for the total solid angle, 4π, and then averaging for the duration of a single GRB, assuming some number of detectable GRBs per year. As in Section 7.3, an average T_{90} of 50 s and 667 expected GRBs per year is assumed. The flux limit obtained in this thesis is then divided by a factor $4\pi \frac{N_{sec}^{year}}{T_{90}^{avg} 667}$. The resulting flux limit is shown in Figure 8.2. It is clear, then, that the Antares sensitivity is similar to the Amanda limit given in ref. (112).

8.2 2008 GRB Results

The 2008 dataset contains 65 satellite triggers corresponding to real GRBs. For the purposes of this thesis 10 of them (randomly chosen) have been unblinded and analysed. The list of the ten GRBs analysed is shown in Table 8.1.

The following procedure has been applied to perform the search for neutrino-induced showers in correlation with GRBs. Shower reconstruction and quality cuts are applied on the runs containing the GRB trigger and well reconstructed showers are sought in the T_{90} time-window. If no events are observed, then the upper limit on the Waxman-Bachall flux of each GRB are calculated using expected background and signal rates. The background rate is calculated using the procedure explained in Chapter 7 and is 1.782×10^{-4} Hz. The signal rate expected by a GRB is calculated using Monte Carlo simulations as described in Chapter 7, and the result is shown in Figure 8.3. This rate is given as a function of the energy and is averaged over all directions of the incoming neutrino and over all possible detector configurations during the year 2008.

As explained in Section 7.3.1, the Antares detector had different configurations during the year 2008. For the first five months of the year only 10 lines of the final 12 were deployed, while from the 30th of May to the end of the year the full 12-line detector was taking data. In addition, the detector response varies with the azimuthal direction of the incoming neutrino, due

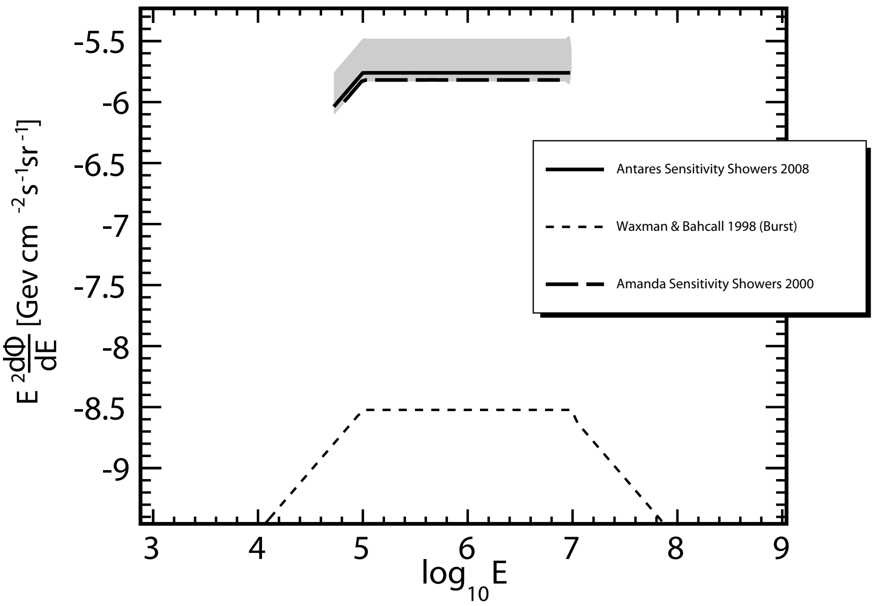

Figure 8.2: Sensitivity of the Antares detector for neutrino-induced showers from GRBs, translated in a diffuse flux limit in order to compare it with the results given by the Amanda collaboration (112). See text for a discussion of the transformation process.

GRB analysed				
GRB	T90 [s]	Time (U.T.)	RA (J2000)	DEC (J2000)
GRB080207	340	21 h 48 m 14 s	13 h 50 m 03.01 s	07:30:08.82
GRB080310	365	01 h 37 m 58 s	14 h 40 m 13.80 s	-00:10:29.60
GRB080413A	55	02 h 54 m 19 s	19 h 09 m 11.75 s	-27:40:39.99
GRB080523	102	21 h 21 m 51 s	01 h 23 m 11.51 s	-64:01:50.92
GRB080604	70	07 h 27 m 01 s	15 h 47 m 51.5 s	20:33:25.9
GRB080913	10	06 h 46 m 54 s	04 h 22 m 54.74 s	-25:07:46.20
GRB081012	20	13 h 10 m 23 s	02 h 00 m 48.22 s	-17:38:17.88
GRB081028	250	00 h 25 m 00 s	08 h 07 m 34.73 s	02:18:29.10
GRB081118	67	14 h 56 m 36 s	05 h 30 m 22.18 s	-43:18:05.30
GRB081230	50	20 h 36 m 12 s	02 h 29 m 19.51 s	-25:08:49.95

Table 8.1: Properties of the 10 GRBs, observed during the year 2008, which were included in the analysis. The name of the GRB contains the date in which it has been measured in the format GRBYYMMDD.

both to the inherent detector acceptance, and to the varying amount of earth the the neutrino must traverse. Therefore, the event rate shown in Figure 8.3 has been calculated separately for a 10-line and a 12-line detector, and expressed as a function of the zenith angle of the incoming neutrino. Figures 8.4(a) and 8.4(b) show the expected neutrino event rate for 10-line

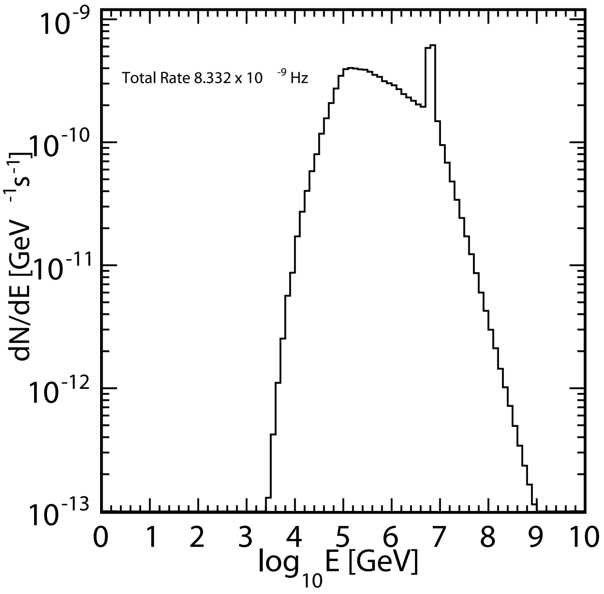

Figure 8.3: Rate of neutrino induced showers from GRBs in the 2008 Antares detector as a function of the energy of the incoming neutrino, averaged over azimuthal angles.

and 12-line detector respectively. It is interesting to note that, although the shower analysis favours electron neutrinos, the rate of tau neutrinos for vertically upgoing events is comparable to that of electron neutrinos. While the analysis in fact is most sensitive to electron neutrinos, many more tau neutrinos are able to traverse the Earth, especially at energies above 1 PeV, due to the tau neutrino regeneration process, therefore the expected rate of tau neutrinos is higher that that of muon neutrinos.

The appropriate detector configuration is chosen given the state of the detector at the time the GRB occurred. The equatorial coordinates of the GRB are translated to Antares local coordinates,and neutrinos are assumed to come from this direction. This information is used to determine the expected signal rate from the particular GRB, following Figures 8.4(c) and 8.4(d).

The shower reconstruction, described in Chapter 6, and the quality selection, described in Chapter 7, are applied to the data around the time that the GRB trigger was received. Surviving events are then sought within the T_{90} of the GRB, with the beginning of the time window taken to be the time of the GRB trigger. In none of the 10 observed GRBs has any neutrino-induced shower been measured. Given the expected background rate, the expected signal rate and the duration of the GRB, it is then possible to calculate the upper limit on the flux of neutrinos emitted by each GRB.

The background rate and the number of observed events (zero) are used to calculate the upper limit on the number of signal events that would occur with repeated measurements $\mu_{90}(n_{obs}, \mu_{bk})$ at a 90% CL using the Feldman-Cousin method (see Section 7.5). To obtain the corresponding limit on the flux emitted by each GRB, μ_{90} is scaled by the flux needed to

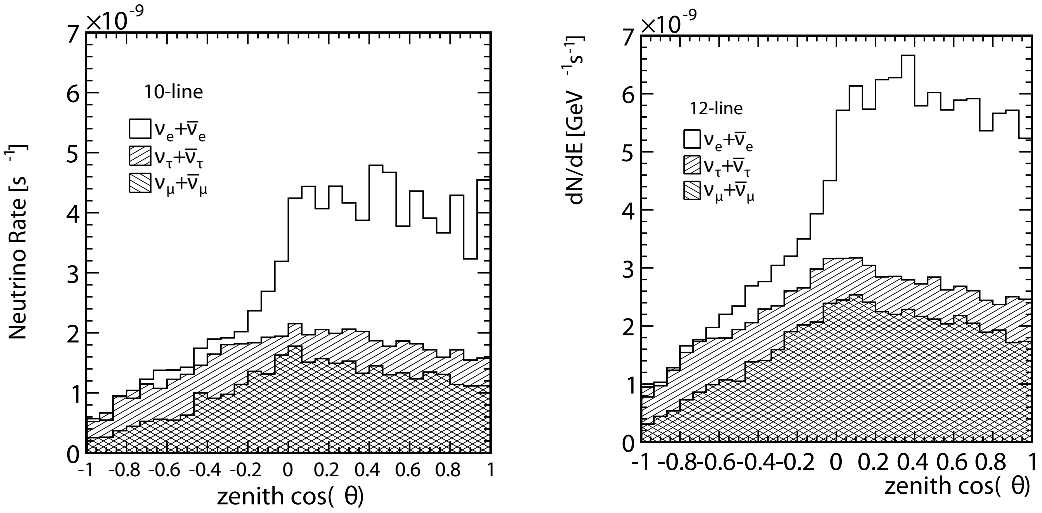

(a) 10-Line single flavours

(b) 12-Line single flavours

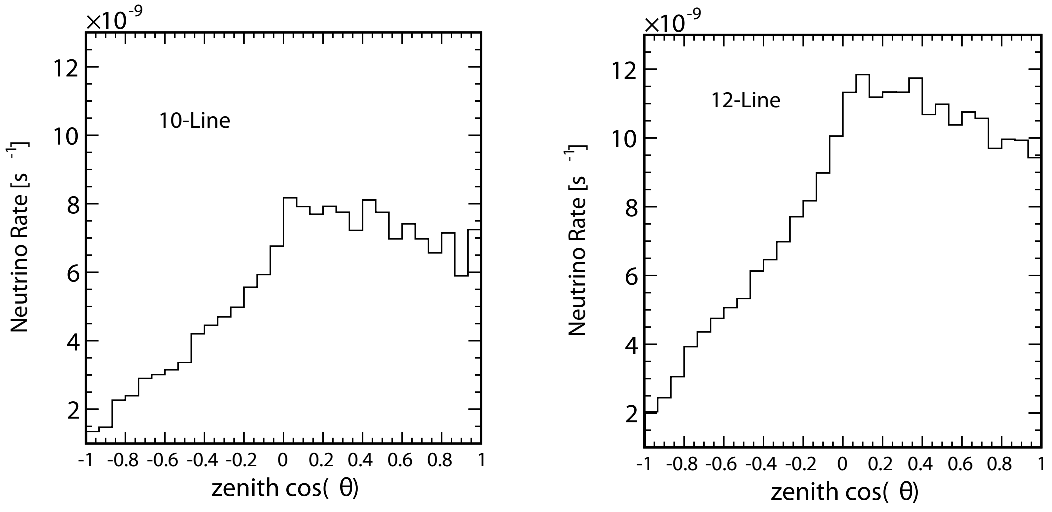

(c) 10-Line all flavours

(d) 12-Line all flavours

Figure 8.4: Figures (a) and (b) show the expected neutrino event rate for each neutrino flavours as a function of the incoming direction of the neutrino and the detector configuration. Figures (c) and (d) show the expected event rate for all neutrino flavours summed together.

give an expected number of events μ_s:

$$\phi_{90}(E_\nu) = \mu_{90}\frac{\phi^{wb}(E_\nu)}{\mu_s} \tag{8.2}$$

Where ϕ^{wb} is the flux model assumed for each GRB and can be written as:

$$\phi^{wb}(E_\nu) = \phi_0 \begin{cases} 10^{-5} \times E_\nu^{-1} & 1 < E_\nu < 10^5\,\mathrm{GeV} \\ E_\nu^{-2} & 10^5 \leq E_\nu < 10^7\,\mathrm{GeV} \\ 10^7 \times E^{-3} & 10^7 \leq E_\nu < 2 \times 10^{10}\,\mathrm{GeV} \end{cases} \tag{8.3}$$

where $\phi_0 = 3.188 \times 10^{-5}$ is the flux normalization. The shape of this flux is an hypothesis of this analysis, but an upper limit on the normalization of the flux, ϕ_{90}^0, can be put using Equation 8.2.

This procedure has been applied for each of the 10 analysed GRBs, and the results are shown in Table 8.2. The GRB with the most restrictive constraint on the flux is that with the highest expected rate and the longest duration. GRB080207 has an expected rate of 6.767×10^{-9} Hz and a T90 of 340s, leading to an upper limit on the normalization of the flux of $3.10 \times 10^{-3}\,\mathrm{GeV}^{-1}\,\mathrm{cm}^{-2}\,\mathrm{s}^{-1}$.

GRB analysed				
Detector	GRB	Expected Signal Rate [Hz]	N_{obs}	Flux Upper Limit $\phi_{90}^0[\mathrm{GeV}^{-1}\,\mathrm{cm}^{-2}\,\mathrm{s}^{-1}]$
10L	GRB080207	6.767×10^{-9}	0	3.10×10^{-3}
10L	GRB080310	3.14×10^{-9}	0	6.22×10^{-3}
10L	GRB080413A	4.99×10^{-9}	0	2.66×10^{-2}
10L	GRB080523	7.25×10^{-9}	0	9.82×10^{-3}
12L	GRB080604	1.137×10^{-8}	0	9.14×10^{-3}
12L	GRB080913	7.73×10^{-9}	0	9.45×10^{-3}
12L	GRB081012	9.95×10^{-9}	0	3.67×10^{-2}
12L	GRB081028	7.71×10^{-9}	0	3.73×10^{-3}
12L	GRB081118	9.97×10^{-9}	0	1.09×10^{-2}
12L	GRB081230	1.176×10^{-8}	0	1.24×10^{-2}

Table 8.2: List of the 10 random GRBs, happened during the year 2008 and included in the analysis. For each GRB the detector configuration at the time of the trigger is shown, together with the expected neutrino rate, the number of observed events and the flux limit placed.

8.3 Discussion of the Results

This thesis has presented a new method for the detection of neutrino-induced showers in coincidence with a Gamma Ray Burst using the Antares detector. This analysis complements the track searches typically performed in neutrino telescope experiments. Although the sensitivity per burst is lower than that of the track search, it can detect neutrinos of any flavour, which are invisible for track based analysis. It can also look for coincidences with GRBs happening in the northern hemisphere, as it does not depend on the direction of the observation. Ten GRBs triggered during the year 2008 have been analysed, and in none of them a signal event was observed within the T_{90} time-window. However, assuming a Waxman-Bachall flux (40) an upper limit on the normalization of this flux can be placed. GRB080207 has an expected rate of 6.767×10^{-9} Hz and a T90 of 340s, leading to an upper limit on the normalization of the flux of $3.10 \times 10^{-3}\,\mathrm{GeV}^{-1}\,\mathrm{cm}^{-2}\,\mathrm{s}^{-1}$.

For both the shower and track search methods, it would be possible to search for events originated from GRBs without using the trigger information. This type of analysis, typically referred to as a "rolling search" analysis, looks for clusters of events occurring within a predetermined time window, but not necessarily in coincidence with an external GRB trigger. A cluster of events that is extremely unlikely to be caused by background fluctuations is then defined as an evidence of a signal from a transient neutrino source. This type of analysis could exploit the same reconstruction and simulation algorithms developed for this thesis, but has the advantage of being sensitive to transient sources that have not triggered a signal in the GRB satellite network. An example of such a transient source would be a choked GRB (see Section 2.6). The disadvantage of this analysis, compared to a triggered search, is that, when no evidence of neutrinos is found, it is impossible to place a limit on the flux of any particular GRB.

The analysis presented in this thesis is focused on the higher energy range of the neutrino spectrum. This is because the flux of prompt neutrinos from GRBs has been calculated using the Fireball model. Different GRB models, such as the Reconnection Model (37), have been shown to produce a much softer neutrino spectrum (38). Currently, it is difficult to put constraints on the magnetization of the plasma of electrons protons and neutrinos that compose the GRB outflow. A way to understand the origin and the mechanism of acceleration of the prompt emission of GRB would be to measure their polarization. For example a strong polarization could suggest a higher rate of scattering of the photons off the shock fronts, adding an extra component to the sole synchrotron emission to the prompt spectrum (113). Linear polarization of the prompt emission could also help to put constrains on the magnetization of the accelerated plasma (114). Unfortunately, the polarization of the gamma component of the emission is still difficult to measure.

Most of the observed Gamma-Ray Bursts are thought to be generated by a supernova explosion. It has been shown, by the observation of neutrinos from the supernova SN1987A (5), that a supernova does indeed generate neutrinos, but in a much lower energy range than that for which Antares is sensitive [1]. Additionally, other processes aside from photopion interactions can occur in a GRB jet and generate neutrinos. The microscopic and acceleration processes in the internal shocks are at the moment only speculative, and improved understanding of these processes could explain some of the additional components in the GRB spectra that have been observed by the Fermi satellite but not completely explained by the Band spectrum (115). For example, $p-p$ and $p-n$ interactions are generally not not taken into account by high energy neutrino experiments when computing the expected neutrino fluxes. These neutrinos have much lower energies than those produced by $p-\gamma$. Showers could provide an interesting method of detection for these lower energy neutrinos. In fact, all neutrino flavours produce a shower in the detector at low energy, regardless of the type of interaction. This is because a low energy muon, for example, traversing the detector will not travel far before decaying, and the resulting

---

[1] Studies are performed to attempt the detection of supernova neutrinos measuring an overall increase in the singles rate in the detector caused by a large number of MeV neutrinos interacting inside the volume of the Antares detector (6).

hadronic shower should be detectable. The difficulty in this type of search is the very high background caused by optical background and atmospherics muons and neutrinos. Focusing the analysis at lower energies (on the order of a few hundreds of MeV to a few GeV) would open a new window upon low energy neutrinos for telescopes like Antares.

The same analysis presented in this thesis, will lead at much better results in the future KM3NeT neutrino observatory. KM3NeT will cover an instrumented volume between 5 and 8 cubic kilometres, while Antares is about $0.035\,\mathrm{km}^3$. With just a linear scaling of the signal and background together, one obtains that the sensitivity increases as the squared root of the volume. In this case this same analysis would improve of a factor 14 compared to the present result in Antares. The different detector configuration of KM3NeT, such as the use of the multi-pmts, can probably allow for a better background rejection. With a bigger volume track reconstruction will be more efficient and a veto on atmospheric muons could improve the background rejection. In this case the sensitivity would increase linearly with the volume, leading to an improvement of a factor 200.

A

Monte Carlo Production Reference

This appendix describes the software parameters used for the Monte Carlo simulations employed in this thesis work. The programs used are described in chapter 5. The software is run using a steering macro written in Python. Most of the production has been made with the software version relative to svn revision 6115.

The idea of SeaTray is to load a "tray" where all the modules and services work, and that contains all data frames. To create this tray, the macro must contain the line:

```
tray = I3Tray()
```

The first part of the macro is dedicated to installing some services that will be then used by the modules. Typically, one must install a geometry service, which contains the geometry of the detector, and a random number generator service:

```
tray.AddService("I3SPRNGRandomServiceFactory","random")(
    ("Seed",seed),
    ("NStreams",seed+1),
    ("StreamNum",1))

tray.AddService("I3AntTextFileGeometryServiceFactory","geometry")(
    ("AntaresGeoFile",geofile),
     ("OMAngularParametrization","Spring09")
    )
```

In this example the random number generator uses as seed an input parameter, `seed`, which is any integer number. The Antares geometry service looks for the file describing the geometry (for this thesis `r12_l00_s01.dat` was used) and requires the version of the angular parametrization of the optical modules (in this example `Spring09`).

Some modules need more services to work. For example, the lepton propagator MMC is written in the programming language Java, and therefore a wrapper is needed:

```
tray.AddService("I3JavaVMFactory","java")(
    ("Options",[expandvars("-Djava.class.path=$I3_BUILD/lib/mmc.jar")
  )
```

The `I3JavaVMFactory` requires the path to the compiled java executable mmc.jar.

The photon propagator module, `Hit Constructor`, needs the service `PSInterface`, which interfaces with Photonics (88), to access tables containing the photon flux and time distribution for the chosen medium properties. The location of the tables used in this analysis, for muon and shower propagation, are given by the directory path and the path and names of the Driver files:

```
tray.AddService("I3PSInterfaceFactory","PSInterface")(
          ("Interface","Photonics"),
          ("TableDirectory","/home/photonics_tables/"),
          ("DriverFilePath",
            "/home/photonics_tables/listfiles/listfiles_ANTARESv01"),
          ("PhotonicsLevel1DriverFile","level1_shower.list"),
          ("PhotonicsLevel2DriverFile","level2_muon.list"),
          ("PhotonicsVerbosity",0)
          )
```

When starting a new production, or when reading a file which is not in `.i3` format, a module that organises the flow of data must be called:

```
tray.AddModule("I3Muxer","muxer")
```

The "muxer" generates streams of data and selects the frame type for each event (such as geometry, physics or calibration). After these preambles it is possible to load the modules used for the simulation.

A.1 Neutrino Generator Production

Neutrino Generator has been used to produce a Monte Carlo dataset that is used to calculate the signal expected from a GRB. It generates a neutrino flux following a set of several parameters, tuned by the user. For all the parameters, the units can be chosen from the I3Units of *SeaTray*, and must be specified in the script. A list of all possible parameters, with a brief description, is given in Table A.1.

Note that NuG randomly generates neutrinos of one flavour (chosen via the `NeutrinoFlavor` option) at the surface of the Earth. The neutrino flavour can also be set using the number defined in the I3Particle class as I3Particle:ParticleType. (NuE = 201, NuMu = 202 or NuTau = 203). Tau decay in water is not simulated by NuG, but to take this effect into account, MMC must be run. Directions are generated isotropically over the range ZenithMin to ZenithMax and AzimuthMin and AzimutMax. The energy spectrum is a power law with an index GammaIndex,

Parameter name	Description	Default Value
EventYear	Event's year	1000
EventDaqTime	Event's DAQ time	1000
FinalTauDecay	Decay of the Tau lepton in water	false
AutomaticMuonFinalVolume	Set the length of the active volume cylinder automatically for muons	true
NoInEarthPropagation	If true, neutrino are injected on the surface of the cylinder, not on the Earth	true
NeutrinoFlavor	Primary Neutrino Type (NuE, nuMu, NuTau)	NuMu
GammaIndex	Index of the neutrino flux according to the power law, i.e. $f = E^{-\mathrm{GammaIndex}}$	1.0
EnergyMinLog	Minimum energy of the injected particles in log scale (in GeV)	2.0
EnergyMaxLog	Maximum energy of the injected particles in log scale	4.0
ZenithMin	Minimum zenith angle of the injected particles	90 deg
ZenithMax	Maximum zenith angle of the injected particles	180 deg
AzimuthMin	Minimum azimuth angle of the injected particles	90 deg
AzimuthMax	Maximum azimuth angle of the injected particles	180 deg
InjectionRadius	Radius of the Injection circle of the cylinder	880 m
DistanceEntrance	Distance of the circle centre to the detector centre	880 m
DistanceExit	Distance from the detector centre to the end of detection volume	200 m
DetectorCenterZ	z-position of the detector center from the surface	1945 m
DetectorDepth	Distance of the centre of the detector from the sea surface	NAN

Table A.1: The settable parameters of the Neutrino Generator module.

sampled from EnergyMinLog to EnergyMaxLog. If GammaIndex is less or equal to zero, an energy between EnergyMin and EnergyMax will be chosen according to a flat distribution. For a given direction, neutrinos are thrown on a circle of radius InjectionRadius and are propagated through the Earth to the detector at depth DetectorDepth. The neutrino interaction volume is defined as a cylinder, the axis of which is the neutrino direction and the radius of which is InjectionRadius. The distance from the start of the volume to the center of the detector is DistanceEntrance and distance from the center of the detector to the end of the cylinder is DistanceExit. For non-shower events, DistanceExit is usually taken to be smaller than DistanceEntrance. More options, relative to the cross section tables or the interaction(s) to be simulated, can be also be set. For the production used in this work the following parameters have been used to perform the production of electron neutrinos:

```
AutomaticMuonFinalVolume = False
NoInEarthPropagation = False
NeutrinoFlavor = "NuE"
GammaIndex = 1.0
EnergyMinLog = 1.0
EnergyMaxLog = 9.0
ZenithMin =    0.0*I3Units.deg
ZenithMax =  180.0*I3Units.deg
AzimuthMin =   0.0*I3Units.deg
AzimuthMax = 360.0*I3Units.deg
InjectionRadius = 250*I3Units.m
DistanceEntrance = 300*I3Units.m
DistanceExit = 200*I3Units.m
DetectorDepth = 2275*I3Units.m
WeightDictName_ = "I3MCWeightDict"
tablesDir_ = expandvars("I3_PORTS/share/anis1.0/")
```

Note that the interaction cylinder must be bigger then the size of the detector plus a few interaction lengths. For the muon and tau generation, besides the obvious change of the neutrino flavour, the Injection radius has been set to 300 m, and also the DistanceExit has been changed to 300 m. This is because tracks can travel longer than showers and produce hits in the detector from further away. The plot in Figure A.1 shows that. If the can size was too small, the distribution of the distance between the true vertex and the centre of the detector would be flat, because the detector could detect showers at higher distances than the ones were generates. These plots, instead, shows that the number of reconstructed shower at big distances does not have a cut off but decrease continuously.

A.2 MMC Propagation

To use MMC in SeaTray, it is necessary to load the module mmc-icetray, which is a C++ wrapper application for the MMC Java program. For this reason it is also necessary to make sure to have java installed on the system, and that the following environment variables are set:

JAVA_HOME should point to your java distribution, e.g.,
`JAVA_HOME=/usr/java/latest` if this variable is set before sourcing the env.sh script setting the rest may not be necessary

LD_LIBRARY_PATH must contain a path to jvm libraries, e.g.,
`LD_LIBRARY_PATH=JAVA_HOME/jre/lib/i386:  /JAVA_HOME /jre/lib/i386/client`

mmc-icetray depends on the MMC and c2j-icetray projects. The MMC project is the original java code, while c2j-icetray is the wrapper that allows SeaTray to run MMC. If the MMC project is not compiled, `ammc -ca` can be run in the mmc/src directory, and the resulting mmc.jar file placed into the $I3_WORK/lib directory.

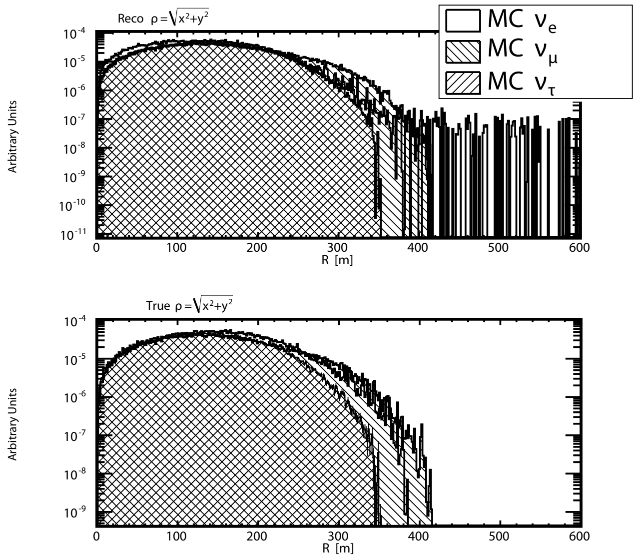

(a) Distance of the shower vertex from the detector centre

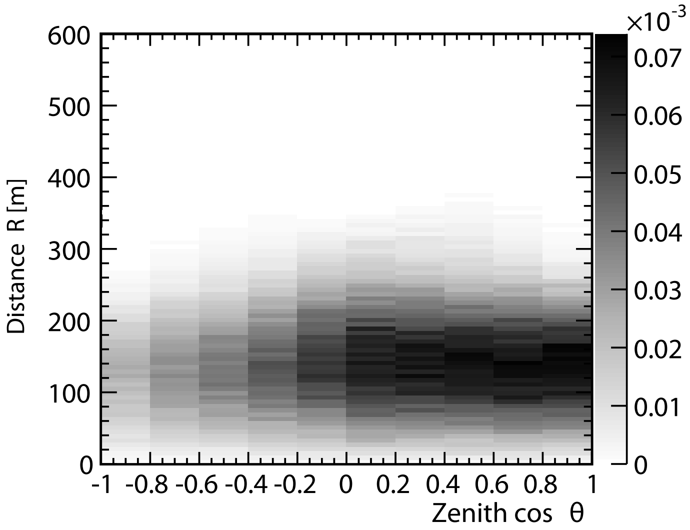

(b) Distance of the shower versus neutrino zenith

Figure A.1: Distance of the true vertex of the shower from the detector centre as a function of the zenith angle of the incoming neutrino. The plot in Figure A.1(a) shows the distance of the true vertex and the reconstructed vertex of the shower from the detector centre. Figure A.1(b) shows the distance of the true shower vertex from the detector centre. It is shown how the distribution does not have any hard cut off.

MMC has **options** and **modes**. The modes define what MMC has to do, and the options define how. The possible modes are:

mode=1 propagate muons, taus, electrons or monopoles only

mode=2 use as phenomenological event generator

mode=3 propagate all leptons

mode<0 add the minus sign to the modes above to output debugging (extra) info

When in modes 1 and 3, MMC must be combined with a lepton generator. When in mode=2, it acts as a lepton generator and propagates the leptons it creates. The default mode is 1. The options will be added to the default options string. The *mediadef* file describes the medium(s) in which the propagation is performed. If the file is not specified or not found, a one-medium configuration is used with the default medium or medium specified with the "-medi" option.

All options are the same as those used in the stand-alone MMC (87). To see all available options, add "-h" to the opts parameter. As a reference, a list is given in Table A.2. The default string of option is the following:

```
opts [default= '-romb=5 -raw -user -sdec -time
                -lpm -bs=1 -ph=3 -bb=2 -sh=2 -frho
                -mediadef=mmc-icetray/resources/mediadef
                -tdir=mmc-icetray/resources']
```

the user options are added to this string. To enable/disable a particular type of interaction, the -c option can be used. For example to decrease ionization losses by a factor of 2, the option `-ci=0.5` can be used.

For the Monte Carlo production used in this thesis, MMC was run in mode 3 with the following options:

```
-gdet=0 -radius=266.11 -length=800 -sdec -time -cont -lpm
-bs=1 -ph=3 -bb=2 -scat -frho -seed=1
-mediadef=$I3_SRC/mmc-icetray/resources/mediadef
```

A.3 Hit Contructor and Photonics

Hit Constructor reads the tree of Monte Carlo particles (`I3MCTree`) and then generates and propagates photons to the detector. It will not, therefore, consider all particles in the tree, but only light producing ones. The list of particles it considers is the following:

μ^+ with length>0

μ^- with length>0

τ^+ with length>0

τ^- with length>0

Monopoles with length>0

All Cascades (i.e. if I3Particle::IsCascade() is true).

If **StoreHCList** is set, Hit Constructor will store (as output) the internal list of particles that are used to generate light. As this is mainly used for debugging ,it is by default turned off. A generation of photon tables for the Antares water has been done by C. Kopper (116).

The Hit Constructor module is called with the following lines:

```
tray.AddModule("I3HitConstructorModule","hit-constructor")(
  ("DetectorMode",-1),
  ("EnableBinning",False),
  ("MaxPEs",50)
  )
```

When the number of p.e. on the PMT exceeds the chosen value of MaxPEs, it is possible to use the EnableBinning option. If set, Hit Constructor will compute hits bin-wise for tracks. DetectorMode is set to -1 for an arbitrary detector as the geometry is already set by other modules.

A.4 TreeHugger and TriggerEfficiency

In order to be able to use the latest version of the program TriggerEfficiency, which is not directly compatible with the SeaTray framework, a module was written by C.J. Reed to transform the standard .i3 format in a .root file readable by Trigger Efficiency. This program is available in the `antares-reader` project. The way it has been used for this thesis is the following:

```
tray.AddModule("AntMCTreeHugger","AntMCTreeMaker")(
    ("OutfName",rootfilename),
    ("EvtHdrName","I3EventHeader"),
    ("EvtTimeMode","AlwaysZero"),
    ("MCGenMode","NuGenWithMMC"),
    ("ParticleFillMode","InIceToMcTrackOnly"),
    ("WeightFillMode","WeightsListOnlyNoW3"),
    ("HitFillMode","NoNoiseNoMerge"),
    ("MCPartTreeName","I3MCTree"),
    ("MCHitSeriesName","MCHitSeriesMap"),
    ("RecoPulseSeriesName","RecoPulseSeriesAfterARS"),
    ("WeightDictName","I3MCWeightDict"),
    ("HitMergWin",I3Units.ns),
    )
```

Most of the options are relative to the names in which the dataclasses are saved in the frame (such as `EvtHdrName` or `MCPartTreeName`). `EvtTimeMode`, in the present version, must be set to “always zero”, which means that the event time is set to zero. `MCGenMode` accepts strings such as “NuGenWithMMC”, to be used when the program is run over a NuG+MMC simulation, “GenhenWithMMC” when the file is generated by Genhen and then propagated with MMC, “MuonGenWithMMC” for muon generation propagated with MMC (no neutrinos), “AntGenhenKM3” for the standard Antares chain, “AntCorsikaKM3” for the Corsika productions of Antares and “AntMupage” for the Antares Mupage production. Further options can be found in the `AntMCTreeHugger.cxx` strings definitions.

The output of TreeHugger can then be run through TriggerEfficiency like any other Antares file. The options given to Trigger Efficiency for the analysis presented in this thesis are:

```
$ANTRS_BIN/TriggerEfficiency -f [inputfile] -n 10000000
 -a file:/afs/in2p3.fr/throng/antares/DETECTOR/r12_c00_s01.det
-A file=/sps/km3net/users/cjreed/AuxNoiseBlends/GOOD_ARS_12line_thresh.dat
-r /sps/km3net/users/cjreed/AuxNoiseBlends/noiseblendL12-basic.root
-o [outputfile] -O -D 1 -L1 -TN -T3 -t 104.858
-C2 -highThreshold=3
```

The output of TriggerEfficiency was then read back into SeaTray using AntRead, run using the I3AntFileARSThresholdServiceFactory with the thresholds from `/sps/km3net/users/cjreed/AuxNoiseBlends/GOOD_ARS_12line_thresh.dat`, and having copied objects from the original MC generation files.

A.5 Neutrino Flux

NeutrinoFlux is a SeaTray service that can provide some “standard” neutrino flux estimates. Conventional atmospheric and cosmic neutrino fluxes are available for astrophysical diffuse and sources. Some examples are shown in Figure A.2(a). The user can choose one of the many models provided and the value of the flux is returned in $\text{GeV}^{-1}\,\text{cm}^{-2}\,\text{s}^{-1}\,\text{srad}^{-1}$ (for a diffuse flux, or $\text{GeV}^{-1}\,\text{cm}^{-2}\,\text{s}^{-1}$ for a point source flux) for the specified neutrino energy. When the Neutrino Flux constructor is initialized, it calls a method to open and read tables of parameters characterizing the chosen models. The astrophysical fluxes can be parametrized as a sum of power laws in given energy intervals of the form

$$A \cdot E^{-B} + C \cdot E^{-D} + \dots \tag{A.1}$$

The A, B, C, D parameters can be different in different energy ranges (for a maximum of 100 different intervals, set in the tables).

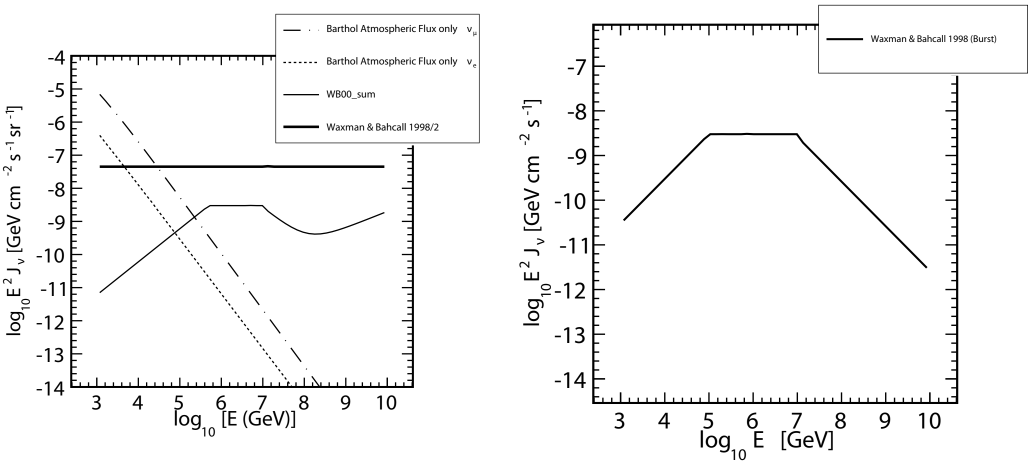

(a) Few example flux models

(b) Flux for a single average GRB

Figure A.2: Figure (a) shows some examples of flux models implemented in NeutrinoFlux. The dashed lines represent the atmospheric neutrino spectrum (for electron and muon neutrinos) following the Bartol flux (117). The thin solid line represents a GRB model flux that takes into account both the forward and reverse shocks (see chapter 2) (118). The solid thick line represents the Waxman-Bachal bound, a theorized upper limit for the diffuse flux of neutrinos (104). Figure (b) shows the Waxmand-Bachal flux for a single burst (40).

Parameter name	Description
-length	Length of the detector volume in meters
-radius	Radius of the detector volume in meters
-width	Width of the detector volume in meters
-height	Height of the detector volume in meters
gdet	[0-2] detector is a cylinder/box/sphere
-vcut	value of vcut used for the 1st region
-ecut	ecut in MeV used for the 2nd region
-medi	medium name
-mediadef	file with media definitions
-tau	propagate taus instead of muons (in mode=1)
-e	propagate electrons instead of muons (in mode=1)
-monopole	[=mass in GeV] propagate monopoles (in mode=1)
-sdec	enable stopped muon/tau decay treatment
-user	enable the mmc_en user line (record the energy at the point of track intersection with the detector cylinder: if this energy is >0 then the particle reaches the detector
-user	=[z] same, but record energy at z, not CPD
-rdmc	enforce compliance with rdmc
-time	precise time of flight calculation
-cont	enable continuous loss randomization
-scat	enable Moliere scattering
-lpm	enable lpm treatment
-bs	=[1-4] select on of the bremsstrahlung cross section: kkp, abb, ps, csc
-ph	=[1-4] photonuclear: bb, bb+bs, allm, bm
-bb	=[bb/bs:1-4 3|4:bb|zeus, allm:1-2(91/7), bm:1]
-sh	=[1-2] nuclear structure function: dutt/butk
-c	[i/b/p/e/d]=[cross section modifier, 0:disable]. i is for ionization lossses, b for bremsstrahlung, p for hotonuclear, e for pair production and d for decay
-rho	multiplicative factor for medium density
-frho	enable smart density factor handling (scales the medium density by a given amount)
-elow	muon energy in GeV below which it is lost
-ebig	upper bound in GeV of the parametric tables
-surf	=[h in meters] propagate to the plane z=[h]
-face	only if detector is on opposite side of it
-romb	number of interpolation points
-seed	[integer] sets random number generator seed
-raw	save tables in raw format
-tdir	=[dir] specify directory for parametric tables

Table A.2: The settable parameters of the MMC module. Acceptable values are given in squared brackets.

B

Reconstruction Software Usage Reference

The software to run both the hit selection and the shower fitter is contained in the SeaTray package. The hit selection employed for the studies presented in this thesis is contained in the `bbport` package (98). The shower fitter is contained in the `grb-shower` package. These two packages are contained in the meta-projects of SeaTray, `searec`. For a user that has installed a different meta-project, it is necessary to checkout these packages separately:

```
svn co $SVN/sandbox/galata/bbport/ bbport
svn co $SVN/icetray/projects/grb-shower/trunk/ grb-shower
```

where `$SVN` is the svn server URL `http://svn.km3net.physik.uni-erlangen.de`.

B.1 Hit Selection and Reconstruction

The first step in running these modules is to make some hit lists (in SeaTray called reco-pulse series maps) in which the time of hits have been shifted so that they are relative to the earliest triggering hit. Assuming there are two reco-pulse series maps named `CalibratedPulses` (L0 hits) and `CalibratedPulses_L1` (L1 hits), the shifted hit lists are obtained by running the module `I3HitTimeShifter`:

```
tray.AddModule("I3HitTimeShifter","timeshifter")(
    ("InputL0HitSeriesMapName","CalibratedPulses"),
    ("InputL1HitSeriesMapName","CalibratedPulses_L1"),
    ("OutputL0HitSeriesMapName","CalibratedPulses_shift"),
    ("OutputL1HitSeriesMapName","CalibratedPulses_L1_shift"),
    ("TriggeredHits","TriggeredCalibratedPulses_selected"),
    ("TimeShiftName","TimeOffset")
    )
```

The names of the hit lists are not important, of course, but they must be consistent among the various modules. The name of the shifted triggered hits list cannot be chosen by the user, but

Parameter name	Description	Default Value
SelectedMapName	Name of the list of selected hits	Selected_Reco-PulseSeries
RecoShowerName	Name of the χ^2 shower fit result in `I3GrbRecoShower` format	RecoShower-Parameters
MRecoShower-Name	Name of the M-estimator shower fit result in `I3GrbRecoShower` format	MRecoShower-Parameters
MCTreeName	Name of the list of MC particles (if available)	I3MCTree
MinUsedLines	Required number of lines with selected hits to perform fit	2
MinUsedHits	Required number of selected hits to perform fit	5
AntaresParticle-Name	Name of the M-estimator shower fit result in `I3Particle` format	RecoShower-AntaresParticle
Sigma	The value of σ to use in the M-estimator	1.0

Table B.1: The settable parameters of the I3ShowerFitter module.

a suffix "_shift" is added to the input triggered list name. The time offset of which the hits are shifted is also saved in the frame.

With the time-shifted hits available, the hit selection can be run directly with `bbport`'s hit selection module (see (98)). For example:

```
tray.AddModule("BBFitHitSelection","bbfitHitSelection")(
    ("InputPulsesName", "CalibratedPulses_shift"),
    ("OutputPulsesName","BBFitSelectedPulses")
    )
```

The resulting selected hits can then be passed to the shower fit module. This module has several options which are summarized in Table B.1. Continuing the example:

```
tray.AddModule("I3ShowerFitter","showerfitter")(
    ("SelectedMapName","BBFitSelectedPulses"),
    ("MCTreeName","OrigMCI3MCTree"),
    ("MRecoShowerName","MesRecoShower"),
    ("Sigma",1.0)
    )
```

The "MCTreeName" is the name of the particle tree containing the Monte Carlo truth. It is therefore an optional parameter that can be omitted. It is used, while reconstructing Monte Carlo events, to have the possibility of checking the behaviour of the reconstruction on the go.

B.2 Tools for the Analysis

The SeaTray project `grb-shower`, developed for this thesis, comes with a set of tools that can be used to develop an analysis. A simple tool to check some of the characteristics of the Monte Carlo simulation is the module `I3SimulationCheck`. This program reads information from the frame, such as the "MCTree", the hit lists, the reconstructed shower and the reconstructed track (if present) and generates a file in Root format (80) containing a set of histograms that can be used to analyse the reconstruction performance, calculate effective areas and to study the hit selection and trigger performance. If the user prefers to do a more detailed analysis, `grb-shower` provides a set of classes and a converter that transforms the standard SeaTray format (.i3) to a Root file, storing all information in the form of Root Trees. This can be done using the module `I3GrbRootWriter`. Many parameters must be defined to use this module, because it can translate most of the information contained in the i3 frame into Root. The list of all the required parameters, with their default values are displayed in Table B.2. The output root file is structured with a header and two root trees. The header is an object of the class `I3AnalysisHeader` and contains information relative to the Monte Carlo production (such as the power index of the generated spectrum and the number of generated events). One of the trees (`ShowerMCTree`) contains the true Monte Carlo information of each event. The other tree (`ShowerFitTree`) contains the information of the reconstructed shower and track, plus the data acquisition run information.

In addition to the analysis tools, some modules have been written to perform the systematics studies. Two modules induce the effects that have been considered: `I3HitTimeSmearer` smears the time of each hit following a gaussian distribution with a standard deviation chosen by the user, and `I3ReduceOMEfficiency` reduces the efficiency of the optical modules throwing hits away with a 1-p probability, where p is set by the user. The program `I3SparkAnalysis` generates many histograms that can be used to study the sparking phenomenon. Finally, the module `I3GrbSystematics` generates plots to evaluate the effect of each systematic effect.

Parameter name	Description	Default Value
RootName	Name of the output root file	ShowerTest.root
WeightDictName	Name of the MC weight list	I3MCWeightDict
AntAdditionalParameters	Name of the header containing extra parameters for Antares	AntMCAdditionalParams
MchitsMapName	Name of the list of MC hits (before PM simulation)	MCHitSeriesMap_noise
L0MapName	Name of the L0 hits list	RecoPulseSeriesAfterARS
L1MapName	Name of the L1 hits list	RecoPulseSeriesAfterARS_L1
SelectedMapName	Name of the selected hits list	RecoShowerAntaresParticle
RecoShowerName	Name of the shower reconstructed with χ^2 method	RecoShowerParameters
MRecoShowerName	Name of the shower reconstructed with M-estimator method	MRecoShowerParameters
BBFitShowerName	Name of the shower reconstructed by BBFit	BBFitOutputBright
BBFitTrackName	Name of the track reconstructed by BBFit	BBFitOutputTrack
TypeOfFile	Can be *SIGNAL* (signal MC), *MUPAGE* (Mupage files), *DATA* (real data)	*SIGNAL*
EventID	Select one event number for one single event, if negative all events are read	all events
MCSummary	Name of the MCSummary	I3MCSummary
MCTree	Name of the MCTree	I3MCTree
TimeShifitName	Name of the TimeShift	TimeOffset_trigger
TriggerKey	Name of the Trigger hierarchy	AntTriggerHierarchy
EventHeader	Name of the Event Header	I3EventHeader

Table B.2: The settable parameters of the I3GrbRootWriter module.

Bibliography

[1] R. Rui. **Talk : Lectures of Experimental Particle Physics**, 2002. 2

[2] I. V. Anicin. **The Neutrino - Its Past, Present and Future**. *ArXiv Physics e-prints physics/0503172*, March 2005. 2, 3

[3] C. L. Cowan, F. Reines, F. B. Harrison, H. W. Kruse, and A. D. McGuire. **Detection of the Free Neutrino: a Confirmation**. *Science*, **124**(3212):103–104, 1956. 3

[4] Q. R. Ahmad and SNO Collaboration. **Measurement of the Rate of nue + d –> p + p + e- Interactions Produced by 8B Solar Neutrinos at the Sudbury Neutrino Observatory**. *Physical Review Letters*, **87**(7):071301, August 2001. 4

[5] K. Hirata, T. Kajita, M. Koshiba, M. Nakahata, and Y. Oyama. **Observation of a neutrino burst from the supernova SN1987A**. *Physical Review Letters*, **58**:1490–1493, April 1987. 4, 132

[6] V Kulikovskiy, M Anghinolfi, H Costantini, and M Taiuti. **Neutrino detection from supernova explosion with the ANTARES telescope.** *Antares internal note*, Nov 2010. 4, 132

[7] E. G. Berezhko. **Composition of Cosmic Rays Accelerated in Active Galactic Nuclei**. *The Astrophysical Journal Letters*, **698**(2):L138, 2009. 4

[8] G. Wilk and Z. Wlodarczyk. **On the chemical composition of cosmic rays of highest energy**. *ArXiv e-prints 006.1781*, June 2010. 4

[9] D. H. Perkins. *Particle astrophysics Publications of the American Astronomical Society*. 4

[10] T. Chiarusi and M. Spurio. **High-energy astrophysics with neutrino telescopes**. *European Physical Journal C*, **65**:649–701, February 2010. 5

[11] N. Gehrels. **The Swift γ-ray burst mission**. *New Astronomy Reviews*, **48**:431 – 435, 2004. 7

[12] J.L. Racusin and et al. **Broadband observations of the naked-eye γ-ray burst GRB 080319B**. *Nature*, **455**:183–188, 2008. 7

[13] P. A. Evans, A. P. Beardmore, K. L. Page, L. G. Tyler, J. P. Osborne, M. R. Goad, P. T. O'Brien, L. Vetere, J. Racusin, D. Morris, D. N. Burrows, M. Capalbi, M. Perri, N. Gehrels, and P. Romano. **An online repository of Swift/XRT light curves of γ-ray bursts**. Astronomy and Astrophysics, **469**:379–385, July 2007. 8

[14] Jonathan Katz. *The Biggest Bangs*. Oxford Oxfordshire: Oxford University Press, 2002. 9

[15] Govert Schilling. *Flash!* Cambridge University Press, Cambridge, 2002. 9

[16] R. W. Klebesadel, I. B. Strong, and R. A. Olson. **Observations of Gamma-Ray Bursts of Cosmic Origin**. *Astrophysical Journal*, **182**:L85, June 1973. 9

[17] D. Band, J. Matteson, L. Ford, B. Schaefer, D. Palmer, B. Teegarden, T. Cline, M. Briggs, W. Paciesas, G. Pendleton, G. Fishman, C. Kouveliotou, C. Meegan, R. Wilson, and P. Lestrade. **BATSE observations of gamma-ray burst spectra. I - Spectral diversity**. Astrophysical Journal, **413**:281–292, August 1993. 9, 11, 27

[18] J. S. Bloom, S. G. Djorgovski, S. R. Kulkarni, and D. A. Frail. **The Host Galaxy of GRB 970508**. *The Astrophysical Journal Letters*, **507**(1):L25–L28, 1998. 10

[19] G. Ghisellini. **Gamma Ray Bursts: Some Facts and Ideas**. In I. Ciufolini, D. Dominici, & L. Lusana, editor, *2001: A Relativistic Spacetime Odyssey*, page 381, 2003. 11

[20] J. Granot, for the Fermi LAT Collaboration, and the GBM Collaboration. **Highlights from Fermi GRB observations**. *ArXiv e-prints 1003.2452*, March 2010. 12, 19

[21] the Fermi LAT Collaboration. **A limit on the variation of the speed of light arising from quantum gravity effects**. *Nature*, **462**:331–334, November 2009. 12

[22] Y.-P. Qin, G.-Z. Xie, S.-J. Xue, E.-W. Liang, X.-T. Zheng, and D.-C. Mei. **The Hardness-Duration Correlation in the Two Classes of Gamma-Ray Bursts**. *Publ. of the Astronomical Society of Japan*, **52**:759, October 2000. 12

[23] S. E. Woosley and J. S. Bloom. **The Supernova Gamma-Ray Burst Connection**. *Annual Review of Astronomy and Astrophysics*, **44**:507–556, September 2006. 12

[24] S. Woosley and T. Janka. **The physics of core-collapse supernovae**. *Nature Physics*, **1**:147 – 154, 2005. 13

[25] Alexei V. Filippenko. **OPTICAL SPECTRA OF SUPERNOVAE**. *Annual Review of Astronomy and Astrophysics*, **35**(1):309–355, 1997. 13

[26] T. J. Galama and et al. **An unusual supernova in the error box of the -ray burst of 25 April 1998**. *Nature*, **395**:670 – 672, 2008. 13

[27] D. H. Hartmann and A. I. MacFadyen. **Hypernovae, collapsars, and gamma-ray bursts**. *Nuclear Physics B - Proceedings Supplements*, **80**(1-3):135 – 142, 2000. Texas Symposium on Relativistic Astrophysics and Cosmology. 14

[28] William H Lee and Enrico Ramirez-Ruiz. **The progenitors of short gamma-ray bursts**. *New Journal of Physics*, **9**(1):17, 2007. 14

[29] R. D. Blandford and C. F. McKee. **Fluid dynamics of relativistic blast waves**. *Physics of Fluids*, **19**:1130–1138, August 1976. 16, 19

[30] P. Mészáros. **Gamma-ray bursts**. *Reports on Progress in Physics*, **69**:2259–2321, August 2006. 16, 21

[31] T. Piran. **The physics of gamma-ray bursts**. *Reviews of Modern Physics*, **76**:1143–1210, October 2004. 16

[32] M. Ruderman. **Theories of gamma-ray bursts**. *New York Academy Sciences Annals*, **262**:164–180, October 1975. 16

[33] Y. Lithwick and R. Sari. **Lower Limits on Lorentz Factors in Gamma-Ray Bursts**. Astrophysical Journal, **555**:540–545, July 2001. 17

[34] F. Melia. *High-Energy Astrophysics by Fulvio Melia. Princeton University Press, 2009.* 2009. 18

[35] A. Shemi and T. Piran. **The appearance of cosmic fireballs**. ApJ Letters, **365**:L55–L58, December 1990. 19

[36] *High Energy Radiation from Black Holes: Gamma Rays, Cosmic Rays, and Neutrinos by Charles D. Dermer and Govind Menon. Princeton Univerisity Press, November 2009.* 20, 23, 24, 25, 29

[37] G. Drenkhahn. **Acceleration of GRB outflows by Poynting flux dissipation**. Astronomy and Astrophysics, **387**:714–724, May 2002. 20, 132

[38] H. B. J. Koers and D. Giannios. **Neutron-rich gamma-ray burst flows: dynamics and particle creation in neutron-proton collisions**. Astronomy and Astrophysics, **471**:395–408, August 2007. 21, 132

[39] S. Heinz and M. C. Begelman. **A Shotgun Model for Gamma-Ray Bursts**. ApJ Letters, **527**:L35–L38, December 1999. 21

[40] E. Waxman and J. Bahcall. **High Energy Neutrinos from Cosmological Gamma-Ray Burst Fireballs**. *Physical Review Letters*, **78**:2292–2295, March 1997. 21, 29, 30, 31, 87, 90, 101, 126, 131, 143

[41] E. Waxman and J. N. Bahcall. **Neutrino Afterglow from Gamma-Ray Bursts: $\sim 10^{18}$ eV**. Astrophysical Journal, **541**:707–711, October 2000. 21

[42] S. Razzaque, P. Mészáros, and E. Waxman. **Neutrino signatures of the supernova: Gamma ray burst relationship**. Phys. Rev. D, **69**(2):023001, January 2004. 21

[43] E. Fermi. **On the Origin of the Cosmic Radiation**. *Physical Review*, **75**:1169–1174, April 1949. 23

[44] H. B. J. Koers and R. A. M. J. Wijers. **The effect of neutrinos on the initial fireballs in gamma-ray bursts**. Monthly Notices of the RAS, **364**:934–942, December 2005. 25

[45] P. Mészáros and E. Waxman. **TeV Neutrinos from Successful and Choked Gamma-Ray Bursts**. *Physical Review Letters*, **87**(17):171102–+, October 2001. 26

[46] O. Mena, I. Mocioiu, and S. Razzaque. **Oscillation effects on high-energy neutrino fluxes from astrophysical hidden sources**. Phys. Rev. D, **75**(6):063003–+, March 2007. 26, 35, 36

[47] D. Guetta and J. Granot. **Observational implications of a plerionic environment for gamma-ray bursts**. Monthly Notices of the RAS, **340**:115–138, March 2003. 27

[48] J. Bluemer and the Pierre Auger Collaboration. **The Pierre Auger Observatory: Results on Ultra-High Energy Cosmic Rays**. *ArXiv e-prints 0807.4871*, July 2008. 28

[49] E. Waxman. **Cosmological Gamma-Ray Bursts and the Highest Energy Cosmic Rays**. *Physical Review Letters*, **75**:386–389, July 1995. 28

[50] X.-Y. Wang and Z.-G. Dai. **Prompt TeV Neutrinos from the Dissipative Photospheres of Gamma-ray Bursts**. ApJ Letters, **691**:L67–L71, February 2009. 29

[51] F. Halzen and D. W. Hooper. **Neutrino Event Rates from Gamma-Ray Bursts**. *The Astrophysical Journal Letters*, **527**(2):L93, 1999. 31

[52] D. Guetta, M. Spada, and E. Waxman. **On the Neutrino Flux from Gamma-Ray Bursts**. Astrophysical Journal, **559**:101–109, September 2001. 31

[53] D. Guetta, D. Hooper, J. Alvarez-Mun˜Iz, F. Halzen, and E. Reuveni. **Neutrinos from individual gamma-ray bursts in the BATSE catalog**. *Astroparticle Physics*, **20**:429–455, January 2004. 31, 36, 38

[54] *Neutrino2010 - Results from MINOS in proceeding of Neutrino2010, Athens Greece*. 33

[55] Particle Data Group and B. Kayser. **Review of Particle Physics - Neutrino Mass, Mixing, and flavour change**. *Physics Letters B*, **667**:1–6, September 2008. 33

[56] S. Razzaque, P. Mészáros, and E. Waxman. **Enhancement of the $\overline{\nu}_e$ flux from astrophysical sources by two-photon annihilation interactions**. Phys. Rev. D, **73**(10):103005–+, May 2006. 34

[57] **Techniques for nuclear and particle Physics experiments by W.R. Leo. (Springer, Berlin and Heidelberg, 1987) pp xvi + 368, Soft cover, DM 80-. ISBN 3-540-17386-2**. *Nuclear Instruments and Methods in Physics Research B*, **34**:290–290, August 1988. 42

[58] J Brunner. **Antares Internal Note - The refraction index at the Antares site**. 2000. 42

[59] W.-M. Yao and et al. **Review of Particle Physics**. *Journal of Physics G Nuclear Physics*, **33**:1–1232, July 2006. 43

[60] Aart Heijboer. *Track reconstruction and point source searches with Antares*. PhD thesis, Universiteit van Amsterdam, Amsterdam, The Netherlands, 2004. 44, 80, 82

[61] T. De Young, S. Razzaque, and D. F. Cowen. **Astrophysical tau neutrino detection in kilometer-scale Cherenkov detectors via muonic tau decay**. *Astroparticle Physics*, **27**:238–243, April 2007. 45

[62] P.Amram and ANTARES collaboration. **Background light in potential sites for the ANTARES undersea neutrino telescope**. *Astroparticle Physics*, **13**(2-3):127 – 136, 2000. 48

[63] et al. P. Amram. **The ANTARES optical module**. *Nuclear Instruments and Methods in Physics Research Section A: Accelerators, Spectrometers, Detectors and Associated Equipment*, **484**(1-3):369 – 383, 2002. 48

[64] P.Amram and ANTARES collaboration. **Sedimentation and fouling of optical surfaces at the ANTARES site**. *Astroparticle Physics*, **19**(2):253 – 267, 2003. 49

[65] J. A. Aguilar and ANTARES collaboration. **The data acquisition system for the ANTARES neutrino telescope**. *NUCL.INSTRUM.METH.A*, **570**:107, 2007. 51

[66] M. Ageron and ANTARES collaboration. **The ANTARES Optical Beacon System**. *NUCL.INSTRUM.METH.A*, **578**:498, 2007. 52, 54, 92

[67] Gabrielle Lelaizant. *Etude des Sursauts Gamma à partir des neutrinos de haute énergie avec le télescope ANTARES - Analyse du positionnement acoustique du déetecteur*. PhD thesis, Université de la Méditerranée Aix-Marseille II, 2008. 54, 60

[68] ANTARES Collaboration and J. A. Aguilar. **Transmission of light in deep sea water at the site of the ANTARES neutrino telescope**. *Astroparticle Physics*, **23**:131–155, February 2005. 54

[69] Juan Antonio Aguilar Sanchez. *Analysis of the Optical Beacon system and search for point-like sources in the ANTARES neutrino telescope*. PhD thesis, Universitat de Valencia, 2008. 55

[70] Juergen Brunner. **Simulation of $^{40}\mathrm{K}$ signals**. Technical report, Antares Internal Note, 1999. 55

[71] Dmitry Zaborov. **Coincidence rate of potassium-40 seen with MILOM**. Technical report, Antares Internal Note, 2006. 55

[72] Maarten De Jong. **The ANTARES Trigger Software**. Technical report, Antares Internal Note, 2005. 56, 80

[73] J. Carr, S. Escoffier, and D. Zaborov. **Proposition for an alternative trigger based on the T3 cluster trigger**. Technical report, Antares Internal Note, 2007. 59, 90

[74] M. Naumann-Godo. *Sensitivity of the Antares neutrino telescope to gamma-ray bursts*. PhD thesis, Erlangen University, 2007. 60

[75] Mieke Bouwhuis. *Detection of Neutrinos from Gamma-Ray Bursts*. PhD thesis, Universiteit Van Amsterdam, 2005. 60

[76] J.D. Myers and Swift coll. **Official NASA Swift website**, 2010. `http://heasarc.gsfc.nasa.gov/docs/swift/swiftsc.html`. 60

[77] J.D. Myers and Fermi coll. **Official NASA Fermi website**, 2010. `http://fermi.gsfc.nasa.gov/`. 60

[78] Claudio Kopper. **A software framework for KM3NeT**. *Nuclear Instruments and Methods in Physics Research Section A*, **602**(1):107 – 110, 2009. Proceedings of the 3rd International Workshop on a Very Large Volume Neutrino Telescope for the Mediterranean Sea. 63

[79] Rene Rivera. **Boost C++ Libraries**, 2004-2007. `http://www.boost.org/`. 64

[80] The Root team. **The ROOT analysis framework**, 1995-2010. `http://root.cern.ch/`. 64, 147

[81] A. Gazizov and M. Kowalski. **ANIS: High energy neutrino generator for neutrino telescopes**. *Computer Physics Communications*, **172**(3):203 – 213, 2005. 64, 65, 66

[82] D. Chirkin and W. Rhode. **Propagating leptons through matter with Muon Monte Carlo (MMC)**. *ArXiv High Energy Physics - Phenomenology e-prints hep-ph/0407075*, July 2004. 64, 65, 69

[83] J. Lundberg, P. Miočinović, K. Woschnagg, T. Burgess, J. Adams, S. Hundertmark, P. Desiati, and P. Niessen. **Light tracking through ice and water - Scattering and absorption in heterogeneous media with PHOTONICS**. *Nuclear Instruments and Methods in Physics Research A*, **581**:619–631, November 2007. 64

[84] Claudine Colnard. *Ultra high energy neutrino simulations*. PhD thesis, Universiteit Van Amsterdam, 2009. 65

[85] J. Pumplin, D. R. Stump, J. Huston, H.-L. Lai, P. Nadolsky, and W.-K. Tung. **New Generation of Parton Distributions with Uncertainties from Global QCD Analysis**. *Journal of High Energy Physics*, **7**:12–+, July 2002. 65

[86] A. Donnachie and P. V. Landshoff. **Small x: two pomerons!** *Physics Letters B*, **437**(3-4):408 – 416, 1998. 66

[87] W. Rhode and D. Chirkin. **Muon Monte Carlo: a new high-precision tool for tracking of muons in medium**. In *International Cosmic Ray Conference*, **3** of *International Cosmic Ray Conference*, pages 1017–+, 2001. 69, 76, 140

[88] J. Lundberg, P. Miocinovic, K. Woschnagg, T. Burgess, J. Adams, S. Hundertmark, P. Desiati, and P. Niessen. **Light tracking through ice and water–Scattering and absorption in heterogeneous media with Photonics**. *Nuclear Instruments and Methods in Physics Research Section A: Accelerators, Spectrometers, Detectors and Associated Equipment*, **581**(3):619 – 631, 2007. 69, 70, 136

[89] P. Miocinovic. *Muon energy reconstruction in the Antarctic muon and neutrino detector array (AMANDA)*. PhD thesis, University of California, Berkeley, 2001. 70

[90] Marek Kowalski. **On the Cherenkov light emission of hadronic and electro-magnetic cascades**. Technical report, IceCube Internal Note, 2002. 71

[91] Stephanie Escoffier. **Performance of the T3 Triggers on MC Data**. Technical report, Antares Internal Note, 2008. 73, 80, 90

[92] ANTARES Collaboration. **Zenith distribution and flux of atmospheric muons measured with the 5-line ANTARES detector**. *ArXiv e-prints 1007.1777*, July 2010. 73

[93] Aart Heijboer. **Point Source Search with 2007 and 2008 data**. Technical report, Antares Internal Note, 2010. 73, 75, 99, 119, 120, 121

[94] David J.L. Bailey. *Monte Carlo tools and analysis methods for understanding the ANTARES experiment and predicting its sensitivity to Dark Matter*. PhD thesis, University of Oxford, United Kingdom, 2002. 74

[95] Teresa ; Sokalski Igor A Labbate, Annalisa ; Montaruli. **GENHEN v6: ANTARES neutrino generator extension to all neutrino flavors and inclusion of propagation through the Earth**. Technical report, ANTARES-SOFT-2004-010. 74

[96] Amanda Cooper-Sarkar and Subir Sarkar. **Predictions for high energy neutrino cross-sections from the ZEUS global PDF fits**. *JHEP*, **01**:075, 2008. 74

[97] J. Brunner and ANTARES Coll. **A Fast Algorithm for Muon Track Reconstruction and its Application to the Antares Neutrino Telescope** . *submitted to AstroParticle Physics*. 81, 113

[98] S Galatà. **Antares Internal Note - The BBfit reconstruction with full detector geometry in Seatray.** Oct 2010. 81, 145, 146

[99] *The behavior of maximum likelihood estimates under nonstandard conditions - proceeding from Fifth Berkeley Symposium on Mathematical Statistics and Probability*, 1967. 84

[100] *Statistical Data Analysis*. Oxford Science Publications, 1998. 84, 104

[101] F James and M Roos. **MINUIT-a system for function minimization and analysis of the parameter errors and correlations**. *Comput. Phys. Commun.*, **10**(6):343–67, 1975. 85, 89

[102] M Bouwhuis. **Data blinding for GRB data analyses**. 2007. 101

[103] **Interplanetary Gamma-Ray Burst Timing Network**. `http://heasarc.nasa.gov/docs/heasarc/missions/ipn.html`. 101, 126

[104] E. Waxman and J. Bahcall. **High energy neutrinos from astrophysical sources: An upper bound**. Phys. Rev. D, **59**(2):023002–+, January 1999. 101, 143

[105] J.D. Myers and BATSE coll. **The CGRO Mission website**, 2001. `http://heasarc.gsfc.nasa.gov/docs/cgro/`. 101

[106] J. Neyman. **Outline of a Theory of Statistical Estimation Based on the Classical Theory of Probability**. *Royal Society of London Philosophical Transactions Series A*, **236**:333–380, August 1937. 104

[107] G. J. Feldman and R. D. Cousins. **Unified approach to the classical statistical analysis of small signals**. Phys. Rev. D, **57**:3873–3889, April 1998. 106, 127

[108] G. C. Hill and K. Rawlins. **Unbiased cut selection for optimal upper limits in neutrino detectors: the model rejection potential technique**. *Astroparticle Physics*, **19**:393–402, June 2003. 107

[109] G. C. Hill, J. Hodges, B. Hughey, A. Karle, and M. Stamatikos. **Examining the Balance Between Optimising an Analysis for Best Limit Setting and Best Discovery Potential**. In L. Lyons & M. Karagöz Ünel, editor, *Statistical Problems in Particle Physics, Astrophysics and Cosmology*, pages 108–+, 2006. 107

[110] S. Razzaque, P. Mészáros, and E. Waxman. **High Energy Neutrinos from Gamma-Ray Bursts with Precursor Supernovae**. *Physical Review Letters*, **90**(24):241103–+, June 2003. 109

[111] A. Hoecker, P. Speckmayer, J. Stelzer, J. Therhaag, E. von Toerne , and H. Voss. **TMVA - Toolkit for Multivariate Data Analysis with ROOT**, 2005. `http://tmva.sourceforge.net/`. 111

[112] A. Achterberg, M. Ackermann, J. Adams, J. Ahrens, K. Andeen, J. Auffenberg, J. N. Bahcall, X. Bai, B. Baret, S. W. Barwick, and et al. **Search for Neutrino-induced Cascades from Gamma-Ray Bursts with AMANDA**. Astrophysical Journal, **664**:397–410, July 2007. 127, 128

[113] D. Eichler and A. Levinson. **Polarization of Gamma-Ray Bursts via Scattering off a Relativistic Sheath**. ApJ Letters, **596**:L147–L150, October 2003. 132

[114] J. Granot. **The Most Probable Cause for the High Gamma-Ray Polarization in GRB 021206**. ApJ Letters, **596**:L17–L21, October 2003. 132

[115] F. Daigne. **Modelling the prompt emission from Gamma Ray Bursts**. In McEnery, Racusin, and Gehrels, editor, *Proceeding GRB2010 conference*, 2011. 132

[116] Claudio Kopper. *Performance Studies for the KM3NeT Neutrino Telescope*. PhD thesis, Friedrich-Alexander-Universitat Erlangen-Nuernberg, 2010. 141

[117] G. D. Barr, T. K. Gaisser, P. Lipari, S. Robbins, and T. Stanev. **Three-dimensional calculation of atmospheric neutrinos**. Phys. Rev. D, **70**(2):023006–+, July 2004. 143

[118] E. Waxman. **Gamma-Ray Bursts, Cosmic-Rays and Neutrinos**. *Nuclear Physics B Proceedings Supplements*, **87**:345–354, June 2000. 143

At the end of each reference, the reader can find the number of the page where the reference is cited.

Glossary

Notation	Description	Page List
T_{90}	Time during which the detector makes 90% of the counts from a gamma-ray bursts	12, 16, 18, 97, 101, 102, 109–111, 127, 129, 131
accretion disc	An accretion disc is a structure formed by diffuse material in circular motion around a central body. Gravity causes material in the disc to spiral inward towards the central body. Gravitational forces compress the material causing the emission of electromagnetic radiation in two jets at the two extremes of the disc	15
afterglow	Afterglows are fainter, fading, longer wavelength (X-ray, IR, UV, optical and radio) emission after a gamma ray burst	10, 12–14, 16, 19
apparent magnitude	The apparent magnitude is the logarithmic measure of how bright an astronomical object appears to an observer on Earth regardless of its intrinsic brightness	7

Notation	**Description**	**Page List**
blast wave	A blast wave is the pressure and flow resulting from the deposition of a large amount of energy in a small very localised volume. The flow field can be approximated as a lead shock wave, followed by a subsonic flow field	15, 16, 23, 24
Bremsstrahlung	Electromagnetic radiation produced by the acceleration of a charged particle when deflected by another charged particle, such as an atomic nucleus	17, 18, 46, 47, 68, 69, 79, 90
Cherenkov radiation	Electromagnetic radiation emitted when a charged particle passes through an insulator at a constant speed greater than the speed of light in that medium	42, 44, 45, 49, 56, 58, 64, 66
effective area	Cross section of a detector with a 100% detection efficiency	72, 73, 103
erg	Unit of energy and mechanical work in the centimetre-gram-second (CGS) system of units. It corresponds to 10^{-7} joules or 624.15 GeV.	7
Fireball model	In the Fireball mode a GRB is an explosion started by an inner engine of only few tens kilometers followed by a radiation dominated fireball. The fireball expands keeping its total energy constant by transforming entropy into kinetic energy. Interaction of shells with the external medium or collision between shells reconvert the kinetic energy in internal energy, ready to be radiated in form of gamma-rays	15, 27, 28, 31, 125, 132
fluence	Fluence is the flux integrated over time. In Standard Units is measured in $[\mathrm{GeV}^{-1}\,\mathrm{m}^{-2}\,\mathrm{srad}^{-1}]$	7, 9, 28, 31, 32, 101
frame	Data recorded by the ARSes chips are organised in time periods of 104.858 ms, called frames.	53, 56, 98
inner engine	In the Fireball Model, it is thought that the GRB is initialized by a inner engine, that is a very compact object emitting a relativistic outflow	15, 16

Notation	Description	Page List
jet	In GRB physics a jet is the collimated outflow of material ejected by the compact object after the explosion. Two opposite jets are formed and the matter of which they are composed is generally relativistic	5, 15, 28, 125
L0	A single hit above threshold in the Antares detector	57, 80, 99, 121
L1	A cluster of hits that happen within 20 ns in different pmts of the same storey. A single hit can also be accepted if its charge exceeds 3 photo electrons.	57, 59, 71, 72, 80
light curve	In astronomy, a light curve is a graph of light intensity of a celestial object or region, as a function of time. The light is usually in a particular frequency interval or band	7, 16, 18
long GRB	Gamma-ray bursts with a T90 longer than 2 seconds	12, 14, 109
M-estimator	Solution of the minimization of a generalised version of the Maximum Likelihood Fit in Robust Statistic analysis	85, 87, 111, 113
mean free path	Average distance covered by a moving particle between successive collisions which modify its direction or energy	3, 125
Monte Carlo	Monte Carlo methods are a class of computational algorithms that rely on repeated random sampling to compute their results. Monte Carlo methods are often used in simulating physical and mathematical systems. Because of their reliance on repeated computation of random or pseudo-random numbers, these methods are most suited to calculation by a computer and tend to be used when it is unfeasible or impossible to compute an exact result with a deterministic algorithm.	40, 64, 66, 71, 75, 76, 84, 98, 102, 103, 107, 108, 120–123, 127

Notation	Description	Page List
PDF	A probability density function, or density of a continuous random variable is a function that describes the relative likelihood for this random variable to occur at a given point. The probability for the random variable to fall within a particular region is given by the integral of this variable's density over the region.	80, 104, 106, 121
redshift	Redshift happens when light seen coming from an object is proportionally shifted to appear more red. It is due to the Doppler effect and occurs whenever a light source moves away from an observer. In the case of extragalactic objects this quantity is related to the distance of the object, because of the expansion of the Universe	10, 32, 101
shell	In the description of GRBs, a shell is the layer of matter within the jet accelerated at the same speed. Multiple layers (or shells) are formed during the explosion of a GRB. Consecutive shells will reach each other creating internal shocks. When a shell expands in the interstellar medium outside the jet, it generates an external shock	16
shock wave	A shock wave (or Shock Front) is a type of propagating disturbance. Like an ordinary wave, it carries energy and can propagate through a medium. In a GRB the mechanism driving these shocks consists of plasma instabilities, that operate on the scale of plasma skin depth, which is typically much shorter than the mean free path. These shocks have extremely high energy particles in them, accelerated via Fermi acceleration. In the Internal Shock scenario the inner engine is assumed to emit many shells with different Lorentz factors colliding into one another. This thermalise a fraction of their kinetic energy. An External Shock happens when the relativistic matter emitted by the jets runs into some external medium, either interstellar or wind earlier emitted by the progenitor	16, 23, 27, 29, 30, 42

Notation	**Description**	**Page List**
short GRB	Gamma-ray bursts with a T90 shorter than 2 seconds	12, 14, 109
SummaryTimeSlice	A summary, generated for each timeslice, containing the number of L0 hits of each optical module (even not triggered)	57, 71
supernova	A supernova is a stellar explosion that is more energetic than a nova. Supernovae are extremely luminous and cause a burst of radiation that often briefly outshines an entire galaxy, before fading from view over several weeks or months	13, 25, 132
synchrotron	Synchrotron emission is a type of Bremsstrahlung radiation, happening when a relativistic charged particle moves in the Coulomb field of a ion.	17, 27, 28
T3 trigger	is the occurrence of at least two L1 hits in three consecutive storeys within a coincidence time window	59, 72, 81, 92
TimeSlice	The set of frames of a 13 ms time period	56, 71, 101
variability time	In a GRB, the variability time is the time in which its light curve changes considerably	15, 16, 18, 30

Acronyms

Notation	Description	Page List
AGN	Active Galactic Nuclei	5
ARS	Analogue Ring Samplers	49, 51–53, 71, 101
BATSE	Burst and Transient Experiment	9
BSS	Bottom String Socket	50, 54, 55
CC	charged current	4, 40, 42, 44–47, 65, 66, 75, 79, 97
CGRO	Compton Gamma Ray Observatory	9
CL	Confidence Level	104, 105, 107, 121, 129
COG	Center Of Gravity	75, 82
CP	Charge Parity	33
DAQ	Data Aquisition	51
DIS	Deep Inelastic Scattering	39

Notation	Description	Page List
DP	Discovery Potential	113
EGRET	Energetic Gamma-Ray Experiment Telescope	9
FPGA	Field Programmable Gate Array	53
GRB	Gamma Ray-Burst	5, 7, 9, 10, 12, 15–18, 21, 23–25, 27–32, 34, 35, 60, 89, 97, 99, 101–103, 108, 109, 125–127, 129, 131, 132
IL	Instrumentation Line	50
ISM	interstellar medium	21
JB	Junction Box	50, 99
LCM	Local Control Module	49–51, 53, 54
MDP	Model Discovery Potential	108, 113, 116
MEOC	Main Electro-Optical Cable	50
MRP	Model Rejection Potential	107, 108

Notation	Description	Page List
NC	neutral current	4, 40, 44–47, 65, 66, 75, 79, 90
OM	Optical Module	48, 49, 54, 71, 118, 119, 121, 123
OMF	Optical Module Frame	49, 50
p.e.	photo electrons	51–53, 69, 80, 83, 141
PeV	peta electronvolt = 10^{15} eV	45
PMT	Photomultiplier Tube	42, 43, 48, 49, 51–55, 57, 58, 62, 69, 71, 81, 83, 87, 98, 99, 118–122, 141
ppm	part per million	55
QE	Quantum Efficiency	49
ROV	Remotely Opertated submarine Vehicle	50
SCM	String Control Module	50
SN	identification number	13
SPM	String Power Module	50
SSC	Synchrotron self-Compton	27
TS	Time Stamp	52

Notation	Description	Page List
TTS	Transit Time Spread	49, 69, 87
TVC	Time to Voltage Converter	52
UHECR	Ultra High Energy Cosmic Ray	28

Acknowledgments

The amount of people I met, and I worked with, during these four years (and a half) of PhD is more than what I can fit in these few lines. This entire experience has formed my life and I will remember it forever.

To achieve this work I passed some very difficult moments, and I can say with no hesitation that I would be still struggling with ROOT and C++ if Corey would have not started to work with me. Most of what I learnt during these years I learnt it from him, and I cannot properly express my gratitude for this. Corey, you have been a great supervisor but, above all, a great friend, a good companion for the drinking nights, and a true Hollywood boy to watch movies with (at least the first bunch of favourite movies)! I really hope we will enjoy a nice Thanksgiving party together again, now that I am a turkey master!

Even if the work was done, this nice booklet would have never been published without the patient and meticulous corrections of my promoter Paul Kooijman, who has supported me and helped me until the very last moment of this work, and possibly even a bit further. It has been a great pleasure to work with Paul, his ideas about the future of neutrino physics are inspiring, but I admit to have especially enjoyed the motorbikes chats! I also need to thank Els de Wolf, for always put an eye on my work, and for the very wise career advice and discussion we had.

A person that I shall not forget to mention is Claudio Kopper: first from Erlangen, than from Amsterdam, he has been the most patient person I ever met, always available for explanations, help and support. Thanks to him I learnt a lot about C++, Python and, above all, IceTray. A continuous source of information and with a solution for every problem, Claudio is really a great person to work with. I would also like to thank Aart Heijboer. Since he (re)joined the group the atmosphere changed completely, and I was caught in his working enthusiasm. It has been very nice to drop by your office, ask you some stupid question, and maybe have a race with Mario Kart (not as many as I wished, though!). It is thanks to Aart that I had access to a nice set of data files, already selected by his knowledgeable hands.

Many people outside my group has been very kind to me. Juergen Brunner provided with continuous help on the computing problems, and his explanations were indispensable to understand the BBFit hit selection. I also need to thank Salvatore Galatà, for his effort in including BBFit into SeaTray.

A somehow constant figure during this years of PhD has been Teresa Montaruli. She helped

me enormously in understanding the physics and astrophysics in Antares, and she and her group provided a great support for the use of the NeutrinoFlux project. I really hope to have the chance to work with Teresa again in the future, as it has been always very instructive. As it has been working with Maurizio Spurio, who has been patient enough to study, improve and support my analysis. For this I am extremely grateful.

During my Antares experience I was lucky enough to have the chance to meet also some extraordinary IceCube people. Surely I have to mention Doug Cowen, always keen in giving me advices and suggestions. Besides the fruitful and interesting discussions about physics, I have to thank Doug for the several lunches and dinners he offered me, in multiple cities around Europe! A special thank goes to Patrick Toale, who helped me a lot in the use of IceTray and even provided me with some extremely useful pieces of code. Talking about code, I need to mention Marek Kowalski, who helped me enormously in the use of Neutrino Generator, and Dima Chirkin for the support in using MMC. My work is somehow on the shoulders of my predecessor, Claudine Colnard, who I thank for her effort in Monte Carlo chain comparison and, of course, for the nice time spent in Amsterdam together.

I also would like to thank all my group at Nikhef for the nice time spent together. Dimitris, my office mate for four long years, I will miss you every moment I am sitting in a office without you! It has been incredibly nice to meet you and to have the chance of spending so much time with you! And thank for showing me the Karate-Do, the way of karate! My other office mate, Akis, has increased the amount of "greekness" (and maybe also geekness) of the office, and for this I am very grateful. Guus, you have been a great and unique friend during my time in Amsterdam, and surely you will continue to be. Many gloomy days were brightened by our coffee breaks and many evenings by our fancy dinners. I will always remember our week in Germany, our several little holidays together and our infinite discussions! Mentioning coffee breaks, I cannot forget Jelena. A great friend, always ready to chat and to discuss about astrophysics, a person I am very happy to have met. Gordon has been a great mate from the very beginning of my PhD to the very end of it. My first shift, spent with you (and let's say it, sneaking in Marseille) has been by far my most enjoyable shift. And so all the parties and meeting and trips! All the meeting and lunches and parties were nicely accompanied by all my Nikhef friends and Antares among which Claudio (Boga), Giada, Ching-Cheng, Tri, Ronald, Michele, Francesco, all PhD students at Nikhef and all Antares memebers around Europe.

But a special thank to the Antares members of the group: Gerard, who hired me in the first place, and who supported me even after leaving the group, always ready to find a little time spot for me in his busy busy schedule. Patrick, with whom I had few but very useful discussions on my work, Maarten, Mieke, Dorothea and Jos.

A very special thank to Rob van der Meer, for the support, the suggestions and the help in applying for jobs.

My interest in Gamma Ray Burst has found a great mentor in Ralph Wijers, who has been very nice and extremely patient in explaining my the physics of GRBs and involved me in very interesting projects.

More than a thank, I would like to give a big hug to my great friends in Amsterdam, with whom me and Ermes spent a wonderful time. Ana and Pieter, always in for a movie/game night, a picnic or a drink in the city. Miruna and Bram, that showed us the very best of Amsterdam and are the greatest connoisseurs of the finest bars and restaurants in the city. Alex Hartsuiker, for his dutch lessons, dutch/indonesian cuisine and in general for the nice time spent together. Sipho, for his great and incalculable help in doing our tax work, but above all for his friendship and for the enjoyable time he shared with us.

A bit out of context, but certainly to remember is Alessio di Domizio, who offered me the possibility of writing about science for a broader public and had the perfect timing of asking me to do that in the very moment I needed it.

Last, but not least, my family. My parents, Sandra and Gianni, who made me for what I am, who supported me with all their power, from the moment of my birth to the rest of my life. Nothing of what I have or what I did could be possible without their continuous support, infinite patience and unconditioned love. I feel uniquely lucky to have such parents and I am very grateful for everything they have always been doing for me.

Ermes. Grazie.

Eleonora Presani
Amsterdam
April 20, 2011

Samenvatting

De zoektocht naar het begrip van ons heelal heeft de mensheid al sinds lange tijd ertoe gebracht om de hemel te bestuderen en processen die in de kosmos plaatsvinden te onderzoeken.

Eeuwenlang hebben we de bewegingen van de zon en de sterren gevolgd. Tegenwoordig richten wij ons echter meer op de processen, die diep in deze hemelse objecten plaatsvinden. We hebben in de loop der jaren veel geleerd maar er blijven nog altijd veel open vragen.

Een voorbeeld is de vraag waar kosmische stralen vandaan komen. Deze geladen deeltjes, die onze aarde bereiken, kunnen extreem hoge energieën hebben. Wat het precies voor deeltjes zijn en welke processen ertoe lijden dat ze tot deze energieën versneld zijn, zijn vragen, die nog niet opgelost zijn. De energie die zulke deeltjes bereiken zijn van macroscopische grootte. Vandaar dat voor de oorsprong van zulke deeltjes gekeken wordt naar de hoogst energetische objecten, die we kennen in het heelal. Voorbeelden van zulke objecten zijn de Actieve Galactische Kernen (AGN) en Gamma Flitsers (GRB).

AGNs komen in het midden van bepaalde melkwegstelsels voor en zijn zeer compacte objecten die continu straling uitzenden. Ze zijn de meest intense bronnen van straling in het heelal, in welk golflengte gebied dan ook. Deze straling wordt, zo denkt men, veroorzaakt door het opnemen van materie door een supermassief zwart gat dat zich in het midden van het melkwegstelsel bevindt.

Gammaflitsers zijn korte maar zeer intense flitsen van gamma straling, die een paar keer per dag in het voor ons zichtbare heelal voorkomen. De intensiteit van deze straling overtreft alle andere bronnen van gamma straling. De GRBs hebben hoogst waarshijnlijk hun oorsprong in de dood van een zeer massieve ster die tot een zwart gat ineenstort. Een ander mogelijk proces is het samengaan van twee compacte massieve objecten, zoals een zwart gat of een neutronen ster. Het proces dat tot de flits van straling leidt is vooralsnog niet volledig begrepen. Hoewel er vele modellen zijn die in staat zijn sommige waarnemingen te kunnen verklaren, blijft het zo dat geen enkel model alle waarnemingen verklaart. Om de processen die aan de Gammaflitsers ten grondslag liggen beter te kunnen begrijpen zou het voordelig zijn om neutrinos te kunnen waarnemen die bij de GRB explosie vrij zouden kunnen komen. Hiermee zou het bewijs geleverd kunnen worden dat de GRB zijn oorsprong heeft in hadronische (proton) interacties. Als dit bewezen zou kunnen worden, dan zou de GRB een unieke candidaat zijn om als bron van de hoog energetische kosmische stralen te dienen.

Het waarnemen van hoogenergetische neutrinos is een bijzondere uitdaging. Deze deeltjes interageren alleen via de zwakke wisselwerking en daardoor passeren ze bijna ongestoord door materie heen. Om toch een kleine maar niet verwaarloosbare kans te hebben een interactie waar te nemen is het daarom noodzkelijk een zeer grote detector te hebben. Neutrinos zijn alleen via hun wisselwerking met materie waar te nemen. Daarbij moet rekening gehouden worden dat zij in drie verschillende gedaaantes voorkomen. Een die bij het electron hoort, een die bij het muon hoort, en een die zich bij het zwaardere tau-lepton schaart. Het muon soort is de minst moeilijke waar te nemen, aangezien het muon dat in de interactie met materie wordt geproduceerd, een lange weg door materie kan afleggen. Aangezien dit deeltje geladen is, zendt het, als het door een transparant medium beweegt, zogenaamde Cherenkov straling uit. Dit gebeurt als zijn snelheid boven de lichtsnelheid in het medium uitgaat. Het licht van de Cherenkov straling is dan waar te nemen, waarmee het spoor van het muon is te reconstrueren. Om neutrinos waar te nemen is dus een groot volume aan transparant materiaal nodig.

Dit verklaart dan ook waarom de Antares detector is opgebouwd in de Middellandse Zee. Het bestaat in feite uit een driedimensionale matrix van lichtsensoren. De sensoren hangen aan verticale kabels die 450 m vanaf de bodem van de zee oprijzen. Het water van de zee dient als het transparante medium. De detector heeft een volume van zo'n twintigste van een kubieke kilometer.

Zoals gezegd komen de neutrinos in drie gedaantes voor en ieder van die neutrinos interageert op zijn eigen manier met de materie. Bij de interactie kan een geladen zwak boson worden uitgewisseld en de neutrinos veranderen daarbij in hun geladen partner (muon neutrino naar muon, electron neutrino naar electron en tau neutrino naar tau). Tegelijkertijd zal de kern waarmee de interactie wordt aangegaan een hoeveelheid deeltjes produceren. Een zogenaamde hadronische cascade. Een tweede proces kan verlopen via het uitwisselen van een neutraal boson. Bij dit soort interacties wordt de cascade gevormd maar de neutrino verandert niet van gedaante. Electronen en taus veroorzaken ook cascades van deeltjes in het zeewater. De deeltjes in deze cascades bewegen ook sneller dan het licht in water en zenden dus Cherenkov licht uit. Dit licht lijkt, omdat de ruimtelijke uitgebreidheid van de cascades klein is in vergelijking met de afstand tussen sensoren, uit een punt te komen en gedraagt zich dus wezenlijk anders dan het licht dat geproduceerd wordt door een lang muon spoor. Dit proefschrift gaat vooral over het detecteren van cascades. De signatuur van deze cascades heeft aanmerkelijk meer last van achtergrond veroorzaakt door deeltjes afkomstig uit de interacties van kosmische straling met de atmosfeer. Gammaflitsen zijn zeer kort, hierdoor is de tijd waarin een neutrino signaal te verwachten is ook kort. Door op de korte tijd dat de GRBs actief zijn te concentreren is het mogelijk de achtergrond voldoende te onderdrukken.

Dit proefschrift presenteert een reconstructie algorithme die voor Antares is ontwikkeld en waarmee het mogelijk is om de tijd en de positie van cascade gebeurtenissen te reconstrueren. Er is in de Antares data van 2008 gezocht naar cascade gebeurtenissen die plaatsvonden in een klein tijdvenster om de tijd waarop GRBs gedecteerd werden door sateliet experimenten. De achtergrond werd gekarakteriseerd door de volledige Antares data ver weg in tijd van de GRBs te analyseren. De snedes werden ingesteeld om het ontdekkings potentieel maximaliseren. Uiteindelijk zijn tien GRBs die in 2008 plaatsvonden geanalyseerd. Er zijn geen gebeurtenissen waargenomen tijdens te GRB periodes. Hierdoor kon een bovenlimiet voor de neutrino intensiteit van ieder van de GRBs worden vastgesteld.

Deze analyse vult de analyses gebaseerd op spoor reconstructie aan. De gevoeligheid is wat minder goed maar daar staat tegenover dat deze analyse infeite gevoelig is voor alle types neutrino. Het vertegenwoordigt de eerste stap in de richting van waarnemen van neutrinos geproduceerd in GRBs. Het volle potentieel zal waarschijnlijk slechts bij de detector die de opvolger wordt van Antares, KM3NeT, worden gerealiseerd. Deze detector waarvoor nu de plannen in een vergevorderd stadium verkeren zal zo'n vijftig tot honderd keer zo groot zijn als Antares. Dit zal leiden tot een enorme verbetering in gevoeligheid. Hierdoor lijkt het niet onmogelijk dat terwijl hier slechts een bovenlimiet kon worden gerealiseerd, dat in de nieuwe detector dit tot een ontdekking zal leiden.